Atomistic modelling of irradiation-induced microstructure evolution in Fe alloys

EBRAHIM MANSOURI

Doctoral Thesis
Stockholm, Sweden, 2024

KTH Royal Institute of Technology
Department of Physics
Nuclear Science and Engineering
SE-10691 Stockholm
Sweden

TRITA-SCI-FOU 2024:28
ISBN 978-91-8040-951-3

Akademisk avhandling som med tillstånd av Kungl Tekniska högskolan framlägges till offentlig granskning för avläggande av Teknologie doktorexamen i fysik fredagen den 14 juni 2024 klockan 13.30 i FB52, AlbaNova, Roslagstullsbacken 21, Kungliga Tekniska Högskolan, Stockholm.

Tryck: Universitetsservice US AB

Abstract

The nuclear reactors of the future require materials that are exceptionally resistant to irradiation-induced degradation. This study presents a theoretical framework, combining density functional theory and interatomic potential methods, to predict microstructural evolution in Fe-based alloys and oxides (Al_2O_3) subjected to damaging irradiation. Our research employs a powerful creation-relaxation algorithm to simulate defect formation and microstructure development under intense irradiation.

We present the pioneering implementation of a first-principles quantum mechanical approach for directly modelling the microstructural evolution of magnetic materials and ceramics under irradiation. A crucial aspect of studies involves investigating the influence of the spatial distribution of Frenkel-pairs (FPs) on the microstructural evolution in Fe. Our findings reveal that spatially localised FP distributions, replicating low-energy transfer irradiation conditions, predict a significantly more moderate microstructure development compared to uniform distributions. This highlights the importance of considering the FP distribution for an accurate prediction of the formation and growth of the dislocation segments under low-energy irradiation conditions.

Furthermore, first-principles calculations suggest that irradiation-induced excess energy can trigger polymorphism in bcc Fe, leading to magnetic instabilities, localised structural constriction, and ultimately local phase transformations. Consequently, under extreme conditions, α-Fe undergoes local transformations into three-dimensional, non-parallel C15 Laves phase structures with highly close-packed stacking and internal short-range ferromagnetism. Notably, the inclusion of antiferromagnetic chromium in bcc Fe significantly enhances the stability of C15 interstitial clusters in concentrated FeCr alloys.

Beyond these structural insights, the investigation delves into the intricate interplay between atomic constituents and their profound impact on the nonlinear magnetic properties of FeCr systems under irradiation. A striking correlation emerges, revealing that the chromium content directly influences the appearance of swelling, a key phenomenon following irradiation-induced damage. Increasing the chromium content mitigates irradiation-induced swelling by approximately 40%, compared to pure Fe, highlighting the profound effect of alloying in Fe-based alloys.

In addition, our first-principles simulations of irradiation-induced damage in bcc FeCrAl and hcp Al_2O_3 predict that while there are relatively small differences in total defect number densities among bcc Fe and its alloys, there are significant discrepancies in defect concentrations between these bcc structures and hexagonal Al_2O_3. Notably, the surviving FP content in alumina is seven times higher than that recorded for FeCrAl alloys. Consequently, the different build-up of surviving damage in Fe alloys and alumina leads to diverse levels of swelling in the irradiated materials, with a remarkable three times higher swelling observed in alumina upon reaching a saturation state after an irradiation dose of approximately 1 displacement per atom (dpa). Furthermore, our observations of amorphous phase formation in damaged corundum alumina, as predicted in this study, corroborate that there are significant irradiation-induced effects in alumina.

These findings not only deepen our fundamental understanding of the responses of structural materials to irradiation, but also pave the way for advanced materials engineering with potential applications in near-future nuclear reactor components.

Sammanfattning

Framtidens kärnreaktorer kräver material med enastående motståndskraft mot strålningsinducerade skador. Denna studie presenterar ett teoretiskt ramverk som kombinerar täthetsfunktionalteori och interatomära potentialmetoder, för att förutsäga mikrostrukturell utveckling i Fe-baserade legeringar utsatta för hårda strålningsmiljöer.

Med fokus på bcc Fe, FeCr, och FeCrAl-legeringar använder vår forskning en sofistikerad algoritm som skapar och relaxerar defekter i gittret för att simulera defektbildning och mikrostruktursutveckling under bestrålning. Vi presenterar här den första studien som använder den här algoritmen med kvantmekaniska förstaprincipersberäkningar som grund för att simulera strålskador direkt i magnetiska material.

En avgörande aspekt av studierna är att undersöka inflytandet av hur den rumsliga fördelningen av Frenkel-par (FP) påverkar den mikrostrukturella utvecklingen i järn. Våra resultat visar att lokaliserade FP-fördelningar, som reproducerar strålningsförhållanden med låg energiöverföring, signifikant mildrar mikrostruktur utvecklingen jämfört med jämnt fördelade FP. Detta understryker vikten av att ta hänsyn till FP-fördelning för korrekt förutsägelse av dislokation ssegmentbildning och tillväxt under lågenergistrålning. Vidare visar förstaprincipberäkningar att strålningsinducerad överskottenergi kan utlösa polymorfism i bcc Fe, vilket leder till magnetisk instabilitet, lokaliserad strukturell begränsning och slutligen lokal fasomvandling. Följaktligen genomgår α-Fe lokala omvandlingar till tredimensionella, icke-parallella C15 Laves fasstrukturer med tätt packade staplingar och intern lokal ferromagnetism under extrema förhållanden. Noterbart är att inkluderingen av antiferromagnetiskt krom i bcc Fe betydligt förbättrar stabiliteten hos interstitiella kluster av C15-typ i koncentrerade FeCr-legeringar.

Utöver dessa strukturella insikter fördjupar undersökningen det komplicerade samspel mellan atomära beståndsdelar och deras djupgående påverkan på de icke-linjära magnetiska egenskaperna hos FeCr-system under bestrålning. En slående korrelation framträder, vilket avslöjar att kromhalten direkt påverkar uppkomsten av svällning, ett avgörande fenomen som kan induceras av bestrålning. Ökande kromhalt mildrar strålningsinducerad svällning med cirka 40%, vilket understryker den avgörande effekt som legering med krom har.

Med hjälp av första-principersberäkningar har vi även simulerat strålskadebeteende i bcc FeCrAl och i Al_2O_3. Vi visar att det är relativt sett små skillnader mellan de olika legeringarnas gensvar, emedan oxiden utvecklas på ett betydande annorlunda sätt. Antalet överlevande FP är sju gånger högre i oxiden än i metallerna, och den resulterande nivån av svällning är tre gånger högre när mikrostrukturell mättnad uppnås efter ca 1 dpa. Vidare ser vi att aluminiumoxiden börjar genomgå en strukturell amorfisering, vilket påvisar att strålskador har betydande inverkan på oxiden.

Dessa fynd fördjupar inte bara vår grundläggande förståelse av strukturmaterialens svar på bestrålning, utan banar också väg för avancerad materialteknik med potentiella tillämpningar inom nära-framtida komponenter för kärnreaktorer.

List of publications

Included publications

I **E. Mansouri** and P. Olsson, *Microstructure and magnetization evolution in bcc iron via direct first-principles predictions of radiation effects*, Physical Review Materials, 2023; 7:123604.

II **E. Mansouri** and P. Olsson, *Modeling of irradiation-induced microstructure evolution in Fe: Impact of Frenkel pair distribution*, Computational Materials Science. 2024; 236:112852.

III **E. Mansouri** and P. Olsson, *First-principles predictions of structural and magnetic phase stability in irradiated* $\alpha - Fe$, Materials Research Letters, 2024; 2347305.

IV **E. Mansouri** and P. Olsson, *Ab initio predictions of irradiation-induced imperfections in FeCr: alloying effects and magnetic ordering on C15 Laves phase stability*, Submitted to Physical Review Letters.

V **E. Mansouri** and P. Olsson, *Atomistic modelling of irradiation-induced microstructure evolution in FeCrAl and* Al_2O_3*: effects of high irradiation doses*, Manuscript in preparation.

Author's contributions

The author conducted all calculations, formal analysis, provided interpretations and conclusions for the results and wrote all the Papers.

Funding and computational resources

This work was financially supported by the Swedish Foundation for Strategic Research (SSF) under Grant No. ARC19-0043 (SUNRISE centre) and the Swedish Research Council (VR) (projects 2017-06458 and 2019-04156). The EUROfusion Consortium (Grant No. 101052200) and the Euratom Research and Training Programme (M4F project No. 755039 and IL TROVATORE project No. 740415) also provided funding (2019-2020). Computational resources were granted by NAISS (PDC at KTH and NSC at LiU) and the CINECA HPC Center. The views expressed are the authors' own and do not reflect the views of the European Union or the European Commission.

Acknowledgement

The pursuit of my Ph.D. in Sweden has been a vigorous journey, demanding determined perseverance and resilience. The complexities of navigating the immigration process presented unforeseen obstacles that tested my resolve. Quite disappointingly, I have encountered instances of discrimination and prejudice from various Swedish institutions, including the Migration Agency, the Security Police, and even the legal system. This experience of discrimination within a nation often considered advanced is deeply concerning and forces me to speak out. In the coming years, I plan to document these events in a book, exposing the injustices I faced and advocating for systemic change that promises fairness and equality.

Undoubtedly, my Ph.D. journey has been punctuated by moments of inspiration and growth. Among these, I found dedicated support in the mentorship of my esteemed supervisor, Professor Pär Olsson. His consistent trust, insightful guidance, and enriching discussions have played a pivotal role in shaping my academic trajectory over the past years.

Although my research has not involved extensive discussions with my second supervisor, Professor Janne Wallenius, I would like to express my appreciation for his insightful contributions during the courses I took with him.

Furthermore, I express my sincere gratitude to my respected colleagues in Nuclear Science and Engineering Division within Department of Physics, particularly Torbjörn, Farnaz, and Faris, whose guidance and encouragement have been invaluable. I also extend my thanks to my dear friends Hamid, Halimeh, and Ghafour for their uplifting conversations and infectious positivity that fuelled my determination to finish my studies.

I also would like to thank my former office mate, Yulia, for the warm conversations and the companionship we shared which were a source of strength and encouragement.

To my love, Arezoo, words cannot express my gratitude for your unwavering support, loyalty, and patience throughout this challenging journey. You have helped me immensely navigate difficult times and personal challenges. Perhaps while I am receiving my Ph.D. in Physics, you have already earned yours in emotional resilience and feeling management. Your uniqueness, my love, is a treasure I will forever cherish.

While pursuing my Ph.D., I learnt the valuable lesson of balancing commitment

with family needs. I am incredibly grateful for the patience of my parents and in-laws, despite the sacrifices they made during my long absences.

Finally, I dedicate this thesis to the countless women, worldwide and particularly in Iran, whose committed pursuit of freedom and equality echoes in the powerful chant "Woman, Life, Freedom."

Acronyms

AF	Antiferromagnetic
AFD	Double-layer antiferromagnetic
bcc	Body-centred cubic
CRA	Creation-relaxation algorithm
DFT	Density Functional Theory
DOS	Density of states
dpa	Displacements per atom
EAM	Embedded atom method
fcc	Face-centred cubic
FM	Ferromagnetic
FP	Frenkel pair
FPI	Frenkel pair insertion
FR	Full relaxation
hcp	Hexagonal close packed
IAP	Interatomic potential
IR	Ionic relaxation
KMC	Kinetic Monte Carlo
LDF	Localised distribution function
MD	Molecular dynamics
NM	Non-magnetic
PKA	Primary knock-on atom
PTM	Polyhedral template matching
SIA	self-interstitial atom
SQS	Special quasi-random structure
TEM	Transmission electron microscopy
UDF	Uniform distribution function
VASP	Vienna *Ab initio* Simulation Package
at.%	Atomic percentage
wt.%	Weight percentage

Contents

List of publications **v**

Acknowledgement **vii**

Acronyms **x**

Contents **1**

List of Figures **3**

List of Tables **7**

1 Introduction **9**
1.1 General overview 9
1.2 Structural materials for near-future nuclear reactors 10
1.3 Radiation-induced damage in materials 11
1.4 Multiscale modelling of irradiation damage 13
1.5 Thesis objectives 15

2 Methodology **17**
2.1 Creation-relaxation algorithm (CRA) 17
2.2 Determination of irradiation-induced structural changes 20
2.3 Spatial distribution of Frenkel pair insertion 21
2.4 Forbidden zone radius 23
2.5 *Ab initio* electronic structure calculations 24
2.6 Embedded atom method (EAM) 27
2.7 Atomic simulation procedures and analysing tools 28

3 Results and discussion **31**
3.1 Simulation cell size and spatial distribution of FPs 32
3.2 Irradiation-induced microstructure evolution in Fe 33
3.2.1 Dislocation loop nucleation and saturation in Fe 37
3.2.2 C15 Laves phase formation in Fe 40

3.3 Radiation-induced demagnetisation in Fe 42
3.4 Irradiation-induced polymorphism in Fe 44
3.5 Microstructure evolution in Fe alloys 47
3.5.1 The C15 Laves phase structure in FeCr alloys 50
3.5.2 Radiation-induced magnetisation and structural change in FeCr 54
3.6 Radiation-induced damage in FeCrAl and Al_2O_3 56
3.6.1 Radiation-induced damage in FeCrAl 57
3.6.2 Radiation-induced damage in Al_2O_3 59

4 Conclusions and outlook **63**

Bibliography **67**

Appended papers **81**

List of Figures

2.1 Flowchart of the CRA model for simulating irradiation damage events and modelling microstructure evolution up to the desired dose limit ϕ. . 19

2.2 Plot of PDFs of standard $\Gamma(\alpha, \theta)$ distribution function for various shape and scale parameters. 23

2.3 The change in a) total energy, b) global pressure, and c) local magnetic moment (μ) of SIAs as a function of approaching distance of atoms forming a $\langle 110 \rangle$-dumbbell. 24

3.1 Comparison of cell size effects on evolution of hydrostatic pressure as a function of irradiation dose within MD-CRA method, using different FP distribution functions in supercells of sizes a) $8 \times a_0$ and b) $50 \times a_0$. . 33

3.2 The dose-dependent evolution of the total number of survived a) FPs, b) I_{mono}, c) I_{C}, along with d) the average sizes of the I_{C} predicted with UDF and LDFs of the SIAs. 35

3.3 Comparison of number densities of a) isolated vacancy and interstitial, b) I_{C} and V_{C}, along with their related c) average and d) largest vacancy and interstitial clusters a function of irradiation dose. 36

3.4 Comparison of interstitial concentration as a function of FP insertion (dpa) predicted by DFT, EAM-M03, and EAM-M07 methods within supercell sizes of 8 and $50 \times a_0$. 37

3.5 The dose-dependent evolution of a) the total DLDs accompanied by directional DLDs with b) $1/2\langle 111 \rangle$, c) $\langle 100 \rangle$, and d) $\langle 110 \rangle$ Burgers vectors for uniform and localised distributions of the SIAs in the supercell size of $50 \times a_0$. 38

3.6 Evolution of cumulative irradiation-induced damage in bcc Fe according to the predictions of the MD-CRA model. The initial nucleation of the dislocation loops occurs around 0.05 dpa, followed by continuous growth until approximately 0.25 dpa. Subsequently, loop coalescence leads to the formation of extended dislocation lines and networks, stabilising at a steady-state length beyond 2 dpa. Dislocation segments featuring $1/2\langle 111 \rangle$ and $\langle 100 \rangle$ Burgers vectors are depicted in green and purple, respectively. 39

3.7 Comparative analysis of the largest C15 clusters generated in irradiated bcc Fe applying MD-CRA simulation with a) EAM-ME03 and b) EAM-MA07 potentials. 41

3.8 The structural backbone of a representative C15-type configuration (blue atoms) predicted by DFT-CRA simulation, characterised by a triangular arrangement of di-interstitial and a hexagonal tri-interstitial ring. The orange clouds, enveloping atoms with spin-down orientation (blue arrows), represent the three-dimensional spin density isosurfaces of atoms that underwent spin flip or quench. Red arrows attached to atoms symbolise the corresponding spin-up orientations. 41

3.9 The average global magnetisation of damaged bcc Fe per atom as a function of irradiation dose. 42

3.10 Variation of local magnetic moments with atomic volumes in damaged bcc Fe structure compared to undamaged. The vertical dashed line separates the LV/LS and HV/HS regions, illustrating the deviations. δM represents reduction in total magnetisation due to irradiation-induced volume expansion (ΔV). 44

3.11 Distribution of local μ of all individual atoms of damaged bcc Fe in relation to their local Ω_a at a dose of 0.22 dpa. The data points (μ - Ω_a) are compared with two aspects: (a) magneto-volume relationships in different iron structures and (b) the equations of state of iron in various magnetic states relative to the α-Fe ground state energy. A black-dashed line divides the LV/LS and HV/HS regions, highlighting discrepancies in the local magnetic moments and atomic volumes of individual atoms in the damaged α-Fe compared to the undamaged bcc structure. In the right panel, the blue-dotted line represents the equilibrium atomic volume of NM/AF ϵ-Fe, while blue-shaded regions indicate volume expansion (ΔV) in damaged α-Fe. Additionally, for better comparison, the magneto-volume curve for the C15-FM structure is inverted to show anti-parallel spin orientation with respect to the host bcc lattice atoms. 46

3.12 The comparison between the partial PDOS and the IDOS of C15-type atoms pre- and post-irradiation: (a) demonstrates the transfer of charge from majority to minority states prior to irradiation, while (b) presents the established partial DOS of atoms comprising the imperfect C15 Laves phase structure post-irradiation. Vertical dashed lines indicate the Fermi energy levels, designated at $E_{\mathrm{F}} = 0$. 46

3.13 Dose-dependent number density of a) FP, b) I_{mono}, and c) I_{C} for different Fe and FeCr systems. 48

3.14 Dose-dependent number density of a) V_{mono} and b) V_{C} for different Fe and FeCr systems. 49

3.15 A comparison between the dose-dependent average size of a) interstitial clusters and b) vacancy clusters in Fe and FeCr alloys. 49

3.16 (a) Population of atoms with C15-type atomic structure and (b) the largest C15 cluster formed in Fe and FeCr alloys as a function of irradiation dose. 50

3.17 A typical perfect C15 cluster (I_2^{C15}) incorporated in a SQS-Fe-5 Cr matrix, represented with yellow-coloured bonds. The golden and dark-blue spheres symbolise Fe and Cr atoms, respectively. 51

3.18 Difference in formation energies of interstitial clusters with C15 and ⟨110⟩-dumbbell configurations as a function of Cr content. 52

3.19 Comparison of the size of C15 clusters formed in damaged bcc a) Fe-10 and b) Fe-15 at.% Cr, respectively. The orange clouds, enveloping atoms with spin-down orientation (blue arrows), represent the three-dimensional spin density isosurfaces of atoms that underwent spin flip. The red arrows symbolise the spin-up orientations. Pink atoms represent host lattice atoms, while blue atoms without attached arrows underwent spin quench. 53

3.20 Representation of the distribution of local magnetic moments of individual atoms within damaged bcc Fe and FeCr alloys relative to their respective local atomic volumes at an irradiation dose of approximately 0.1 - 0.2 dpa. The individual C15 clusters, separately formed in each system, with corresponding μ - Ω_a distribution in blue-circled points are depicted to illustrate their magnetic moment alignments in Fe and FeCr alloys. The green and orange data points represent the μ - Ω_a relationships for Fe and Cr atoms, respectively. 54

3.21 Dose-dependent evolution of averaged irradiation-induced swelling in Fe and FeCr systems. (b) DFT prediction of swelling as a function of Cr content for pure Fe and binary FeCr alloys. 55

3.22 Averaged change in global M per atom relative to corresponding swelling in various Fe and FeCr systems. The left panel (a) displays the results of DFT-IR calculations ($\Delta P/B$), while the right panel (b) presents the outcomes of DFT-FR calculations ($\Delta V)/V_0$) for several snapshots of the CRA trajectories. In the right panel, dashed lines fitted to the data points depict instances where ΔM) has not yet reached saturation values. 56

3.23 Dose-dependent number density of the a) FP, b) I_{mono}, and c) I_{C} for Fe, Fe-10 at.%Cr and Fe-10 at.%Cr with different Al content. 57

3.24 (a) Population of C15-type atomic structure and (b) the largest C15 Laves phase structures formed in Fe10%Cr with diverse Al contents as a function of irradiation dose. 58

3.25 The largest C15 clusters formed in irradiated bcc Fe-10%Cr-6%Al applying DFT-CRA simulation. Orange spheres are Fe, blue spheres are Cr and teal spheres are Al. 58

3.26 Dose-dependent evolution of the number densities of a) FP, b) isolated defects, and c) defect clusters formed in α-Al_2O_3. 59

3.27 Comparison of irradiation-induced swelling in Fe-based alloys and in Al_2O_3. * Swelling in Al_2O_3 was simulated with the method of simultaneously implanting five FP at a time. 61

List of Tables

3.1 Comparison of defect number densities across different spatial distributions of SIAs within dose intervals of 1.75 to 2 dpa. The table presents the defect number densities of survived FP, isolated defects, and defect clusters, along with the percentage difference relative to the UDF. Negative values indicate a reduction compared to the UDF. 34

Chapter 1

Introduction

1.1 General overview

With the expanding global population, the dependence on energy is on the rise, fuelled by increasing demands due to the advent of new technologies and extensive development, causing additional energy needs for improving quality of life. Therefore, ensuring secure and stable long-term energy supplies which address diminishing fossil fuels and global climate change underscores the demand for more diverse and reliable energy resources.

Despite significant growth in installed capacity, the intermittency of renewable energy sources still makes them impractical for base-load power generation. Thus, it would be prudent to also invest in new base load-capable nuclear energy systems while extending the life of the current reactor fleet, which demonstrated remarkable safety, accessibility, cost-efficiency, and environmental sustainability. Consequently, ongoing efforts focus on the development of near-future fusion and Generation-IV nuclear reactor technologies. For example, the International Forum on Generation-IV [1] aims to address technological challenges in various domains, including sustainability, safety and reliability, proliferation resistance, and physical protection under extended service or even accident conditions.

Undoubtedly, the selection of structural materials for developing Generation-IV nuclear reactor technologies poses significant challenges. Enhanced economics and reliability are prerequisites for each Generation-IV system, and an improvement in structural material performance would facilitate higher operating temperatures and pressures, longer lifetimes, and reduced downtime. As such, the greatest material challenges include addressing issues related to irradiation resistance, enhancing the high-temperature strength, and optimising mechanical properties for stable performance.

The primary objective of this study is to improve the theoretical models available using both first-principles approaches and semi-empirical interatomic potentials for predicting and investigating irradiation-induced microstructural evolution in

various sets of model materials based on iron, chromium and aluminium. This chapter provides a brief review of irradiation-induced damage in structural materials and summarises the scopes of the thesis project.

1.2 Structural materials for near-future nuclear reactors

For the emerging concepts of Generation-IV and fusion nuclear reactor technologies, enormous efforts have been dedicated to develop new materials and evaluate the performance of proposed structural materials intended to operate as core components or close to the core. The fusion and Generation-IV reactors are designed to operate under extreme conditions. In particular, most Generation-IV concepts are engineered to operate under elevated temperatures, intense fast neutron fluxes, and exposure to corrosive coolants such as liquid lead or molten salt [2]. Additionally, the Generation-IV program aims for prolonged plant lifetimes of up to 60 years, enhanced fuel burn-ups, and extended cycle lengths when compared to current reactor designs [3].

Consequently, mechanical stability and irradiation resistance become critically important factors for withstanding such challenging environments for longer time spans. Among the different proposed options, high-chromium ferritic and ferritic-martensitic steels, along with advanced steel grades, such as oxide dispersion-reinforced alloys, are currently considered prospective structural materials suitable for use in reactor core components, specifically in applications such as fuel cladding and wrapper materials [4–6]. This preference comes from their ability to satisfy stringent high-dose requirements, mainly due to their exceptional resistance to void swelling [7] and reduced thermal expansion compared to, for example, austenitic steels [8].

Furthermore, to enhance the corrosion resistance of fuel cladding composed of ferritic steel in corrosive heavy metal coolants, especially in liquid-lead fast reactors, the incorporation of aluminium has proven to be effective [9,10]. This additive element forms a highly oxidation-resistant layer on the outer surface, creating a protective Al_2O_3 scale, either as self-healing alumina forming alloys or as coatings, at elevated temperatures in steam or liquid-lead environment. Consequently, FeCrAl ferritic alloys are being considered to replace Zircaloy due to their superior corrosion resistance at high temperatures, following the Fukushima nuclear power plant accident [6,11]. In practice, a specific FeCrAl alloy, i.e., Fe-10 at.% Cr-4 at.% Al, is already being produced on a large-scale in Sweden and is currently undergoing investigation to assess its mechanical properties, performance, and resistance to corrosion and erosion in liquid lead [12–15].

Still, it remains crucial to continue both theoretical and experimental investigations into irradiation-induced damage in Fe-based alloys. Therefore, numerous studies have been conducted to show irradiation-induced formation of defect structures in Fe-based alloys. These structures encompass both point defects and clusters of defects, which can be further aggregated into larger clusters. Specifically,

vacancies agglomerate onto voids and vacancy-type dislocation loops, while interstitials can combine to form C15 Laves phase structures [16, 17] and interstitial-type dislocation loops [18–20]. The following section will present a brief review of irradiation-induced degradation, addressing the topic broadly in terms of structural materials and delving specifically into its implications for Fe-based alloys.

1.3 Radiation-induced damage in materials

Studies on irradiation-induced damage, at its core, investigate the interactions of energetic particles such as neutrons, charged particles, or electromagnetic radiation with atoms and ions within materials. This expansive field of research holds paramount significance not only in the domain of nuclear reactor technology but also within the broader scope of basic material science. It serves as a fundamental exploration, shedding light on the intricate physical properties influenced by irradiation.

The primary radiation damage event begins when an energetic particle collides with a solid material and transfers a portion of its kinetic energy to lattice atoms, displacing them from their original positions. If the transferred energy exceeds the displacement threshold energy [21], a stable pair of defects consisting of a vacancy and a self-interstitial atom (SIA), a so-called Frenkel pair (FP), is formed. Energy transfers in the range of a few tens of electron volts are sufficient to induce atomic displacements to generate FPs. In a typical nuclear reactor environment, neutrons boast energies up to a few MeV, enabling their energy transfer to lattice atoms to exceed the displacement threshold and knock the atoms out of their lattice positions [22]. The displaced primary knock-on atom (PKA) engages with neighbouring atoms, conveying energy to them and also displacing them. Gradually the displaced atoms come to a stop. Many of these energy transfers are forceful enough to displace significant amounts of additional atoms, initiating a cascade event in which one displacement triggers others [23]. Thus, recoiled atoms vacate their original positions, creating vacancies. Some of the displaced atoms come to occupy interstitial sites. These vacant positions (vacancies) and interstitial sites (SIAs) are individually classified as point defects [24]. It is evident that the number of interstitials is precisely equal to the number of vacancies produced.

The quantity of FPs generated is also referred to as the number of displacements, and their cumulative density is expressed as the number of displacements per atom (dpa). As described by Kinchin and Pease [22] and quantified by Norgett *et al.* [25], the dpa, indicated by ϕ, is a dimensionless positive definite parameter used to express irradiation exposure dose. As this quantity reaches unity, on average each atom has undergone a displacement once.

As a result, understanding the relevant properties of irradiated materials is elucidated by tracking the fate of the two key crystal defects created during the primary event of radiation damage, namely vacancies and SIAs or simply FPs [26]. It is important to note that the preceding depiction of primary damage represents a

simplified model for radiation damage. In the crystallographic context of the metal lattice, energy and atoms can traverse significant distances from the cascade core through mechanisms like focusing, channelling, replacement collisions, or propagation as crowdions [27]. Following this, SIAs often organise into a diffuse shell around the cascade edge, while the core, often referred to as a depleted zone, becomes enriched with vacancies, as illustrated in theoretical models and simulations [28–31].

Combined theoretical and experimental studies of body-centred cubic (bcc) tungsten [32, 33] have revealed that cascade events can directly generate extended defects like vacancy and interstitial clusters even at very low temperatures, where both vacancies and SIAs are typically immobile due to thermal limitations [34]. The formation of these defect clusters likely arises from athermal interactions, such as those driven by elastic interchanges or expanded strain fields induced by energetic irradiating particles or PKAs [35]. Additionally, the kinetic energy transferred directly from the recoil event during the collision cascade may also play a role in the interaction between these immobile defects and those newly created through the collision process [26].

During prolonged irradiation, point defects undergo evolution due to thermally activated diffusion but also through propagated elastic deformation. Some defects annihilate, while others form defect clusters independently or in conjunction with solute atoms, forming extended defects. The accumulation of such defects and clusters leads to the formation of complex microstructural segments, including voids, dislocation loops, radiation-enhanced or induced solute segregation in alloys, and precipitation of secondary phases [36–38]. These microstructures and their evolution cause significant changes in the physical and mechanical properties of the materials. Hardening, embrittlement, and dimensional changes such as creep, growth, and swelling are typical examples of macroscopic effects of irradiation [39–41]. Subsequently, alloys with high resistance to the adverse effects of irradiation are of great technological interest for the nuclear energy sector.

As previously noted, Fe-based alloys, including FeCr and FeCrAl, have emerged as promising candidates for utilisation in upcoming nuclear reactors due to their exceptional resistance to irradiation-induced degradation, high-temperature stability, and mechanical strength, and the latter case, significantly enhanced corrosion resistance [4, 42]. Consequently, comprehending their response to irradiation and anticipating their behaviour under such conditions hold profound significance in the realms of material science and engineering. This understanding is crucial in various applications such as material processing [43], the confinement of radioactive waste [44], and advanced nuclear reactor technology [45], where materials are consistently exposed to irradiation in the form of gamma photons and energetic particles.

Finally, numerous theoretical and experimental studies, as well as research programmes, have been carried out to explore the impact of irradiation on the physical and mechanical properties of actual or model materials [46–51]. However, due to limitations in nano-scale analysis capabilities, experimental observations of irradiation-induced microstructure evolution remain relatively scarce at the atomic

level [52]. Therefore, in recent years, extensive efforts have been dedicated to the development of multiscale modelling approaches. These approaches aim to facilitate a comprehensive understanding of the relationship between microstructure evolution and changes in the physical properties of irradiated materials [37, 53–55].

1.4 Multiscale modelling of irradiation damage

In recent years, materials science has undergone a dramatic transformation thanks to the rise of multiscale computer modelling. This has been fuelled by two key factors: a surge in computing power and breakthroughs in simulation methods and theory [56–58]. As a result, it is now possible to create incredibly detailed simulations of material properties, especially for situations where experiments would be too difficult or expensive to conduct.

One key area benefiting from multiscale modelling approach is the study of irradiation-induced or enhanced damage in structural materials. This is practically important to understand the multiscale nature of irradiation-induced microstructural evolution in structural materials, for applications in nuclear reactor technologies, where materials are continuously subjected to intense neutron or high-energy particle fluxes at elevated operating temperatures. Therefore, to understand the complex damage caused by irradiation, from the atomic-scale formation of tiny defects to the large-scale microstructure evolutions in an irradiated material, one needs comprehensive approaches that can consider different sizes and timescales.

Atomic-scale simulations based on Density Functional Theory (DFT) and classical molecular dynamics (MD) methods based on interatomic potentials are extensively used to understand how irradiation alters atomic structures, ultimately impacting their properties on the micro scale. These simulations not only provide data for larger models but also reveal processes beyond the reach of experiments. The DFT calculations in particular, provide detailed electronic structure information and can predictively address effects such as magnetisation, bonding and charge transfer.

As mentioned, the primary form of irradiation damage in metals arises from displacement cascades induced by the recoil of atoms, i.e. PKAs, resulting from collisions with energetic particles such as neutrons or charged particles [23]. These cascades, occurring on the nano-meter scale and picosecond timescales, play a pivotal role in determining the response of the material to irradiation. MD simulations, adopted to capture atomic-scale dynamics, provide a powerful tool to explore the intricacies of irradiation-induced imperfections in structural materials. They can mimic the high-energy recoil events (up to hundreds of keV) that occur in fission and fusion reactor components [59, 60]. This allows us to perceive the massive displacement of thousands of atoms and how point defects like vacancies and SIAs form and evolve.

These cascade events create zones with a high concentration of point defects, which can significantly affect the material properties and performance [23]. Inter-

estingly, MD simulations reveal a crucial detail [61]: during the cooling phase after a cascade, the majority of the created SIAs and vacancies recombine. This recombination explains a key discrepancy, e.g. why the actual number of survived defects often differs from predictions based on simpler models like the Norgett-Robinson-Torrens model [62], showing a more complex relationship between the energy of the irradiation and how efficiently defects are produced in different materials [61].

In addition to MD simulations, the recent success of quantum mechanics-based methods, particularly DFT [63–66], in simulating irradiation-induced defects at the atomic scale offers new avenues for understanding the intricate processes linked to irradiation damage. Unlike classical MD, which relies heavily on interatomic potentials (IAPs) and force fields, DFT provides a more fundamental description of the electronic structure based on quantum mechanics, by explicitly solving the Kohn-Sham equations. This allows for more accurate predictions of material properties and behaviour under irradiation, especially for chemically complex systems like FeCrAl and high-entropy alloys, where accurate IAPs may not be readily available.

DFT emerges as a powerful tool for modelling radiation damage due to its ability to capture electronic structure and magnetic property changes that are inaccessible to classical MD methods. Unlike the MD reliance on pre-defined potentials, DFT leverages quantum mechanics, enabling accurate calculations of defect formation and migration energies. These detailed insights unlock the mechanisms governing radiation damage at the atomic level.

Furthermore, DFT simulations can play an important role in assessing the impact of alloying elements on radiation tolerance [67, 68]. By modelling interactions between defects and alloying elements (e.g., acting as defect sinks), one can identify optimal material compositions for enhanced radiation resistance. However, despite its reliability, DFT is quite limited by the very demanding computational cost.

Nevertheless, successful simulations of threshold displacement energies in materials like graphene [69], Si [70] and Fe [66] demonstrate aspects of its potential. DFT calculations are also very commonly used for calibrating classical MD potentials, further enhancing our understanding of radiation damage.

Moreover, DFT calculations can be integrated with kinetic Monte Carlo (KMC) simulations to predict the long-term evolution of irradiation-induced microstructures under appropriate conditions [55, 71, 72]. KMC simulations are based on input parameters such as defect binding energies and migration barriers, which can be obtained from DFT calculations.

By coupling DFT with KMC, researchers can simulate irradiation conditions over extended time scales and predict the evolution of defects, dislocations, and other microstructural features under irradiation [73–75].

Here, in this study, we coupled the first-principles calculation with the straightforward but powerful creation-relaxation algorithm (CRA) to evolve an irradiated microstructure and to dynamically study and trace the response of chemically complex and systems to irradiation-induced damage. This directly mimics low-energy irradiation damage events at low temperatures but has wider implications as well and can be adapted to study cascade damage conditions. The details of the DFT

and MD methods along with the CRA algorithm will be reviewed in detail in the Methodology section.

1.5 Thesis objectives

The primary focus of this study is to model irradiation damage events and to further analyse the resulting irradiation-induced microstructure evolution in iron-based alloys and associated oxides (Al_2O_3). In order to do so, we adopt and develop atomistic simulation methods to study microstructure evolution. In particular, the first adaptation of the creation-relaxation algorithm (CRA) to use electronic structure methods as driving physics model has been here developed and implemented. The intrinsic model limitations of the CRA are such that this is directly relevant under non-diffusive conditions. Direct experimental validation of atomic-scale modelling is always non-trivial, but would here essentially encompass low-energy irradiation events at low temperatures. The study particularly emphasises investigating magnetic and electronic effects in dynamically evolving irradiation-induced microstructures and the influence of SIAs distributions on the subsequent formation of defect structures.

Additionally, by employing advanced simulation techniques, i.e., DFT- and MD-driven CRA models, the research aims to delve into the intricate interplay of atomic constituents, shedding light on the non-linear magnetic properties of FeCr systems under irradiation.

Finally, the study explores the correlations between the chromium content in FeCr alloys and the emergence of irradiation-induced swelling, along with the stability of the C15 Laves phase structures. These investigations provide crucial insights into the dynamics of defect formation in Fe-based systems under extreme conditions. Ultimately, this research effort contributes to a deeper understanding of the behaviour of structural materials under irradiation, offering potential applications in nuclear environments and advancing the field of materials engineering.

Chapter 2

Methodology

At the heart of these irradiation damage studies lies atomic-scale computer simulations, particularly DFT and MD methods. These techniques allow to understand how irradiation fundamentally affects the materials at the atomic scale, its electronic structure, and how these effects degrade material properties in micro scale. Not only can these simulations provide valuable data for larger-scale models, but they also offer a window into processes that cannot be directly observed in experiments.

Here, in this chapter, we reviewed the coupled first-principles and IAP methods with the simple but powerful CRA model [76], that is used to evolve the microstructure of Fe-alloys that undergo irradiation and to study the response of chemically and magnetically complex systems to irradiation-induced damage.

2.1 Creation-relaxation algorithm (CRA)

This study applied the CRA approach to directly generate low-energy damage events and to qualitatively investigate the resulting microstructure evolution in different model materials such as Fe-based alloys and oxides (Al_2O_3). The comprehensive details of CRA model can be found in **Papers I, II** and in Ref. [76]. In here and the coming subsections, a brief overview of the model will be provided, accompanied by discussions of the key factors considered for modelling low-energy irradiation events.

In late 80s, Y. Limoge and A. Rahman developed a computationally efficient method to simulate radiation damage in materials to model amorphisation in crystal structures [77]. This technique works by gradually incorporating point defects, i.e. FP, in a perfect lattice structure. This allows to study how these defects build up and potentially cause the material to become amorphous.

Recently, Derlet and Dudarev adapted this model to study irradiation-induced microstructure evolution in Fe and W [76]. Their approach involves repeatedly inserting a single FP at random locations within a relatively large simulation cell.

To ensure a uniform distribution of SIAs, the algorithm randomly selects an atom, creating a vacancy, and displacing the selected atom to a random coordinate within the simulation cell to generate a SIA. Following each insertion, atomic positions are optimised using a relaxation algorithm (e.g. conjugate gradient minimisation) to achieve a local minimum in the potential energy landscape, performed either in a fixed cell (constant volume) or with variable cell dimensions. By employing this process at a constant volume, one can track the evolution of the microstructural imperfections in response to the stress field induced by the FP insertion (FPI).

Furthermore, a variable keeps track of the total number of FPs inserted for irradiation dose determination. That is, after each successful insertion and relaxation of FP, the dose parameter (ϕ) is updated by dividing the current count of FPI by the total number of lattice sites (N) in the simulation cell. This provides a deterministic measure of the accumulated irradiation dose in terms of displacements per atom (dpa), as fully described in [76]. The dose parameter in the CRA model is defined as:

$$\phi = n/N. \tag{2.1}$$

As mentioned, the CRA model is a computational approach designed to simulate how microstructures evolve in materials under irradiation. This is accomplished by mimicking the creation and relaxation of point defects (FPs). For a detailed breakdown of the CRA approach, one can refer to the flowchart presented in Figure 2.1.

A simulation cell with a desired size and crystallographic structure is constructed (step 1 of the flowchart). The choice of supercell size, in this study, was guided by the specific physical phenomena investigated and the computational method employed. Smaller supercells, constructed by $8 \times 8 \times 8$ copies of primitive unit cell1, were used for calculations concerning magnetic and alloying effects in Fe-based alloys utilising DFT. DFT, renowned for its exceptional predictive capabilities and robustness, facilitated precise analysis in this context. In contrast, larger supercells, typically with dimensions of $50 \times a_0$ [1], were used to investigate the large-scale microstructural evolution of pure Fe through MD simulations. Such simulations necessitated a larger simulation space to adequately capture the intricate long-range interactions inherent in the defected system and large-scale defect features that are built up during the irradiation.

Beyond the considerations of the simulation cell size and FP distribution, the inherent randomness of the FP insertion can occasionally lead to situations where the inserted atom lands too close to another existing atom. For very short interatomic distances, the empirical potentials employed in this study rely on the screened Coulomb interaction model from Ziegler, Biersack, and Littmark (ZBL) [78], which guarantee a fully accurate short-range repulsive force, particularly relevant when dealing with close atomic proximity. However, if a chosen potential does not have a short range parameterisation, and in the context of DFT-driven CRA calculations,

[1] In this study, it has been consistently referred to the supercell size throughout the text using its side length notation, typically as $N \times a_0$, where N is the multiplication of the primitive cell in all directions. Here, a_0 represents the lattice constant.

which utilise the projector-augmented wave description [79], the lack of a physically correct repulsive force can lead to an unreliable evolution.

Therefore, to circumvent these nonphysical scenarios during the simulations, we implemented a strategy that involves the definition of a virtual spherical exclusion zone surrounding each atom. This zone, marked as 'forbidden zone', dictates the forbidden region for FP insertion prior to the relaxation step (step 6). If the random coordinate selection places an atom within another atom's restricted zone, the inserted atom is displaced outwards directly towards the zone boundary. The relaxation process then begins from this new position.

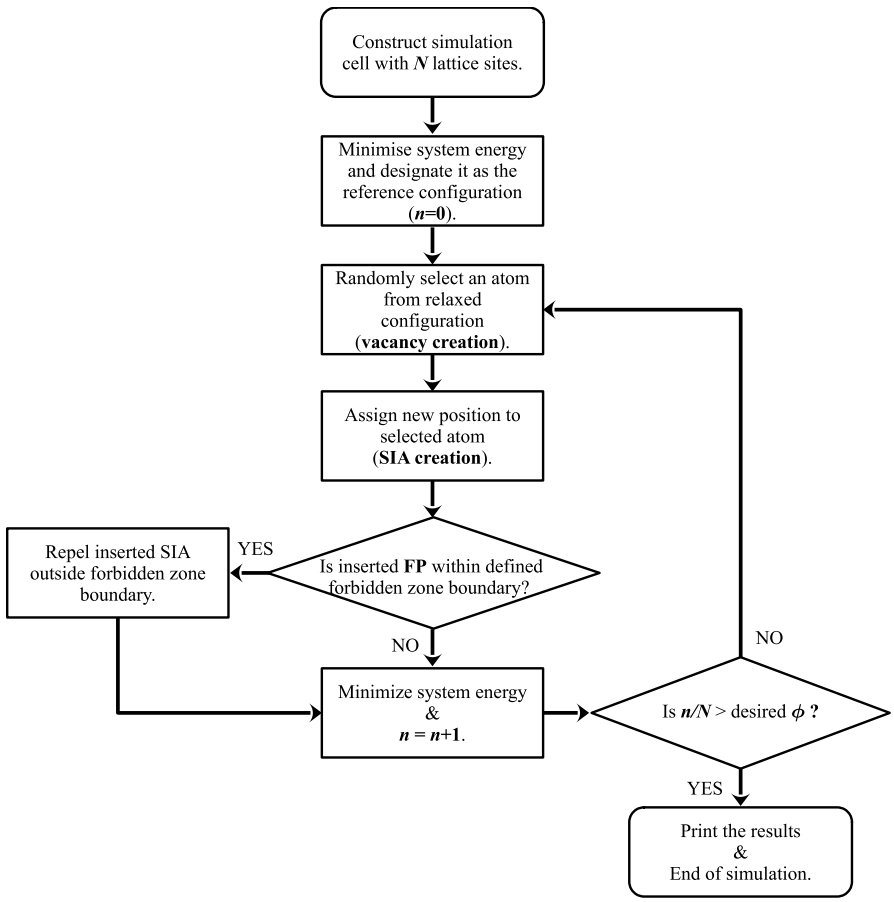

Figure 2.1: Flowchart of the CRA model for simulating irradiation damage events and modelling microstructure evolution up to the desired dose limit ϕ.

Based on our calculations for bcc Fe, a reasonable radius for this exclusion zone is approximately 0.7 Å. The justification for this specific value selection will be elaborated upon in section 2.4. Consequently, all atoms within the simulation cell

are relaxed to their minimum energy states, establishing a reference configuration for the next FPI by incrementing the number of FPI (i.e., $n = n+1$). The algorithm enters a loop that continues until a target irradiation dose is reached (step 7 of the flow diagram: $\phi \leq n/N$).

Inside the loop, a random atom is chosen from the cell and removed, creating a vacancy (step 3). This removed atom is then reinserted back into the cell at a different location according to a predefined distribution function, effectively creating a SIA (step 4). The algorithm checks if the SIA inserted has landed within the forbidden zone of another atom (step 5). If so, its position is adjusted to be just outside this zone to avoid unrealistic atomic configurations. Finally, an energy minimisation routine is then employed to relax all atomic positions within the cell. This step simulates the material response to the newly introduced defect and allows the system to reach a new local minimum energy configuration (step 6).

The loop continues to iterate through steps 3 - 7 until the calculated dose, Eq. (2.1), reaches a predefined target value, signifying the desired level of simulated irradiation.

In general, the CRA approach allows us to investigate the step-by-step evolution of microstructures under irradiation. The model starts with a pristine structure and progressively introduces FPs into it, simulating the accumulation of point defects and their interactions.

The foundation of the robust CRA model framework lies in establishing a well-defined simulation cell. The choice of simulation cell size is critical and depends on the spatial scale of the microstructure under investigation. For example, modelling and analysing irradiation-induced extended defects such as dislocation loop formation and their subsequent evolution require a relatively large simulation cell, as described in **Paper II**. This ensures that the cell can accommodate the nucleation and dose-dependent evolution of defects beyond the tightly clustered and strictly localised ones, such as dislocation segments. Once an appropriate simulation cell size is determined, ensuring the quality of the FP distribution becomes crucial. This matter will be discussed in more details in the following subsection.

2.2 Determination of irradiation-induced structural changes

Exploring irradiation-induced microstructural changes in model materials in this study often involves two primary computational approaches integrated into relaxation calculations. The first, full relaxation (FR), allows for changes in the supercell volume, the ionic positions as well as the supercell shape, providing direct access to volumetric alterations and potential induced structural anisotropy. In contrast, the ionic relaxation (IR) method focuses on monitoring hydrostatic pressure fluctuations, relaxing only the ionic positions after each FPI. During FR, the system reaches a state of zero global pressure. This allows for the evolution of both supercell volume and shape, leading to explicit volumetric changes, e.g., swelling, especially in scenarios involving FPIs. However, FR calculations, especially within

DFT, can be computationally expensive. To address this limitation, we primarily employed IR, which efficiently optimises only ionic positions while maintaining the supercell volume and shape. In this study, and for DFT calculations, FR was then selectively applied to specific configurations extracted from one CRA trajectory. This approach balances computational efficiency with obtaining valuable insights into the system's behaviour.

As mentioned, under fixed-volume conditions (IR), irradiation-induced change in material's structure can be estimated by correlating the change in global hydrostatic pressure (ΔP) with the bulk modulus (B) of the material. This relationship can be expressed using the following equation [80]:

$$\frac{\Delta V}{V_0} = -\frac{\Delta P}{B}. \tag{2.2}$$

Here, $\frac{\Delta V}{V_0}$ represents the relative volumetric change, and B is the bulk modulus. This equation highlights how the internal pressure changes caused by irradiation relate to the resulting volumetric changes in the material. This combined approach provides a robust and coherent understanding of how microstructural evolution in irradiated Fe manifests through dimensional changes and pressure fluctuations.

2.3 Spatial distribution of Frenkel pair insertion

Intuitively, a spatially localised distribution of SIAs, i.e that the SIA appears close to its vacancy, better represents a realistic low-energy irradiation event, such as those caused by low-energy recoiling PKAs from electron or proton irradiation. This is particularly true for relatively large supercells (e.g., side length $> 20\times a_0$). In larger simulation cells, displacing SIAs too far from their original lattice sites, within the CRA conditions, becomes physically unrealistic for simulating low-energy damage regimes.

As demonstrated in **Paper I**, using a small supercell with a side length of $8\times a_0$ revealed no significant difference between employing spatially uniform or localised distributions of SIAs when predicting irradiation-induced microstructure evolution.

Regardless of the distribution function, the average displacement of the SIAs remained consistent around half the supercell side length, which translates to approximately 11.3 Å in this case. Notably, as showed in **Paper II**, within larger supercells, the displacement of SIAs exhibits a greater dependence on supercell dimensions. Therefore, the selection of FP distribution strategy was tailored to the supercell size. For supercells with dimensions smaller than $10\times a_0$, both uniform and localised atomic displacements implemented through the CRA algorithm yielded comparable results. However, in larger supercells and under the simulated irradiation conditions applied in this study, employing a localised FP distribution aligns better with the physical realities of low-energy irradiation events.

In the case of uniform atomic displacements, a continuous linear probability density function (PDF) is employed. Mathematically, a continuous random variable

x is considered uniformly distributed over the interval [a, b] if its PDF, denoted as *f(x)*, is defined as [81, 82]:

$$f(x) = \begin{cases} \frac{1}{b-a} & \text{for } a \leq x \leq b, \\ 0 & \text{otherwise.} \end{cases} \tag{2.3}$$

This function guarantees the generation of a random number uniformly distributed within the interval [a, b]. The anticipated average displacement, or expectation value $\bar{x}$, can be expressed as:

$$\bar{x} = \frac{b-a}{2}. \tag{2.4}$$

To simulate localised atomic displacements, the gamma distribution function was selected. This function serves a widespread application because of its relationship with both the exponential and normal distributions. Furthermore, the gamma distribution offers a compelling representation of the localised nature of atomic displacements from their lattice positions. The standard gamma distribution, denoted as $\Gamma(\alpha, \theta)$, possesses two freely adjustable parameters, α and θ. Its PDF is expressed as [82]:

$$f(x; \alpha, \theta) = \frac{x^{\alpha-1} e^{-x/\theta}}{\Gamma(\alpha)\theta^{\alpha}}, \quad x \geq 0. \tag{2.5}$$

Within the standard gamma distribution, $\Gamma(\alpha, \theta)$, the parameters α and θ govern the shape and scale of the distribution, respectively. It is important to note that $\Gamma(\alpha)$ also represents the gamma function expressed as:

$$\Gamma(\alpha) = \int_0^{\infty} x^{\alpha-1} e^{-x} dx. \tag{2.6}$$

For integer and positive α Eq. (2.6) leads to:

$$\Gamma(n) = (n-1)\Gamma(n-1) = (n-1)!. \tag{2.7}$$

The expectation value (i.e., mean displacement) of the $\Gamma(\alpha, \theta)$ can be also expressed as:

$$\bar{x} = \alpha\theta. \tag{2.8}$$

Moreover, the mean displacement of SIAs considered in the CRA model and described by gamma function should incorporate well-controlled spontaneous FP recombination distances to minimise bias in modelling of defect evolution. Previous research [83] suggests that the recombination distance for FPs in irradiated bcc Fe varies between $1.9a_0$ [84] and $3.3a_0$ [85], depending on temperature and the type of irradiating particle. Therefore, for the CRA model applied in this study, the mean displacement range of $2.0a_0$ to $3.5a_0$ (as per Eq. (2.8)) was chosen.

Finally, Figure 2.2 depicts the PDFs of the standard gamma distribution for various combinations of α and θ parameters, which control the mean displacements, facilitating a visual comparison. Gamma distributions are a well-estab-

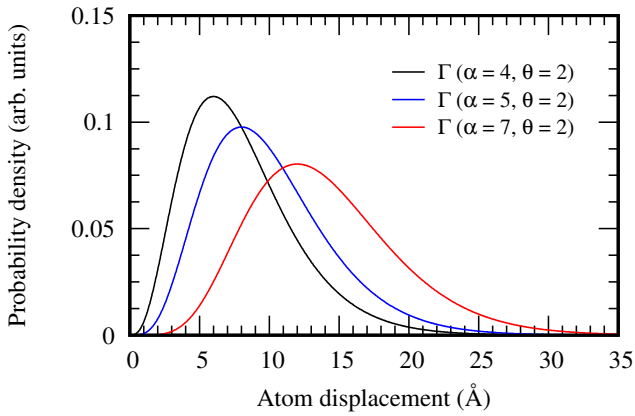

Figure 2.2: Plot of PDFs of standard $\Gamma(\alpha, \theta)$ distribution function for various shape and scale parameters.

lished choice for modelling non-negative quantities exhibiting a rightward skew. This property makes them suitable for representing various random variables such as times, weights, and lengths [82]. In this study, we leverage the ability of the gamma distribution to capture localised atomic displacements during low-energy irradiation events. We employ two specific gamma distribution functions, $\Gamma(4, 2)$ and $\Gamma(5, 2)$, corresponding to targeted mean displacements of 8 Å and 10 Å (using Eq. (2.8)), respectively, which lie slightly outside the mean recombination radius for FPs in iron [83].

2.4 Forbidden zone radius

As mentioned, our simulations utilised both DFT, which is very computationally expensive for truly short ranged interactions, and Embedded atom method (EAM) potentials which are connected to the ZBL screened Coulomb interaction, offering a robust description of short-range repulsion forces crucial for accurate modelling of irradiation damage.

These IAPs effectively prevent the formation of unrealistic high-energy structures during relaxation, particularly when introducing random atom insertions that could lead to excessively close atomic spacing. For IAPs that lack a pronounced short-range repulsion or for peseudopotentials used in DFT, careful consideration is, however, necessary. Based on insights from our previous DFT-driven CRA calculations (**Paper I**), a precautionary approach was implemented to avoid introducing atoms at nonphysically close distances and disrupting the simulation's integrity. Therefore, we defined a virtual spherical zone around each atom. This restricted region prohibits atom insertion prior to the relaxation step, ensuring the maintenance of structural coherence. The following explains the method and motivation

for choosing 0.7 Å as the radius of the forbidden zone in iron alloys.

Using DFT, we introduced a FP defect (with a vacancy at the origin and a SIA at the mid-lattice site, creating a ⟨110⟩-dumbbell configuration) within a bcc Fe supercell containing 250 atoms. To ensure accuracy, calculations employed a 350 eV cut-off energy and a 6 × 6 × 6 k-point mesh for the Brillouin zone integration. The conjugate gradient algorithm optimised both the lattice parameters and the electronic structure. The initial separation between dumbbell atoms was approximately 2 Å.

Introducing a single FP altered the pressure and magnetisation in bcc Fe by 9.9 k_B and -1.7 μ_B, respectively. Additionally, the local magnetic moments of the SIAs decreased to -0.2 μ_B. To analyse the impact of interatomic distance on the FP, we incrementally reduced the separation between the dumbbell's constituent atoms while keeping the other ions fixed. Self-consistent electronic calculations were performed at each distance.

Figure 2.3 shows the changes in total energy, hydrostatic pressure, and local magnetic moment of the SIA as a function of interatomic distance. At a separation of about 0.7 Å, the local magnetic moments turned positive, and the total energy change became significant, exceeding the FP formation energy by a factor of 33. This shift was also reflected in the hydrostatic pressure, which increased by an order of magnitude compared to the pressure induced by the FP. These results highlight the significant influence of interatomic proximity on the properties and stability of a systems with an incorporated FP.

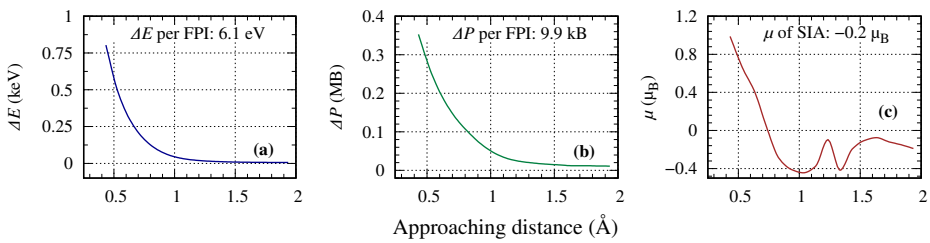

Figure 2.3: The change in a) total energy, b) global pressure, and c) local magnetic moment (μ) of SIAs as a function of approaching distance of atoms forming a ⟨110⟩-dumbbell.

Therefore, to prevent the modelling of unrealistic irradiation-damage events, a virtual restricted region with a radius of 0.7 Å, which corresponds to approximately one-third of the equilibrium interatomic separation in the SIA, was adopted. This approach ensures realistic atomic interactions by preventing the insertion of atoms at distances that can lead to artificial structural distortions.

2.5 *Ab initio* electronic structure calculations

Understanding the complex electronic structure of materials relies on theoretical frameworks that connect fundamental physics with observable properties. *Ab initio*

electronic structure calculations are the primary method used in this endeavour. These calculations directly tackle the time-dependent Schrödinger equation for a quantum system, as described by

$$i\hbar\frac{\partial\Psi(r,t)}{\partial t} = H\Psi(r,t). \tag{2.9}$$

Where i is the imaginary unit, $\hbar$ is the reduced Planck constant, $\Psi(r,t)$ is the wave function, representing the state of the system at position r and time t. H is the Hamiltonian operator, representing the total energy of the non-relativistic quantum system with mutually interacting nuclei and electrons. The Hamiltonian can be written in the form of:

$$H = T_{\mathrm{e}} + T_{\mathrm{n}} + V_{\mathrm{e-e}} + V_{\mathrm{e-n}} + V_{\mathrm{n-n}}, \tag{2.10}$$

which includes the kinetic energies of electrons (T_{e}) and nuclei (T_{n}), as well as electron-electron ($V_{\mathrm{e-e}}$), electron-nucleus ($V_{\mathrm{e-n}}$), and nucleus-nucleus ($V_{\mathrm{n-n}}$) potential energies. For a system consisting of N nuclei and n electrons, the Schördinger equation presents analytical challenges due to its complexity. To address this, Max Born and Robert Oppenheimer proposed an approximation method [86] aimed at simplifying the equation. This approach involves decoupling the electronic and ionic components, assuming that the movement of nuclei is significantly slower than that of electrons. Consequently, within the timescale of electronic motion, the nuclei are considered stationary, leading to a reduction of the Hamiltonian to the electronic component:

$$H = T_{\mathrm{e}} + V_{\mathrm{e-e}} + V_{\mathrm{e-n}}. \tag{2.11}$$

The Born-Oppenheimer approximation notably simplifies the complexity of the system, yet the resulting wave function still depends on N bodies, necessitating further approximations for an effective solution. This is where DFT plays a crucial role in addressing this challenge by reformulating the N-body quantum problem. Unlike traditional methods such as Hartree [87, 88] and Hartree-Fock [89], DFT focuses on the electron density as the fundamental quantity rather than the wave function.

The DFT formalism is based on the two theorems of P. Hohenberg and W. Kohn [90]. The Hohenberg-Kohn (HK) theorems showed that electron density, not wave functions, is enough to describe a quantum-mechanical system. Through this connection, the total energy of a system of interacting electrons can be expressed as a functional of its electron density, represented as $E_{\mathrm{HK}}[n(r)]$.

Minimising the system's energy functional, $E_{\mathrm{HK}}[n(r)]$, allows us to find both the ground state energy and density. However, finding an exact functional for $E_{\mathrm{HK}}[n(r)]$ remains a challenge. To address this, Walter Kohn and Lu Sham [91] proposed an ingenious approach. They replaced the complex system of interacting electrons with a simpler one: independent electrons moving in an effective potential. This allowed them to define a single-electron Hamiltonian and write the Kohn-Sham (KS) equations, making calculations significantly more tractable. The KS Hamiltonian

describes the behaviour of non-interacting electrons within an effective potential, $v_{\text{eff}}(r)$, taking the form:

$$\left[-\frac{\hbar^2}{2m} \bigtriangledown^2 + v_{\text{eff}}(r)\right] \varphi_i = \varepsilon_i \varphi_i(r). \tag{2.12}$$

Where m is the mass of electron, $\varphi_i(r)$ is the electron orbital. Here ε_i is the orbital energy of the corresponding KS orbital, and the density for an N-electron system is $v_{\text{eff}}(r)$, takes the form:

$$n(r) = \sum_{i=1}^{N} \left|\varphi_i(r)^2\right|. \tag{2.13}$$

The KS equation is solved iteratively using a self-consistent field (SCF) approach. In each iteration, the single-electron KS equation is solved to obtain wave functions, typically employing a conjugate gradient method. These wave functions are then used to update the electron density. Convergence is achieved when the density change between iterations falls below a pre-defined threshold. For atomic structure optimisation, an additional loop can be implemented where atomic positions are adjusted iteratively until the forces acting on each atom reach a minimum, signifying the system's ground-state energy with respect to the atomic configuration. This SCF procedure ensures the consistency between the electron density and the potential field, ultimately leading to the determination of the ground-state energy and electronic structure of the system.

In summary, DFT emerges as a powerful tool for studying radiation damage in materials at the atomic level. By introducing well-defined defects, such as vacancies, interstitials, and FPs, into a simulated material (defined by composition, structure, and atom count), electronic structure calculations allow to elucidate the fundamental mechanisms governing defect formation and evolution under irradiation.

First, the atomic positions and lattice parameters of the pristine material can be relaxed and optimised, providing a stable reference point. Then, the defect formation energies are computed to assess the likelihood of different defect types forming under irradiation. Specialised software packages such as Vienna *Ab initio* Simulation Package (VASP) [92–95] utilise advanced techniques (plane-wave basis sets [96], projector augmented waves [79] and ultrasoft pseudopotentials [95]) to solve the KS equations and calculate electronic properties crucial to understanding radiation effects. Rigorous validation and verification are essential, involving comparisons with experimental data and other computational methods. Finally, sensitivity analyses ensure the robustness of the results and identify potential limitations. Through this comprehensive approach, DFT provides valuable insight into the intricate processes that govern radiation damage in materials.

2.6 Embedded atom method (EAM)

The core concept of classical MD revolves around applying classical mechanics to determine the energy of a system and the forces between atoms based on their positions. In this approach, atoms are considered as point-like particles following Newton's laws of motion [97]. By solving the equations of motion for each atom, one can simulate the behaviour of a system comprised of N atoms. Central to this process is the interatomic potential (IAP), a mathematical function that governs the forces between atoms according to their relative positions [57].

The chosen IAP function significantly impacts the accuracy and efficiency of the simulation, especially when one aims to simulated irradiation damage events [78,98]. Ideally, an appropriate IAP should accurately capture both attractive and repulsive forces between atoms. This ensures a stable and realistic representation of the atomic lattice structure. Commonly used IAPs in computational material science include empirical or semi-empirical potentials, which rely on either fitting parameters derived from experimental data, and/or more sophisticated *ab initio* methods based on quantum mechanical calculations [98]. Among the different IAP models, the EAM is often used to describe the interactions between atoms in metallic systems [99].

In the EAM formalism, the total energy of the system is, as proposed by Daw and Baskes [100, 101], typically expressed as a sum of contributions from pairwise interactions between atoms and an embedding energy term that accounts for the influence of the electron density on each atom. In this view, each atom in the metal is embedded in the electron gas created by the other atoms. The functions can then be empirically fitted to properties of the bulk metals. The generality of the functions has been extensively tested by applying them to surfaces and many other defects for a range of different metals and alloys. This generalisation allowed calculations of complex metallic structures to be done within the approximate embedding-energy framework. The EAM is thus a significant improvement in simplified total-energy calculations for metallic systems. Mathematically, the total energy E of a metallic system described by the EAM potential can be written as:

$$E = \sum_i F_i(\rho_i) + \frac{1}{2} \sum_{i \neq j} \Phi_{i,j}(r_{i,j}). \tag{2.14}$$

Where F_i is the embedding energy function for atom i, ρ_i is the electron density at the position of atom i, $\Phi_{i,j}(r_{i,j})$ is the pairwise interaction potential between atoms i and j, and $r_{i,j}$ is the distance between atoms i and j.

The embedding energy function F_i is often expressed in terms of the electron density ρ_i at the location of atom i, and it represents the energy required to embed atom i into the electron density of its neighbouring atoms (host atoms). The pairwise interaction potential $\Phi_{i,j}(r_{i,j})$, describes the energy associated with the interaction between atoms i and j as a function of their separation distance $r_{i,j}$.

Overall, the EAM potential provides a physically realistic description of atomic interactions in metallic systems by considering both pairwise interactions between

atoms and the influence of the electron density on each atom's embedding energy. This approach allows for accurate representation of various properties of metallic materials, such as lattice structure, elastic properties, and diffusion behaviour, making it a valuable tool in materials science research and computational modelling.

2.7 Atomic simulation procedures and analysing tools

Atomic simulations progress through a series of meticulously defined steps. First, the system is established by specifying the number of atoms (N), their initial positions, and the size of the simulation box, which represents the volume of the structure. This box essentially acts as a microscopic window into the material. In the case of MD simulation, a suitable IAP function is chosen, serving as the blueprint for the forces governing atomic interactions based on their relative positions. The interatomic potentials used in this study are EAM-type potentials developed by Mendelev (ME03) [102], Marinica (MA07 [103, 104]), and Ackland (AC04) [105]. These potentials have been shown to be appropriate for studying irradiation induced damage in bcc Fe [104, 106–108].

To mimic a bulk system, periodic boundary conditions are applied so that the simulation box seamlessly repeats, creating the illusion of continuous material. The heart of the simulation lies in the force calculation step, where the chosen IAP and the current positions of atoms dictate the forces acting on each one. Subsequently, powerful numerical integration techniques like conjugate gradient or Verlet algorithms come into play. For the calculation used in this study, the conjugate gradient minimisation technique was used.

These techniques solve the equations of motion for each atom based on the calculated forces, effectively determining their new positions and velocities for the next step. This iterative process of force calculation and position update continues for a predefined number of steps, mimicking the quasi-dynamic evolution of the atomic system. Throughout the simulation, valuable data such as atomic positions, energies, and stress are collected for post-simulation analysis, providing insights into the behaviour of the material at the atomic level [109].

In the context of irradiation damage, MD simulations can model the consequences of interactions of energetic particles (e.g. neutrons or ions) with the material [23, 57]. These interactions can cause collisions that displace atoms from their original lattice sites, leading to the formation of defects, such as vacancies and self-interstitials. To simulate such events, one may introduce additional forces or velocities to selected atoms representing the colliding particles. By analysing the subsequent atomic motion, one can gain insight into the nature and evolution of irradiation-induced damage in various materials.

Although MD simulations offer a powerful tool, they are not without limitations. The accuracy is highly dependent on the chosen IAP and the computational resources available. Simulating large systems on long timescales can be computationally expensive. However, ongoing research continues to refine IAPs and develop

more efficient simulation algorithms, pushing the boundaries of MD for exploring ever-more complex phenomena in materials science, including irradiation-induced damage.

Finally, the study used a script code, written in PYTHON, within the CRA model framework to create and insert FPs into the model materials under consideration. Subsequent structural relaxation was performed using either MD simulation implanted in LAMMMPS [110] or first-principles calculation using VASP. PYTHON and OVITO [111] were then utilised for microstructure analysis. Specifically, Wigner-Seitz analysis in OVITO quantified the vacancy and interstitial content within the simulation cells. To define the clusters of defects, a cutoff criterion was established based on bond lengths in bcc Fe [107, 112]: 3.5 for the clusters of vacancies (midpoint between the second and third closest neighbours) and 4.1 for the interstitial clusters (midpoint between the third and fourth nearest neighbours).

Furthermore, a dislocation extraction algorithm [111] implemented in OVITO (using default parameters) was employed to identify all types of extended defects such as dislocation loops, lines and networks arising from defect interactions within the simulation cells. Polyhedral template matching (PTM) analysis [113] with a root mean square deviation of 0.25 in OVITO was used to detect and analyse other irradiation-induced crystal structures, such as the C15 Laves phase, within damaged model materials.

Finally, the formation energy of a defect (such as an interstitial cluster with a C15 Laves phase or dumbbell structure) is quantified by its impact on the total energy compared to an unperturbed system. For a pure supercell with atom type A, containing n atoms, the formation energy is given by:

$$E_{\mathrm{f}}^{nA} = E[nA] - nE[A], \tag{2.15}$$

where E[A] is the total energy per A atom in a supercell of the same size as used for the defect calculation. In a dilute alloy with n Fe atoms and p Cr atoms, the formation energy is:

$$E_{\mathrm{f}}^{(nFe+pCr)} = E[nFe + pCr] - (nE[Fe] + pE[Cr]), \tag{2.16}$$

where the reference energies are defined as above. For dilute alloys, solute atoms can be treated as defects or not, depending on the representation chosen. If solute atoms are considered part of the unperturbed system, as in the case of concentrated alloys, this must be reflected by using the reference energy of the alloy.

Chapter 3

Results and discussion

Building upon the foundation laid in the previous chapter, this chapter delves into the consequences of irradiation-induced damage and microstructural evolution in different model materials, especially in Fe-based alloys and Al_2O_3. As reviewed previously, irradiation events induce point defects within the irradiated materials. As these defects accumulate with increasing irradiation dose, they can coalesce into extended defects such as dislocation loops and voids, significantly altering the material properties.

One crucial property affected by irradiation is dimensional stability. Swelling, a common form of degradation of material properties, occurs in irradiated materials. Understanding and quantifying the extent of this dimensional change is of paramount importance for nuclear engineers, as it can impact the performance and safety of nuclear reactor components.

This chapter leverages the insights from **Papers I, II**, and **III**, which explored the irradiation-induced microstructural evolution in model material Fe. These papers meticulously investigated the influence of simulation cell sizes and the quality of FP distributions on microstructural imperfections using both first-principles and classical interatomic potential methods.

Additionally, the formation of other intriguing interstitial clusters, such as the C15 Laves phase structures within bcc Fe (α-phase), was reviewed in particular detail within the DFT framework. **Paper IV** along with its corresponding Supplemental Material, and **Paper V**, extend this investigation by exploring the effects of alloying elements such as chromium (Cr) and aluminium (Al) on the irradiation-induced damage in Fe-based alloys. These articles examine the impact of Cr and Al on the stability of the C15 Laves phase structure, their magnetic properties in irradiated Fe-based alloys (FeCr and FeCrAl), and their influence on irradiation-induced swelling.

3.1 Simulation cell size and spatial distribution of FPs

A critical starting point in modelling irradiation-induced microstructural evolution is the selection of an appropriate simulation cell size. This choice is driven by the specific physical phenomena of interest and the available computational resources. For example, while studying radiation damage formation in Fe-based alloys, the DFT-driven CRA model was employed to model irradiation damage in quantum-mechanic framework. Due to the inherent computational demands of DFT, we utilised supercells with a maximum size of $8\times a_0$ (where a_0 is the bcc lattice constant). These supercells, which contain 1024 atoms, were chosen to be as large as computationally possible to minimise interactions between defects and their periodic images, a common artefact in simulations with periodic boundary conditions. However, these sizes may be insufficient to fully capture the dose-dependent evolution of extended defects, particularly large interstitial dislocation loops, which can extend beyond the size of the supercell.

To investigate the formation and evolution of such extended defects, we transitioned to classical MD simulations employing the CRA model (MD-CRA). MD simulations offer a computationally more efficient alternative to DFT, making them well suited for studying the quasi-dynamics of large-scale defect formation and interactions, such as those observed with dislocation loops, line, and networks [114].

Alongside determining the appropriate simulation size based on the chosen method (i.e. DFT or MD), the distribution of FP defects within the supercell is also crucial. As mentioned previously, the CRA model resemble quite closely low-energy, low-temperature irradiation conditions, such as electron irradiation, which primarily generate stable isolated FP defects. Therefore, the quality of FP distributions is contingent upon the dimensions of the simulation cell.

In smaller simulation cells (e.g., smaller than $10\times a_0$), while limited differences should be observed in the evolving microstructure, the spatial displacements of defects may still influence their interactions and subsequent evolution. For example, Figure 3.1 compares the predictions of MD-CRA dose-dependent evolutions of hydrostatic pressure change (ΔP) using various distribution functions, including the uniform distribution function (UDF) as well as localised distribution functions (LDF) of gamma type (LDF-$\Gamma(5,2)$ and LDF-$\Gamma(4,2)$), within the smallest supercell ($8\times a_0$) and a typical large supercell ($50\times a_0$).

As seen in Figure 3.1(a), regardless of the type of spatial distribution of SIA, the dose-dependent evolution of the microstructures, in terms of global pressure change, is quite consistent in the $8\times a_0$ supercell, as expected, given that the mean displacement of the SIAs is of the order of the simulation cell size regardless of the choice of distribution function. Furthermore, after an initial linear increase, the global pressure reaches a steady-state saturation after approximately 0.05 dpa, consistent with previous studies [76], particularly for irradiation doses below 0.2 dpa. However, supercells with a side length of $50\times a_0$ reveal a more intricate evolution of the irradiation-induced microstructure, including at least three distinct stages that smaller supercells cannot capture.

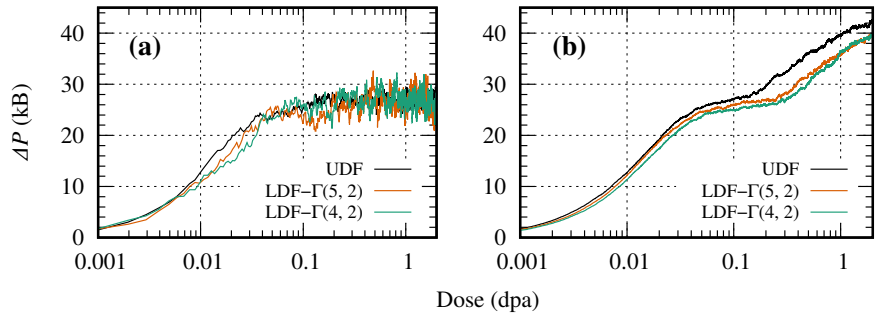

Figure 3.1: Comparison of cell size effects on evolution of hydrostatic pressure as a function of irradiation dose within MD-CRA method, using different FP distribution functions in supercells of sizes a) $8\times a_0$ and b) $50\times a_0$.

Furthermore, within a large supercell, the use of LDF-$\Gamma(4,2)$ and LDF-$\Gamma(5,2)$ distribution functions consistently results in a lower irradiation-induced pressure compared to the UDF, with an average reduction of approximately 9% across the entire irradiation dose (Figure 3.1(b)). This trend suggests that the uniform displacement of SIAs leads to a greater accumulation of surviving point defects, and therefore deposited energy, within the irradiated structure (as detailed in **Paper II**). This phenomenon can be attributed to a lower rate of correlated FP recombination compared to scenarios that apply a spatially localised distribution of SIAs. Consequently, the uniform distribution of SIAs is expected to result in a higher number of surviving FPs, ultimately leading to the formation of even larger interstitial clusters.

3.2 Irradiation-induced microstructure evolution in Fe

As explained in **Papers I, II**, and indicated in Figure 3.1(b), the pressure change is a direct consequence of microstructural damage accumulation and evolution as a function of FPI. That is, the linearly evolving global pressure is attributed to the linear accumulation of isolated point defects (mono interstitial (I_{mono}) and mono vacancy (V_{mono})). This is followed by the nucleation and growth of defect clusters, such as interstitial clusters (I_{C}) or vacancy clusters (V_{C}) at an early stage of the irradiation dose.

For example, once the number density of I_{C} reaches a maximum, the stress fields generated from embedded damage force them to coalesce and transform into extended I_{C}, such as dislocation loops [76]. Subsequently, these loops join to form dislocation lines, which ultimately collapse into dislocation networks.

The rationale behind these predictions comes from the analysis of the evolving defect concentrations illustrated in Figure 3.2 and outlined in Table 3.1, considering a supercell dimension of $50\times a_0$. Table 3.1 provides a detailed overview of the mean

defect populations, derived from both the UDF- and LDF-CRA methodologies. These mean values are calculated within dose intervals ranging from 1.75 to 2 dpa, where the evolution of the microstructures seem to approach saturation levels in supercells of size $50\times a_0$. Furthermore, the percentage difference, denoted as X, for each parameter forecast by the LDF-CRA model is computed relative to that of the UDF-CRA, expressed as follows:

$$X^{LDF-UDF}(\%) = \frac{X^{LDF} - X^{UDF}}{X^{UDF}} \times 100. \tag{3.1}$$

Across different types of FP distribution functions, Figure 3.2(a) and Table 3.1 reveal a notable trend: the total density of I_{C} estimated using LDF surpasses that predicted by the UDF by approximately 11% within the dose range of 1.75 to 2 dpa, corresponding to microstructure saturation. particularly, this difference is noticeable during intermediate irradiation doses (0.1 to 0.5 dpa), as shown in Figures 3.2(c) and (d), where a higher frequency of smaller interstitial clusters forms in conjunction with locally distributed SIAs. Subsequently, as illustrated in Figure 3.2(c), I_{C} densities gradually decrease with increasing irradiation, indicating their agglomeration and transformation into dislocation segments. In addition, the nucleation of dislocation loops is shown to coincide with the reduction in peak population of I_{C}. This suggests that the choice of SIA displacement influences the onset and progression of dislocation loop nucleation. Specifically, compared to LDFs, dislocation segments may form more rapidly with the UDF, implying a delayed transformation with the former approach.

It would be also of interest to investigate how vacancy defect populations evolve with irradiation without thermally assisted diffusion, compared to interstitial defects. As listed in Table 3.1, UDF-CRA model predicts a consistently higher number density for surviving V_{C} compared to LDFs, approximately by 12 to 14%, compared with $\Gamma(4,2)$ and $\Gamma(5,2)$ respectively. This difference arises primarily from the enhanced recombination between vacancies and nearby SIAs under the influence of localised SIA distributions.

Table 3.1: Comparison of defect number densities across different spatial distributions of SIAs within dose intervals of 1.75 to 2 dpa. The table presents the defect number densities of survived FP, isolated defects, and defect clusters, along with the percentage difference relative to the UDF. Negative values indicate a reduction compared to the UDF.

Defect No. density (10^{27} m^{-3})	UDF	$\Gamma(5,2)$, $X^{\Gamma(5,2)-UDF}$	$\Gamma(4,2)$, $X^{\Gamma(4,2)-UDF}$
FP	2.99	2.63, (-12%)	2.66, (-11%)
I_{mono}	0.21	0.24, (14%)	0.25, (19%)
V_{mono}	1.43	1.43, (0.0%)	1.44, (0.7%)
I_{C}	0.09	0.10, (11%)	0.10, (11%)
V_{C}	0.51	0.44, (-14%)	0.45, (-12%)

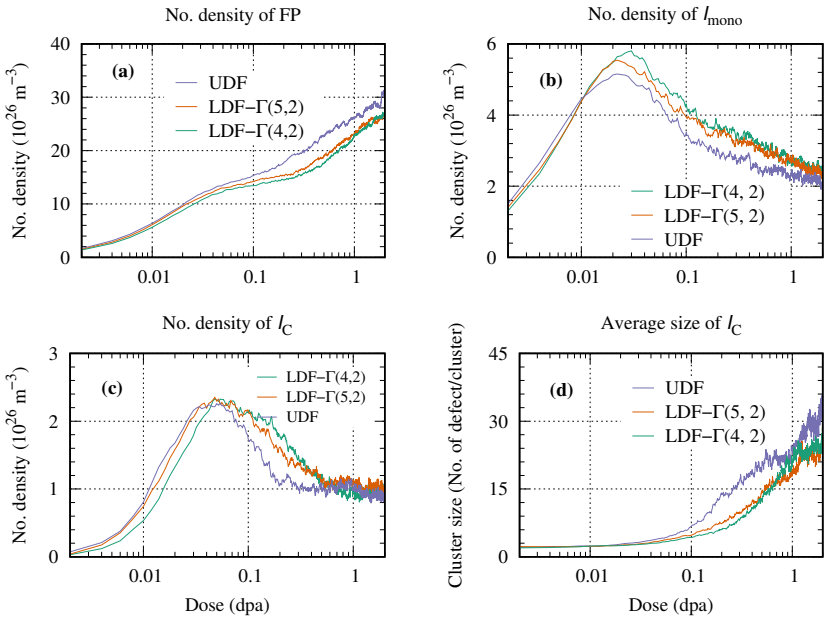

Figure 3.2: The dose-dependent evolution of the total number of survived a) FPs, b) I_{mono}, c) I_{C}, along with d) the average sizes of the I_{C} predicted with UDF and LDFs of the SIAs.

Figure 3.3 shows the evolution of the interstitial and vacancy number densities (top panels) alongside their corresponding average and largest cluster sizes (bottom panels) within the $50\times a_0$ supercell for the spatially localised FP distribution (LDF-$\Gamma(5,2)$). For low dose values (below 0.01 dpa), both interstitial and vacancy contents are identical and exhibit a rapid rise. However, near a dose of ϕ 0.02 dpa, the concentration of isolated interstitial defects starts to diverge from that of vacancies and begins to decrease. At the highest dpa values investigated, the isolated interstitial number density plateaus at approximately 2.4×10^{26} m^{-3}, while the isolated vacancy number density stabilises around 1.4×10^{27} m^{-3}, almost an order of magnitude higher.

This highlights the difference in behaviour between the vacancies and SIAs within the microstructure under modelled low-temperature, low-energy irradiation conditions. That is, in the absence of thermally activated diffusion, interstitials exhibit a greater propensity to diffuse and react in response to stress and strain fields (lattice deformation) compared to the relatively immobile vacancies. These stresses and strains in irradiated materials originate at the microscopic level due to the substantial elastic relaxation volumes of irradiation-induced point defects [115]. These defects cause significant local distortions in the atomic lattice. For example, DFT calculations predict an elastic relaxation volume of Ω_{relax} = 18.17 Å^3 for a $\langle110\rangle$-SIA and Ω_{relax} = -3.045 Å^3 for a vacancy in bcc [115].

This significant positive difference in relaxation volumes between SIAs and vacancies plays a crucial role in microstructure evolutions. As these defects accumulate within the microstructure as a result of irradiation, they lead to global volumetric expansion, which will be discussed later in this chapter. Consequently, materials exposed to irradiation experience stresses, resulting in macroscopic swelling and heterogeneous deformation. The different responses of vacancies and inter-

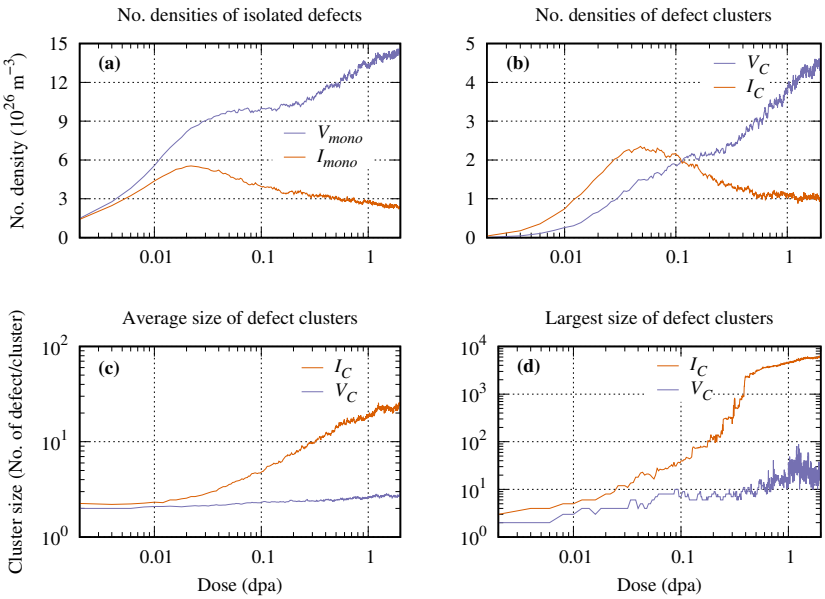

Figure 3.3: Comparison of number densities of a) isolated vacancy and interstitial, b) I_C and V_C, along with their related c) average and d) largest vacancy and interstitial clusters a function of irradiation dose.

stitial defects to irradiation are further confirmed by the trends observed in the average (Figure 3.3(c)) and largest (Figure 3.3(d)) defect cluster sizes predicted by the EAM-CRA model for irradiated bcc Fe. The observed trends likely reflect the influence of these relaxation volume differences on defect cluster formation, size and evolution. Finally, as shown in Figures 3.1 - 3.3, the damaged structure stabilises in terms of global hydrostatic pressure change and interstitial/vacancy defect contents at sufficiently high doses (above $\sim$ 2 dpa), consistent with findings reported in [76].

Additionally, Figure 3.4 compares the DFT-CRA prediction of number densities of interstitial defects, in a supercell size of $8\times a_0$, with those predicted with different interatomic potentials of M03 and M07 within simulation cell sizes of $50\times a_0$. As a result of using small supercells, large interstitial clusters and significant dislocation growth are not expected. Therefore, none of the DFT and EAM methods predicted the nucleation of finite size dislocation loops in the supercell sizes smaller than

$10\times a_0$, implying that the dislocation loops are unlikely to form out of the small interstitial clusters. The clusters must first grow larger or coalesce before they can merge into dislocation loops.

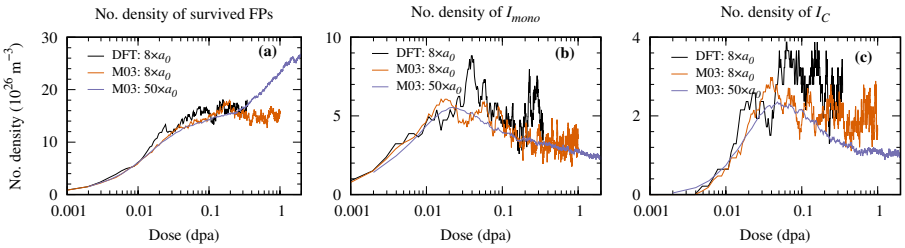

Figure 3.4: Comparison of interstitial concentration as a function of FP insertion (dpa) predicted by DFT, EAM-M03, and EAM-M07 methods within supercell sizes of 8 and $50\times a_0$.

It is intriguing to observe a strong consistency in the defect number densities (FPs, I_{mono}, and I_{C}) anticipated by both DFT- and EAM-driven CRA techniques across different supercell sizes, as depicted in Figure 3.4. Remarkable agreement is evident among the results derived from various methodologies up to approximately 0.2 dpa, despite the considerable variations in supercell dimensions. Discrepancies begin to emerge as the larger cells enter the stage of accumulation of large I_{C} and their transformation into dislocation segments, a phase that cannot be captured by the smaller cells utilised in this investigation.

3.2.1 Dislocation loop nucleation and saturation in Fe

Limited capture of extended dislocation segments in small simulation cells required the use of larger cells to analyse their evolution using the EAM-CRA method. Therefore, using large supercells, the total and directional (e.g., $1/2\langle 111\rangle$, $\langle 100\rangle$, and $\langle 110\rangle$ Burgers vectors) dislocation line densities (DLDs), ρ_D, were evaluated dividing the total dislocation line length by the corresponding supercell volume. A detailed discussion on the impact of cell size on DLD formation can be found in **Paper II**. Here, we focus on the dependence of DLD evolution on the quality of SIA distributions specifically in $50\times a_0$ supercells.

Figure 3.5(a) shows that the type of SIA distribution influences the nucleation of DLD. Nucleation begins around 0.04 dpa for UDF and 0.07 dpa for LDF-$\Gamma(4,2)$. These doses correspond to when the peak population of I_{C} starts to diminish (compare Figures 3.2 (c) and 3.5 (a)) and transforms into interstitial dislocation loops.

Additionally, Figure 3.5(a) and (b) show that the transformation of I_{C} into dislocation loops is significantly faster with UDFs compared to localised SIA distributions. Applying LDFs also lead to an increased annihilation rate of FPs, resulting in a slower accumulation of ρ_D. Consequently, the peak for $1/2\langle 111\rangle$ dislocation

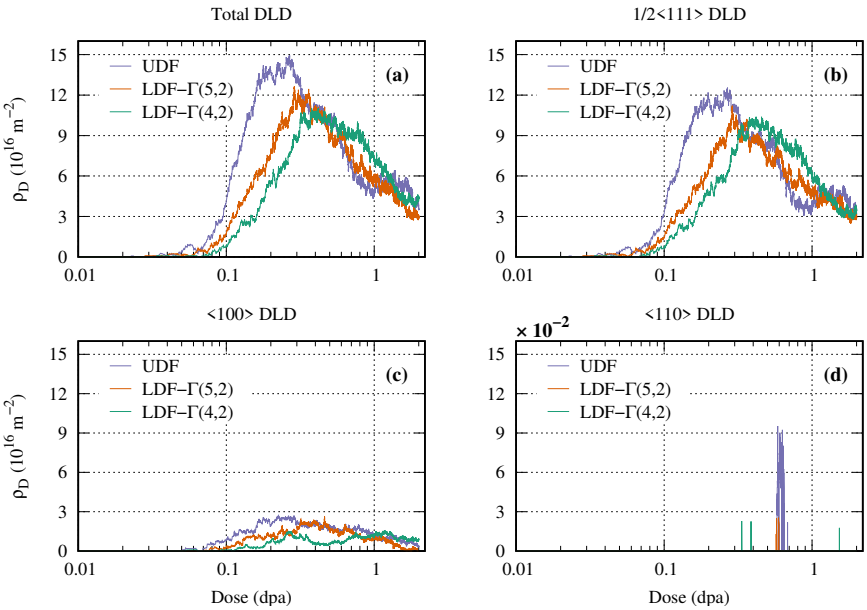

Figure 3.5: The dose-dependent evolution of a) the total DLDs accompanied by directional DLDs with b) $1/2\langle 111\rangle$, c) $\langle 100\rangle$, and d) $\langle 110\rangle$ Burgers vectors for uniform and localised distributions of the SIAs in the supercell size of $50\times a_0$.

segments with UDF is about 12% higher than those predicted with LDFs, indicating a higher probability for formation of $1/2\langle 111\rangle$ segments using UDF.

This increase in DLDs is a direct consequence of the formation of larger interstitial clusters that arise from uniformly distributed FPs. Furthermore, LDFs lead to a shift in the peak of total DLDs towards higher irradiation doses compared to UDF.

Notably, except for minor ρ_D attributed to the $\langle 110\rangle$ Burgers vector (Figure 3.5(d)), $1/2\langle 111\rangle$ dislocation segments dominate over $\langle 110\rangle$ ones. This observation aligns with the predicted lower formation energy of $1/2\langle 111\rangle$ interstitial defects in bcc Fe reported in both DFT [116] and EAM [117] calculations. Moreover, a recent experimental observation of self-ion irradiated ultra-high purity Fe at low temperature proved that the observable population of $1/2\langle 111\rangle$ dislocation segments dominated the $\langle 100\rangle$ and that there was no observable trace of $\langle 110\rangle$ dislocation segments [118].

Figure 3.6 shows the evolution of the dislocation segments, which can be broadly categorised into three distinct stages. The observed trend is similar to what has qualitatively been observed in experimentally irradiated tungsten [119] and to the results of theoretical CRA simulation of damaged Fe [76].

Referring to Figure 3.6, the first stage commences with the nucleation of dislocation loops at approximately 0.05 dpa, coinciding with the observed decrease in

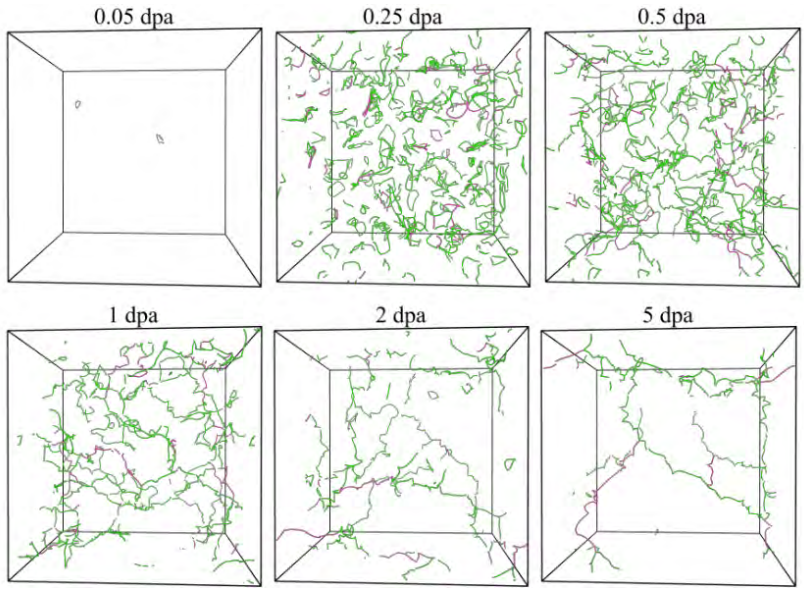

Figure 3.6: Evolution of cumulative irradiation-induced damage in bcc Fe according to the predictions of the MD-CRA model. The initial nucleation of the dislocation loops occurs around 0.05 dpa, followed by continuous growth until approximately 0.25 dpa. Subsequently, loop coalescence leads to the formation of extended dislocation lines and networks, stabilising at a steady-state length beyond 2 dpa. Dislocation segments featuring $1/2\langle 111\rangle$ and $\langle 100\rangle$ Burgers vectors are depicted in green and purple, respectively.

the peak population of interstitial clusters (refer to Figures 3.2(c) and 3.5(a)). This stage is then followed by a linear growth regime and accumulation of $1/2\langle 111\rangle$ and $\langle 100\rangle$ dislocation loops, which extends to approximately 0.25 dpa. The specific dose range for this growth phase depends on the type of SIA distribution employed.

Stage two is characterised by a decrease in DLDs after 0.3 dpa. This signifies a transition from isolated dislocation loops into the formation of a more extensive dislocation lines through the accumulation and coalescence of these loops, as depicted in Figure 3.6 at about 0.5 dpa.

Finally, stage three is the formation and growth of dislocation networks at irradiation doses exceeding 2 dpa. This suggests that the accumulation and coalescence of dislocation lines observed in stage two leads to the formation of a stable dislocation network structure, illustrated in Figure 3.6.

3.2.2 C15 Laves phase formation in Fe

Following the previous discussion on formation and evolution of large-scale extended interstitial dislocation segments, another potential consequence of extensive irradiation in bcc Fe is the local transformation of small interstitial defects into a three--dimensional structure such as a local C15 Laves phase interstitial cluster. Previous studies using various simulation techniques, including cascade simulations [103, 120], FP accumulation [108], and this study, consistently predict the formation of such non-parallel three-dimensional C15 Laves phase clusters within the damaged bcc Fe. As demonstrated by Marinica *et al.*, the C15 cluster in bcc Fe is a stable and immobile feature that may preferentially accommodate clusters of four or more SIAs [16, 17].

This structure also exhibits a significant antiferromagnetic (AF) presence in Fe, as demonstrated in [16], where a C15 cluster was artificially incorporated into bcc Fe. This finding is further supported by our dynamic modelling of irradiation damage events, as detailed in (**Papers I** and **III**). The atoms in the C15 cluster are normally ferromagnetically ordered with respect to each other, but the cluster as a whole is AF with respect to the surrounding lattice. These characteristics suggest that C15 structures play a critical role in understanding the response of Fe-based alloys to intense irradiation. However, it is important to note that our DFT-CRA and EAM-driven, i.e., EAM-ME03, CRA simulations observed a limited presence of C15-type interstitial clusters, compared to large interstitial dislocation segments. Furthermore, the choice of IAPs predicted different sizes and frequencies of C15 clusters. As demonstrated in **Paper II** and illustrated in Figure 3.7, the EAM-MA07 methods yielded the largest C15 cluster, consisting of a substantial assembly of perfect and imperfect C15 Laves phase structures with 109 SIAs. Conversely, the MD simulation using the EAM-ME03 potential resulted in a considerably smaller cluster comprising only 24 SIAs. These findings underscore the potential impact of different EAMs on predicting the size and stability of C15 Laves phase structures in irradiated Fe. [16]. It is also important to distinguish between perfect and imperfect C15-type clusters. Perfect C15 clusters exhibit a fully enclosed geometry (Figure 3.7(a)), resembling a closed cage for optimal packing efficiency. Conversely, imperfect C15 clusters, also referred as Laves phase backbone polyhedral, possess an open morphology(Figure 3.8).

This open cage-like geometry, evident in the DFT-CRA calculations in bcc Fe, likely arises due to the presence of missing or displaced atoms within the cluster structure. In terms of defects, perfect C15 clusters are formed by 12 SIAs positioned at the edges of a truncated tetrahedron. These 12 SIAs are surrounded by 10 vacancies, effectively equivalent to a net insertion of 2 SIAs, as described in [16]. Employing different SIA distribution functions, we observed that such choice has a minimal influence on the overall content of C15 Laves phase structures (including both imperfect and perfect C15-type clusters) at higher radiation doses (beyond 0.2 dpa). The first-principles DFT-CRA calculations, in this study, reveal the formation of a localised short-range FM C15 cluster (blue atoms) within the bcc

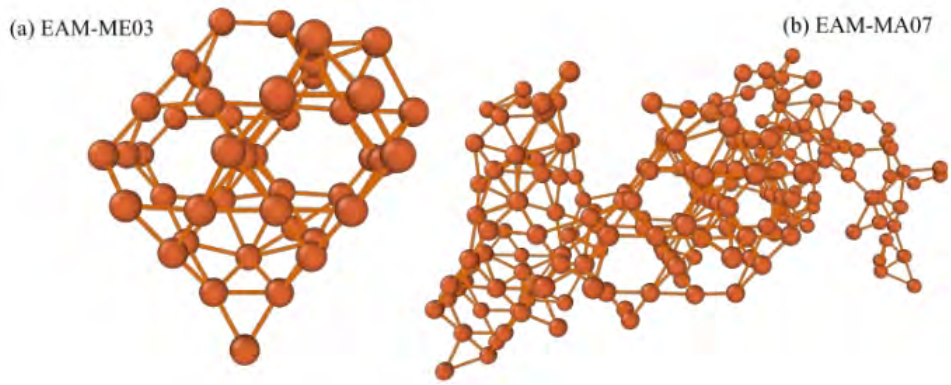

Figure 3.7: Comparative analysis of the largest C15 clusters generated in irradiated bcc Fe applying MD-CRA simulation with a) EAM-ME03 and b) EAM-MA07 potentials.

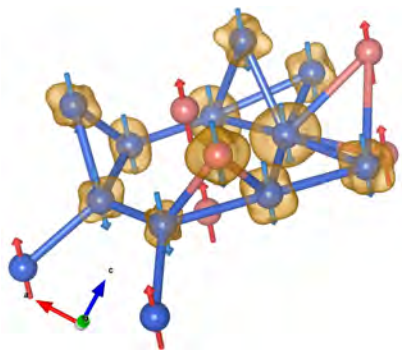

Figure 3.8: The structural backbone of a representative C15-type configuration (blue atoms) predicted by DFT-CRA simulation, characterised by a triangular arrangement of di-interstitial and a hexagonal tri-interstitial ring. The orange clouds, enveloping atoms with spin-down orientation (blue arrows), represent the three-dimensional spin density isosurfaces of atoms that underwent spin flip or quench. Red arrows attached to atoms symbolise the corresponding spin-up orientations.

Fe lattice (pink atoms), appearing from an irradiation dose of 0.1 dpa. While the atoms constructing this imperfect C15 cluster exhibit AF order relative to the surrounding host Fe atoms, they possess short-range FM ordering internally. This internal ordering is visualised by the three-dimensional isosurfaces of the spin density map (orange clouds) surrounding the C15 cluster atoms, consistent with the DFT prediction by Marinica *et al.* [16]. Consequently, they exhibit spin flip or moment quench and stabilise at an average μ of -0.7 μ_B, suggesting a potential for detection using advanced magnetic induced mapping techniques coupled with transmission electron microscopy (TEM) [121].

3.3 Radiation-induced demagnetisation in Fe

Compared to classical EAM methods, DFT offers a significant advantage in studying the magnetic response of materials under irradiation. This is because DFT explicitly considers the electronic structure, allowing for the prediction of possible magnetic transformations induced by irradiation damage, which classical models such as EAM cannot capture. It is, however, noteworthy that interatomic potentials have been developed that use a Ginzburg–Landau model to include magnetic moments [122].

As shown in Figure 3.9, the DFT-CRA method with IR calculations and 250 eV cut-off energy, demonstrate a clear trend in terms of irradiation-induced demagnetisation: the global magnetisation (M) of the bcc Fe exhibits a linear decrease with increasing irradiation dose, reaching a saturation level around 0.05 dpa, with a total reduction of 0.12 μ_B/atom. However, employing the FR method with higher accuracy (energy convergence criterion of 0.1 meV) and a larger cut-off energy (350 eV) allows for the relaxation of the entire damaged structure, thereby mitigating the demagnetisation effect. Essentially, FR calculations activate the magneto-volume effect, resulting in greater volume relaxation and, consequently, a smaller change in global magnetisation, which stabilises at about -0.04 μ_B per atom (Figure 3.9). This behaviour is discussed in detail in **Paper I**.

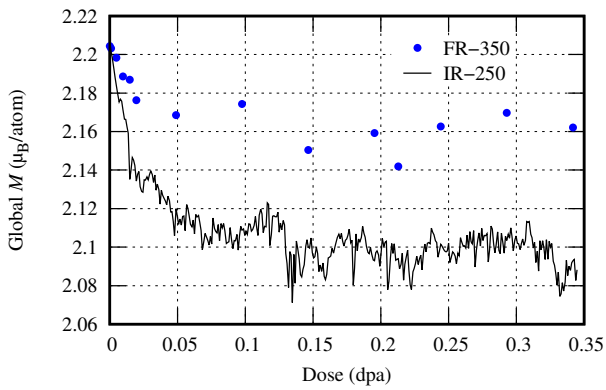

Figure 3.9: The average global magnetisation of damaged bcc Fe per atom as a function of irradiation dose.

A recent experimental study of self-ion irradiation of a 200 nm Fe film found that it induced both structural and magnetic changes [123]. The 100 nm top and bottom sublayers of the Fe film responded differently to 490 keV Fe^+ ion irradiation at room temperature at dose of 0.5 dpa. As explained in [123], the recoil and implantation probability profile of the Fe^+ irradiation demonstrates that radiation damage primarily occurs up to a depth of 100 nm in the top layer, which is exposed to the ion irradiation. For depths exceeding 100 nm (i.e., within the remaining100

nm of the bottom layer), both irradiation-induced damage and implantation effects become relevant.

Additionally, x-ray reflectivity measurements revealed that the two sublayers have distinctly different atomic densities. Specifically, the top and bottom sublayers were observed to reach atomic densities of 8.9×10^{28} atoms/m^3 and 9.2×10^{28} atoms/m^3, respectively, at the maximum dose of 341 dpa. Consequently, the top sublayer of Fe exhibits a higher magnetic moment, compared to the unirradiated Fe, while the bottom sublayer shows a lower magnetic moment.

The qualitative and quantitative agreement with experimental observations of 0.15 μ_B/atom reduction in the bottom sublayer of the aforementioned Fe films irradiated at dose of 0.5 dpa [123] highlights the effectiveness of DFT in predicting such behaviour. However, for the top layer, the experimental result is not in qualitative agreement with our results. Indeed, our simulations represent a perfect bulk material at absolute zero temperature, whereas the experiments involve thin films with surfaces at room temperature. Additionally, the simulations capture a decrease in the local magnetic moments of individual atoms with increasing dose, further supporting the notion of irradiation-induced quenching of magnetism.

Figure 3.10 explores the relationship between the local magnetic moments (μ) and atomic volumes (Ω_a) of all 1024 individual atoms, extracted from a single DFT-CRA trajectory, following damage insertion equivalent to 0.1 dpa. These volumes were calculated on the basis of the surrounding Voronoi polyhedral cell analysis. The atomic displacement resulting from FPI alters the atomic environment by introducing stress fields and causing rearrangements. This leads to variations in Ω_a, which consequently affects local μ. To clarify this further, the μ - Ω_a correlation in Figure 3.10 is categorised into two states: high-volume/high-spin (HV/HS) and low-volume/low-spin (LV/LS).

These states are defined based on the typical values of μ and Ω_a of an iron atom within an undamaged bcc Fe structure: 11.32 Å^3/atom for Ω_a and 2.2 μ_B for the local μ. The vertical dashed line in Figure 3.10 highlights the deviation of these properties of displaced atoms compared to the undamaged state. Atoms located to the right (left) of the line represent the HV/HS (LV/LS) state. In fact, vacancies caused by irradiation, lead to an increase in the associated volume of the neighbouring atoms and hence an increased local magnetisation. In contrast, atoms surrounded by SIAs or forming interstitial clusters experience a volume reduction and a decrease in local magnetisation, as also demonstrated for the C15 interstitial cluster (Figure 3.8).

As detailed in **Paper III**, by DFT-driven FR calculation, the defected bcc Fe (α-phase) exhibits an average reduction in total magnetisation (δM) by -0.043 μ_B/atom within the expanded volume (ΔV), as illustrated in Figure 3.10. The different changes in total M with IR and FR calculations are attributed to magneto-volume effects that need to be taken into account when performing the IR calculation.

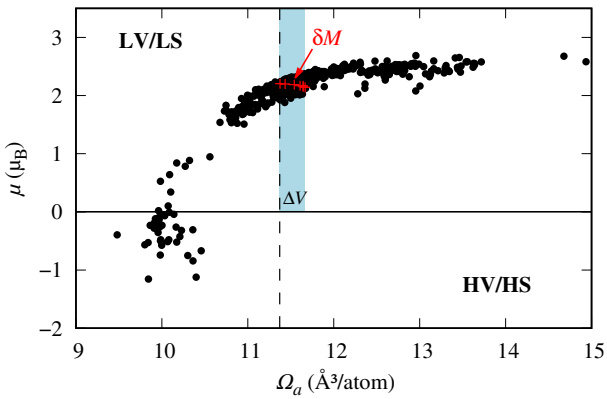

Figure 3.10: Variation of local magnetic moments with atomic volumes in damaged bcc Fe structure compared to undamaged. The vertical dashed line separates the LV/LS and HV/HS regions, illustrating the deviations. δM represents reduction in total magnetisation due to irradiation-induced volume expansion (ΔV).

3.4 Irradiation-induced polymorphism in Fe

The analysis of μ and related Ω_a in damaged bcc α-phase, as shown in Figure 3.10, offers insights into potential irradiation-induced polymorphism. Notably, atoms within the LV/LS region, experiencing reduced interatomic spacing, exhibit spontaneous spin arrangements ranging from +1 μ_B to -1 μ_B. This behaviour aligns with an AF ordering with high packing density. Moreover, some atoms exhibit near-zero magnetic moments (0 μ), suggesting a highly packed, non-magnetic (NM) configuration similar to the hexagonal close-packed (hcp) ϵ-phase of iron, which is known to be NM at low temperatures and high pressures [124].

While the DFT-CRA simulations focus on damaged bcc Fe, insights from related studies are valuable. Krauss and Krey [125] performed numerical simulations of a hypothetical amorphous iron structure at absolute zero temperature. Although different from the bcc structures used in this study, their work revealed a significant correlation between the local magnetic moment and the atomic volume in amorphous iron. Interestingly, the average trend they observed aligns with the global volume dependence reported by Moruzzi *et al.* [126] for the local magnetic moments in the AF state of face-centred cubic (fcc) γ-Fe.

Furthermore, first-principles calculations predict the existence of alternative magnetic states in fcc Fe. Beyond the conventional AF ordering, a double-layer antiferromagnetic (AFD) state exhibits stronger intra-layer coupling, leading to a doubling of short-range FM order compared to the regular AF structure [127]. This

short-range FM coupling inherent in the AFD state is believed to play a crucial role in explaining the anti-Invar effect in iron, providing further experimental support for its existence [127].

The significant increase in per-atom total energy (δE = 97.5 meV/atom) observed in irradiated Fe suggests a strong thermodynamic driving force for structural transformations. This energy increase may potentially trigger a transition from the initial FM α-phase to the AFD γ-phase or the NM/AF ϵ-phase. To support this notion, the irradiated α-Fe exhibits a decrease in per-atom total magnetisation (δM=-0.043 μ_{B}/atom) within the irradiation-induced volume expansion of ΔV (Figure 3.11(a)), aligning closely with the magneto-volume behaviour of the AFD γ-phase, described by Herper *et al.* [127]. This intersection suggests a potential irradiation-induced local transformation from α to γ.

However, data points within the HV/HS region, shown in Figure 3.11(a), generally follow the bcc magneto-volume relationship. This implies that a large portion of the damaged material retains its bcc structure under irradiation, with the formation and aggregation of vacancies, as observed in experimentally self-ion-irradiated Fe films [123]. Consequently, local magnetic moments near vacancies slightly increase, slowly approaching the value of a free Fe atom ($\sim$ 4 μ_{B}) [128].

In contrast, the LV/LS region shows a significantly complex deviation from the magneto-volume relation in the bcc lattice, aligning more closely with highly packed structures such as local FM-C15 Laves phase structure, AFD fcc, and even NM/AF hcp (Figure 3.11(a)). To solidify this observation, a more comprehensive analysis, comparing the equations of states for these structures with the μ - Ω_a data distribution, is provided in Figure 3.11(b). The suggested NM/AF ϵ-Fe phase formation by the current DFT-CRA calculations aligns ideally with the energetic considerations for NM and AF ϵ-Fe, as depicted in Figure 3.11(b). In fact, the scattering of μ - Ω_a data points around the vertical blue-dotted line, indicating the energy-volume ground state of the NM/AF ϵ-phase, providing additional support for the possible formation of the NM/AF close-packed structure under cryogenically irradiated α-Fe.

As indicated, the theoretical projection of a transition from FM bcc to NM hcp under heightened pressure aligns with experimental observations utilising x-ray magnetic circular dichroism spectroscopy [129,130]. This transition is attributed to a contraction in interatomic spacing, resulting in an overlap between the $3d$-state and $4s$-state valance bands. This overlap induces the dispersion of $3d$ electrons by reducing the density of states (DOS) of the valence electrons at the Fermi energy (E_{F}), consequently weakening the conditions conducive to FM ordering [131,132].

Interestingly, an intriguing finding within the restricted range of atomic volumes ($9.5 < \Omega_a < 15.4$) depicted in Figure 3.11(a) is the evident FM ordering demonstrated by C15-type atoms (illustrated by data points enclosed in red circles). This observation suggests a multifaceted interaction between the magnetic characteristics of C15 clusters and the underlying bcc structure under irradiation. The discernible short-range FM ordering in C15 clusters prompts a detailed examination of their electronic configuration. For example, a detailed analysis of the partial projected

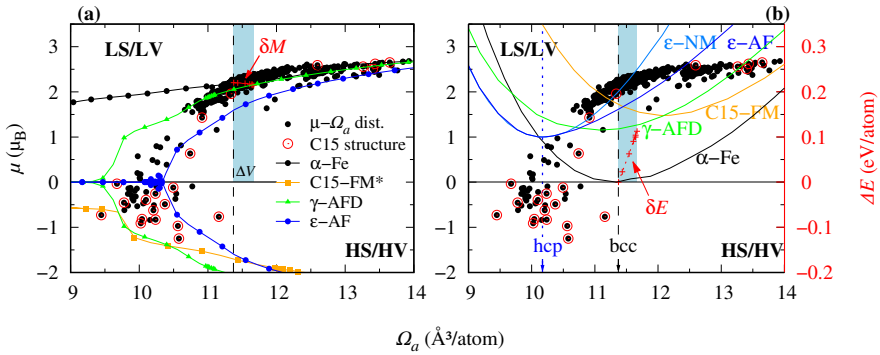

Figure 3.11: Distribution of local μ of all individual atoms of damaged bcc Fe in relation to their local Ω_a at a dose of 0.22 dpa. The data points (μ - Ω_a) are compared with two aspects: (a) magneto-volume relationships in different iron structures and (b) the equations of state of iron in various magnetic states relative to the α-Fe ground state energy. A black-dashed line divides the LV/LS and HV/HS regions, highlighting discrepancies in the local magnetic moments and atomic volumes of individual atoms in the damaged α-Fe compared to the undamaged bcc structure. In the right panel, the blue-dotted line represents the equilibrium atomic volume of NM/AF ϵ-Fe, while blue-shaded regions indicate volume expansion (ΔV) in damaged α-Fe. Additionally, for better comparison, the magneto-volume curve for the C15-FM structure is inverted to show anti-parallel spin orientation with respect to the host bcc lattice atoms.

DOS (PDOS) for a representative C15 configuration (shown in Figure 3.8) reveals a charge transfer phenomenon upon irradiation, which is schematically illustrated in Figure 3.12.

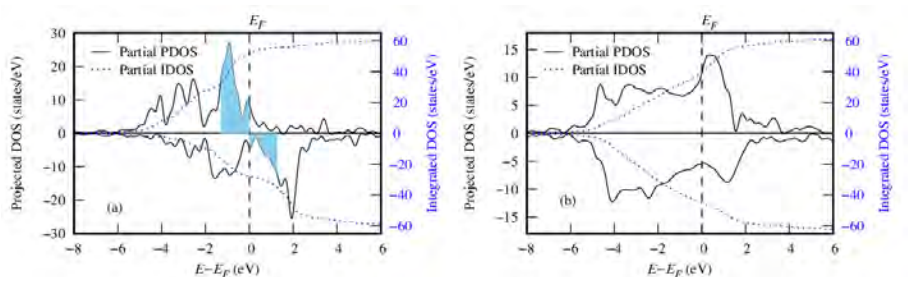

Figure 3.12: The comparison between the partial PDOS and the IDOS of C15-type atoms pre- and post-irradiation: (a) demonstrates the transfer of charge from majority to minority states prior to irradiation, while (b) presents the established partial DOS of atoms comprising the imperfect C15 Laves phase structure post-irradiation. Vertical dashed lines indicate the Fermi energy levels, designated at $E_{\mathrm{F}} = 0$.

This charge transfer phenomenon, from majority spin states situated below E_{F} to unoccupied minority states above it, is consistent with the intricate interplay between magnetism and structure under irradiation discussed previously. The resultant 26% decrease in partial PDOS at E_{F} (determined through the comparison

of integrated DOS (IDOS)) suggests a deterioration in FM ordering induced by the formation of a C15 cluster, in line with the upward displacement of E_F (Figure 3.12(a)). The shaded region in Figure 3.12(a) serves to qualitatively represent the transferred charge phenomena, reflecting the magnetic properties of the atoms that constitute the C15 cluster after irradiation. This analysis underscores how alterations induced by irradiation in the electronic structure of C15 clusters can affect their magnetic characteristics, thus contributing to the overall complexity of irradiated bcc Fe.

3.5 Microstructure evolution in Fe alloys

Up to this point, the focus has primarily been centred on modelling of irradiation-induced damage in pure Fe and analysing the evolution of the resulting microstructure within it. Following this, an investigation into defect structures within the FeCr and FeCrAl alloys, characterised by their varying alloying element compositions, is undertaken in this section and in section 3.6, respectively.

Figure 3.13 illustrates the dose-dependent evolution of survived FP, isolated interstitials, and interstitial cluster contents as predicted by DFT-driven CRA simulations for both the Fe and FeCr systems. The simulations were performed within supercells with side lengths of $8\times a_0$. Generally, there are no significant discrepancies observed among these aforementioned parameters for both pure Fe and FeCr alloys in terms of alloying effects. As depicted in Figure 3.13 (a), regardless of the model material considered, the FP densities accumulate with sharp linear rates for irradiation doses below 0.05 dpa, before starting to reach a steady-state saturation beyond 0.05 dpa. This behaviour suggests a resistance to further substantial microstructural evolution induced by irradiation, as discussed previously.

It is important to emphasise that the observed two-stage microstructure evolution within a relatively small simulation cells, despite representing a mutually interacting many-body systems, is not indicative of the inadequacy of the CRA model to anticipate larger-scale defects, such as dislocation loops in irradiated structures. Rather, this phenomenon is attributed to the specific conditions necessary for the formation of extended defects within the limitations of the simulation setup. This underscores the nuanced relationship between simulation conditions and the resulting microstructural evolution, highlighting the complex interplay between system size, defect formation dynamics, and computational constraints.

To continue, Figure 3.13(b) and Figure 3.13(c) respectively show the number densities of surviving isolated interstitials and remaining interstitial clusters, I_C, which were developed in response to strain fields around groups of near-by SIAs. Additionally, unlike FP evolution, the dose-dependent evolution of I_{mono} is not really monotonic. This behaviour suggests that while new interstitials are continuously introduced using the CRA algorithm, some annihilate with pre-existing vacancies or coalesce into other pre-existing interstitial clusters, leading to fluctuations in their number densities.

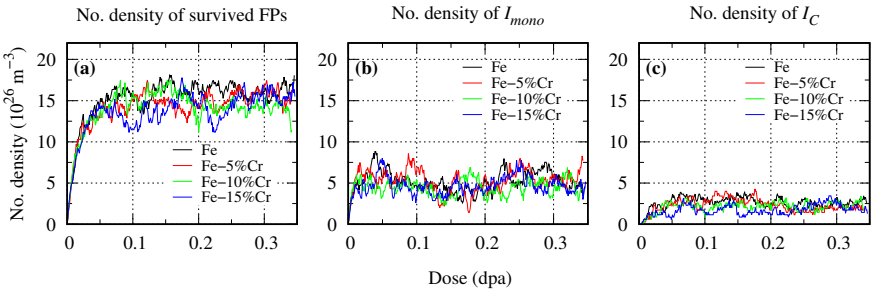

Figure 3.13: Dose-dependent number density of a) FP, b) I_{mono}, and c) I_{C} for different Fe and FeCr systems.

Figures 3.14(a) and (b) depict the concentration of evolving isolated vacancies and their related clusters, respectively, in Fe and FeCr alloys subjected to increasing damage insertion. Similarly to the total defect population (Figure 3.13 (a)), the vacancies also evolve into two stages: rapid linear growth and ultimate steady-state saturation. However, the fate of V_{mono} and I_{mono} diverges as irradiation progresses, similar to what was clearly observed in large simulation cells in this study (Figure 3.3(a)) and Ref. [76].

Compared with the average number density of evolving V_{mono} (Figure 3.14(a)), the I_{mono} (Figure 3.13(b)) shows that the concentration of remaining isolated interstitial initially increases rapidly, reaches a peak around 0.05 dpa and then gradually decreases. This indicates different responses of interstitials and vacancies to irradiation. That is, the SIAs exhibit a tendency for athermal diffusion under stress/strain field, whereas vacancies remain still immobile during supersaturation of point defects. Therefore, vacancies evolve with monotonic growth until they reach the saturation state, as discussed in section 3.2 for large-scale supercells.

Furthermore, the average number density of isolated vacancies (Figure 3.14(a)) is roughly twice that of isolated SIAs (Figure 3.13(b)) within the saturation dose range of 0.05 - 0.35 dpa. This suggests a much lower athermal elastic interaction for vacancies compared to SIAs, as also discussed in [115]. Furthermore, comparing Figures 3.13(c) and 3.14(b) indicates that the average concentration of V_{C} is approximately 30% lower than that for I_{C}, regardless of the type of system. These discrepancies can be explained by the fact that the magnitude of the relaxation volumes of Fe or Cr vacancies is, in general, much lower than those of SIAs in FeCr alloys [115].

Analysis of dose-dependent defect cluster populations suggests that, under irradiation and without thermally activated migration, point defects in Fe alloys can undergo athermal evolution to form defect clusters. This phenomenon aligns with experimental and theoretical observations during cryogenic irradiation of Fe [26] and tungsten [32, 33], attributed to elastic interactions between nano-scale defects within collision cascades.

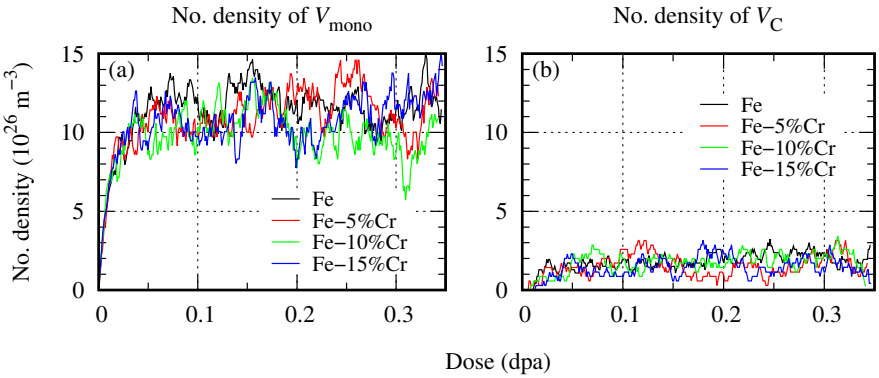

Figure 3.14: Dose-dependent number density of a) V_{mono} and b) V_{C} for different Fe and FeCr systems.

Moreover, as the irradiation dose (FPI number) increases, the induced defects interact differently with their surrounding pre-existing defects. Vacancies exhibit a weak interacting nature, leading to a higher overall isolated population compared to interstitials. Additionally, interstitial defects show a higher tendency to form larger or more stable clusters compared to vacancies, as highlighted in Figure 3.15. On average and regardless of system type, the average size of I_{C} is twice as large as that of V_{C}.

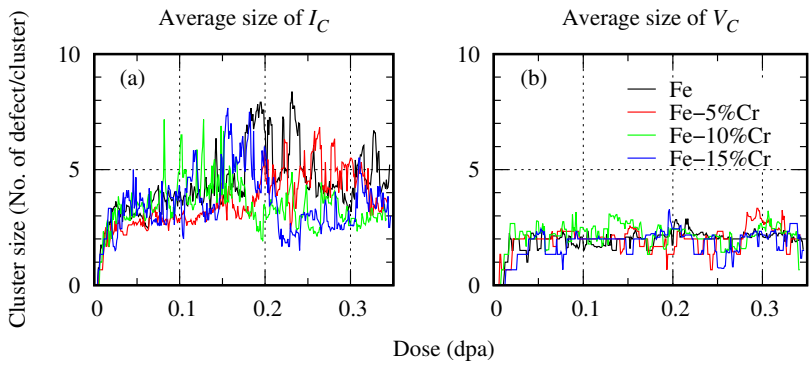

Figure 3.15: A comparison between the dose-dependent average size of a) interstitial clusters and b) vacancy clusters in Fe and FeCr alloys.

Finally, the resulting CRA predictions of interstitial defect evolution (Figures 3.13 (c) and 3.15 (a)) suggests a balance between cluster formation and other processes like defect interactions or annihilation occurring at later stages of irradiation. Therefore, further analysis is necessary to understand the exact nature of the interstitial clusters formed in FeCr alloys. These clusters may differ from the imperfect

C15 Laves phase structures previously observed in pure Fe. Furthermore, investigating the influence of chromium concentration on the size and stability of these defect clusters can provide valuable insights.

3.5.1 The C15 Laves phase structure in FeCr alloys

This section presents novel findings on C15 Laves phase formation in Fe-based alloys, building upon the theoretical predictions for pure Fe. To the best of author's knowledge, this is the first reported observation of both perfect and imperfect C15-type structures, including clusters of triangular and/or hexagonal di-interstitial rings, throughout dynamic modelling of irradiation damage event in binary FeCr alloys. Furthermore, this study demonstrates a stabilising effect of alloying Cr on C15 Laves phase formation. First-principles calculations, in conjunction with the employed CRA model, suggest that chromium actually promotes the formation of larger, perfect C15-type clusters, particularly in Fe-10 and Fe-15 at.% Cr matrices.

Figure 3.16 displays the dose-dependent evolution of atomic C15-type structures and the largest C15-type clusters found in damaged bcc Fe and FeCr alloys with varying Cr contents. As shown in Figure 3.16(a), the C15-type structure content is independent of the Cr concentration. However, the size of C15 clusters in FeCr matrix (Figure 3.16 (b)) exhibits a meaningful correlation with Cr content exceeding 5 at.%. This suggests a significantly higher tendency for SIAs to aggregate within C15 structures in alloys with higher Cr concentrations. The substitution of Fe with Cr atoms weakens the general FM ordering in the system, favouring the formation of the C15 Laves phase. This is likely facilitated by an increase in AF ordering and a potential quenching of magnetisation.

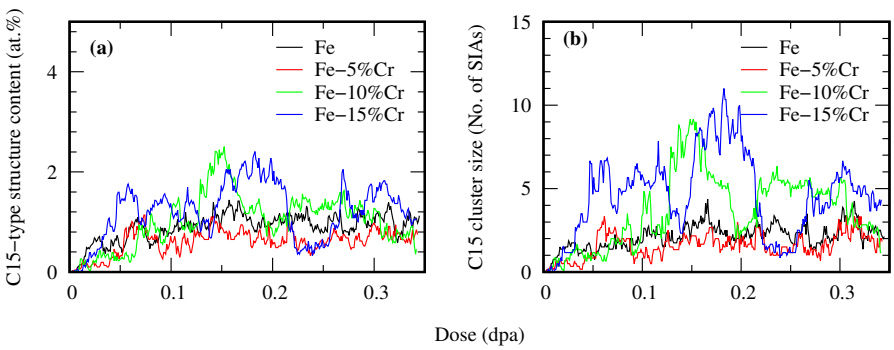

Figure 3.16: (a) Population of atoms with C15-type atomic structure and (b) the largest C15 cluster formed in Fe and FeCr alloys as a function of irradiation dose.

To further explore the potential link between Cr addition and C15 Laves phase stability, supplemental simulations were conducted. These simulations involved calculating the formation energy (using Eqs. 2.15 and 2.16) of a perfect, non-parallel interstitial C15 cluster (I_2^{C15}), as shown in Figure 3.17, and comparing it with the

formation energy of the equivalently corresponding di-interstitial cluster in ⟨110⟩-dumbbell configuration ($I_2^{\langle 110\rangle}$) in bcc alloy structures. These calculations were performed for both pure iron and various FeCr alloys modelled using the special quasi-random structure (SQS) disordering. To facilitate this analysis, a I_2^{C15} cluster was artificially introduced into supercells containing 250+2 atoms (achieved by removing 10 and inserting 12 atoms). This methodology is in accordance with the previously established procedures described in [16, 17].

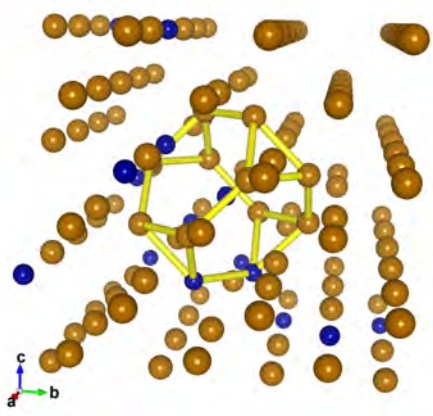

Figure 3.17: A typical perfect C15 cluster (I_2^{C15}) incorporated in a SQS-Fe-5 Cr matrix, represented with yellow-coloured bonds. The golden and dark-blue spheres symbolise Fe and Cr atoms, respectively.

To ensure a comprehensive evaluation, the formation energy of C15 clusters within the SQS-FeCr matrix was assessed by randomly inserting a single I_2^{C15} cluster into various positions within each SQS-FeCr alloy. This strategy improves the accuracy of model predictions and minimises any bias in formation energy calculations arising from the specific distribution of Cr atoms around the C15 clusters. Further details regarding these complementary calculations are provided in **Paper IV**. Furthermore, to facilitate a direct comparison, the formation energy of an equivalent $I_2^{\langle 110\rangle}$ cluster was also calculated. Consequently, an $I_2^{\langle 110\rangle}$ cluster was meticulously placed at the same randomly chosen location previously designated for I_2^{C15} inclusion.

Consistent with previous studies [17], the formation energy of the I_2^{C15} cluster is generally higher than $I_2^{\langle 110\rangle}$ in pure Fe [16], as indicated in Figure 3.18. However, as more Cr added to the bcc Fe lattice, the difference in the formation energy of SIA clusters with non-parallel I_2^{C15} and parallel $I_2^{\langle 110\rangle}$ configurations, denoted as $\Delta E^{I_2^{C15}-I_2^{\langle 110\rangle}}$, decreases from 1 eV for pure Fe to approximately 0.4 eV for Fe-15

at.% Cr (a 60% drop). This highlights that, compared to pure Fe, the SIAs in concentrated SQS-FeCr alloys exhibit a higher tendency to cluster into the C15 Laves phase, rather than adopting a parallel dumbbell configuration, as shown in Figure 3.18.

The scattered data points in Figure 3.18 is related to the inclusion of I_2^{C15} clusters at different locations within each SQS-FeCr matrix. It should be noted that, depending on the concentration of Cr atoms, the formation energy of I_2^{C15} cluster is energetically more favourable than that of the $I_2^{\langle 110 \rangle}$ cluster in SQS-FeCr alloys containing 15 - 50 at.% Cr. Furthermore, the incorporated C15 cluster in AF pure Cr lattice led to the greatest $\Delta E^{I_2^{C15} - I_2^{\langle 110 \rangle}}$ of 5.5 eV, signifying that the optimised Cr content for stabilisation of the C15 clusters could be between 15 - 50 at.% Cr.

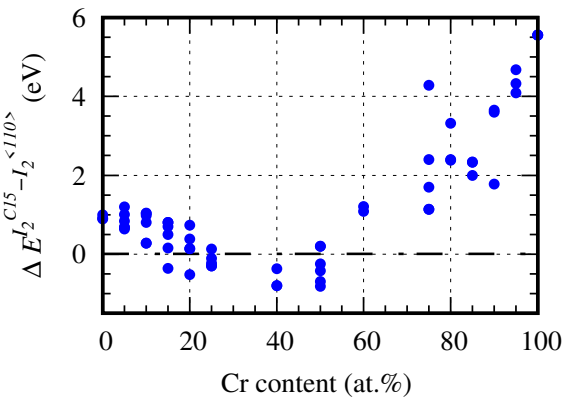

Figure 3.18: Difference in formation energies of interstitial clusters with C15 and ⟨110⟩-dumbbell configurations as a function of Cr content.

Upon examining all CRA trajectories for both Fe and FeCr alloys, it became evident that the formation of large C15 clusters with higher Cr content is not coincidental. The largest clusters of C15 type observed among all damaged Fe trajectories exhibit open cage structures, characterised by triangular and/or hexagonal di-interstitial rings, as previously depicted in Figure 3.8. In contrast, the formation of a perfect closed cage-like C15 clusters is predominant in FeCr systems with higher Cr content, specifically in 10-at.% and 15-at.% Cr, as illustrated in Figure 3.19.

In particular, as indicated in **Paper I** and **III**, C15-type structures exhibit strong antiferromagnetic alignment with the bcc host Fe atoms, as previously predicted by Marinica *et al.* in [16], while demonstrating local short-range ferromagnetism. However, in the present study, as illustrated through Figures 3.20(a) - (d), the inclusion of more Cr atoms decreases the short-range ferromagnetism of C15 clusters formed in the host bcc Fe lattice, transforming their magnetic state into locally short-range AF or even NM states in FeCr alloys with higher Cr concentra-

tions, as thoroughly discussed in **Paper IV**.

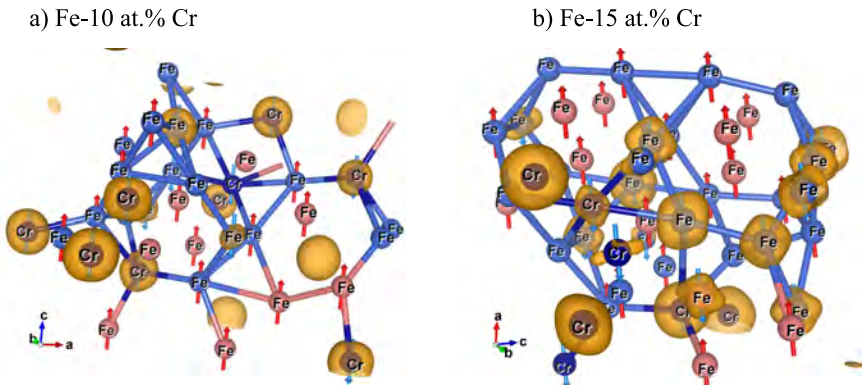

Figure 3.19: Comparison of the size of C15 clusters formed in damaged bcc a) Fe-10 and b) Fe-15 at.% Cr, respectively. The orange clouds, enveloping atoms with spin-down orientation (blue arrows), represent the three-dimensional spin density isosurfaces of atoms that underwent spin flip. The red arrows symbolise the spin-up orientations. Pink atoms represent host lattice atoms, while blue atoms without attached arrows underwent spin quench.

To elaborate on this observation, Figure 3.20 illustrates the distributions of local magnetic moments of all individual Fe and Cr atoms against their corresponding local atomic volumes (Voronoi cell) within both Fe and concentrated FeCr alloys between irradiation doses of 0.1 - 0.2 dpa. As previously demonstrated, the atoms that form C15 clusters tend to antiferromagnetically pair with ferromagnetic atoms in the host Fe lattice under constrained configurations. The addition of Cr atoms weakens the FM ordering and introduces additional AF ordering into the host Fe martix, making C15 to become either AF or even NM features. An inverse correlation exists between the size of the C15 clusters and the magnitude of their total magnetic moment.

The difference in behaviour of the C15 clusters in Fe and FeCr alloys could be related to the different magneto-volume effects of the systems, resulting from the different relaxation volumes of Fe and Cr vacancies and SIAs. A study by Wróbel *et al.* [115], using DFT calculations, showed that the alloying environment significantly impact the magnetic properties and atomic-level distortions (elastic dipoles and relaxation volumes) of point defects in bcc Fe, bcc Cr, and their disordered alloys.

The impact of relaxation volumes on the magnetism of defects in Fe-Cr alloys has been extensively investigated and discussed in [115]. This influence arises from variations in the local volume-moment of defects containing Fe-Fe and Fe-Cr dumbbells, as also reported in other studies [133–135]. Furthermore, variations in the magnitudes of magnetic moments associated with defects significantly affect the formation energy of these defects. DFT calculations [115], applying ionic and full relaxation calculations, demonstrated that the relaxation volumes and formation energies of SIA in dumbbell configurations within disordered Fe-Cr alloys decrease

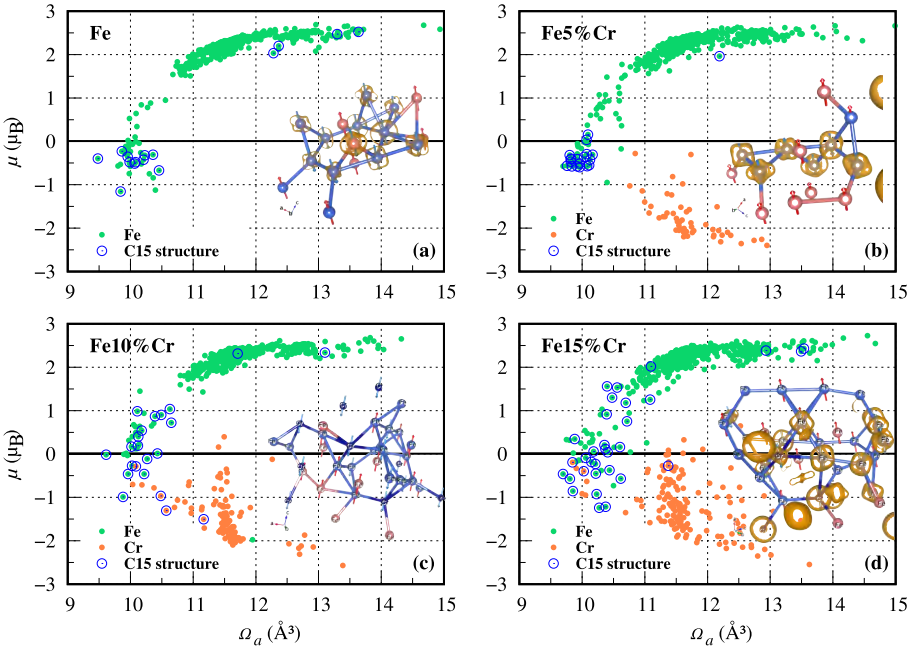

Figure 3.20: Representation of the distribution of local magnetic moments of individual atoms within damaged bcc Fe and FeCr alloys relative to their respective local atomic volumes at an irradiation dose of approximately 0.1 - 0.2 dpa. The individual C15 clusters, separately formed in each system, with corresponding μ - Ω_a distribution in blue-circled points are depicted to illustrate their magnetic moment alignments in Fe and FeCr alloys. The green and orange data points represent the μ - Ω_a relationships for Fe and Cr atoms, respectively.

with increasing Cr content. In addition, as shown by Marinica [16], the negative formation energy of clusters of four or more SIAs in the form of C15 structures, alongside the reduction in the formation energy of dumbbells with increasing Cr content in the SQS-FeCr alloys, supports the hypothesis of stabilisation of the C15 cluster with increasing Cr content proposed in this study.

3.5.2 Radiation-induced magnetisation and structural change in FeCr

In this study, the relationship between Cr content and irradiation-induced volume expansion (swelling) was explored in Fe-based alloys. Using Eq. (2.2), swelling was continuously monitored by calculating the ratio of global pressure change (ΔP) to bulk modulus (B), through volume conserving calculations. Bulk moduli for each FeCr system were chosen based on experimentally available data from literature [65,136] at room temperature. Additionally, swelling can be estimated directly by calculating the relative volume change, represented as $\Delta V/V_0$, through FR cal-

culations, where both the volume and shape of the supercell along with the ionic positions were consistently relaxed.

As shown in Figure 3.21(a), direct first-principles calculations unveil a consistent trend across various Fe-based systems: swelling initially increases linearly and then plateaus at the early stage of irradiation dose (0.05 dpa). Importantly, a robust correlation emerges between saturated swelling and Cr content in Fe-based alloys beyond 0.05 dpa. For example, swelling in Fe is approximately 40% higher than that of Fe containing 15-at.% Cr. As Cr content increases, FeCr alloys demonstrate enhanced resistance to irradiation-induced volume expansion under the CRA conditions.

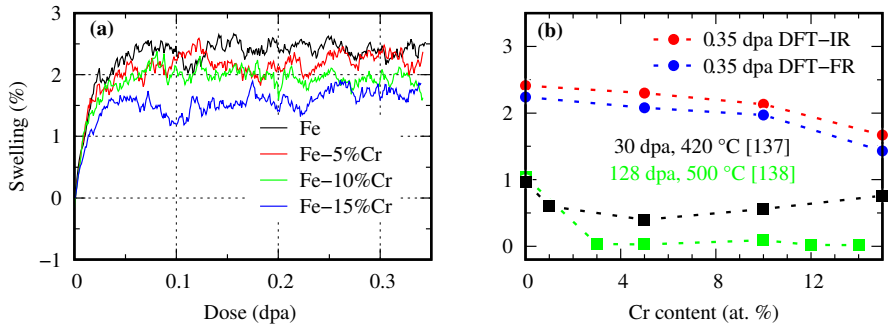

Figure 3.21: Dose-dependent evolution of averaged irradiation-induced swelling in Fe and FeCr systems. (b) DFT prediction of swelling as a function of Cr content for pure Fe and binary FeCr alloys.

Several studies [137–139] have investigated the influence of chromium alloying on volumetric swelling under high-temperature and extensive irradiation conditions. As depicted in Figure 3.21(b), these experiments, despite employing high irradiation doses and elevated temperatures, demonstrate that even small Cr additions (3 wt.%) significantly suppress peak swelling in high-purity Fe-Cr alloys. In particular, pure Fe exhibits a peak swelling of around 1%, while Fe-Cr alloys show a remarkable relative reduction of approximately 90%. This data underscores the critical role of Cr concentration in mitigating irradiation-induced swelling.

Considering the absence of thermally activated diffusion in our damaged structures, as well as the uniformity in the number density and size of the vacancy clusters in Fe-based alloys (Figures 3.13 - 3.15), the magneto-volume relationships of the FeCr systems may play a role in responding differently to irradiation. Therefore, exploring the correlation between the change in total M and related volume expansion may elucidate the relationship between Cr content and swelling in Fe-based alloys, as illustrated in Figure 3.22. This correlation emerges from various relaxation calculations, including IR and FR, derived from DFT-CRA calculations.

As depicted in Figure 3.22(a), a clear linear correlation emerges between Cr content and the change in global magnetisation, leading to diverse responses of

Fe-based alloys to irradiation damage. Incorporation of Cr atoms into the bcc Fe structure results in a decrease in FM ordering, thus weakening ferromagnetism and resulting in a reduced magneto-volume effect.

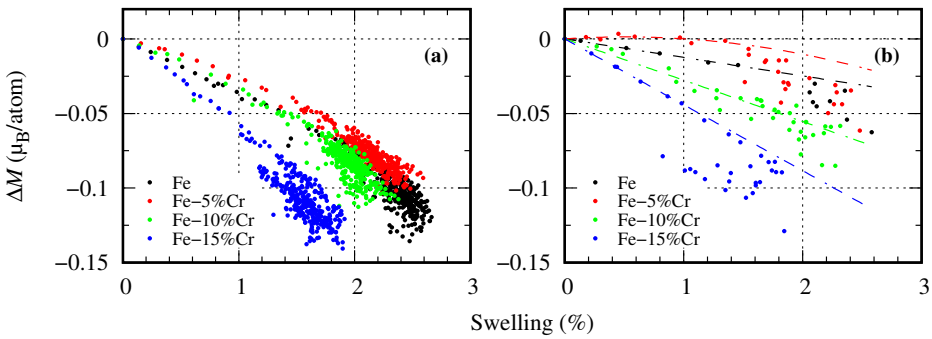

Figure 3.22: Averaged change in global M per atom relative to corresponding swelling in various Fe and FeCr systems. The left panel (a) displays the results of DFT-IR calculations ($\Delta P/B$), while the right panel (b) presents the outcomes of DFT-FR calculations ($\Delta V)/V_0$) for several snapshots of the CRA trajectories. In the right panel, dashed lines fitted to the data points depict instances where ΔM) has not yet reached saturation values.

DFT-FR calculations with enhanced accuracy (Figure 3.22(b)) further reveal a notable nonlinear relationship between Cr content and irradiation-induced swelling in damaged Fe alloys. Figures 3.22(a) and (b) demonstrate that within the conditions applied in this study, ΔM exhibits a linear decrease followed by a steady-state saturation, with data points scattered around the final values (Figure 3.21). Interestingly, Fe-Cr alloys respond differently to irradiation with respect to magnetisation changes compared to pure Fe. For example, adding 5 at.% Cr suppresses the change in total M, while further Cr additions accelerate the reduction in M and subsequently in swelling at a higher rate than pure Fe.

3.6 Radiation-induced damage in FeCrAl and Al_2O_3

Our discussions on bcc Fe and FeCr systems have raised a crucial question: how does the addition of aluminium to a Fe-10% Cr matrix impact its structural properties and their evolution under irradiation? As highlighted in Chapter 1, incorporating aluminium has been shown to enhance the corrosion resistance of FeCr alloys, making them ideal for applications like fuel cladding for certain advanced reactor types, such as lead fast reactors [12, 14]. This improvement stems from the formation of a thin and highly oxidation-resistant Al_2O_3 layer on the surface, acting as a protective barrier at elevated temperatures in steam or liquid-lead environments. Consequently, understanding the possibly dissimilar responses of FeCrAl and Al_2O_3 to irradiation is critical for ensuring mechanical stability of components made from FeCrAl.

Building on **Papers II** and **V**, our DFT-driven CRA simulations employed multiple FPI technique within the simulation cells, particularly for the DFT-driven CRA modelling of irradiation damage event in non-magnetic Al_2O_3. In this case, a simultaneous five-FPI (5-FPI) scenario was adopted to efficiently achieve dose values of 1 dpa. This method reproduced the dose-dependent evolutions of energy and pressure changes observed in single FPI (i.e., 1-FPI) simulations but allowed for a considerably faster dose evolution, computationally.

It is worth noting that for studying damage structure in large-supercells used in MD-driven CRA simulation, the number of FP insertions ranged from 10 to 1000 concurrent FPI, as described in **Paper II**.

3.6.1 Radiation-induced damage in FeCrAl

Expanding on the results shown in Figure 3.13 (section 3.5), Figure 3.23 shows the dose-dependent average number densities of FPs, I_{mono} and I_{C} for Fe-10Cr-xAl alloys with varying Al concentrations (2, 4, and 6 at.%), as detailed in **Paper V**. Notably, the defect number densities for these FeCrAl systems exhibit minimal variation across different Al contents. However, Figure 3.23(b) highlights a clear difference in the behaviour of the I_{mono} population in Fe-10Cr-6Al within the dose interval 0.25 - 0.35 dpa with a pronounced decrease in the number density of isolated interstitials. This suggests the potential collapse of individual SIAs into larger clusters. Interestingly, as indicated in (Figure 3.24), DFT-CRA simulations reveal a remarkable influence of aluminium on the formation of the C15 cluster in the Fe-10Cr matrix within the dose range of 0.25 - 0.35 dpa. In these dose limits, the atomic percentage of C15 Laves phase structure in FeCrAl with 6 at.% Al is the highest seen so far in all studied materials and consequently the largest C15 cluster was recorded, as indicated in Figure 3.25. This proposes that addition of aluminium may effectively stabilise the formation of C15 cluster defects within the FeCrAl matrix, invoking interest for future investigation.

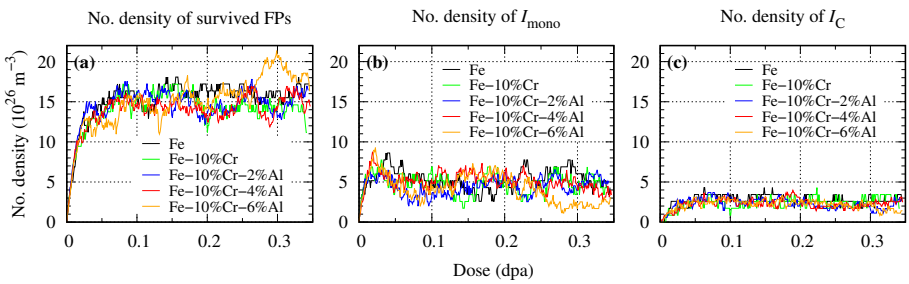

Figure 3.23: Dose-dependent number density of the a) FP, b) I_{mono}, and c) I_{C} for Fe, Fe-10 at.%Cr and Fe-10 at.%Cr with different Al content.

Indeed, further analysis of the cluster structure, shown in Figure 3.25, may reveal or relate the role of the addition aluminium (even as impurity element) in

stabilising the C15 cluster formation, similar to what has been argued for the role of chromium in bcc Fe before. Here, the lower atomic relaxation volume and non-magnetic nature of aluminium seem to be essential in understanding a probable link between its concentration and the formation of C15 structures in irradiated bcc Fe alloys.

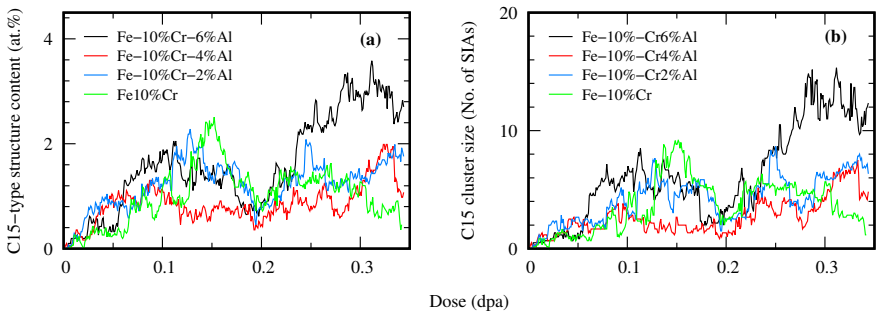

Figure 3.24: (a) Population of C15-type atomic structure and (b) the largest C15 Laves phase structures formed in Fe10%Cr with diverse Al contents as a function of irradiation dose.

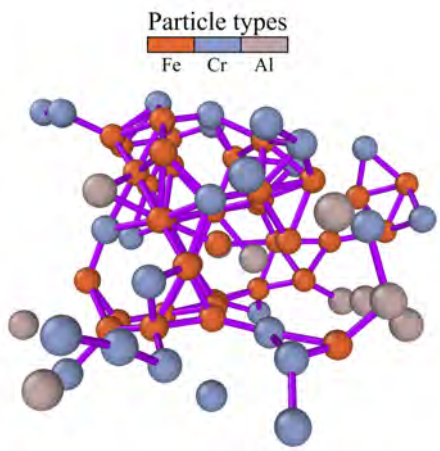

Figure 3.25: The largest C15 clusters formed in irradiated bcc Fe-10%Cr-6%Al applying DFT-CRA simulation. Orange spheres are Fe, blue spheres are Cr and teal spheres are Al.

PTM analysis, as shown in Figure 3.25, strengthens the conceivable connection between the aluminium content and the C15 cluster stability. A higher number of Al atoms appears to promote the formation of C15 clusters, particularly in alloys with sufficient chromium content (e.g., 10 at.% or more). This observation aligns with the well-established NM/AF character of giant C15 clusters enriched in chromium.

It suggests a potential synergistic effect between Al and Cr, favouring the formation and stability of larger, non-magnetic C15 clusters. Notably, typical such clusters formed in FeCrAl, predicted by the DFT-driven CRA, reveals that Al atoms occupy both the central core and periphery of the C15 cluster.

These findings open exciting avenues for further exploration. Understanding the atomic-level mechanisms by which Al influences C15 cluster characteristics and investigating how these clusters through the Al content impacts the mechanical properties of FeCrAl alloys are crucial next steps.

3.6.2 Radiation-induced damage in Al_2O_3

The incorporation of aluminium into ferritic alloys has been shown to significantly enhance their corrosion resistance, particularly in high-temperature liquid Pb. This beneficial effect is due to the formation of thin layers of amorphous and nano-scale alumina (Al_2O_3) which forms at elevated temperatures [140, 141]. The alumina scale is necessary to protect the steel from corrosion.

There is a scarcity of studies on irradiation damage on FeCrAl steels, and a potential concern is that if the swelling of the underlying steel alloy differ significantly from that of the alumina scale layer, then the alumina scale could spall off during operation, exposing the metallic alloy to interact directly with the liquid metal. Therefore, from a materials engineering perspective, it is crucial to evaluate irradiation-induced swelling behaviour in both the metallic bcc FeCrAl phase and the corundum ceramic Al_2O_3 phase.

As a starting point, the DFT-CRA predictions of this study reveal a significant disparity in the defect number densities for the oxide and metallic matrices, see **Paper V** for more details. The concentration of surviving FPs at saturation levels (0.5 - 1 dpa) in Al_2O_3 (Figure 3.26(a)) is roughly seven times higher than that predicted for FeCrAl (Figure 3.23(a)) at saturation levels of 0.05 - 0.35 dpa. This suggests a significantly lower rate of recombination between vacancies and SIAs in Al_2O_3, particularly at very low temperature regimes.

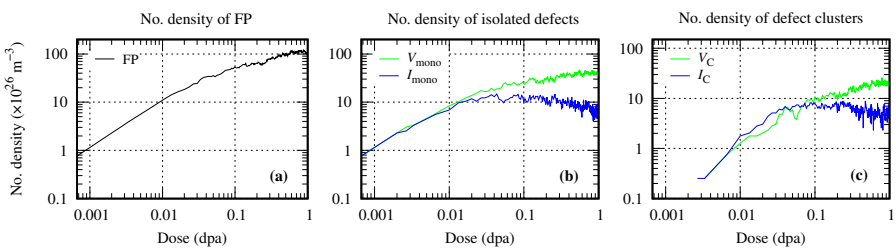

Figure 3.26: Dose-dependent evolution of the number densities of a) FP, b) isolated defects, and c) defect clusters formed in α-Al_2O_3.

Furthermore, a comparison of Figures 3.23 and 3.26 reveals distinct differences in the microstructural evolution of corundum Al_2O_3 compared to bcc metallic struc-

tures, particularly at intermediate irradiation doses ranging from 0.05 to 0.5 dpa. In damaged Al_2O_3, an initial rapid linear increase in defect density leads to supersaturation of FP defects at doses below 0.05 dpa. Subsequently, these defects begin to recombine with pre-existing point defects, resulting in a gradually decelerating evolution rate between 0.05 and 0.5 dpa. Finally, saturation occurs for irradiation doses beyond 0.5 dpa. This behaviour indicates the presence of three distinct stages in the microstructural evolution of damaged Al_2O_3, whereas Fe alloys with approximately the same simulation cell size evolve through two distinct stages, in this limited simulation cell size.

Several factors may contribute to the different microstructural evolutions observed in alumina compared to Fe-based alloys. Firstly, in addition to having different crystal structures and localised bonding, the oxygen and aluminium atoms in Al_2O_3 have lower relaxation volumes than the $3d$-metals in FeCrAl alloys. This difference in relaxation volume affects the response of SIAs to the stress field induced by FPI in alumina compared to metallic Fe alloys. Consequently, SIAs in Al_2O_3 may accumulate more and recombine less with vacancies compared to those in FeCrAl. Secondly, the different migration barriers and pathways for charged point defects in hexagonal Al_2O_3, compared to the point defects in bcc metallic alloys, influence their mobility, leading to different defect buildup dynamics. For instance, theoretically calculated migration energies range from 1 to 2.5 eV [142, 143], while experimental measurements indicate migration energies around 5 eV [144] in the oxides, while the Fe-based metals have migration barriers of significantly less than 1 eV for all point defects [145, 146].

Furthermore, *ab initio* calculations [147] shows that migration of interstitial oxygen atoms leads to the formation of dumbbells with regular oxygen atoms. It has been proved that optimised configuration of fixed dumbbell is a more preferable alternative to recombination of interstitial oxygen atom with oxygen vacancy. Additionally, the nature of charged point defects in ceramic Al_2O_3 versus defects in metallic alloys may contribute to the distinct microstructural evolution in these materials. For example, charged oxygen interstitial anions can be trapped by regular oxygen sublattice atoms or charged aluminium interstitial cations to form complex clusters, which may reduce the recombination rate.

A clear consequence of different defect accumulation rates in ceramic and metallic materials, as illustrated in Figure 3.27, is seen in the difference in irradiation-induced swelling between alumina and Fe alloys. The swelling in alumina is estimated to be about three times higher than that predicted in Fe alloys at very low temperatures. This outcome is a direct consequence of the accumulation of a significantly greater number of surviving FP defects within the alumina scale. It should be noted that the bulk modulus for estimating the swelling (via Eq. (2.2)) of alumina is selected according to available experimental data in the literature [148]. Moreover, the bulk modulus for Fe-10%Cr-4%Al is chosen to be equal to that of Fe-10%Cr alloys, as the difference between Fe-10Cr and the addition of Al has been shown to be less than 1% at room temperature, according to MD simulation [149].

The enhanced swelling in crystalline alumina with respect to the underlying

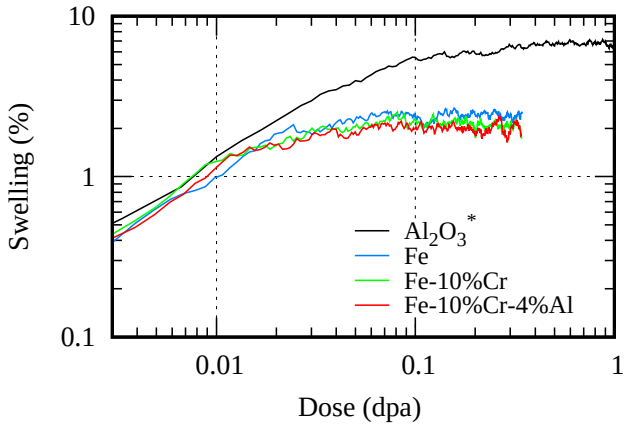

Figure 3.27: Comparison of irradiation-induced swelling in Fe-based alloys and in Al_2O_3. * Swelling in Al_2O_3 was simulated with the method of simultaneously implanting five FP at a time.

alloy could be a cause for concern since it would risk spalling off at elevated levels of irradiation. However, in the real steel application, the alumina scale is rarely purely crystalline, and thus should exhibit very high radiation damage tolerance.

Chapter 4

Conclusions and outlook

This thesis leveraged an advanced computational model, the creation-relaxation algorithm, and integrated it with first-principles DFT calculations and classical interatomic EAM potentials. This powerful combination allowed for atomistic simulation of irradiation-induced events with exceptional accuracy, allowing for a comprehensive analysis of the resulting microstructural evolutions.

The CRA model stochastically introduces Frenkel pairs, that is, vacancies and SIAs, into any reference atomic structure. Subsequently, the model rigorously relaxes the defective system to reach its local minimum energy configuration. This process enables the identification and characterisation of microstructural imperfections that emerge dynamically within the specified model material.

To properly model low-energy, low-temperature irradiation conditions, the CRA method was refined by incorporating a selection of local and uniform distribution functions. This integration allows the model to realistically capture the statistical distribution of SIAs within the defected material, reflecting the conditions achievable in a controlled irradiation experiment.

Furthermore, the model was enhanced by incorporating a complementary algorithm to regulate the proximity of inserted atoms to one another, defining a virtually restricted volume around each atom termed the forbidden zone. This feature is particularly crucial in scenarios where interatomic potentials lack strong short-range repulsive forces, which is also pertinent for pseudopotentials used in first-principles calculations. Consequently, if an inserted atom is positioned too closely to another, due to the stochastic nature of insertion, the internal algorithm adjusts the position by displacing it outward to the zone boundary, initiating relaxation from that point onwards.

With these enhancements, this study investigated the microstructure evolution induced by radiation in bcc Fe alloys and Al_2O_3 employing a combined methodology of EAM potentials and DFT calculations within the CRA framework. The investigation successfully captured the evolving microstructure, induced by irradiation, as a function of the simulated irradiation dose across various supercell sizes,

highlighting the distinct evolutions of vacancy and interstitial defects and defect clusters.

In smaller simulation cells, two stages of microstructural evolution under CRA conditions were observed: an initial linear build-up of point defects followed by steady-state saturation of clustering defects. Conversely, employing larger supercells with different types of spatial distribution of FPs leads to variations in the microstructure evolutions, with localised distribution of FPs resulting in slower microstructural development compared to that rendered by uniform distributions, delaying dislocation nucleation to higher doses.

This study also explored the formation of other types of interstitial clusters within damaged Fe-based model materials. Specifically, DFT predicts the formation of non-parallel, three-dimensional C15 Laves phase structures, exhibiting strong antiferromagnetic characteristics with internal short-range ferromagnetic ordering. MD-driven CRA calculations highlight the size and occurrence dependency of C15 clusters on the interatomic potential used, with the Marinica potential predicting the largest and most stable C15 clusters for clusters of four or more SIAs. Conversely, the Mendelev potential shows better agreement with DFT simulations, especially for the smaller C15 clusters formed dynamically in small supercells.

Despite the potential used, the predicted C15 cluster sizes are likely to fall below the detection limits of conventional TEM techniques. However, the average local magnetic moment of the C15 cluster, as predicted by the DFT-CRA model, suggests a remarkable potential for experimental detection using advanced magnetic-induced mapping techniques when coupled with TEM.

Furthermore, DFT-driven CRA calculations indicate the possibility of polymorphism occurring in irradiated α-Fe, suggesting the potential formation of NM/AF ϵ-phase and an AFD γ-phase, based on the excess energy deposited in the irradiated system and the local magnetic moment - atomic volume relationship. Besides, the DFT-CRA approach revealed a strong correlation between chromium and aluminium content on the stability of large C15 clusters in concentrated FeCr alloys compared to that in pure Fe. Chromium atoms also play a crucial role in mitigating irradiation-induced swelling, providing some part of the context for the experimental observation of how low-to-moderate Cr content can strongly suppress irradiation-induced swelling in Fe alloys. The non-linear dependence of swelling on Cr concentration is proposed to be due mainly due to reduction of mobility of glissile SIA clusters in low to moderate Cr concentrations, given that the Cr atoms interact with the SIAs in the gliding loops. This effect then vanishes due to percolation when the Cr content is high enough. There may also be a secondary attribution due to the significantly larger negative relaxation volume of vacancies in Cr sites compared to Fe sites.

Finally, the extensive DFT-based metadata generated from this study on complex damaged systems such as FeCr and FeCrAl alloys presents a valuable resource for developing interatomic potentials using machine learning approaches. Such potentials could allow investigations of large-scale microstructural evolution in similar systems that are currently beyond the reach of DFT-CRA calculations.

From the DFT-driven CRA simulations on FeCrAl system, further investigation is required to understand the mechanisms through which alloying elements, specifically Al and Cr atoms, influence the stabilisation of the C15 Laves phase in the FeCrAl matrices. Furthermore, calculating the formation energies of larger perfect clusters of incorporated C15 in Fe alloys will help to determine whether the observed tendency of SIAs to form giant C15 structures in high-chromium alloys is energetically favourable.

Leveraging the extensive metadata generated from our DFT-driven CRA simulations on FeCrAl alloys and alumina, future research could involve developing machine-learning interatomic potentials to investigate the irradiation-induced microstructure evolution in large-scale simulation cells in those chemically complex systems. This approach would allow for a more comprehensive understanding of the behaviour of these materials under irradiation conditions.

The CRA model with FP insertion effectively replicates damage evolution in various model materials under low-energy irradiation conditions, such as electron irradiation. However, for modelling high-energy irradiation events based on creation-relaxation algorithm, like neutron bombardments, the damage morphology and energy transfer to lattice atoms differ significantly due to the nature of the irradiating particles. To improve the accuracy of the modelling, a different approach for high-energy damage events is wanted. We propose substituting FP insertion with void (vacancy cluster) insertion to capture these events more accurately. Preliminary simulations using the EAM in Fe and FeCr alloys demonstrate the feasibility of void insertion. This method involves randomly selecting an atom and a specific number of its nearest neighbours for void creation, followed by localised redistribution of the selected atoms to form SIA clusters. Further validation is required before void insertion can be established as a standard approach for simulating neutron irradiation.

Finally, the CRA model can be also extended to study microstructure evolution in many other systems of interest, such as ceramic uranium nitride (UN) or uranium dioxide (UO_2) fuels, where the irradiation cross section for one atomic species differs significantly from the other. By modifying the algorithm to bias atom selection towards a specific atomic species, one can study how the microstructure evolves in a matrix for which the constituent atoms have different displacement cross sections. This would broaden the applicability of the CRA model, providing valuable insights into the irradiation response of a wider range of materials.

Bibliography

[1] H. Kamide, G. Rodriguez, P. Guiberteau, N. Kawasaki, B. Hatala, A. Alemberti, S. Bourg, Y. Huang, F. Serre, M. A. Fuetterer, D. Shropshire, M. Moore, F. Reilly, P. Paviet, G. Cojazzi, L.-Y. Cheng, T. Sofu, L. Edwards, R. Garbil, and E. Loewen, "Generation IV International Forum - GIF, Annual Report 2020," tech. rep., Nuclear Energy Agency, Nuclear Energy Agency of the OECD (NEA), 2021. INIS-FR–21-0718.

[2] D. Buckthorpe, "1 - Introduction to Generation IV nuclear reactors," in *Structural Materials for Generation IV Nuclear Reactors* (P. Yvon, ed.), pp. 1–22, Woodhead Publishing, 2017.

[3] OECD and N. E. Agency, *Nuclear Power Plant Life Management and Longer-term Operation*. OECD Nuclear Energy Agency, 2006.

[4] J. Henry and S. A. Maloy, "9 - Irradiation-resistant ferritic and martensitic steels as core materials for Generation IV nuclear reactors," in *Structural Materials for Generation IV Nuclear Reactors* (P. Yvon, ed.), pp. 329–355, Woodhead Publishing, Jan. 2017.

[5] C. Ganguly and V. V. Inozemtsev, *Structural materials for liquid metal cooled fast reactor fuel assemblies : operational behaviour*. IAEA nuclear energy series, no. NF-T-4.3, Vienna: International Atomic Energy Agency, 2012.

[6] K. A. Terrani, S. J. Zinkle, and L. L. Snead, "Advanced oxidation-resistant iron-based alloys for LWR fuel cladding," *Journal of Nuclear Materials*, vol. 448, pp. 420–435, May 2014.

[7] B. H. Sencer, J. R. Kennedy, J. I. Cole, S. A. Maloy, and F. A. Garner, "Microstructural analysis of an HT9 fuel assembly duct irradiated in FFTF to 155dpa at 443°C," *Journal of Nuclear Materials*, vol. 393, pp. 235–241, Sept. 2009.

[8] R. L. Klueh and A. T. Nelson, "Ferritic/martensitic steels for next-generation reactors," *Journal of Nuclear Materials*, vol. 371, pp. 37–52, Sept. 2007.

[9] S. Takaya, T. Furukawa, G. Müller, A. Heinzel, A. Jianu, A. Weisenburger, K. Aoto, M. Inoue, T. Okuda, F. Abe, S. Ohnuki, T. Fujisawa, and A. Kimura, "Al-containing ODS steels with improved corrosion resistance to liquid lead–bismuth," *Journal of Nuclear Materials*, vol. 428, pp. 125–130, Sept. 2012.

[10] S. Takaya, T. Furukawa, K. Aoto, G. Müller, A. Weisenburger, A. Heinzel, M. Inoue, T. Okuda, F. Abe, S. Ohnuki, T. Fujisawa, and A. Kimura, "Corrosion behavior of Al-alloying high Cr-ODS steels in lead–bismuth eutectic," *Journal of Nuclear Materials*, vol. 386-388, pp. 507–510, 2009.

[11] B. A. Pint, K. A. Terrani, Y. Yamamoto, and L. L. Snead, "Material Selection for Accident Tolerant Fuel Cladding," *Metallurgical and Materials Transactions E*, vol. 2, pp. 190–196, Sept. 2015.

[12] G. Jiang, D. Xu, P. Feng, S. Guo, J. Yang, and Y. Li, "Corrosion of FeCrAl alloys used as fuel cladding in nuclear reactors," *Journal of Alloys and Compounds*, vol. 869, p. 159235, July 2021.

[13] P. Dömstedt, J. Ejenstam, and P. Szakálos, "High Temperature Corrosion of a Lean Alloyed FeCrAl-steel and the Effects of Impurities in Liquid Lead," in *2020 IEEE International Conference on Environment and Electrical Engineering and 2020 IEEE Industrial and Commercial Power Systems Europe (EEEIC / I&CPS Europe)*, pp. 1–6, 2020.

[14] P. Dömstedt, M. Lundberg, and P. Szakálos, "Corrosion studies of a low alloyed Fe–10Cr–4Al steel exposed in liquid Pb at very high temperatures," *Journal of Nuclear Materials*, vol. 531, p. 152022, Apr. 2020.

[15] E. Airiskallio, E. Nurmi, M. H. Heinonen, I. J. Väyrynen, K. Kokko, M. Ropo, M. P. J. Punkkinen, H. Pitkänen, M. Alatalo, J. Kollár, B. Johansson, and L. Vitos, "High temperature oxidation of Fe–Al and Fe–Cr–Al alloys: The role of Cr as a chemically active element," *Corrosion Science*, vol. 52, pp. 3394–3404, Oct. 2010.

[16] M.-C. Marinica, F. Willaime, and J.-P. Crocombette, "Irradiation-Induced Formation of Nanocrystallites with C15 Laves Phase Structure in bcc Iron," *Physical Review Letters*, vol. 108, p. 025501, Jan. 2012.

[17] L. Dézerald, M.-C. Marinica, L. Ventelon, D. Rodney, and F. Willaime, "Stability of self-interstitial clusters with C15 Laves phase structure in iron," *Journal of Nuclear Materials*, vol. 449, pp. 219–224, June 2014.

[18] I. M. Robertson, M. A. Kirk, and W. E. King, "Formation of dislocation loops in iron by self-ion irradiations at 40K," *Scripta Metallurgica*, vol. 18, pp. 317–320, Apr. 1984.

[19] J. Gao, E. Gaganidze, B. Kaiser, and J. Aktaa, "Evolution mechanisms of irradiation-induced helium bubbles, C15 clusters and dislocation loops in ferrite/martensite steels: A cluster dynamics modeling study," *Journal of Nuclear Materials*, vol. 557, p. 153212, Dec. 2021.

[20] E. Wakai, A. Hishinuma, Y. Kato, H. Yano, S. Takaki, and K. Abiko, "Radiation-Induced α'-Phase Formation on Dislocation Loops in Fe-Cr Alloys During Electron Irradiation," *Le Journal de Physique IV*, vol. 05, pp. C7–286, Nov. 1995. Publisher: EDP Sciences.

[21] G. S. Was, "The Radiation Damage Event," in *Fundamentals of Radiation Materials Science: Metals and Alloys* (G. S. WAS, ed.), pp. 3–76, New York, NY: Springer, 2017.

[22] G. H. Kinchin and R. S. Pease, "The Displacement of Atoms in Solids by Radiation," *Reports on Progress in Physics*, vol. 18, pp. 1–51, Jan. 1955. Publisher: IOP Publishing.

[23] G. S. Was, "The Damage Cascade," in *Fundamentals of Radiation Materials Science: Metals and Alloys* (G. S. WAS, ed.), pp. 131–165, New York, NY: Springer, 2017.

[24] G. S. Was, "Point Defect Formation and Diffusion," in *Fundamentals of Radiation Materials Science: Metals and Alloys* (G. S. WAS, ed.), pp. 167–205, New York, NY: Springer, 2017.

[25] M. J. Norgett, M. T. Robinson, and I. M. Torrens, "A proposed method of calculating displacement dose rates," *Nuclear Engineering and Design*, vol. 33, pp. 50–54, Aug. 1975.

[26] K. Nordlund, S. J. Zinkle, A. E. Sand, F. Granberg, R. S. Averback, R. E. Stoller, T. Suzudo, L. Malerba, F. Banhart, W. J. Weber, F. Willaime, S. L. Dudarev, and D. Simeone, "Primary radiation damage: A review of current understanding and models," *Journal of Nuclear Materials*, vol. 512, pp. 450–479, 2018.

[27] G. S. Was, "The Displacement of Atoms," in *Fundamentals of Radiation Materials Science: Metals and Alloys* (G. S. WAS, ed.), pp. 77–130, New York, NY: Springer, 2017.

[28] J. A. Brinkman, "Production of Atomic Displacements by High-Energy Particles," *American Journal of Physics*, vol. 24, pp. 246–267, Apr. 1956. Publisher: American Association of Physics Teachers.

[29] J. R. Beeler, "Displacement Spikes in Cubic Metals. I. α-Iron, Copper, and Tungsten," *Phys. Rev.*, vol. 150, pp. 470–487, Oct. 1966.

[30] D. J. Bacon, A. F. Calder, F. Gao, V. G. Kapinos, and S. J. Wooding, "Computer simulation of defect production by displacement cascades in metals," *Nuclear Instruments and Methods in Physics Research Section B: Beam Interactions with Materials and Atoms*, vol. 102, pp. 37–46, Aug. 1995.

[31] A. Seeger, "ON THE THEORY OF RADIATION DAMAGE AND RADIATION HARDENING," tech. rep., U.S. Department of Energy Office of Scientific and Technical Information, Oct. 1959.

[32] X. Yi, A. E. Sand, D. R. Mason, M. A. Kirk, S. G. Roberts, K. Nordlund, and S. L. Dudarev, "Direct observation of size scaling and elastic interaction between nano-scale defects in collision cascades," *Europhysics Letters*, vol. 110, p. 36001, May 2015. Publisher: EDP Sciences, IOP Publishing and Società Italiana di Fisica.

[33] A. E. Sand, K. Nordlund, and S. L. Dudarev, "Radiation damage production in massive cascades initiated by fusion neutrons in tungsten," *Journal of Nuclear Materials*, vol. 455, pp. 207–211, Dec. 2014.

[34] D. R. Mason, X. Yi, M. A. Kirk, and S. L. Dudarev, "Elastic trapping of dislocation loops in cascades in ion-irradiated tungsten foils," *Journal of Physics: Condensed Matter*, vol. 26, p. 375701, Aug. 2014. Publisher: IOP Publishing.

[35] L. Reali, M. Boleininger, M. R. Gilbert, and S. L. Dudarev, "Macroscopic elastic stress and strain produced by irradiation," *Nuclear Fusion*, vol. 62, p. 016002, Dec. 2021. Publisher: IOP Publishing.

[36] C. Cawthorne and E. J. Fulton, "Voids in Irradiated Stainless Steel," *Nature*, vol. 216, pp. 575–576, Nov. 1967.

[37] P.-W. Ma, D. R. Mason, and S. L. Dudarev, "Multiscale analysis of dislocation loops and voids in tungsten," *Physical Review Materials*, vol. 4, p. 103609, Oct. 2020. Publisher: American Physical Society.

[38] A. J. Ardell and P. Bellon, "Radiation-induced solute segregation in metallic alloys," *Current Opinion in Solid State and Materials Science*, vol. 20, pp. 115–139, June 2016.

[39] S. Zinkle, "Radiation-Induced Effects on Microstructure," *Comprehensive Nuclear Materials*, vol. 1, p. 65, 2012.

[40] G. S. Was, *Fundamentals of Radiation Materials Science.* New York, NY: Springer, 2017.

[41] D. Kaoumi, J. Adamson, and M. Kirk, "Microstructure evolution of two model ferritic/martensitic steels under in situ ion irradiation at low doses (0–2dpa)," *Journal of Nuclear Materials*, vol. 445, pp. 12–19, Feb. 2014.

[42] J. Ejenstam, B. Jönsson, and P. Szakalos, "Optimizing the Oxidation Properties of FeCrAl Alloys at Low Temperatures," *Oxid Met*, vol. 88, pp. 361–370, Oct. 2017.

[43] R. E. Smallman, I. R. Harris, and M. A. Duggan, "Microstructure and materials processing," *Journal of Materials Processing Technology*, vol. 63, pp. 18–29, Jan. 1997.

[44] W. J. Weber and F. P. Roberts, "A Review of Radiation Effects in Solid Nuclear Waste Forms," *Nuclear Technology*, vol. 60, pp. 178–198, Feb. 1983.

[45] P. Spätig, J.-C. Chen, and G. R. Odette, "Chapter 11 - Ferritic and Tempered Martensitic Steels," in *Structural Alloys for Nuclear Energy Applications* (G. R. Odette and S. J. Zinkle, eds.), pp. 485–527, Boston: Elsevier, 2019.

[46] L. Koch, F. Granberg, T. Brink, D. Utt, K. Albe, F. Djurabekova, and K. Nordlund, "Local segregation versus irradiation effects in high-entropy alloys: Steady-state conditions in a driven system," *Journal of Applied Physics*, vol. 122, p. 105106, Sept. 2017.

[47] S. M. Bruemmer, E. P. Simonen, P. M. Scott, P. L. Andresen, G. S. Was, and J. L. Nelson, "Radiation-induced material changes and susceptibility to intergranular failure of light-water-reactor core internals," *Journal of Nuclear Materials*, vol. 274, pp. 299–314, Sept. 1999.

[48] W. Liu, Y. Ji, P. Tan, H. Zang, C. He, D. Yun, C. Zhang, and Z. Yang, "Irradiation Induced Microstructure Evolution in Nanostructured Materials: A Review," *Materials*, vol. 9, p. 105, Feb. 2016. Number: 2 Publisher: Multidisciplinary Digital Publishing Institute.

[49] C. S. Deo, E. Y. Chen, and R. Dingeville, "Atomistic modeling of radiation damage in crystalline materials," *Modelling and Simulation in Materials Science and Engineering*, vol. 30, p. 023001, Dec. 2021. Publisher: IOP Publishing.

[50] Y. Li, S. Hu, X. Sun, and M. Stan, "A review: applications of the phase field method in predicting microstructure and property evolution of irradiated nuclear materials," *npj Computational Materials*, vol. 3, pp. 1–17, Apr. 2017.

[51] J.-P. Crocombette and D. Ghaleb, "Molecular dynamics modeling of irradiation damage in pure and uranium-doped zircon," *Journal of Nuclear Materials*, vol. 295, pp. 167–178, June 2001.

[52] S. Dudarev, "Density Functional Theory Models for Radiation Damage," *Annual Review of Materials Research*, vol. 43, no. 1, pp. 35–61, 2013.

[53] L. Malerba, M. J. Caturla, E. Gaganidze, C. Kaden, M. J. Konstantinović, P. Olsson, C. Robertson, D. Rodney, A. M. Ruiz-Moreno, M. Serrano, J. Aktaa, N. Anento, S. Austin, A. Bakaev, J. P. Balbuena, F. Bergner, F. Boioli, M. Boleininger, G. Bonny, N. Castin, J. B. J. Chapman, P. Chekhonin, M. Clozel, B. Devincre, L. Dupuy, G. Diego, S. L. Dudarev, C. C. Fu, R. Gatti, L. G§lébart, B. Gómez-Ferrer, D. Gonçalves, C. Guerrero, P. M. Gueye, P. Hähner, S. P. Hannula, Q. Hayat, M. Hernández-Mayoral, J. Jagielski, N. Jennett, F. Jiménez, G. Kapoor, A. Kraych, T. Khvan, L. Kurpaska, A. Kuronen, N. Kvashin, O. Libera, P. W. Ma, T. Manninen, M. C. Marinica, S. Merino, E. Meslin, F. Mompiou, F. Mota, H. Namburi, C. J. Ortiz, C. Pareige, M. Prester, R. R. Rajakrishnan, M. Sauzay, A. Serra, I. Simonovski, F. Soisson, P. Spätig, D. Tanguy, D. Terentyev, M. Trebala, M. Trochet, A. Ulbricht, M.Vallet, K. Vogel, T. Yalcinkaya, and J. Zhao, "Multiscale modelling for fusion and fission materials: The M4F project," *Nuclear Materials and Energy*, vol. 29, p. 101051, Dec. 2021.

[54] M. J. Caturla, A. Gras Martıi, J. J. Jimènez-Rodrıguez, J. C. Jimènez Saez, and M. C. Pèrez-Martin, "Molecular Dynamics Simulations of Energy Deposition in Solids," in *Advances in Quantum Chemistry*, vol. 45 of *Theory of the Interaction of Swift Ions with Matter. Part 1*, pp. 79–98, Academic Press, Jan. 2004.

[55] C. Domain, C. S. Becquart, and L. Malerba, "Simulation of radiation damage in Fe alloys: an object kinetic Monte Carlo approach," *Journal of Nuclear Materials*, vol. 335, pp. 121–145, Oct. 2004.

[56] J.-P. Crocombette and F. Willaime, "1.08 - *Ab initio* Electronic Structure Calculations for Nuclear Materials," in *Comprehensive Nuclear Materials* (R. J. M. Konings, ed.), pp. 223–248, Oxford: Elsevier, 2012.

[57] W. Cai, J. Li, and S. Yip, "1.09 - Molecular Dynamics," in *Comprehensive Nuclear Materials* (R. J. M. Konings, ed.), pp. 249–265, Oxford: Elsevier, 2012.

[58] C. S. Becquart and B. D. Wirth, "1.14 - Kinetic Monte Carlo Simulations of Irradiation Effects," in *Comprehensive Nuclear Materials* (R. J. M. Konings, ed.), pp. 393–410, Oxford: Elsevier, 2012.

[59] D. J. Bacon and Y. N. Osetsky, "Multiscale modelling of radiation damage in metals: from defect generation to material properties," *Materials Science and Engineering: A*, vol. 365, pp. 46–56, Jan. 2004.

[60] K. Nordlund and F. Djurabekova, "Multiscale modelling of irradiation in nanostructures," *Journal of Computational Electronics*, vol. 13, pp. 122–141, Mar. 2014.

[61] K. Nordlund, S. J. Zinkle, A. E. Sand, F. Granberg, R. S. Averback, R. Stoller, T. Suzudo, L. Malerba, F. Banhart, W. J. Weber, F. Willaime, S. L. Dudarev, and D. Simeone, "Improving atomic displacement and replacement calculations with physically realistic damage models," *Nature Communications*, vol. 9, p. 1084, Mar. 2018.

[62] M. T. Robinson and I. M. Torrens, "Computer simulation of atomic-displacement cascades in solids in the binary-collision approximation," *Physical Review B*, vol. 9, pp. 5008–5024, June 1974. Publisher: American Physical Society.

[63] H. C. Herper, E. Hoffmann, and P. Entel, "*Ab initio* Investigations of Iron-Based Martensitic Systems," *Le Journal de Physique IV*, vol. 07, pp. C5–76, Nov. 1997. Publisher: EDP Sciences.

[64] C. Domain and C. S. Becquart, "*Ab initio* calculations of defects in Fe and dilute Fe-Cu alloys," *Physical Review B*, vol. 65, p. 024103, Dec. 2001. Publisher: American Physical Society.

[65] P. Olsson, I. A. Abrikosov, L. Vitos, and J. Wallenius, "*Ab initio* formation energies of Fe–Cr alloys," *Journal of Nuclear Materials*, vol. 321, pp. 84–90, Sept. 2003.

[66] P. Olsson, C. S. Becquart, and C. Domain, "*Ab initio* threshold displacement energies in iron," *Materials Research Letters*, vol. 4, pp. 219–225, Oct. 2016.

[67] A. Bakaev, D. Terentyev, G. Bonny, T. Klaver, P. Olsson, and D. Van Neck, "Interaction of minor alloying elements of high-Cr ferritic steels with lattice defects: An *ab initio* study," *Journal of Nuclear Materials*, vol. 444, pp. 237–246, Jan. 2014.

[68] P. Olsson, T. P. C. Klaver, and C. Domain, "*Ab initio* study of solute transition-metal interactions with point defects in bcc Fe," *Physical Review B*, vol. 81, p. 054102, Feb. 2010. Publisher: American Physical Society.

[69] J. C. Meyer, F. Eder, S. Kurasch, V. Skakalova, J. Kotakoski, H. J. Park, S. Roth, A. Chuvilin, S. Eyhusen, G. Benner, A. V. Krasheninnikov, and U. Kaiser, "Accurate Measurement of Electron Beam Induced Displacement Cross Sections for Single-Layer Graphene," *Phys. Rev. Lett.*, vol. 108, p. 196102, May 2012.

[70] E. Holmström, A. Kuronen, and K. Nordlund, "Threshold defect production in silicon determined by density functional theory molecular dynamics simulations," *Phys. Rev. B*, vol. 78, p. 045202, July 2008.

[71] E. Martínez, M. J. Caturla, and J. Marian, "DFT-Parameterized Object Kinetic Monte Carlo Simulations of Radiation Damage," in *Handbook of Materials Modeling: Applications: Current and Emerging Materials* (W. Andreoni

and S. Yip, eds.), pp. 2457–2488, Cham: Springer International Publishing, 2020.

[72] L. Messina, M. Chiapetto, P. Olsson, C. S. Becquart, and L. Malerba, "An object kinetic Monte Carlo model for the microstructure evolution of neutron-irradiated reactor pressure vessel steels," *physica status solidi (a)*, vol. 213, no. 11, pp. 2974–2980, 2016. _eprint: https://onlinelibrary.wiley.com/doi/pdf/10.1002/pssa.201600038.

[73] C.-C. Fu, J. D. Torre, F. Willaime, J.-L. Bocquet, and A. Barbu, "Multiscale modelling of defect kinetics in irradiated iron," *Nature Materials*, vol. 4, pp. 68–74, Jan. 2005.

[74] L. Gámez, B. Gámez, M. J. Caturla, D. Terentyev, and J. M. Perlado, "Object Kinetic Monte Carlo calculations of irradiated Fe–Cr dilute alloys: The effect of the interaction radius between substitutional Cr and self-interstitial Fe," *Nuclear Instruments and Methods in Physics Research Section B: Beam Interactions with Materials and Atoms*, vol. 269, pp. 1684–1688, July 2011.

[75] C. S. Becquart, C. Domain, U. Sarkar, A. DeBacker, and M. Hou, "Microstructural evolution of irradiated tungsten: *Ab initio* parameterisation of an OKMC model," *Journal of Nuclear Materials*, vol. 403, pp. 75–88, Aug. 2010.

[76] P. M. Derlet and S. L. Dudarev, "Microscopic structure of a heavily irradiated material," *Physical Review Materials*, vol. 4, p. 023605, Feb. 2020.

[77] Y. Limoge, A. Rahman, H. Hsieh, and S. Yip, "Computer simulation studies of radiation induced amorphization," *Journal of Non-Crystalline Solids*, vol. 99, pp. 75–88, Jan. 1988.

[78] K. Nordlund, N. Runeberg, and D. Sundholm, "Repulsive interatomic potentials calculated using Hartree-Fock and density-functional theory methods," *Nuclear Instruments and Methods in Physics Research Section B: Beam Interactions with Materials and Atoms*, vol. 132, pp. 45–54, Oct. 1997.

[79] P. E. Blöchl, "Projector augmented-wave method," *Physical Review B*, vol. 50, pp. 17953–17979, Dec. 1994. Publisher: American Physical Society.

[80] D. V. Schroeder, *An introduction to thermal physics.* an Francisco, CA: Addison Wesley, 17th edition ed., 2000.

[81] J. Proakis, "Probability, random variables and stochastic processes," *IEEE Transactions on Acoustics, Speech, and Signal Processing*, vol. 33, pp. 1637–1637, Dec. 1985. Conference Name: IEEE Transactions on Acoustics, Speech, and Signal Processing.

[82] F. M. Dekking, C. Kraaikamp, H. P. Lopuhaä, and L. E. Meester, *A Modern Introduction to Probability and Statistics: Understanding Why and How*. Springer Texts in Statistics, Springer London, 2010.

[83] K. Nakashima, R. E. Stoller, and H. Xu, "Recombination radius of a Frenkel pair and capture radius of a self-interstitial atom by vacancy clusters in bcc Fe," *Journal of Physics: Condensed Matter*, vol. 27, p. 335401, Aug. 2015. Publisher: IOP Publishing.

[84] J. A. Horak and T. H. Blewitt, "Fast neutron irradiation induced resistivity in metals," *physica status solidi (a)*, vol. 9, no. 2, pp. 721–730, 1972.

[85] J. Dural, J. Ardonceau, and J. C. Jousset, "Endommagement du fer par irradiation aux électrons à 20 K," *Journal de Physique*, vol. 38, pp. 1007–1011, Aug. 1977. Publisher: Société Française de Physique.

[86] M. Born and R. Oppenheimer, "Zur Quantentheorie der Molekeln," *Annalen der Physik*, vol. 389, no. 20, pp. 457–484, 1927.

[87] D. R. Hartree, "The calculation of atomic structures," *Reports on Progress in Physics*, vol. 11, p. 113, Jan. 1947.

[88] D. R. Hartree, "The Wave Mechanics of an Atom with a Non-Coulomb Central Field. Part I. Theory and Methods," *Mathematical Proceedings of the Cambridge Philosophical Society*, vol. 24, no. 1, pp. 89–110, 1928.

[89] V. Fock, "Näherungsmethode zur Lösung des quantenmechanischen Mehrkörperproblems," *Zeitschrift für Physik*, vol. 61, pp. 126–148, Jan. 1930.

[90] P. Hohenberg and W. Kohn, "Inhomogeneous Electron Gas," *Phys. Rev.*, vol. 136, pp. B864–B871, Nov. 1964.

[91] W. Kohn and L. J. Sham, "Self-Consistent Equations Including Exchange and Correlation Effects," *Phys. Rev.*, vol. 140, pp. A1133–A1138, Nov. 1965.

[92] G. Kresse and J. Hafner, "*Ab initio* molecular dynamics for liquid metals," *Physical Review B*, vol. 47, pp. 558–561, Jan. 1993.

[93] G. Kresse and J. Furthmüller, "Efficiency of ab-initio total energy calculations for metals and semiconductors using a plane-wave basis set," *Computational Materials Science*, vol. 6, pp. 15–50, July 1996.

[94] G. Kresse and J. Furthmüller, "Efficient iterative schemes for *ab initio* total-energy calculations using a plane-wave basis set," *Physical Review B*, vol. 54, pp. 11169–11186, Oct. 1996.

[95] G. Kresse and D. Joubert, "From ultrasoft pseudopotentials to the projector augmented-wave method," *Phys. Rev. B*, vol. 59, pp. 1758–1775, Jan. 1999. Publisher: American Physical Society.

[96] D. J. Singh and L. Nordström, "Planewave Pseudopotential Methods," in *Planewaves, Pseudopotentials and the LAPW Method*, pp. 23–41, Boston, MA: Springer US, 2006.

[97] K. Binder, J. Horbach, W. Kob, W. Paul, and F. Varnik, "Molecular dynamics simulations," *Journal of Physics: Condensed Matter*, vol. 16, p. S429, Jan. 2004.

[98] G. J. Ackland, "1.10 - Interatomic Potential Development," in *Comprehensive Nuclear Materials* (R. J. M. Konings, ed.), pp. 267–291, Oxford: Elsevier, 2012.

[99] M. S. Daw, S. M. Foiles, and M. I. Baskes, "The embedded-atom method: a review of theory and applications," *Materials Science Reports*, vol. 9, pp. 251–310, Mar. 1993.

[100] M. S. Daw and M. I. Baskes, "Semiempirical, Quantum Mechanical Calculation of Hydrogen Embrittlement in Metals," *Phys. Rev. Lett.*, vol. 50, pp. 1285–1288, Apr. 1983.

[101] M. S. Daw and M. I. Baskes, "Embedded-atom method: Derivation and application to impurities, surfaces, and other defects in metals," *Phys. Rev. B*, vol. 29, pp. 6443–6453, June 1984.

[102] M. I. Mendelev, S. Han, D. J. Srolovitz, G. J. Ackland, D. Y. Sun, and M. Asta, "Development of new interatomic potentials appropriate for crystalline and liquid iron," *Philosophical Magazine*, vol. 83, Dec. 2003.

[103] D. J. Bacon, F. Gao, and Y. N. Osetsky, "The primary damage state in fcc, bcc and hcp metals as seen in molecular dynamics simulations," *Journal of Nuclear Materials*, vol. 276, pp. 1–12, Jan. 2000.

[104] L. Malerba, M. C. Marinica, N. Anento, C. Björkas, H. Nguyen, C. Domain, F. Djurabekova, P. Olsson, K. Nordlund, A. Serra, D. Terentyev, F. Willaime, and C. S. Becquart, "Comparison of empirical interatomic potentials for iron applied to radiation damage studies," *Journal of Nuclear Materials*, vol. 406, pp. 19–38, Nov. 2010.

[105] G. J. Ackland, M. I. Mendelev, D. J. Srolovitz, S. Han, and A. V. Barashev, "Development of an interatomic potential for phosphorus impurities in α-iron," *Journal of Physics: Condensed Matter*, vol. 16, p. S2629, June 2004.

[106] D. A. Terentyev, T. P. C. Klaver, P. Olsson, M.-C. Marinica, F. Willaime, C. Domain, and L. Malerba, "Self-Trapped Interstitial-Type Defects in Iron," *Physical Review Letters*, vol. 100, p. 145503, Apr. 2008. Publisher: American Physical Society.

[107] D. Terentyev, C. Lagerstedt, P. Olsson, K. Nordlund, J. Wallenius, C. S. Becquart, and L. Malerba, "Effect of the interatomic potential on the features of displacement cascades in α-Fe: A molecular dynamics study," *Journal of Nuclear Materials*, vol. 351, pp. 65–77, June 2006.

[108] A. Chartier and M. C. Marinica, "Rearrangement of interstitial defects in α-Fe under extreme condition," *Acta Materialia*, vol. 180, pp. 141–148, Nov. 2019.

[109] D. Frenkel and B. Smit, *Understanding molecular simulation: from algorithms to applications*, vol. 1. Academic Press San Diego, 2002.

[110] A. P. Thompson, H. M. Aktulga, R. Berger, D. S. Bolintineanu, W. M. Brown, P. S. Crozier, P. J. in 't Veld, A. Kohlmeyer, S. G. Moore, T. D. Nguyen, R. Shan, M. J. Stevens, J. Tranchida, C. Trott, and S. J. Plimpton, "LAMMPS - a flexible simulation tool for particle-based materials modeling at the atomic, meso, and continuum scales," *Computer Physics Communications*, vol. 271, p. 108171, Feb. 2022.

[111] A. Stukowski, "Visualization and analysis of atomistic simulation data with OVITO–the Open Visualization Tool," *Modelling and Simulation in Materials Science and Engineering*, vol. 18, p. 015012, Dec. 2009.

[112] C. Björkas and K. Nordlund, "Comparative study of cascade damage in Fe simulated with recent potentials," *Nuclear Instruments and Methods in Physics Research Section B: Beam Interactions with Materials and Atoms*, vol. 259, pp. 853–860, June 2007.

[113] P. M. Larsen, S. Schmidt, and J. Schiøtz, "Robust structural identification via polyhedral template matching," *Modelling and Simulation in Materials Science and Engineering*, vol. 24, p. 055007, May 2016. Publisher: IOP Publishing.

[114] G. S. Was, "Dislocation Microstructure," in *Fundamentals of Radiation Materials Science: Metals and Alloys* (G. S. WAS, ed.), pp. 301–378, New York, NY: Springer, 2017.

[115] J. S. Wróbel, M. R. Zemła, D. Nguyen-Manh, P. Olsson, L. Messina, C. Domain, T. Wejrzanowski, and S. L. Dudarev, "Elastic dipole tensors and relaxation volumes of point defects in concentrated random magnetic Fe-Cr alloys," *Computational Materials Science*, vol. 194, p. 110435, June 2021.

[116] F. Willaime, C. C. Fu, M. C. Marinica, and J. Dalla Torre, "Stability and mobility of self-interstitials and small interstitial clusters in α-iron: *ab initio* and empirical potential calculations," *Nuclear Instruments and Methods in Physics Research Section B: Beam Interactions with Materials and Atoms*, vol. 228, pp. 92–99, Jan. 2005.

[117] R. Alexander, M.-C. Marinica, L. Proville, F. Willaime, K. Arakawa, M. R. Gilbert, and S. L. Dudarev, "*Ab initio* scaling laws for the formation energy of nanosized interstitial defect clusters in iron, tungsten, and vanadium," *Physical Review B*, vol. 94, p. 024103, July 2016. Publisher: American Physical Society.

[118] R. Schäublin, B. Décamps, A. Prokhodtseva, and J. F. Löffler, "On the origin of primary $\frac{1}{2}$ a0 <111> and a0 <100> loops in irradiated Fe(Cr) alloys," *Acta Materialia*, vol. 133, pp. 427–439, July 2017.

[119] S. Wang, W. Guo, T. Schwarz-Selinger, Y. Yuan, L. Ge, L. Cheng, X. Zhang, X. Cao, E. Fu, and G.-H. Lu, "Dynamic equilibrium of displacement damage defects in heavy-ion irradiated tungsten," *Acta Materialia*, vol. 244, p. 118578, Jan. 2023.

[120] F. Gao, D. J. Bacon, Y. N. Osetsky, P. E. J. Flewitt, and T. A. Lewis, "Properties and evolution of sessile interstitial clusters produced by displacement cascades in \alpha-iron," *Journal of Nuclear Materials*, vol. 276, pp. 213–220, Jan. 2000.

[121] G. Varnavides, S. Ribet, R. Yalisove, J. Moore, C. Ophus, and M. C. Scott, "Simultaneous Electrostatic and Magnetic Vector Potential Phase Retrieval Using Electron Ptychography," *Microscopy and Microanalysis*, vol. 29, pp. 278–279, Aug. 2023.

[122] S. L. Dudarev and P. M. Derlet, "A 'magnetic' interatomic potential for molecular dynamics simulations," *Journal of Physics: Condensed Matter*, vol. 17, p. 7097, oct 2005.

[123] K. Papamihail, K. Mergia, F. Ott, Y. Serruys, T. Speliotis, G. Apostolopoulos, and S. Messoloras, "Fe^+ ion irradiation induced changes in structural and magnetic properties of iron films," *Nuclear Materials and Energy*, vol. 9, pp. 459–464, Dec. 2016.

[124] G. Cort, R. D. Taylor, and J. O. Willis, "Search for magnetism in hcp ϵ-Fe," *Journal of Applied Physics*, vol. 53, pp. 2064–2065, Mar. 1982.

[125] U. Krauss and U. Krey, "Local magneto-volume effect in amorphous iron," *Journal of Magnetism and Magnetic Materials*, vol. 98, pp. L1–L6, July 1991.

[126] V. L. Moruzzi, P. M. Marcus, and J. Kübler, "Magnetovolume instabilities and ferromagnetism versus antiferromagnetism in bulk fcc iron and manganese," *Physical Review B*, vol. 39, pp. 6957–6961, Apr. 1989.

[127] H. C. Herper, E. Hoffmann, and P. Entel, "*Ab initio* full-potential study of the structural and magnetic phase stability of iron," *Physical Review B*, vol. 60, pp. 3839–3848, Aug. 1999. Publisher: American Physical Society.

[128] W. Pepperhoff and M. Acet, "The magnetism of iron," in *Constitution and Magnetism of Iron and its Alloys*, pp. 15–55, Berlin, Heidelberg: Springer Berlin Heidelberg, 2001.

[129] V. Iota, J.-H. P. Klepeis, C.-S. Yoo, J. Lang, D. Haskel, and G. Srajer, "Electronic structure and magnetism in compressed 3d transition metals," *Applied Physics Letters*, vol. 90, p. 042505, Jan. 2007.

[130] N. V. Barge and R. Boehler, "Effect of non-hydrostaticity on the α-ϵ transition of iron," *High Pressure Research*, vol. 6, pp. 133–140, Dec. 1990.

[131] S. Khmelevskyi, A. V. Ruban, and P. Mohn, "Electronic structure analysis of the pressure induced metamagnetic transition and magnetovolume anomaly in Fe3C—cementite," *Journal of Physics: Condensed Matter*, vol. 17, p. 7345, Nov. 2005.

[132] M. Ekman, B. Sadigh, K. Einarsdotter, and P. Blaha, "*Ab initio* study of the martensitic bcc-hcp transformation in iron," *Physical Review B*, vol. 58, pp. 5296–5304, Sept. 1998. Publisher: American Physical Society.

[133] D. Nguyen-Manh, M. Y. Lavrentiev, and S. L. Dudarev, "Magnetic origin of nano-clustering and point defect interaction in Fe–Cr alloys: an ab-initio study," *Journal of Computer-Aided Materials Design*, vol. 14, pp. 159–169, Dec. 2007.

[134] P. Olsson, C. Domain, and J. Wallenius, "*Ab initio* study of Cr interactions with point defects in bcc Fe," *Physical Review B*, vol. 75, p. 014110, Jan. 2007. Publisher: American Physical Society.

[135] C. S. Becquart, R. Ngayam Happy, P. Olsson, and C. Domain, "A DFT study of the stability of SIAs and small SIA clusters in the vicinity of solute atoms in Fe," *Journal of Nuclear Materials*, vol. 500, pp. 92–109, Mar. 2018.

[136] G. R. Speich, A. J. Schwoeble, and W. C. Leslie, "Elastic constants of binary iron-base alloys," *Metallurgical Transactions*, vol. 3, pp. 2031–2037, Aug. 1972.

[137] E. A. Little and D. A. Stow, "Void-swelling in irons and ferritic steels: II. An experimental survey of materials irradiated in a fast reactor," *Journal of Nuclear Materials*, vol. 87, pp. 25–39, Nov. 1979.

[138] A. Bhattacharya, E. Meslin, J. Henry, A. Barbu, S. Poissonnet, and B. Décamps, "Effect of chromium on void swelling in ion irradiated high purity Fe-Cr alloys," *Acta Materialia*, vol. 108, pp. 241–251, 2016.

[139] Y.-R. Lin, A. Bhattacharya, D. Chen, Y. Zhao, J.-J. Kai, J. Henry, and S. J. Zinkle, "The role of Cr concentration and temperature on cavity swelling with co-injected helium in dual-ion irradiated Fe and Fe-Cr alloys," *Materials & Design*, vol. 223, p. 111134, Nov. 2022.

[140] K. Reszka, J. Morgiel, Z. Żurek, and A. Jaroń, "Characterization of Alumina Scale Formed on FeCrAl Steel," *Archives of Metallurgy and Materials*, vol. 59, no. 1, pp. 77–81, 2014. Publisher: Polska Akademia Nauk. Czasopisma i Monografie PAN.

[141] A. A. Alazemi and O. M. Ibrahim, "The Microstructure Formation of a Protective Oxide-Scale Layer on Small-Diameter FeCrAl Fibers.," *Materials (Basel, Switzerland)*, vol. 15, Oct. 2022. Place: Switzerland.

[142] R. H. Doremus, "Diffusion in alumina," *Journal of Applied Physics*, vol. 100, p. 101301, 11 2006.

[143] A. H. Heuer, "Oxygen and aluminum diffusion in α-al2o3: How much do we really understand?," *Journal of the European Ceramic Society*, vol. 28, no. 7, pp. 1495–1507, 2008.

[144] A. Heuer and K. Lagerlof, "Oxygen self-diffusion in corundum (alpha-al2o3): A conundrum," *Philosophical Magazine Letters*, vol. 79, no. 8, pp. 619–627, 1999.

[145] L. Messina, T. Schuler, M. Nastar, M.-C. Marinica, and P. Olsson, "Solute diffusion by self-interstitial defects and radiation-induced segregation in ferritic Fe–X (X=Cr, Cu, Mn, Ni, P, Si) dilute alloys," *Acta Materialia*, vol. 191, pp. 166–185, June 2020.

[146] L. Messina, M. Nastar, T. Garnier, C. Domain, and P. Olsson, "Exact ab initio transport coefficients in bcc $\mathrm{Fe} - X(X = \mathrm{Cr}, \mathrm{Cu}, \mathrm{Mn}, \mathrm{Ni}, \mathrm{P}, \mathrm{Si})$ dilute alloys," *Physical Review B*, vol. 90, p. 104203, Sept. 2014. Publisher: American Physical Society.

[147] Y. F. Zhukovskii, A. Platonenko, S. Piskunov, and E. A. Kotomin, "*Ab initio* simulations on migration paths of interstitial oxygen in corundum," *Nuclear Instruments and Methods in Physics Research Section B: Beam Interactions with Materials and Atoms*, vol. 374, pp. 29–34, 2016.

[148] O. L. Anderson, D. Isaak, and H. Oda, "High-temperature elastic constant data on minerals relevant to geophysics," *Reviews of Geophysics*, vol. 30, no. 1, pp. 57–90, 1992.

[149] H. Dai, M. Yu, Y. Dong, W. Setyawan, N. Gao, and X. Wang, "Effect of Cr and Al on Elastic Constants of FeCrAl Alloys Investigated by Molecular Dynamics Method," *Metals*, vol. 12, no. 4, 2022.

Paper I

Microstructure and magnetization evolution in bcc iron via direct first-principles predictions of radiation effects

E. Mansouri and P. Olsson
Physical Review Materials 7, 123604 (2023)

Microstructure and magnetization evolution in bcc iron via direct first-principles predictions of radiation effects

Ebrahim Mansouri* and Pär Olsson†
KTH Royal Institute of Technology, Nuclear Engineering, Roslagstullsbacken 21, 114 21 Stockholm, Sweden

(Received 6 September 2023; accepted 15 November 2023; published 21 December 2023)

We here model the radiation-induced microstructure evolution in bcc iron using the creation-relaxation algorithm directly driven by density functional theory calculations and compare to interatomic potential simulations. The method is in essence a relatively simplified model without thermally driven diffusion. The microstructure evolution in this model is driven mostly by the stress field introduced by sequential direct damage insertions. The defect populations and the corresponding defect cluster characteristics have been analyzed as a function of irradiation dose. Different distribution functions have been investigated for the self-interstitial atom implantation, to make model predictions as close as possible to actual irradiation conditions under which defects are produced. The stability and magnetic characteristics of the defect structures that are formed are studied. Our first-principles simulations revealed that the C15 structure can be dynamically formed during the irradiation of the material and that the constituent atoms align antiferromagnetically to the lattice. For doses on the order of a fraction of 1 displacement per atom, the model material Fe experiences mechanical changes caused by continuous irradiation and approaches a saturation state of about 2% swelling. The radiation-induced change in the local magnetic moments as well as the charge density differences for some isolated and clustered defects have been investigated. The results revealed a net reduction in total magnetization per atom and a tendency for interstitial sites to have a spin polarization opposing the intrinsic atomic site spins when the coordination number was increased compared to that of the initial lattice structure. It is suggested that radiation-induced damage could be traced using nondestructive measures of bulk magnetization changes.

DOI: 10.1103/PhysRevMaterials.7.123604

I. INTRODUCTION

With emerging Generation IV nuclear reactors and future fusion reactor systems, it is required to develop different alloys whose in-reactor mechanical properties are expected to be more robust due to more aggressive environments than in current nuclear reactors [1]. During the operating lifetime of nuclear reactors, structural materials are constantly exposed to radiation in the form of energetic particles of various kinds, creating isolated point defects (i.e., vacancies and self-interstitials) and significant concentrations of extended defect clusters [2,3]. Upon accumulation of these irradiation-induced defects and clusters, complex microstructural segments are formed, including voids, dislocation loops, radiation-enhanced or induced solute segregation in alloys, and precipitation of secondary phases [4–6]. The microstructural evolution can cause significant changes in the physical and mechanical properties of the materials. Hardening, embrittlement, and dimensional changes such as creep, growth, and swelling are typical examples of macroscopic effects of irradiation [2,7,8]. Subsequently, alloys with high resistance to the adverse effects of irradiation are of great technological interest especially for the nuclear energy sector.

Indicating and exploring the long-term evolution of the microstructures and their associated physical property changes under irradiation conditions are complex and demanding tasks. Consequently, many studies and research programs have been conducted to investigate the effects of irradiation on the physical and mechanical properties of real or model materials [9–14]. Due to the limitation of nanoscale analysis capabilities, the experimental observations of irradiation-induced microstructure evolution remain relatively rare at the atomic scale [15]. Therefore, multiscale modeling approaches have been extensively developed to facilitate elucidating the relationship between microstructure evolution and physical property changes of irradiated material in recent years [5,13,16–18].

For example, Domain *et al.* applied the object kinetic Monte Carlo (OKMC) method to investigate the dynamics of the thermally activated microstructure evolution in Fe and FeCu alloys [19] for irradiation doses far below 1 displacement per atom (dpa).[1] Indeed, their study was relevant for reactor pressure vessel steels in light water reactors where

*Corresponding author: ebrman@kth.se
†Corresponding author: polsson@kth.se

[1]Displacement per atom (dpa) is a dimensionless positive-definite parameter that can be used to measure irradiation exposure [20]. As described by Kinchin and Pease [21] and quantified by Norgett *et al.* [22], atomic displacement is expressed by a dpa parameter φ.

the density of the defects is relatively low, and the lifetime dose is well below 1 dpa. Nevertheless, applying the OKMC approach to dose limits higher than 1 dpa, where the concentrations of isolated and extended defects are relatively high, e.g., in materials near the reactor cores, has so far proved problematic due to the high computational cost of modeling an environment with both slowly and rapidly diffusing defects, continuously created during operation. Furthermore, to improve the OKMC predictions even further, incorporation of both linear and nonlinear elastic interactions between almost all kinds of simple and complex defects are necessary but challenging [23,24]. Therefore, to model the microstructure evolution, there has been quite some activity focusing on directly applying interatomic potentials and molecular dynamics (MD) simulations over the past few decades [14,25,26], with different levels of assumptions and approximations included.

Granberg *et al.* applied the MD method to study defect accumulation and evolution in Fe-based alloys [27] and tungsten [25] using massive amounts of overlapping cascade simulations at room temperature. They generated isolated and extended defects through primary knock-on atoms induced by random initiation of thousands of subsequent displacement cascade events at room temperature. The time between the events is orders of magnitude shorter than the realistic one in representative conditions. While this method neglects many diffusion-driven events and mechanisms, an equivalent dose of 0.12 dpa was achieved in Fe and FeCr alloys [27]. Despite successfully reproducing the microscopic dynamics of atomic collisions under massive overlapping cascades, it was difficult to uncover the intermediate stages of defect evolution, as discussed by Derlet and Dudarev in Ref. [26].

Since the late 1980s, a simple yet powerful computational simulation technique was introduced by Limoge *et al.* for studying the irradiation-induced amorphization in noncrystalline materials by successive introduction of point defects, either Frenkel pairs (FPs) or isolated interstitials [28]. The approach has been widely adopted and adapted by various researchers over the past decades [29–32]. For instance, Derlet and Dudarev reformulated and integrated it with interatomic potentials and molecular statics, to explore the radiation-induced microstructure evolution of two model materials, Fe and W [26]. They successively introduced a FP defect consisting of a vacancy and self-interstitial atom (SIA) into a simulation cell through random selection and displacement of lattice atoms. After the defect was inserted, the atomic positions were relaxed to their local energy minima to track the accumulation of defects and their evolution at zero temperature, where the microstructure evolves solely as a result of the induced stress field from continuous FP insertions (FPIs). This process, named as the creation-relaxation algorithm (CRA), allows one to demonstrate the development of microstructure imperfections over several stages, including a linear accumulation of point defects ($\varphi \sim 0.01$ dpa), formation of interstitial clusters ($\varphi \sim 0.1$ dpa), creeping formation of dislocation loops (0.7 dpa), and finally saturation of the dislocation network ($\varphi \sim 1.5$ dpa).

Given that the CRA model ignores the high-energy characteristics of defect production, it addresses one of the significant challenges for OKMC simulations by directly considering linear and nonlinear lattice deformations caused by defect accumulations. In contrast to overlapping cascade simulations, the CRA model significantly reduces the computational effort by neglecting the high-energy stages of radiation damage production, allowing for the exploration of high dose values (e.g., up to 2.5 dpa and beyond) in larger simulation cells. Thus, the CRA model identifies the stages of isolated and extended defect accumulation and demonstrates microstructure evolution into a final steady-state structure at high dose levels without thermal activation.

Before the CRA model was introduced, Chartier and Marinica [29] employed a similar technique to study the interactions between dislocations and small C15 Laves phase inclusions, with an icosahedral structure, in the body-centered cubic (bcc) Fe structure under irradiation conditions. They applied an embedded-atom method (EAM) potential, referred to as M07 [33], to simulate the formation of three-dimensional C15 clusters by accumulating FPs. Their findings revealed a complex interplay between two-dimensional interstitial defects ($1/2\langle 111\rangle$ and $\langle 100\rangle$ loops) and three-dimensional C15 clusters. However, using the Mendelev *et al.* EAM potential (M03) [34], Derlet observed minimal icosahedral content during the nucleation of the dislocation loop stage and therefore was unable to resolve other possible mixed Laves C15/dislocation loop structures. The study highlighted differences in observed structures, indicating that the choice of interatomic potentials may account for these disparities. In fact, the M03 potential used in Ref. [26] is a quite energetically unfavorable potential for large C15 cluster formation, as shown in [35].

Furthermore, both studies attribute the generation of damage to electron irradiation under low-temperature conditions, which predict the production of FPs. Moreover, the investigations conducted in both studies employed relatively large supercells with side lengths exceeding $80 \times a_0$,[2] allowing for a large displacement and uniform distribution of SIAs. However, it should be noted that this uniform distribution of implanted SIAs, though it simplifies the simulation, may introduce an unrealistic assumption on the mean free path of a dynamically created SIA in a newly born FP that could impact the nature of microstructure evolution during the initial stages of irradiation.

Finally, in this study, we propose a first-principles driven CRA model using density functional theory (DFT) for the simulation of defect production, energy minimization, and microstructure evolution. Consequently, by applying a DFT-driven CRA model, one can reproduce the radiation-induced microstructure evolution while resolving the evolving electronic structure and tracing its effects, with additional value in detailed information on aspects such as local and global magnetization and charge density evolution, as well as the potential to expand to complex alloys without loss of quality in the physical description. Indeed, the DFT method provides a solid benchmark to validate the results achieved by using interatomic potentials. It also provides a tool to investigate the possible effects of radiation-induced microstructure on the quenching and polarization of local magnetic moments and

[2] a_0 is referred to as the lattice parameter.

charge density difference distributions around isolated defects and defect clusters, e.g., C15-type clusters. In contrast to the aforementioned studies based on a semiempirical potential drive CRA that utilized large supercells, our study employs a relatively small supercell ($8 \times a_0$ with 1024 atomic sites), eliminating the need to consider spatially localized or uniform SIA distributions within the simulation cell. To accurately model low-energy defect production, such as electron irradiation, it should be more appropriate to employ a locally distributed SIA implantation model in large supercells.

The current study is structured into three distinct sections. Section II describes the CRA model in detail and outlines the computational specifics. Section III delves into the discourse of the findings and provides a comprehensive discussion of the results. Subsequently, the study conclusion is presented in its dedicated section. Furthermore, in Appendix A, an explication of the forbidden zone radius (FZR) criterion is expounded upon. Appendix B elucidates the three distinct spatial distribution functions employed for SIA distributions. Finally, the Supplemental Material pertinent to this study are comprehensively detailed in [36].

II. METHODS

A. CRA

This study applied the CRA approach to directly generate Frenkel pairs, mimicking low-energy damage events, and to qualitatively simulate a bulk radiation dose and microstructural evolution in bcc Fe. Using the canonical definition of dpa [26], one may determine the irradiation dose by dividing the FPI number, n, by the total number of lattice sites, $N(\varphi = n/N)$. Considering the importance of the algorithm used in this study, as well as the slight differences we applied in our calculation requirements compared to those applied in Ref. [26], the CRA model is briefly reviewed and rewritten according to our simulation conditions:

(1) Construction of a simulation cell with N lattice sites of a desired size and crystallography.

(2) Determination of the radius of a forbidden zone; explained in Appendix A.

(3) Relaxation of the ionic positions in the cell before insertion and considering this cell as a reference configuration.

(4) Setting n to 0.

(5) Random selection and removal of an atom within the simulation cell, creating a vacancy.

(6) Insertion of the randomly selected atom into the simulation cell according to a selected distribution function, creating a SIA.

(7) Inspection whether the inserted atom is inside the forbidden zone of another atom and then conditional modification of its position to just outside the forbidden zone.

(8) Relaxation of all ionic positions by adopting an energy minimization method to find a new global potential energy minimum for all the atoms in the cell.

(9) Setting n to $n + 1$ and updating the value of the dose parameter φ to n/N.

(10) Iteration of steps (5)–(9) until the algorithm reaches the desired target dpa value.

Two main differences exist between our simulation requirements and those applied in [26]. For noticeably short distances, the empirical potentials in [26] are connected to the Ziegler, Biersack, and Littmark [37] screened Coulomb interaction. In this study, we only used a projector augmented wave description [38] with a minimal set of explicit valence electrons. Therefore, we are not guaranteed to achieve a fully appropriate short-range repulsive form, potentially leading to unreliable forces if the inserted atom is placed too close to another atom. Consequently, we defined a virtual spherical zone encompassing each atom within which the inserted atoms cannot be implanted before the relaxation step. If an atom is placed inside the forbidden zone of another atom due to the random coordinate selection, it is displaced directly outwards from the atom to the zone boundary, and from there, the relaxation starts. According to our calculations, this forbidden zone can be reasonably selected as about 0.7 Å in bcc Fe. In Appendix A, we have shown how this value has been assigned as a criterion for the forbidden zone radius. We can note that as long as the selected value is not too small (nonphysical forces) the resulting relaxation is quite stable with respect to the parameter value.

During energetic recoils initiated by an incoming particle, the spatial distribution of the resulting damage, be it in the form of cascade debris for high-energy impacts, or a distribution of isolated FPs, covers between a few angstrom up to a few nanometers. The characteristic size of the resulting distribution of defects scales very weakly with the energy of the incoming particle due to the many-body collision effects. Consequently, for modeling low-energy irradiation damage in large cells ($>10 \times a_0$ or so), especially within the CRA framework, the spatial distribution of the SIA implantation is critical for improving model prediction. In other words, when the recoil atoms are scattered in a realistic irradiation condition under low-energy defect production, such as in electron irradiation, their displacements typically range within a few lattice parameters. Therefore, to model low-energy irradiation conditions, it is more important to displace randomly selected atoms in accordance with a spatially localized distribution model, especially in large supercells compared to this range. Thus we applied three different spatial distributions of SIAs—a uniform random distribution and two nonuniform localized random distributions—according to which the SIAs are dispersed. In this way, we investigated whether the distribution of SIAs would lead to different microstructure evolutions. We could also prove that a uniform distribution of SIAs is a valid approach for small simulation cells. More details on the distribution functions can be found in Appendix B.

A PYTHON code was employed for damage creation and insertion. Additionally, PYTHON and OVITO [39] were used for analyzing the microstructure evolutions. A Wigner-Seits analysis implemented in OVITO was conducted to identify the remaining vacancy and SIAs in the simulation cells after the relaxation. For two defects to be considered as clustered together, cut-off criteria were set at the midpoint between the second and third nearest neighbor distances (3.5 Å) for vacancies and between the third and fourth nearest neighbor distances (4.1 Å) for SIAs, in accordance with literature [40,41]. Furthermore, considering that the C15 atoms have a distinctive icosahedral coordination, we apply the polyhedral template matching (PTM) analysis [42], with a

root-mean-square deviation value of 0.25, implemented in OVITO to recognize them.

B. *Ab initio* calculation details

The main focus of this study is to use electronic structure calculations in the framework of DFT for the energy minimization during the CRA direct damage insertion. We used the projector augmented plane wave method [38] implemented in the Vienna *ab initio* simulation package (VASP) [43]. The conjugate gradient method [44] was used to perform the energy minimization after every FPI [steps (5)–(9) of the CRA]. The exchange-correlation term was treated in the generalized gradient approximation, as parametrized by Perdew, Burke, and Ernzerhof [45,46]. All calculations were spin polarized, and periodic boundary conditions, along with the supercell approach, were employed. For the CRA modeling of radiation-induced microstructure evolution, we used a supercell of $8 \times 8 \times 8$ copies of the bcc orthogonal unit cell, comprised of 1024 atoms. For this relatively large supercell, the Brillouin zone was sampled by the gamma point in k space. To improve the prediction of the model and lower the statistical noise, we used four distinct CRA trajectories for each condition.

In our simulations, we utilized diverse degrees of freedom to steer the response of the irradiated system to FPIs. This governs how the system evolves under irradiation, including adjustments in ionic positions, simulation cell volume, and cell shape. For an evolving system under intense irradiation, full relaxation (relaxing ionic positions, volume, and shape of cell) calculation is ideal after each damage insertion. However, full relaxation demands significant computational resources in DFT. To address this, we limited the simulations to ionic relaxations, which adjusts only ionic positions while preserving the volume and shape of the supercell. Full relaxation was applied selectively in specific snapshots of a CRA trajectory, optimizing insights without introducing extensive computational costs.

For volume-conserving simulations, we employed a cut-off energy of 250 eV and a 1 meV energy convergence criterion for the self-consistent electronic loop. However, for fully relaxed calculations, we used a higher 350 eV cut-off energy to prevent volumetric changes from affecting energy and forces due to varying volume and included plane waves. To enhance accuracy, we reduced the energy minimization convergence criterion to 0.1 meV in this simulation set.

To explore irradiation-induced structural changes, two approaches can be employed. In the full relaxation calculation paradigm, tracking the supercell volume offers insights into volumetric changes. Alternatively, the ionic relaxation calculation method tracks hydrostatic pressure changes. Full relaxation achieves a global pressure convergence to zero, causing the supercell volume and shape to evolve, leading to explicit volumetric swelling in the case of FPIs. In contrast, fixed volume conditions allow estimation of radiation-induced swelling by relating the global hydrostatic pressure change (ΔP) to the bulk modulus (B), expressed as [47]

$$\frac{\Delta V}{V_0} = \frac{-\Delta P}{B}, \tag{1}$$

where $\Delta V/V_0$ is the relative volumetric change as a result of FPIs.

Using the DFT-CRA method, we also investigated the irradiation-induced change in the electronic charge distribution and in the global and local magnetization. Accordingly, isosurfaces depicting the variations in spin and charge densities surrounding those defects were computed using VESTA [48].

Additionally, for a more comprehensive analysis of variations in magnetization and charge density near isolated point defects, a series of supplementary calculations (see the Supplemental Material [36]) were conducted with higher accuracy in smaller supercells. Firstly, a supercell comprising $5 \times 5 \times 5$ copies of a bcc unit cell was used to separately calculate the induced change in magnetization and stress tensor components around a vacancy, SIA, or FP defects, respectively, with higher computational accuracy (denser Γ-centered $6 \times 6 \times 6$ k-point mesh and 350 eV cut-off energy). Secondly, the magnetovolume relationship [49] was examined in a standard ferromagnetic bcc Fe conventional unit cell with a denser k-point mesh of $11 \times 11 \times 11$ and 350-eV cut-off energy.

To explore the potential influence of atomic volume fluctuations induced by FPI on local magnetic moments, a Voronoi analysis was employed. This analysis, established using planes bisecting distances to atomic neighbors, was conducted using OVITO.

C. Interatomic potential calculation details

The EAM-CRA simulations that are directly comparable to the DFT-CRA results were performed in a supercell with side length of $8 \times a_0$ comprising 1024 atomic sites. The conjugate gradient method was used, and the simulations were performed with LAMMPS [50] to relax the structure and determine the new local potential energy minimum. In parallel to DFT, two distinct relaxation methods were used: one for simulations with fixed volume and another for simulations with fixed pressure.

To reduce statistical error and improve radiation-induced damage prediction, five CRA trajectory profiles were used. The EAM potentials of M03 and M07 were applied to model and investigate the atomic structure of Fe under irradiation within the CRA model.

III. RESULTS AND DISCUSSION

A. The evolution of energy and pressure changes with uniform and localized distribution of SIAs

We evaluated the reliability and accuracy of the EAM potentials used in this study by comparing to the predictions of the DFT-CRA method for prediction of radiation-induced microstructure evolution in terms of energy and pressure changes.

According to the definition of the canonical dpa [26], the FPI number divided by the number of lattice sites to achieve an irradiation dose of 1 dpa, 1024 FPs must be inserted into a supercell containing 1024 atomic sites. Using the EAM-CRA method, it is quite fast to reach doses of 1 dpa in such small supercells. For the DFT-CRA method, however, which involves a relatively large system of mutually interacting electrons and

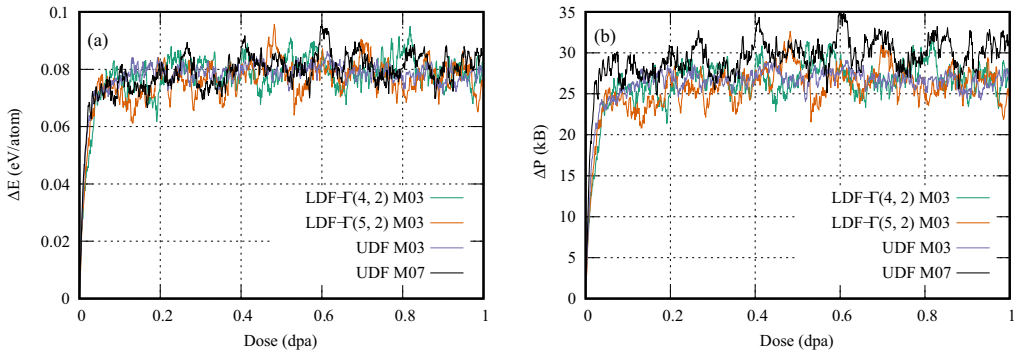

FIG. 1. Comparison of (a) energy change per atom and (b) hydrostatic pressure change as a function of FPI with different EAM-CRA methods.

ions, we stopped the simulation after 0.35 dpa since continuing the simulation to 1 dpa was not expected to yield much additional information.

First, the different SIA implantation distribution functions have been examined with the EAM-CRA model. As described in Appendix B, the mean displacement of the SIAs with a uniform distribution function (UDF) is about 11.3 Å in a supercell with the side length of $8 \times a_0$. In contrast, it is about 8 Å with a localized distribution function (LDF) such as the Γ(4,2) in the same supercell. Figure 1 compares the microstructure evolution of uniform and localized distributions of SIAs predicted by the EAM-CRA method, using different EAM potentials. Regardless of the type of spatial distribution of SIAs, the dose-dependent evolution of microstructure in the simulation cell is quite similar, as could be expected, given that the mean displacement of the SIAs is of the order of the simulation cell size. However, as mentioned earlier, in larger supercells ($> 10 \times a_0$), using a localized distribution of the SIAs would be logical if the objective is to simulate low-energy electron irradiation, which is one of the experimental conditions that the CRA model most closely resembles. From here on in this work, all results were obtained using the spatially uniform SIA implantation distribution within the supercells.

Figure 2 displays the change in total energy per atom (ΔE/atom) and the change in hydrostatic pressure (ΔP) as a function of dpa, extracted from the DFT-CRA and EAM-CRA methods. As shown, the EAM and DFT predictions are qualitatively comparable. Following an initial linear increase in both energy and pressure, a saturation stage develops after around 0.05 dpa, in agreement with earlier studies [26,27,40,51] (see Fig. S1 in [36]).

As shown in Fig. S1(a) in [36], regardless of the supercell size, the EAM-CRA model used in this study showed also entirely quantitative and qualitative agreement with the results reported in [26] in terms of ΔE/atom. However, depending on the size of the simulation cell, the pressure evolution [Fig. S1(b) in [36]] goes through at least three distinct stages. In summary, these stages include a rapid linear defect accumulation regime, a creeping dislocation loop formation stage, and a steady-state dislocation network formation stage [26,52,53]. As a result of using small supercells, large interstitial clusters and significant dislocation growth are not observed in this study. We see that in small supercells, only two stages of microstructure evolution are apparent: a quick linear accumu-

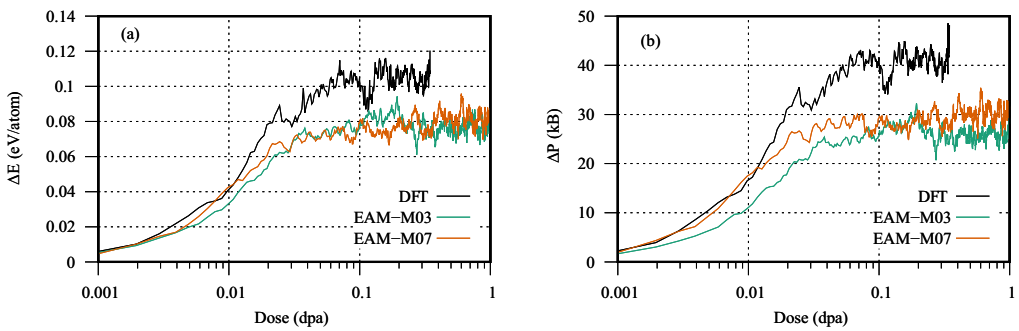

FIG. 2. Comparison of DFT and EAM estimating the average changes in (a) energy per atom and (b) global pressure as a function of dpa (FP insertion number divided by the number of lattice sites) in Fe.

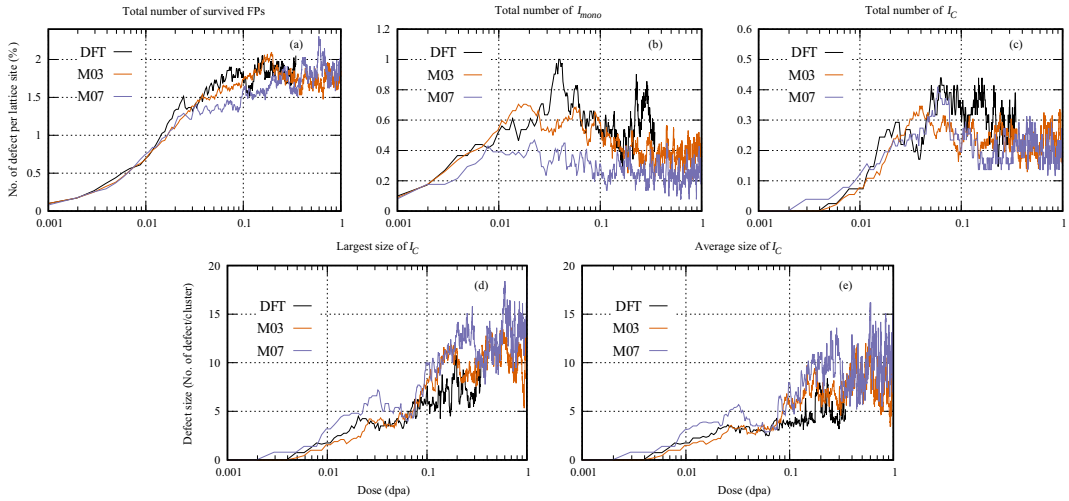

FIG. 3. Interstitial defect content per lattice site (top) and their cluster sizes (bottom) as a function of FP insertion (dpa) predicted by DFT, EAM-M03, and EAM-M07 methods.

lation of isolated point defects and a steady-state formation of small defect clusters, as also depicted in Fig. 2. Therefore, none of the DFT and EAM methods predicted the nucleation of stable dislocation loops in the supercell sizes used in this study, implying that the dislocation loops are unlikely to form out of the small interstitial clusters. The clusters must first grow larger or coalesce before they can merge into dislocation loops [26].

B. The evolution of the microstructure as a function of dose

The EAM potentials were further evaluated by comparing the microstructure evolution predicted by the DFT-CRA and EAM-CRA methods in terms of defect accumulation. Accordingly, we traced the defect populations and the cluster sizes, i.e., the total number of SIAs composing a cluster, as a function of irradiation dose. In addition, particular attention has been awarded to the irradiation-induced formation and evolution of three-dimensional C15 clusters.

Figure 3 shows the evolution of self-interstitial defect content per lattice site (top) and the cluster sizes (bottom) resulting from subsequent FP insertions in the model material Fe. As seen from the top graphs, the total number of survived FPs grows linearly for doses below 0.02 dpa and then stabilizes around a dose level of 0.05 dpa. Both the DFT and EAM methods qualitatively predict similarly evolving microstructures in Fe, within the conditions applied in this study. However, there is a statistically significant discrepancy between the DFT and EAM methods in estimating the number of isolated self-interstitial (I_{mono}) defects as well as the SIA cluster sizes. For example, the M07 potential overestimates the size of the interstitial cluster (I_C) by a factor of 2, while it estimates roughly half the number of I_{mono}, compared with the DFT results. This suggests that the M07 potential favors SIA cluster formation due to overstabilization.

Moreover, Fig. S2 in the Supplemental Material [36] compares the evolution of survived FPs predicted from different methodologies used in this study with those extracted from Ref. [26]. The number of survived FPs saturated at a dose of 0.05 dpa in supercells used in this study ($8 \times a_0$). Beyond 0.05 dpa, however, the number of survived FPs increases with a different linear slope using EAM-CRA, indicating nucleation and growth of dislocations in the sizable supercells used in Ref. [26]. In the present study, this evolution is only partly covered (up to about 0.2 dpa).

Although a qualitative similarity exists between the results of DFT and EAM simulations in predicting the microstructure evolution, for a thorough comparison of DFT versus EAM predictions, we determined the saturation-level average of several quantities (i.e., defect populations and their cluster sizes) from 0.05 dpa to the end of the irradiation dose and tabulated them in Table I. Accordingly, for the DFT results, the saturation level ranges from 0.05 to 0.35 dpa, while for the EAM data, it ranges from 0.05 to 1 dpa. In addition, the standard deviation, s_x, is also calculated for each quantity.

Table I shows that the DFT and EAM methodologies predict almost the same number of survived FPs. Moreover, the DFT-CRA method reveals that the number of survived isolated vacancies is roughly twice the number of isolated interstitial defects, even without the presence of dynamical bias. As shown in Table I and in the bottom graphs in Fig. S3 [36], the average and largest size of the interstitial clusters are significantly greater than those of the vacancy clusters. This suggests that the larger elastic strain field generated by SIAs leads to a stronger tendency to form a new structure phase, e.g., C15-type clusters as proposed by Dézerald *et al.* [54], rather than to remain as isolated point defects.

TABLE I. DFT and EAM predictions of the saturation level for defect populations and cluster sizes, along with their standard deviations (in parentheses). DFT data have been averaged over 0.05–0.35 dpa, whereas EAM data have been averaged over 0.05–1 dpa.

	Interstitial defect (s_x)			Vacancy defect (s_x)		
Method	DFT	EAM-M03	EAM-M07	DFT	EAM-M03	EAM-M07
No. of survived FP	18.6 (1.1)	18.0 (1.1)	18.2 (1.8)	18.6 (1.1)	18.0 (1.3)	18.2 (1.8)
No. of isolated defects	6.0 (1.3)	4.1 (0.8)	2.6 (0.7)	13.8 (1.3)	12.1 (0.9)	12.5 (1.5)
No. of defect clusters	3.2 (0.6)	2.4 (0.4)	2.1 (0.5)	2.2 (0.5)	2.4 (0.5)	2.4 (0.6)
Average size of the cluster[a]	4.6 (1.3)	7.3 (1.9)	9.4 (2.5)	2.0 (0.3)	2.2 (0.3)	2.3 (0.4)
Largest size of the cluster	6.8 (1.5)	10.0 (1.9)	12.1 (2.4)	2.2 (0.3)	2.6 (0.5)	2.6 (0.6)

[a]The defect cluster size equals the number of defects per cluster (No. defect/cluster).

A comparison between DFT and EAM predictions can also be identified from the bottom graphs in Fig. 3, showing the average and most significant cluster sizes of the SIAs. Despite similar qualitative trends, the EAM potentials imply that the average size of the interstitial clusters is roughly twice that of those anticipated by DFT simulations. It should be noted that these EAM potentials are based on DFT data but are not fitted on large defect clusters. Therefore, such discrepancies may be expected, and even later developed potentials relying on machine learning algorithms rarely include large variations of defect cluster energetics in their fitting database.

As mentioned earlier, the formation of nonparallel C15-type clusters has been already predicted to be energetically more favorable than other extended clusters in bcc Fe [35,54]. Using PTM analysis, we also traced the existence and formation of icosahedral structures to identify a possible formation of perfect or imperfect C15 Laves phase structures in our damaged bcc Fe cells. It is worth noting that clusters containing more than 12 SIAs are categorized as perfect C15 clusters, whereas those with fewer than 12 SIAs are classified as Laves phase backbone polyhedral structures or imperfect C15-type clusters. Figure 4 illustrates that the dose-dependent evolution of C15-type structures varies strongly depending on the methodology used for dose limits above 0.1 dpa where the average size of the interstitial clusters is larger than four SIAs.

Both DFT and EAM methods, regardless of the type of potential used, consistently predict the transformation of SIAs into C15-type clusters for doses below 0.1 dpa, where the average size of the interstitial clusters is smaller than four SIAs. However, our analysis revealed that above 0.1 dpa and up to the available DFT-driven irradiation dose of 0.35 dpa, where the formation of larger interstitial clusters is expected, the transformation of interstitial clusters into giant C15 structures is less frequent in irradiated bcc Fe when using the DFT method or the M03 potential compared to the M07 one. Therefore, the overall results obtained from the DFT and the EAM methods suggest that the M07 potential might overstabilize the formation of C15 clusters, in a more significant fashion than for SIA clusters in general, as was noted above. This result is expected, as the development of the M07 potential is based on the lower formation energy of three-dimensional C15 clusters, as suggested by *ab initio* calculations [35]. As also shown in Fig. 4, the frequent appearance of perfect C15 structures (clusters greater than 12 SIAs) is significant for the case of the M07 potential as compared to DFT and the M03 potential. It seems the dynamical evolution of complex cluster growth has not been fully captured by the potential fitting and that predictions using M07 may overestimate the prevalence of these clusters, at least in the simulation cells used in this study.

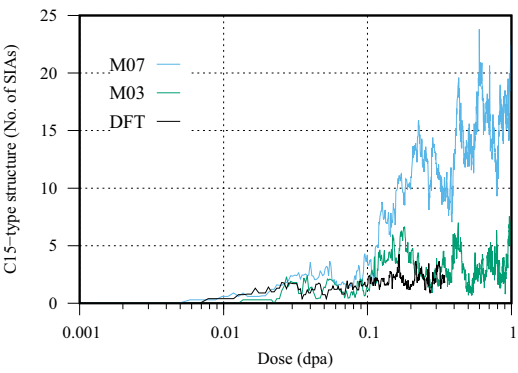

FIG. 4. The largest C15-type structures as a function of irradiation dose predicted by different methodologies.

As the predicted vacancy-related populations with either method or choice of EAM potential were compatible, we refrain from displaying them here. Instead, additional analysis of evolving vacancies and their clusters are provided in the Supplemental Material [36], Figs. S3 and S4. Those two graphs describe the evolution of vacancy-related defect populations and compare them with interstitial-related defects predicted by DFT and EAM potentials.

C. Radiation-induced structural change

Another way of studying the microstructure evolution is to trace the average change in physical properties such as the lattice constant and in volume expansion, i.e., swelling. Using the DFT- and EAM-CRA methods, we estimated the extent to which the model material Fe may experience radiation-induced volume expansion within the limit of the CRA conditions.

Referring to Eq. (1), we calculated the swelling using two different approaches. From the fixed volume CRA simulations, one can estimate the equivalent volumetric swelling by dividing the evolving global hydrostatic pressure by the appropriate bulk modulus (i.e., $\Delta P/B$) [47], as shown in Fig. 5. In addition, to directly determine the evolution of volumetric expansion, we fully relaxed the simulation cells

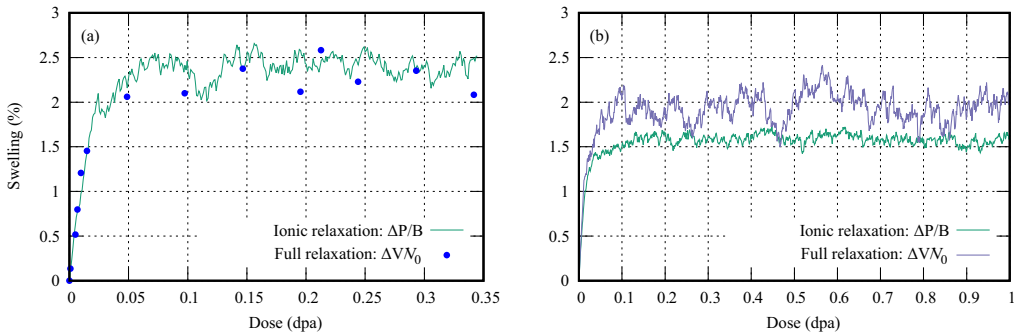

FIG. 5. A comparison of the (a) DFT and (b) EAM predictions of radiation-induced swelling with ionic and full relaxation calculations. Data points on DFT graphs correspond to snapshots taken from full relaxation calculation trajectory.

in several snapshots of a DFT-CRA trajectory. Due to the time-consuming nature of the full relaxation calculation in DFT the selected number of such snapshots was quite limited. In the full relaxation calculations, with cut-off energy 250 eV, we found that the explicit swelling ($\Delta V/V_0$) is approximately 30% lower than that predicted from ionic relaxation ($\Delta P/B$) calculations (see Fig. S5 in [36]). This apparent discrepancy is in part due to the low cut-off energy used for the full relaxation calculations which, given that the simulation cell undergoes volumetric expansion, changes the number of plane waves included in the expansion. To resolve this, we expanded the cut-off energy to 350 eV. As shown in Fig. 5, by doing so, the estimated swelling by ionic relaxation, with 250 eV cut-off energy, well resembled the directly calculated volumetric expansion, $\Delta V/V_0$, with 350 eV cut-off energy. It is worth noting that the results of full relaxation calculation with DFT are more closely matched to the fixed pressure calculation with EAM methods.

Similar structural changes have been reported in a 490 keV self-ion irradiation of 200 nm and 60 nm thick Fe films at room temperature [55,56], respectively. The lattice constant and the grain sizes, as measured by the grazing incidence x-ray diffraction technique, have been reported to initially undergo an abrupt increase at the early stage of irradiation and finally to a slow saturating steady state, similar to what we qualitatively predicted from our CRA model [see Figs. 5 and S6(a) [36]]. It has also been found that the bcc crystalline structure remains present and stable even after the high irradiation dose of 341 dpa. Our PTM analysis [Fig. S6(b)] in [36] also revealed that about 70% of the bcc structure still remains in the saturation stage of the damaged structure, within the CRA conditions.

D. Radiation-induced change in global and local magnetism

One of the extraordinary advantages of the DFT method over EAM simulations is that it allows one to study the possible magnetic transformation of a damaged structure, which cannot be accessed by means of classical EAM simulations. Herein, the irradiation-induced changes in global and local magnetization of the damaged bcc structures are investigated using the DFT-CRA model with ionic and full relaxation calculations. We first considered the evolution of the global magnetization (M) per atom as a function of dose in the supercells with the side length of $8 \times a_0$. In the early stage of FPIs, as shown in Fig. 6, the M decreases linearly with increasing irradiation dose. Upon reaching the saturation level (0.05 dpa), the total M fluctuates around 2.1 μ_B/atom as the number of survived FPs stabilizes.

Although making a direct correlation between the outcomes yielded by DFT calculations in absolute temperature and the findings gathered from experimental studies at room temperature might not be entirely suitable, yet qualitatively speaking, it is noteworthy that reductions in both total M and lattice parameter have been documented in recent investigations involving a 490 keV self-ion irradiation of 200 nm Fe films (composed of two top and bottom sublayers) at room temperature [55]. As mentioned by the author, the responses of those two sublayers seems to link to the impacts of Fe^+ irradiation: the top layer corresponded to regions primarily affected by irradiation damage, while the bottom layer pertained to both Fe^+ ion implantation and irradiation damage. As a result, the top Fe sublayer exhibited a higher magnetic moment than that of the unirradiated Fe sample whereas the bottom sublayer exhibited a lower average magnetization. In comparison with our simulation results, where magnetization

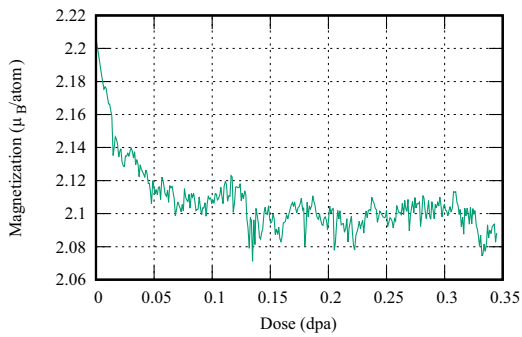

FIG. 6. The average magnetization per atom as a function of dose.

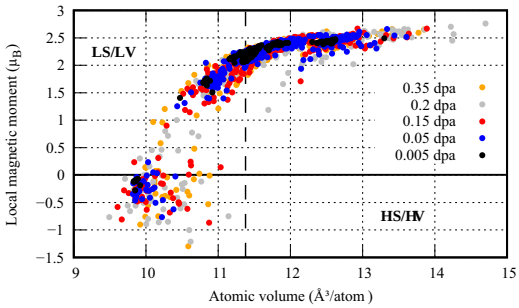

FIG. 7. Local magnetic moments of all atoms in different FPI stages for different irradiation dose levels, as a function of atomic volume. The vertical dashed line distinguishes LS/LV and HS/HV regions, highlighting deviations in atomic volume and local magnetic moments of atoms in the damaged bcc Fe structure with respect to the undamaged one.

is strictly decreasing with irradiation dose, the bottom layer evolution resembles this more. It is natural that a region with a higher SIA content will experience a quenching of magnetization, given both the decrease in average available free volume where there is a surplus of self-interstitials as well as the well-known strong direct magnetic quenching effects on SIAs themselves. For the top layer, the experimental result is, however, not in qualitative agreement with our results. An irradiated magnetic bulk material should not experience a growing magnetization, unless the swelling, and thus magnetovolume effect, can dominate over the defect-induced quenching. That we are simulating a perfect bulk, and the top layer is a thin substrate with a free surface may be part of the explanation of the discrepancy.

As explained in Sec. VII in the Supplemental Material [36], there is a net decrease of 1.72 μ_B (equivalent to 6.8×10^{-3} μ_B/FP in these simulation cells) in the global M. This decrease is attributed to the insertion of the FP, which comprises the individual contributions of a single SIA ($-2.93\,\mu_B$) and a single vacancy ($+1.05\,\mu_B$), albeit in a slightly volume-expanded cell. Indeed, in the presence of a SIA (vacancy), the available atomic volume surrounding the defect decreases (increases), thus reducing (raising) the magnetic moments of the atoms enclosing that interstitial (vacant) site. Therefore, the linear reduction in the total M (Fig. 6) can be attributed to the linear accumulation of survived FPs below 0.05 dpa. Beyond 0.05 dpa, however, the number of FPs reaches saturation and interstitial clusters begin to nucleate. Consequently, the change in global M is no longer a linear function of individual FP defects. Therefore, it deviates from the linear decreasing regime and fluctuates around -0.12 μ_B/atom.[3]

Moreover, it is informative to examine the local magnetic moments of the constituent atoms as a function of dose (FPI number). As shown in Fig. 7, the local magnetic moment of the 1024 atoms (taken from several snapshots of a single CRA trajectory) is plotted with respect to their atomic volumes, computed as the surrounding Voronoi polyhedral cell. Increasing the irradiation dose alters the local environment of the lattice sites, inducing various stress fields around atoms and causing different atomic rearrangements with diverse atomic volumes. Consequently, atoms that undergo a change in their local stress field, in comparison to the post-irradiation conditions, will encounter varying atomic volume and local magnetic moments. To enable a comprehensive understanding of the correlation between atomic volume and local magnetic moments of atoms, we categorized the volume and local moments of atoms into two states: high-volume/high-spin (HV/HS) and low-volume/low-spin (LV/LS). These states are referenced against the atomic volume (11.32 Å) and local magnetic moment (2.2 μ_B) of a typical iron atom within an undamaged bcc Fe structure. As shown in Fig. 7, the vertical dashed line facilitates the deviation of atomic volume and local magnetic moment of the atoms from those in the undamaged bcc Fe structure. Therefore, the right (left) side of the dashed line corresponds to the HV/HS (LV/LS) state. Atoms with neighboring vacant sites undergo an increase in volume and consequently an increase in local magnetization. Meanwhile, an atom that is in close proximity to interstitial atoms experiences a reduction in its atomic volume and ultimately a decrease in its local magnetization.

As seen in Fig. 7, in the LV/LS region, which refers to the accumulation of SIAs in the damaged structure, it is potentially favorable, both magnetically and structurally, for SIAs to form a locally new crystal structure within the host bcc Fe structure, as we already observed in our simulation [see Fig. S6(b) in [36]].

For example, with an extensive numerical simulation of fictitious amorphous iron at absolute zero temperature, which has similarities to our DFT-CRA evolution at saturation, Krauss and Krey [57] showed a significant connection between the magnitude of the local magnetic moment and the associated local volume of a specific atom in amorphous Fe. Although both these values exhibited considerable variation on a site-to-site basis, their averaged correlation closely aligned with the global volume dependency of local magnetic moments in the antiferromagnetic (AFM) state of face-centered cubic (fcc) Fe, as also computed by Moruzzi *et al.* [58].

Another alternative for the evolution of SIAs, in a massively irradiated structure, is to transform into a C15 Laves phase structure. As demonstrated earlier by Marinica *et al.* [35], the C15 Laves phase in bcc Fe has been established as a stable and immobile framework for the evolution of SIAs. This structural configuration is also marked by significant AFM moments. Such configurations may also emerge during displacement cascade events and has the capability to grow through capturing of further SIAs [35,59,60]. Therefore, C15 structures are assumed to play a critical role in forecasting the radiation-induced evolution of the microstructure in iron-based materials. As previously noted, a limited quantity of extended C15-type interstitial clusters was observed in our DFT-CRA trajectories.

[3]This value can also be obtained by multiplying the total number of survived FPs (∼18) by the global magnetization change per FP (i.e., 6.8×10^{-3} μ_B).

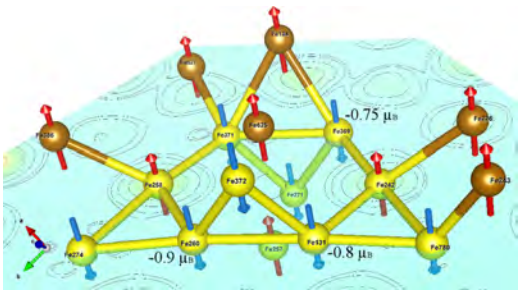

FIG. 8. The structural backbone of a representative C15-type configuration (yellow atoms) formed through DFT-CRA simulation, characterized by a triangular arrangement of di-interstitial and a hexagonal tri-interstitial ring. Blue and red arrows attached to atoms symbolize the corresponding spin-down and spin-up orientations, respectively.

In Fig. 8, an illustrative representation of a prototypical C15-type cluster (yellow color atoms) is provided, with constituent atoms accompanied by their respective site indices. This feature highlights the core framework of the C15-type structure, emerging from the DFT-CRA simulation, which comprises both a triangular configuration of a di-interstitial and a hexagonal tri-interstitial ring formation. Notably, within this example cluster, specific atoms like Fe131 or Fe260 exhibit AFM orientation, quantified at -0.8 and $-0.9\,\mu_B$, respectively. A comparison to a conventional FM bcc Fe atom emphasizes this difference. Further examination of the projected density of states (DOS) and integrated DOS of Fe131, compared to a pristine lattice atom, highlights the influence of neighboring atoms within the cluster (refer to Fig. 9). As shown, in a damaged structure where lattice deformation occurs, the interaction with surrounding atoms induces a separation between t_{2g} and e_g d-orbitals,[4] prompting a reconfiguration of d-orbitals [61]. Consequently, a deviation from the initial majority and minority spin populations, depicted in Fig. 9(b), near and at the Fermi level, results in distinct spin orientations and local magnetic moments for the displaced atoms.

Finally, we investigate the interplay between swelling and global M in the damaged Fe structure using different types of relaxation conditions. Initially, we traced the radiation-induced swelling from ionic relaxation conditions [Fig. 5(a)]. It is noteworthy that these calculations might overestimate the radiation-induced swelling due to the assumption of a constant cell volume. To accurately account for the impact of volume relaxation, we initiated an exploration of magnetovolume instability in a standard pristine FM bcc Fe cell. By progressively expanding the cell volume while maintaining ion positions fixed, we computed the per-atom change in total M within an electronically converged structure. This

[4]Generally, the d-orbitals can be categorized into two distinct sets referred to as t_{2g} (comprising d_{xy}, d_{xz}, and d_{yz}) and e_g (encompassing $d_{x^2-y^2}$ and d_{z^2}) orbitals. However, within specific crystal field environments, these five d-orbitals undergo division into varied configurations, contingent upon the symmetry characteristics of the neighboring d-orbital electrons [61].

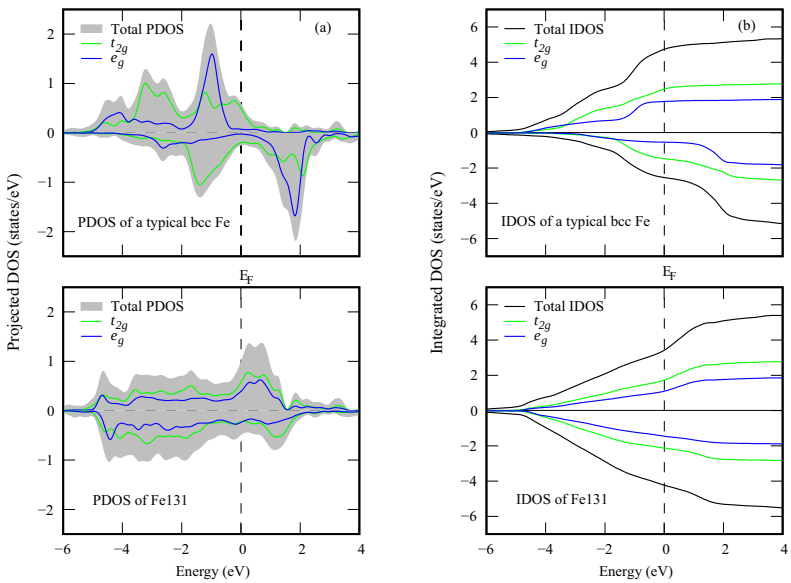

FIG. 9. Comparison of the (a) projected density of states (PDOS) and (b) integrated density of states (IDOS) for the Fe131 atom in the C15-type structure (bottom panels) with that of a typical Fe atom in a standard bcc structure (top panels). The dashed lines show the Fermi energy levels, set at $E_F = 0$.

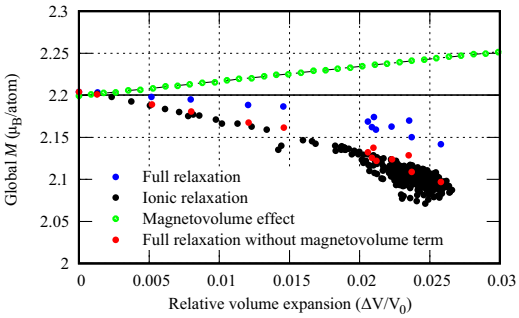

FIG. 10. Total magnetization per atom with relative volume expansion. The results of full relaxation calculation with and without magnetovolume effect are shown with blue- and red-filled circles, respectively.

insight allows us to correct the estimated swelling, by introducing the magnetovolume term to the M change obtained from ionic relaxation calculations. Conversely, by subtracting the magnetovolume term from full relaxation computation results, one can replicate the outcomes of ionic relaxation for predicting swelling. The effectiveness of this approach is evident from Fig. 10, where removing the magnetovolume term from full relaxation calculation results (blue-filled circles) aligns the global M shifts (red-filled circles) with data points extracted from ionic relaxation calculations (black-filled circles). This correction mechanism offers an avenue for fast ionic relaxation calculations while explicitly accounting for radiation-induced swelling through correction with the magnetovolume effect.

Moreover, Fig. 10 demonstrates that up to a relative volume change of 2%, isolated defects accumulate linearly, with the count of FPI nearly matching the number of survived isolated point defects. As the relative volume change surpasses $\Delta V/V_0 > 2\%$, the clustering of SIAs into larger features, e.g., C15 Laves phase, signals a transition from a linear point defect buildup to a stable pattern of larger and larger clusters as the irradiation dose escalates. This progression of microstructure evolution highlights the intricate interplay between volume changes and defect clustering phenomena.

IV. CONCLUSION

In summary, we have introduced a first-principles approach to investigate microstructure evolution. Through the utilization of the CRA model, we explored the radiation-induced microstructure evolution and defect clustering in heavily irradiated bcc Fe. The validation of EAM-CRA results against DFT-CRA predictions shows the level of accuracy to which the EAM methodology is reliable and for which quantities. Additionally, our study addressed magnetization changes within the evolving microstructure. While the EAM-CRA model holds promise for investigating microstructure evolution in large supercells, the DFT-CRA excellently provides electronic structure information for exploring effects such as magnetization charge evolution and holds great promise for studying systems with complex chemistry.

Analyzing a 1024-atom supercell highlighted the minor differences between uniform and localized SIA implantation distributions, whereas larger supercells necessitate the use of localized SIA distribution for modeling of low-energy damage conditions. We found qualitative agreement between EAM potentials and DFT methodology for several properties. However, the EAM-M07 potential seemed to overstabilize the transformation of large SIA clusters into C15 Laves phase structures in a highly defected bcc Fe lattice.

Moreover, our investigation revealed a two-stage microstructure evolution under CRA conditions: initial linear accumulation of isolated point defects followed by steady-state clustering, irrespective of thermally activated diffusion, as reported in experimental observations.

Importantly, our study demonstrated the usefulness of access to electronic structure effects through the correlation of magnetovolume effects in the DFT-CRA ionic relaxation calculations to reproduce precise microstructure transformation observed in full relaxation conditions.

Finally, our integrated approach merges first-principles theory and innovative modeling to elucidate radiation-induced microstructure evolution mechanisms and can be applied to chemically complex systems which are not accessible via interatomic potential-based simulations. These findings enhance our comprehension of these processes, offering insights for more efficient materials science and radiation damage studies.

ACKNOWLEDGMENTS

The authors are grateful for insightful discussions with Sergei Dudarev and Peter Derlet. This work was conducted with financial support from the Swedish Foundation for Strategic Research (SSF) under Grant No. ARC19-0043 (the SUNRISE center) and Swedish Research Council (VR) within projects 2017-06458 and 2019-04156. It was joined to the framework of the EUROfusion Consortium, funded by the European Union via the Euratom Research and Training Programme (Grant Agreement No. 101052200—EUROfusion). The work was also partly funded by the Euratom Research and Training Programme 2019–2020 under Grant Agreements No. 755039 (M4F project) and No. 740415 (IL TROVATORE project). The views and opinions expressed are, however, those of the authors only and do not necessarily reflect those of the European Union or the European Commission. Neither the European Union nor the European Commission can be held responsible for them. The computational resources were provided by the Swedish National Infrastructure for Computing (SNIC; PDC at KTH and NSC at LiU) and by the CINECA HPC Center in Italy.

APPENDIX A: THE FZR CRITERION

Employing the DFT approach, we established the FZR criterion within a bcc Fe structure. The corresponding supercell encompassed $5 \times 5 \times 5$ copies of a bcc Fe unit cell, comprising 250 lattice sites. To ensure precision, a cut-off energy of 350 eV was employed, accompanied by a $6 \times 6 \times 6$ k-point sampling of the Brillouin zone. Both lattice parameter

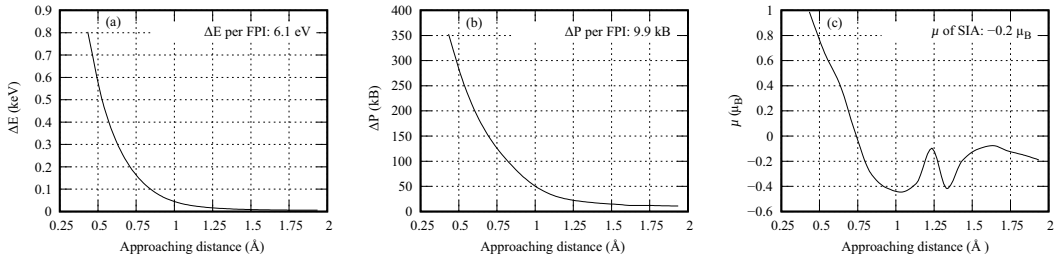

FIG. 11. The change in (a) total energy, (b) global pressure, and (c) local magnetic moment of a SIA as a function of the approaching distance of atoms forming a ⟨110⟩-dumbbell.

optimization and electronic structure calculation were executed using the conjugate gradient algorithm.

Following a complete relaxation calculation, a FP was introduced into the supercell, comprising a vacancy at the origin and an interstitial at the midlattice site. In essence, this led to the establishment of a ⟨110⟩-dumbbell configuration. Initially, the distance between the atoms constituting the dumbbell configuration was approximately 2 Å, while the distance between the vacancy and the center of mass of the ⟨110⟩-dumbbell measured 12.26 Å. This substantial separation ensured the absence of interaction or recombination between the SIAs and vacancy.

The calculated formation energy of the FP, approximately 6.1 eV, is in complete agreement with findings from other DFT studies [62,63]. Furthermore, the introduction of a single FP leads to changes in global pressure and total magnetization of the system by approximately 9.9 kB and $-1.7\,\mu_B$, respectively. In addition, the local magnetic moments of the SIAs equally decrease to $-0.2\,\mu_B$.

To investigate the variations in total energy and hydrostatic pressure changes as well as local magnetic moment of SIAs, we incrementally reduced the distance between the two constituent atoms of a ⟨110⟩-dumbbell. Subsequently, self-consistent electronic calculations were conducted while maintaining the positions of other ions constant.

In Fig. 11, we analyzed the interplay of total energy and hydrostatic pressure changes as well as the local magnetic moment (μ) of SIAs concerning varying interatomic distances. Notably, at an interatomic separation of approximately 0.7 Å, the local magnetic moment of SIAs shifts to a positive value while the total energy change becomes remarkably pronounced, surpassing the FP formation energy by a factor of 33. This shift is also evident in the hydrostatic pressure, displaying an order of magnitude increase compared to FP-induced pressure. These findings underscore the substantial influence of interatomic proximity on SIA properties and system stability.

In summary, establishing a virtual restricted region encompassing lattice atoms finds justification through a proportional fractional delineation based on the equilibrium interatomic separation. Notably, this virtual threshold is defined to circumvent the incorporation of atoms at distances closer than this critical value, i.e., 0.7 Å, within the model. Indeed, this precaution is rooted in recognizing that the local magnetic moment does not attain its negative value under the perturbed circumstances; it assumes an unfavorable disposition. The designated distance safeguards against introducing nonphysical elements into the CRA model, mitigating the distortions arising from undue atom proximity.

APPENDIX B: SPATIAL DISTRIBUTION FUNCTIONS

1. Uniform spatial continuous distribution function

For a uniform atom displacement, one can use a continuous distribution function. By definition, a continuous random variable x has a uniform distribution over an interval $[a, b]$, shown as $x \in \text{uniform}\,[a, b]$, if its probability density function (PDF) is given by [64,65]

$$f(x) = \begin{cases} \frac{1}{b-a}, & a \leqslant x \leqslant b \\ 0, & \text{otherwise} \end{cases} \tag{B1}$$

Using this function will uniformly produce a random number within the interval $[a, b]$ and its expected value (i.e., mean displacement) is given by

$$EX = \frac{b-a}{2}. \tag{B2}$$

For example, the mean value of the atom displacement with the uniform distribution function in a box with side length of $8 \times a_0$ ($a_0 = 2.831$ Å) is 11.32 Å.

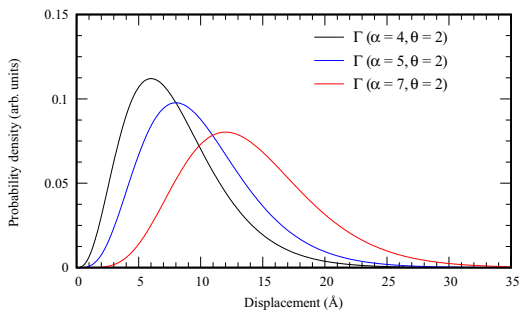

FIG. 12. Plot of PDFs of standard $\Gamma(\alpha,\theta)$ distribution function for various shape and scale parameters.

2. Localized spatial continuous distribution function

For a localized atom displacement, we applied the gamma distribution function. The gamma distribution function is a widely used distribution due to its relation to exponential and normal distribution functions. The standard gamma distribution, $\Gamma(\alpha,\theta)$, has two free parameters, labeled as α and θ, and its PDF is given as [65]

$$f(x;\alpha,\theta) = \frac{x^{\alpha-1}e^{-x/\theta}}{\Gamma(\alpha)\theta^{\alpha}}, \quad 0 < x < \infty. \tag{B3}$$

The parameters α and θ are shape and scale parameters, respectively. $\Gamma(\alpha)$ is also the gamma function [65]. As shown in Fig. 12, the PDFs of a standard gamma distribution are plotted for different α and θ parameters for comparison.

The expected value (i.e., mean displacement) of the $\Gamma(\alpha,\theta)$ is given by the following formula.

$$EX = \alpha \times \theta. \tag{B4}$$

Gamma distributions are used to model non-negative quantities skewed to the right. In other words, they can often be applied to model random times, weights, and lengths. In our study, we used two gamma distribution functions, $\Gamma(4,2)$ and $\Gamma(5,2)$, with mean displacements of 8 and 10 Å, respectively.

[1] K. L. Murty and I. Charit, Structural materials for Gen-IV nuclear reactors: Challenges and opportunities, J. Nucl. Mater. **383**, 189 (2008).

[2] S. J. Zinkle, Radiation-induced effects on microstructure, Compr. Nucl. Mater. **1**, 65 (2012).

[3] A. Aitkaliyeva, L. He, H. Wen, B. Miller, X. M. Bai, and T. Allen, Irradiation effects in Generation IV nuclear reactor materials, in *Structural Materials for Generation IV Nuclear Reactors*, edited by P. Yvon (Elsevier, New York, 2017), p. 253.

[4] C. Cawthorne and E. J. Fulton, Voids in irradiated stainless steel, Nature (London) **216**, 575 (1967).

[5] P.-W. Ma, D. R. Mason, and S. L. Dudarev, Multiscale analysis of dislocation loops and voids in tungsten, Phys. Rev. Mater. **4**, 103609 (2020).

[6] A. J. Ardell and P. Bellon, Radiation-induced solute segregation in metallic alloys, Curr. Opin. Solid State Mater. Sci. **20**, 115 (2016).

[7] D. Kaoumi, J. Adamson, and M. Kirk, Microstructure evolution of two model ferritic/martensitic steels under in situ ion irradiation at low doses (0–2 dpa), J. Nucl. Mater. **445**, 12 (2014).

[8] M. Hernández-Mayoral and M. J. Caturla, Microstructure evolution of irradiated structural materials in nuclear power plants, in *Understanding and Mitigating Ageing in Nuclear Power Plants*, edited by P. G. Tipping (Woodhead Publishing, Cambridge, UK, 2010), p. 189.

[9] L. Koch, F. Granberg, T. Brink, D. Utt, K. Albe, F. Djurabekova, and K. Nordlund, Local segregation versus irradiation effects in high-entropy alloys: Steady-state conditions in a driven system, J. Appl. Phys. **122**, 105106 (2017).

[10] S. M. Bruemmer, E. P. Simonen, P. M. Scott, P. L. Andresen, G. S. Was, and J. L. Nelson, Radiation-induced material changes and susceptibility to intergranular failure of light-water-reactor core internals, J. Nucl. Mater. **274**, 299 (1999).

[11] W. Liu, Y. Ji, P. Tan, H. Zang, C. He, D. Yun, C. Zhang, and Z. Yang, Irradiation induced microstructure evolution in nanostructured materials: A review, Materials **9**, 105 (2016).

[12] C. S. Deo, E. Y. Chen, and R. Dingeville, Atomistic modeling of radiation damage in crystalline materials, Model. Simul. Mater. Sci. Eng. **30**, 023001 (2021).

[13] Y. Li, S. Hu, X. Sun, and M. Stan, A review: Applications of the phase field method in predicting microstructure and property evolution of irradiated nuclear materials, npj Comput. Mater. **3**, 16 (2017).

[14] J.-P. Crocombette and D. Ghaleb, Molecular dynamics modeling of irradiation damage in pure and uranium-doped zircon, J. Nucl. Mater. **295**, 167 (2001).

[15] S. L. Dudarev, Density functional theory models for radiation damage, Annu. Rev. Mater. Res. **43**, 35 (2013).

[16] L. Malerba *et al.*, Multiscale modelling for fusion and fission materials: The M4F Project, Nucl. Mater. Energy **29**, 101051 (2021).

[17] M. J. Caturla, A. Gras Martı, J. J. Jiménez-Rodrıguez, J.-C. Jiménez Saez, and M.-C. Pérez-Martın, Molecular dynamics simulations of energy deposition in solids, in *Advances in Quantum Chemistry* (Academic, New York, 2004), Vol. 45, p. 79.

[18] C. Domain, C. S. Becquart, and L. Malerba, Simulation of radiation damage in Fe alloys: An object kinetic Monte Carlo approach, J. Nucl. Mater. **335**, 121 (2004).

[19] D. J. Bacon and Yu. N. Osetsky, Multiscale modelling of radiation damage in metals: From defect generation to material properties, Mater. Sci. Eng.: A **365**, 46 (2004).

[20] K. Nordlund *et al.*, Improving atomic displacement and replacement calculations with physically realistic damage models, Nat. Commun. **9**, 1084 (2018).

[21] G. H. Kinchin and R. S. Pease, The displacement of atoms in solids by radiation, Rep. Prog. Phys. **18**, 1 (1955).

[22] M. J. Norgett, M. T. Robinson, and I. M. Torrens, A proposed method of calculating displacement dose rates, Nucl. Eng. Des. **33**, 50 (1975).

[23] D. R. Mason, A. E. Sand, and S. L. Dudarev, Atomistic-object kinetic Monte Carlo simulations of irradiation damage in tungsten, Model. Simul. Mater. Sci. Eng. **27**, 055003 (2019).

[24] L. Casillas-Trujillo, A. S. Ervin, L. Xu, A. Barashev, and H. Xu, Dynamics of Interaction between dislocations and point defects in bcc iron, Phys. Rev. Mater. **2**, 103604 (2018).

[25] F. Granberg, J. Byggmästar, and K. Nordlund, Molecular dynamics simulations of high-dose damage production and defect evolution in tungsten, J. Nucl. Mater. **556**, 153158 (2021).

[26] P. M. Derlet and S. L. Dudarev, Microscopic structure of a heavily irradiated material, Phys. Rev. Mater. **4**, 023605 (2020).

[27] F. Granberg, J. Byggmästar, and K. Nordlund, Defect accumulation and evolution during prolonged irradiation of Fe and FeCr alloys, J. Nucl. Mater. **528**, 151843 (2020).

[28] Y. Limoge, A. Rahman, H. Hsieh, and S. Yip, Computer simulation studies of radiation induced amorphization, J. Non-Cryst. Solids **99**, 75 (1988).

[29] A. Chartier and M.-C. Marinica, Rearrangement of interstitial defects in alpha-Fe under extreme condition, Acta Mater. **180**, 141 (2019).

[30] M. J. Sabochick and N. Q. Lam, Radiation-induced amorphization of ordered intermetallic compounds CuTi, $CuTi_2$ and Cu_4Ti_3: A molecular-dynamics study, Phys. Rev. B **43**, 5243 (1991).

[31] S. Aidhy, P. C. Millett, T. Desai, D. Wolf, and S. R. Phillpot, Kinetically evolving irradiation-induced point defect clusters in UO_2 by molecular dynamics simulation, Phys. Rev. B **80**, 104107 (2009).

[32] C. Jiang, M.-J. Zheng, D. Morgan, and I. Szlufarska, Amorphization driven by defect-induced mechanical instability, Phys. Rev. Lett. **111**, 155501 (2013).

[33] L. Malerba *et al.*, Comparison of empirical interatomic potentials for iron applied to radiation damage studies, J. Nucl. Mater. **406**, 19 (2010).

[34] M. I. Mendelev, S. Han, D. J. Srolovitz, G. J. Ackland, D. Y. Sun, and M. Asta, Development of new interatomic potentials appropriate for crystalline and liquid iron, Philos. Mag. **83**, 3977 (2003).

[35] M.-C. Marinica, F. Willaime, and J.-P. Crocombette, Irradiation-induced formation of nanocrystallites with C15 Laves phase structure in bcc iron, Phys. Rev. Lett. **108**, 025501 (2012).

[36] See Supplemental Material at http://link.aps.org/supplemental/10.1103/PhysRevMaterials.7.123604 for predictive capabilities of EAM-CRA methodologies across varied supercell sizes; comprehensive comparisons of defect populations and their cluster sizes using diverse methodologies and supercell sizes; different DFT-CRA calculation methods in comparing swelling anticipation against estimated values through $\Delta P/B$ ratio and affirming the reliability of ionic relaxation calculations; DFT-CRA predictions with experimentally measured radiation-induced changes in lattice constants and crystalline structures; irradiation-induced changes in stress tensor components; and the intricacies of irradiation-induced changes in local magnetization and charge density around point defects. It also contains Refs. [26,55,62,63].

[37] K. Nordlund, N. Runeberg, and D. Sundholm, Repulsive interatomic potentials calculated using Hartree-Fock and density-functional theory methods, Nucl. Instrum. Methods Phys. Res., Sect. B **132**, 45 (1997).

[38] P. E. Blöchl, Projector augmented-wave method, Phys. Rev. B **50**, 17953 (1994).

[39] A. Stukowski, Visualization and analysis of atomistic simulation data with OVITO–the open visualization tool, Model. Simul. Mater. Sci. Eng. **18**, 015012 (2009).

[40] C. Björkas and K. Nordlund, Comparative study of cascade damage in Fe simulated with recent potentials, Nucl. Instrum. Methods Phys. Res. Sect. B **259**, 853 (2007).

[41] D. Terentyev, C. Lagerstedt, P. Olsson, K. Nordlund, J. Wallenius, C. S. Becquart, and L. Malerba, Effect of the interatomic potential on the features of displacement cascades in α-Fe: A molecular dynamics study, J. Nucl. Mater. **351**, 65 (2006).

[42] P. M. Larsen, S. Schmidt, and J. Schiøtz, Robust structural identification via polyhedral template matching, Modell. Simul. Mater. Sci. Eng. **24**, 055007 (2016).

[43] G. Sun, J. Kürti, P. Rajczy, M. Kertesz, J. Hafner, and G. Kresse, Performance of the Vienna ab initio simulation package (VASP) in chemical applications, J. Mol. Struct.: THEOCHEM **624**, 37 (2003).

[44] T. Harte, G. D. Bruce, J. Keeling, and D. Cassettari, Conjugate gradient minimisation approach to generating holographic traps for ultracold atoms, Opt. Express **22**, 26548 (2014).

[45] J. P. Perdew, K. Burke, and M. Ernzerhof, Generalized gradient spproximation made dimple, Phys. Rev. Lett. **77**, 3865 (1996).

[46] J. P. Perdew, Generalized gradient approximations for exchange and correlation: A look backward and forward, Phys. B (Amsterdam, Neth.) **172**, 1 (1991).

[47] D. V. Schroeder, *An Introduction to Thermal Physics* (Oxford University Press, New York, 2021), Vol. 27.

[48] K. Momma and F. Izumi, VESTA: A three-dimensional visualization system for electronic and structural analysis, J. Appl. Crystallogr. **41**, 653 (2008).

[49] H. Hasegawa, A theory of magneto-volume effects of itinerant-electron magnets. I. Spontaneous volume magnetostriction, J. Phys. C: Solid State Phys. **14**, 2793 (1981).

[50] A. P. Thompson *et al.*, LAMMPS - a flexible simulation tool for particle-based materials modeling at the atomic, meso, and continuum scales, Comput. Phys. Commun. **271**, 108171 (2022).

[51] J. Byggmästar, F. Granberg, and K. Nordlund, Effects of the short-range repulsive potential on cascade damage in iron, J. Nucl. Mater. **508**, 530 (2018).

[52] X. Jin, A. Boulle, A. Chartier, J.-P. Crocombette, and A. Debelle, Analysis of strain and disordering kinetics based on combined RBS-channeling and x-ray diffraction atomic-scale modelling, Acta Mater. **201**, 63 (2020).

[53] A. Chartier, C. Onofri, L. Van Brutzel, C. Sabathier, O. Dorosh, and J. Jagielski, Early stages of irradiation induced dislocations in urania, Appl. Phys. Lett. **109**, 181902 (2016).

[54] L. Dézerald, M.-C. Marinica, L. Ventelon, D. Rodney, and F. Willaime, Stability of self-interstitial clusters with C15 Laves phase structure in iron, J. Nucl. Mater. **449**, 219 (2014).

[55] K. Papamihail, K. Mergia, F. Ott, Y. Serruys, Th. Speliotis, G. Apostolopoulos, and S. Messoloras, Fe^+ ion irradiation induced changes in structural and magnetic properties of iron films, Nucl. Mater. Energy **9**, 459 (2016).

[56] K. Papamihail, K. Mergia, F. Ott, Y. Serruys, Th. Speliotis, G. Apostolopoulos, and S. Messoloras, Magnetic effects induced by self-ion irradiation of Fe films, Phys. Rev. B **93**, 100404(R) (2016).

[57] U. Krauss and U. Krey, Local magneto-volume effect in amorphous iron, J. Magn. Magn. Mater. **98**, L1 (1991).

[58] V. L. Moruzzi, P. M. Marcus, and J. Kübler, Magnetovolume instabilities and ferromagnetism versus antiferromagnetism in bulk fcc iron and manganese, Phys. Rev. B **39**, 6957 (1989).

[59] D. J. Bacon, F. Gao, and Yu. N. Osetsky, The primary damage state in fcc, bcc and hcp metals as seen in molecular dynamics simulations, J. Nucl. Mater. **276**, 1 (2000).

[60] F. Gao, D. J. Bacon, Yu. N. Osetsky, P. E. J. Flewitt, and T. A. Lewis, Properties and evolution of sessile interstitial clusters produced by displacement cascades in α-iron, J. Nucl. Mater. **276**, 213 (2000).

[61] S. Blundell, *Magnetism in Condensed Matter* (Oxford University Press, Oxford, 2001), p. 45.

[62] P. Olsson, C. Domain, and J. Wallenius, *Ab initio* study of Cr interactions with point defects in bcc Fe, Phys. Rev. B **75**, 014110 (2007).

[63] P. Olsson, C. S. Becquart, and C. Domain, *Ab initio* threshold displacement energies in iron, Mater. Res. Lett. **4**, 219 (2016).

[64] F. M. Dekking, C. Kraaikamp, H. P. Lopuhaä, and L. E. Meester, *A Modern Introduction to Probability and Statistics: Understanding Why and How* (Springer, London, 2010).

[65] J. Proakis, Probability, random variables and stochastic processes, IEEE Trans. Acoust., Speech, Signal Process. **33**, 1637 (1985).

Paper II

Modeling of irradiation-induced microstructure evolution in Fe: Impact of Frenkel pair distribution

E. Mansouri and P. Olsson
Computational Materials Science 236, 112852 (2024)

Computational Materials Science 236 (2024) 112852

Contents lists available at ScienceDirect

Computational Materials Science

journal homepage: www.elsevier.com/locate/commatsci

Full Length Article

Modeling of irradiation-induced microstructure evolution in Fe: Impact of Frenkel pair distribution

Ebrahim Mansouri *, Pär Olsson *

KTH Royal Institute of Technology, Nuclear Science and Engineering, Roslagstullsbacken 21, 114 21, Stockholm, Sweden

ARTICLE INFO

Keywords:
Irradiation-induce damage
Frenkel pair
C15 Laves phase
Dislocation loops

ABSTRACT

This study investigated the irradiation-induced microstructure evolution in Fe, employing the Creation-Relaxation Algorithm and different interatomic potentials. The influence of self-interstitial atoms (SIAs), which were either locally or uniformly being distributed during the creation of the Frenkel pairs, was investigated on the evolving microstructure. The spatially localized distribution of SIAs, mimicking the low-energy transfer irradiation conditions, moderated the microstructure development, compared to uniform distribution of SIAs, delaying the nucleation of dislocation for higher irradiation doses. Introducing multiple Frenkel pairs facilitated a cumulative irradiation dose of 5 dpa in large supercells. In small supercells, the accumulation of SIAs led to the formation of an artificially stabilized self-interacting planar interstitial cluster, suggesting a minimum cell dimension of 10 nm for an accurate modeling of microstructure evolution when the development of the dislocation network is of interest. The formation and evolution of the C15 Laves phase structure were explored. The evolving C15 structure developed larger clusters with uniformly distributed SIAs, and their sizes depended on the interatomic potential employed. Finally, a comparison with experimental measurements demonstrated that the density and the average size of interstitial dislocation loops aligned well with those observed in experimentally irradiated ultra-high purity Fe at low and room temperatures.

1. Introduction

Fe-based alloys have gained particular attention as structural materials for generation-IV nuclear reactors due to their excellent resistance to radiation-induced damage, high-temperature stability, and mechanical strength [1]. They are used in critical applications such as reactor pressure vessels [2] and fuel cladding [3,4]. Therefore, the study of microstructure imperfections and their dynamic evolutions in Fe-based structural materials holds profound significance in material science and engineering, particularly in materials processing [5], confinement of radioactive waste [6,7], and in advanced nuclear reactor technology [8,9] where the materials are constantly exposed to irradiation in the form of gamma photons and energetic particles.

The accumulation of radiation-induced point defects (vacancies and interstitials) and radiation-enhanced defect structures (dislocation lines and networks) leads to the formation of complex microstructural features such as voids [10], dislocation loops and evolving networks [11–14], and chemical segregation [15,16]. Consequently, these evolving microstructures affect the physical and mechanical properties of the irradiated materials when the density of the defects or the rate of generation is significantly high.

Moreover, investigation of microstructure evolution under diverse irradiation conditions and their correlated physical and mechanical changes are multiscale, multiphysics processes. Therefore, numerous experiments and theoretical studies have been conducted to evaluate the evolution of radiation-induced or enhanced microstructures in real or model materials [17–20]. As experimental tracking of microstructures evolution is challenging, theoretical multiscale modeling approaches have been developed in parallel with the experimental efforts to elucidate the relationship qualitatively and quantitatively between microstructure evolution and property changes.

Within dose limits well below 1 displacement per atom (dpa), where the density of defects is relatively low, the Object Kinetic Monte Carlo (OKMC) method has been widely employed to assesses microstructure evolution in materials like Fe [21] and its alloys [22,23]. Nevertheless, ensuring accurate predictions within OKMC requires the determination of various parameters, including both linear and non-linear elastic interactions, which affect the full interactions between defects and defect

* Corresponding authors.
E-mail addresses: ebrman@kth.se (E. Mansouri), polsson@kth.se (P. Olsson).

https://doi.org/10.1016/j.commatsci.2024.112852
Received 21 November 2023; Received in revised form 2 February 2024; Accepted 2 February 2024
Available online 10 February 2024

clusters. Despite its utility, applying OKMC simulations to densely-packed defects and extended microstructure remains a challenge [24–26].

Alternatively, Molecular Dynamics (MD) simulations employing overlapping cascade events directly create and accumulate defects, offering insights into microstructure evolution [27–30]. The cascade process towards creation of damages involves two phases: initiation of Primary Knock-on Atoms (PKA) and the subsequent thermal spike [6,31]. This leads to the accumulation of self-interstitial atoms (SIAs) and vacancies, forming primary damage in materials [32]. Using massive repetition of fully dynamic cascade events, for reproducing primary damages to achieve desired irradiation dose levels in terms of dpa, demands extensive computational efforts, thereby imposing significant limitations on attainable dose levels. Furthermore, as the cumulative dose increases, thousands of these events contribute to the formation of isolated defects and extended clusters, leading to an evolution from the linear accumulation of isolated point defects to the establishment of steady-state dislocation line networks [33]. The ability to pinpoint those stages of microstructure evolution utilizing overlapping cascade events is proven to be limited by data fluctuations arising from factors such as the comparable simulation cell sizes to the spatial scale of a dynamic cascade events, uncertainties related to minor impact parameter interactions, the range of interaction potential cut-off [33,34], and potential non-adiabatic quantum–mechanical effects [35,36].

In 1988, Y. Limoge and A. Rahman introduced a computationally efficient simulation method aimed at studying the irradiation-induced damage in non-crystalline materials [37]. This technique involves the successive introduction of point defects, which may include Frenkel pairs (FPs) or isolated interstitials, into a perfect structure for modeling of amorphization. More recently, Derlet and Dudarev redefined this method to explore radiation-induced microstructure evolution in Fe and W [33]. The revised approach, known as the Creation-Relaxation Algorithm (CRA), addresses data fluctuations encountered in the overlapping cascade method, revealing distinct microstructure evolution stages at high dose levels. The model introduces a single FP defect, comprising a vacancy and a SIA, randomly into the simulation cell, ensuring uniform atom distribution by re-assigning random spatial coordinates to the selected atoms, leaving behind a vacancy and manifesting as a self-interstitial. All atoms are then relaxed to reach a local energy minimum, and the subsequent microstructure evolution is traced at zero temperature, resulting from the induced stress of the FP insertion.

Given that the CRA model introduces a single FP, the high-energy defect production regime is not explicitly treated. Nevertheless, the model considers linear and non-linear lattice deformations induced by defect accumulations, thereby remedying significant challenges present in the OKMC models. Moreover, the model significantly minimizes the computational efforts by bypassing the initial phase of the damage production, enabling large dose level to be explored even in larger simulation cells. However, with the CRA model implementation used in [33], the SIAs, created in a simulated low-energy damage production regime, were uniformly distributed within a relatively large simulation cell with a side length of 80 $\times$ a_0.[1] This can be seen as an issue in representability since actual irradiation events generating FPs would not generate such a long-ranged uniform distribution of defects but would carry an important element of locality in the generation events.

The present study expands upon the CRA model, investigating its effectiveness with uniform and localized SIA distributions across various supercell sizes. Intuitively speaking, spatially localized distribution of SIAs more likely represents an actual low-energy irradiation event, i.e. low-energy recoiled PKA, such as electron or proton irradiation in relatively large supercell sizes (e.g. side length $>$ 20 $\times$ a_0 and so). That is, for modeling a low-energy damage regime in the larger supercells using CRA model, it is not physically meaningful to displace the SIAs too far away from their original lattice sites.

As demonstrated in [38], a small supercell with a side length of 8 $\times$ a_0 revealed no distinction between employing spatially uniform or localized distributions of SIAs in predicting irradiation-induced microstructure evolutions. Regardless of the type of distribution functions, the average displacement of SIAs remained consistently comparable, amounting to approximately half of the supercell side length, i.e. about 11.3 Å in that case. In such cases, the displacement of SIAs exhibits significant variations with respect to supercell dimensions. Additionally, our findings indicate that employing the CRA model within a compact 8 $\times$ a_0 supercell renders impossible the nucleation and growth of dislocation lines from small interstitial clusters, thus revealing only two stages of microstructure evolution, i.e. linear built-up of isolated pint defects and steady-state saturation of defect clusters. Consequently, we extend the application of the CRA model across various supercell sizes to elucidate the potential influence of supercell dimensions on microstructure evolution in the model material Fe.

As mentioned, the implanted CRA model in [33] inserts only a sequential single FP before relaxation calculation. In this study, however, we also examine the effect of simultaneously incorporating more than one FP (e.g. 5, 10 and up to 500 FPIs) before relaxation, similar to a method employed by Chartier and Marinica [39], highlighting a complex interplay between the interstitial clusters, dislocation loops and lines as well as non-parallel C15 Laves phase structures in body-centered cubic (bcc) Fe. With this strategy, we can achieve higher dose rates in substantially less computational time.

As reported elsewhere, the formation of tridimensional interstitial clusters, such as C15 Laves phase structures, is likely to occur in cascade simulations in bcc Fe [40,41]. Additionally, Density Functional Theory (DFT) calculations have confirmed that the C15 cluster structure possesses the most favorable energy configuration for bundles of four or more SIAs [42,43] in bcc Fe. According to Derlet and Dudarev, however, the existence of the C15 Laves phase was found to be rare in their CRA-based simulations, using the embedded atom method (EAM) potential of Mendelev *et al.* (ME03) [44]. While using EAM potential of Marinica *et al.* (MA07) [42,45], Chartier *et al.* [39] showed that the complex C15 clusters may be significantly formed within the accumulation of multiple FPIs simulation. The variation between these two former studies is likely attributed to the choice of EAM potentials. Therefore, to assess the probable influence of different EAM potentials on the formation of the C15 structure in damaged bcc Fe, we further investigated scenarios involving locally and uniformly distributed SIAs for those aforementioned EAM potentials.

It is noteworthy that the DFT-driven CRA simulations [38] has unveiled a notable agreement between the outcomes generated by EAM-ME03 and EAM-M07 potentials and those found using the first-principles calculation methodology in prediction of all types of defect densities and their related cluster sizes except for the formation of the C15 structure from interstitial clusters larger than 4 SIAs. For such clusters, the prediction of MA07 has been shown to over-stabilize the formation of C15 structure. In contrast, both the EAM-ME03 and DFT methods show more aligned outcomes in this regard. Particularly, the EAM-ME03 results closely match the DFT predictions, indicating a less frequent development of extended C15 clusters from large interstitial clusters ($>$4 SIA) in smaller supercells (8 $\times$ a_0). This agreement notably relates to the expectation and persistence of the C15 Laves phase structure in irradiated bcc Fe. Hence, the EAM-ME03 potential appears to be a more suitable choice for simulating radiation damage evolution in bcc Fe as compared to the EAM-MA07.

In addition, recent experimental investigations into displacement damage defects in other bcc structures, such as tungsten, have not revealed any traces of the C15 phase in heavily Cu^{+3}-irradiated samples [46]. This absence suggests that the formation of giant, detectable C15 structures is less likely to occur in irradiated tungsten.

[1] a_0 is lattice parameter.

Similarly, our DFT-driven CRA simulation showed that the formation of the large and detectable tridimensional C15-type clusters may not be anticipated in damaged Fe structures [38]. Indeed, as the atomic icosahedral C15 clusters grow in size, strong distortions and accompanying strains are expected. These conditions lead to an unstable structure, transforming into other forms of energetically more favorable extended defects, such as ½ ⟨111⟩ or ⟨100⟩ dislocation segments, as described by Chartier and Marinica [39] in damaged bcc iron. Consequently, the small dimensions of such features fall below the resolution limits of transmission electron microscopy (TEM), making them undetectable through conventional techniques.

It is important to note, however, that our first-principles study demonstrates that C15-type clusters exhibit antiferromagnetic alignment with the bcc host atoms in defected iron [38]. Therefore, this suggests the potential for detection using advanced magnetic-induced mapping TEM, as detailed in [47].

The present study is structured into three sections. Section II elucidates the computational details, while Section III is dedicated to the comprehensive discussion of the study's results. Subsequently, the study conclusion is presented in its dedicated section. Furthermore, Appendix A provides a clarification of the different spatial distribution functions utilized for SIA displacement. For the Supplementary Material pertinent to this study, one may refer to Appendix B.

2. Methods

This study applied the CRA model to simulate irradiation damage events and to quantify the irradiation dose in terms of canonical dpa, defined in Ref. [33]. The details of the CRA model can be found in Ref. [33] and in our previous study [38]. Irradiation-induced microstructure evolutions were investigated for several simulation cell sizes comprising $l \times l \times l$ copies of conventional bcc Fe structure, where l varies from 8 to 80, representing the lateral side length of the supercell.

The conjugate gradient approach [48] was used to relax the structure and find a new local potential energy minimum. We performed fixed volume relaxation calculations (NVE ensemble[2]) while maintaining the supercell shape constant and relaxing the ion positions. This allows to accelerate our simulations and study microstructure evolution (e.g. swelling) without losing much information. With fixed pressure condition, however, the shape of the supercell evolves, resulting in explicit volumetric changes while demanding longer computational time. Using fixed volume conditions, one may estimate irradiation-induced swelling by relating the global hydrostatic pressure (ΔP) to the empirical bulk modulus (B) as given by [51]

$$\frac{\Delta V}{V_0} = \frac{-\Delta P}{B}, \tag{1}$$

where $\Delta V_0/V$ is the relative volumetric change because of the damage simulation.

For structure relaxations, we used the EAM potentials of Bonny *et al.* [52], mainly for FeCr alloy, which incorporates the ME03 potential of iron [44], and MA07 potential to model the atomic structure of bcc Fe. When not otherwise specified, the EAM potential used is the ME03 one.

In this study, both employed potentials are grounded in the Ziegler, Biersack, and Littmark [53] screened Coulomb interaction, indicating a robust short-range repulsion form. This characteristic renders these potentials well-suited for the precise modeling of irradiation-induced damage phenomena. The efficacy of these potentials in preventing the formation of nonphysical high-energy structures during relaxation processes is particularly noteworthy, especially when confronted with the potential challenge of random atom insertion leading to highly condensed atomic spacing.

In cases where potentials lack a pronounced short-range feature, or in DFT-driven CRA simulation, careful consideration is essential. Specifically, a precautionary approach must be adopted to prevent the insertion of atoms at extremely short atomic distances, which could technically and physically disrupt the integrity of the simulation. Drawing insights from our recent DFT-driven CRA calculation [38], a pragmatic solution was implemented. A virtual spherical zone, with an optimized radius of 0.7 Å, was defined around each atom. Within this zone, inserted atoms were prohibited from implantation before the relaxation step, ensuring the maintenance of structural coherence in the simulated system.

Similar to our previous work [38], a chosen number of FPs were introduced to a supercell, and then the SIAs were distributed according to uniform and localized distribution functions, described in Appendix A. Therefore, with the Uniform Distribution Function (UDF), the displacement of SIA on average has a significantly larger mean displacement of $l \times a_0/2$, thus depending on the size of the supercell. Whereas, with the Localized Distribution Functions (LDFs), the mean displacement of SIAs is calculated to be 8 or 10 Å. These mean displacements are independent of the supercell size yet dependent on the chosen parameters of the gamma distribution functions, denoted as $\Gamma(\alpha, \theta)$. The standard $\Gamma(\alpha, \theta)$ is characterized by two essential parameters, α and θ, determining the shape and scale properties of the gamma distribution [54]. Here in this study, we examined two sets of α and θ parameters e.g. Γ(4, 2) and Γ(5, 2) for SIA distributions.

Moreover, to speed up our simulation and validate our hypothesis of reducing computational effort by increasing the number of coincident FPIs, we simultaneously inserted multiple FPs (i.e. 10, 25, 50, 100, and 500 FPIs) before the ionic relaxation.

For FP creation and insertion, a PYTHON code was employed, and consequently the structural relaxation was performed in LAMMPS [50]. Additionally, PYTHON and OVITO [55] were used for analyzing the microstructure evolutions. Wigner-Seitz analysis implemented in OVITO was conducted to analyze the vacancy and interstitial contents in simulation cells. For two defects to be clustered together, a cut-off criterion was set at the midpoint between the 2nd and 3rd nearest neighbor distances (i.e. 3.5 Å) for vacancies and between the 3rd and 4th nearest neighbor distances (i.e. 4.1 Å) for interstitials within the bcc Fe structure [56,57]. To identify all types of dislocation lines resulting from FPIs in the simulation cells, we applied a Dislocation Extraction Algorithm [58], using default parameters, implemented in OVITO.

Given the unique icosahedral coordination of C15 atoms, we utilized the polyhedral template matching analysis [59], employing a Root-Mean-Square Deviation[3] threshold of 0.25 to identify these atoms. After identifying atoms with icosahedral structures, we further categorized such clusters based on their atomic content. Specifically, clusters with higher than three but fewer than 12 SIAs with icosahedral coordination were classified as imperfect icosahedral C15 clusters, while those with 12 or more SIAs were designated as perfect C15 clusters. Additionally, in line with our approach for interstitial clusters, we applied midpoint distance of third- and fourth-nearest neighbor distances as a criterion for defining the relevant atomic clusters.

3. Results and discussion

3.1. The effects of spatial distribution of SIA, simultaneous multiple FPIs, and cell size on the microstructure evolution

An appropriate approach for modeling low-energy damage events, within the CRA framework, in a relatively small supercell is to distribute SIAs uniformly in the simulation cell [38]. To determine if the spatial

[2] Microcanonical or NVE ensemble is evaluated NVE: number of particles N, volume V, and energy E are constant [49,50].

[3] It is a measure of the spatial deviation from the ideal structure template, i.e. the quality of the match [59].

distribution of SIAs may affect the microstructure evolution in larger supercells, we applied three different spatial distribution functions as described in Appendix A. As mentioned in [33], there the SIAs were evenly distributed within a supercell with a side length of 80 × a_0. To reproduce their results, we initially used a smaller supercell with a side length of 50 × a_0 and uniformly distributed the SIAs within the supercell. To further reduce computational efforts, we also introduced a strategy of concurrently inserting 10 FPIs instead of the conventional sequential insertion of a single FPI.

As shown in Fig. 1, the evolutions of energy difference (ΔE) per atom and hydrostatic pressure change (ΔP) as a function of dose have been validated and compared with those extracted from Ref. [33]. Aside from the different cell sizes and the higher number of simultaneously inserted FPs in this study, the ΔE and ΔP are clearly consistent with those reported in Ref. [33]. Henceforth, we opted for 50 × a_0 supercells to expedite computations while enabling us to reach higher desired irradiation dose within a shorter time fame, unless otherwise specified.

Given that we inserted ten simultaneous FPs, it is relevant to explore how this increased number of concurrent FPIs may impact microstructure evolution. It is essential to note that augmenting the quantity of FPIs primarily affects the simulated rate at which incident particles interact with lattice atoms and does not significantly alter the energy profile of the modeled irradiation event. Our analysis, as illustrated in Figs. S1–S4 and summarized in Table S1 in the Supplementary Material, reveals no substantial discrepancies in microstructure evolution concerning energy and pressure changes when employing varying numbers of concurrent FPIs. Notably, our results indicate that the insertion of 10 FPIs induces a slightly smoother change in energy and pressure, compared with Ref. [33]. Therefore, for the remainder of our simulations, we have adopted the use of 10 FPs for modeling the irradiation dose.

Fig. 2 shows the evolutions of ΔE per atom and ΔP as a function of dose for various types of SIAs distributions. Notably, the predicted ΔE using LDF-Γ(4, 2) and LDF-Γ(5, 2) SIA distribution functions are consistently lower than that predicted by the UDF, with reductions of about 6.1 % and 4.3 %, respectively, averaged over the entire irradiation dose. This trend suggests that a uniform displacement of SIAs leads to greater energy accumulation within the irradiated structure, due to a lower rate of FP recombination when compared to the localized distribution of SIAs. Consequently, the uniform distribution of SIAs is expected to result in a higher number of survived FPs, leading to the formation of larger interstitial clusters.

This phenomenon is further corroborated by the examination of irradiation-induced pressure changes throughout the entire dose range. For instance, at the end of the irradiation dose, the ΔP value obtained with the CRA-UDF model is 7 % higher than that predicted by the CRA-LDF models. This disparity implies a higher degree of swelling (as estimated by the $\Delta P/B$ ratio) in the Fe model material at low temperatures, within the limitations of the CRA model.

For a more precise understanding of how specific SIA distributions influence microstructural evolution, we analyzed evolving defect populations and their corresponding cluster sizes, representing the number of defects forming a cluster. Figs. 3 and 4 present these data as a function of irradiation dose. Additionally, Table 1 and 2 provide a summary of average defect populations and cluster sizes, obtained using both the UDF- and LDF-CRA models. The averaged values are taken for dose intervals between 1.75 and 2 dpa, where the microstructure appears to approach saturation levels. The percentage difference, denoted as X, of each parameter predicted by LDF is also calculated with respect to that of the UDF by

$$X^{LDF-UDF}(\%) = \frac{X^{LDF} - X^{UDF}}{X^{UDF}} \times 100. \quad (2)$$

As summarized in Table 1, the number density of survived FPs is approximately 11 to 12 % lower with LDFs compared to the UDF. These differences are attributed to a higher likelihood of recombination between vacancies and locally distributed SIAs, particularly due to greater overlap in the stress fields resulting from locally distributed SIAs and the shorter displacement of SIAs with the LDFs as compared to when they are uniformly distributed. Consequently, as depicted in Fig. 2(b), the anticipated swelling is clearly reduced with LDFs due to the decreased count of survived FP defects.

Furthermore, Fig. 3(c) and (d) show that using UDF tends to cause SIAs to aggregate into larger clusters, whereas employing LDFs increases the likelihood of SIAs accumulating in smaller interstitial clusters or to remain isolated. Referring to Table 1 and regardless of LDF used, the total number density of interstitial clusters (I_C) estimated with LDFs is approximately 11 % higher than for predictions made by the UDF within the dose interval of 1.75 to 2 dpa. This trend becomes more evident in Fig. 3(b) and (c), illustrating a higher occurrence of smaller interstitial clusters forming with locally distributed SIAs during the early stages of irradiation (e.g. from 0.05 to 1 dpa).

After reaching their maximum number density (Fig. 3(b)), I_C gradually decrease over irradiation dose, indicating their agglomeration and transformation into dislocation segments. As will be demonstrated later, the nucleation of dislocation loops corresponds to the reduction in the peak population of I_C. Consequently, the nucleation and formation of dislocation loops depend on the type of distribution function used for the SIA displacement. That is, the transformation of I_C into dislocation segments occurs more rapidly for the UDF and with a delay for the LDFs.

Referring to Table 2, both UDF and LDFs predict a nearly equal number of survived mono vacancy (V_{mono}) for dose limits between 1.75 and 2 dpa. However, a closer look at dose levels below 1 dpa, as shown in Fig. 4, reveals meaningful discrepancies between UDF and LDFs in predicting the survived V_{mono} (Fig. 4(a)) and vacancy cluster, V_C, (Fig. 4 (b)). Specifically, UDF estimates, on average, a higher number density of survived V_{mono} compared to LDFs. This difference primarily arises from the increased rate of vacancy recombination with locally distributed SIAs.

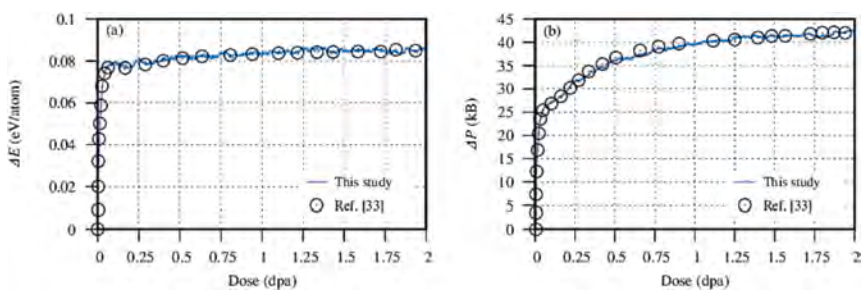

Fig. 1. Comparison between the results of the current study and those in Ref. [33] for a) the evolution of energy change per atom and b) pressure change as functions of irradiation dose.

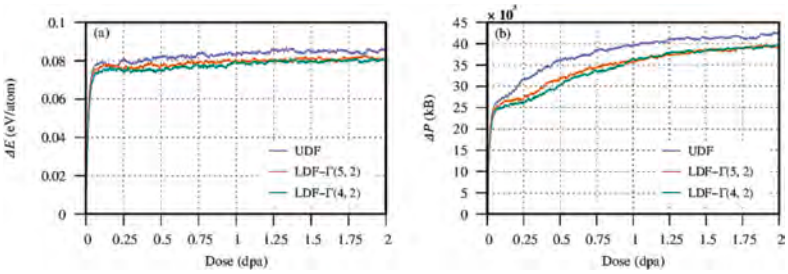

Fig. 2. Comparison of a) ΔE per atom and b) ΔP as functions of irradiation dose resulting from direct damage insertion with uniform and localized distributions of the SIAs.

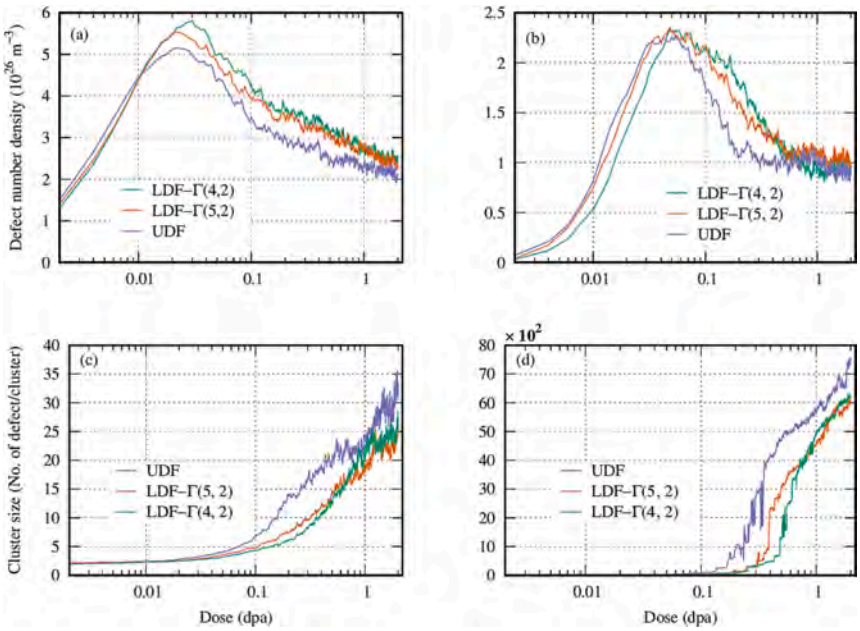

Fig. 3. The dose-dependent evolution of the total number of survived a) I_{mono}, b) I_C, along with c) the average and d) the largest sizes of the I_C predicted with UDF and LDFs of the SIAs.

Beyond 1 dpa, the behavior of uniformly distributed SIAs begins to resemble that of the locally distributed SIAs. Consequently, both UDF and LDFs predict a similar number density for survived V_{mono}, suggesting the infrequent formation of V_C in irradiated bcc Fe at low temperatures in higher irradiation dose. This implies distinct differences in the vacancy-related defect evolutions in comparison with that of the SIAs. It is worth noting that the qualitative differences in the responses of interstitials and vacancies to irradiation have been previously reported in the context of the CRA-driven DFT method, particularly within small supercells [38].

As observed, the choice of SIA displacement distribution led to varying microstructural evolutions, particularly at the onset of irradiation. Our study reveals that the localized distribution of SIAs may offer a more accurate representation of low-energy irradiation-induced microstructure evolution, particularly within relatively large supercells. Consequently, for the subsequent phases of our simulations, we consistently employed the LDF-Γ(5, 2) function to locally displace the SIAs generated by the CRA model in all supercell configurations.

Moving forward, our investigation delved into the evolution of microstructures across various supercell sizes. Within the supercell size range of 8 to 60 $\times$ a_0, all simulation parameters, including the EAM potential, the number of FPIs and the choice of SIA distribution, remained consistent. However, for supercell sizes of 70 $\times$ a_0 and 80 $\times$ a_0, we specifically augmented the number of FPIs to 500 to mitigate demanding computational requirements. Results pertaining to the use of 500 FPIs in supercell sizes exceeding 60 $\times$ a_0 are also presented in the Supplementary Material, specifically in Figs. S1, S4, and S5.

As shown in Fig. 5(a), significant data fluctuations in ΔE are observed within small supercells (i.e., $l < 20$). Expanding the supercell size mitigates these fluctuations, and irrespective of cell size, the energy changes tend to stabilize at approximately 0.08 eV/atom during the early stages of irradiation. Additionally, Fig. 5(b) illustrates that the $\Delta P/B$ ratio, i.e. swelling, exhibits considerable noise in the small cells, revealing only two distinct stages of microstructure evolution for supercell sizes smaller than 20 $\times$ a_0. This observation aligns with recent DFT-CRA calculations [38].

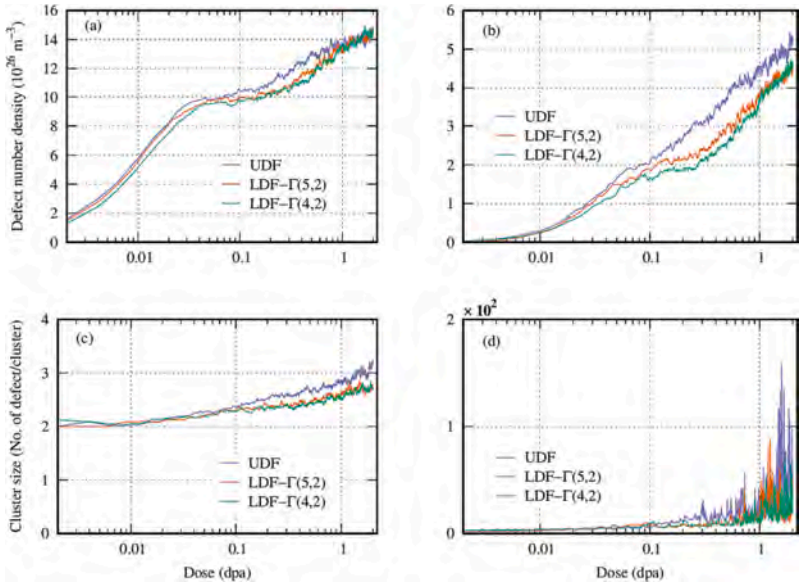

Fig. 4. The dose-dependent evolution of the total number of survived a) V_{mono}, b) V_C, along with c) the average and d) the largest sizes of the V_C predicted with UDF and LDFs of the SIAs.

Table 1
Concentration of survived FP, mono interstitial (I_{mono}), and I_C, along with the average and the largest sizes of I_C are computed and compared across varying spatial distributions of SIAs within dose intervals ranging from 1.75 to 2 dpa. The percentage difference for each parameter (indicated in parentheses) is also calculated in relation to the UDF. Negative values signify a reduction in the respective values compared to those of the UDF.

Defect number density and cluster size	UDF	Γ(5, 2), $X^{\Gamma(5,2)-}_{UDF}$	Γ(4, 2), $X^{\Gamma(4,2)-}_{UDF}$
FP (10^{27} m^{-3})	2.99	2.63, (−12 %)	2.66, (−11 %)
I_{mono} (10^{27} m^{-3})	0.21	0.24, (14 %)	0.25, (19 %)
I_C (10^{27} m^{-3})	0.09	0.1, (11 %)	0.1, (11 %)
Average size of I_C (No. of defect/cluster)	30	23, (−24.35 %)	24, (−19.48 %)
Largest size of I_C (No. of defect/cluster)	7053	5894, (−16.42 %)	6122, (−13.19 %)

Table 2
Concentration of V_{mono} and V_C along with the average and the largest sizes of V_C are computed and compared across varying spatial distributions of SIAs within dose intervals ranging from 1.75 to 2 dpa. The percentage difference for each parameter (indicated in parentheses) is also calculated in relation to the UDF. Negative values signify a reduction in the respective values compared to those of the UDF.

Vacancy concentration and cluster size	UDF	Γ(5, 2), $X^{\Gamma(5,2)-}_{UDF}$	Γ(4, 2), $X^{\Gamma(4,2)-}_{UDF}$
V_{mono} (10^{27} m^{-3})	1.43	1.43, (0 %)	1.44, (0.7 %)
V_C (10^{27} m^{-3})	0.51	0.44, (−13.7 %)	0.45, (−11.7 %)
Average size of V_C (No. of defect/cluster)	3.07	2.69, (−12.3 %)	2.71, (−11.7 %)
Largest size of V_C (No. of defect/cluster)	53	21, (−60.4 %)	29, (−45.3 %)

As indicated in Fig. 6(a) and (b), in small supercells, a linear accumulation of point defects occurs well before reaching 0.05 dpa, followed by a saturation of defect clusters beyond this point. Consequently, the nucleation and growth of dislocation segments, along with the saturation of dislocation lines into dislocation networks, cannot be observed within such small supercells. This limitation arises from the inability of dislocations to nucleate from small interstitial clusters [38] and from unavoidably strong self-interactions across the periodic images of the supercell (see Figs. S6 and S7 in supplemented document).

Conversely, in larger supercells (see Fig. 5(b) and Fig. 6), at least three distinct evolving microstructures become apparent, corroborating findings from other theoretical studies [33,39] and experimental observation [17]. Compared with small supercells, there is a transition of large I_C into dislocation loops, followed by a subsequent transformation of dislocation loops into the slow saturation of extended dislocation networks.

Moreover, previous studies with various simulation techniques, including cascade simulations [40,41], FP accumulation [39], and recent MD/DFT-driven CRA calculations [33,38] have consistently predicted the formation of tridimensional I_C in bcc Fe. These clusters manifest as either C15 Laves phase structures or as the structural backbone of a representative C15-type configuration characterized by triangular arrangement of di-interstitial and hexagonal tri-interstitial rings, all of which locally exhibit icosahedral coordination.

DFT calculations have also confirmed the favorable energy configuration of C15 clusters for four or five SIAs in bcc Fe [42,43]. Notably, our recent DFT-driven CRA study demonstrated notable agreements with the ME03 and MA07 potentials in predicting the formation of C15 Laves phase structures from about 4 SIAs in small supercells [38]. In the present study, we investigated the total occurrence of icosahedral structures in bcc Fe using different type of SIA distributions and interatomic potentials. We initially employed the ME03 potential and applied various SIA distribution functions to study a possible relation between the evolution of C15-type clusters with SIA dispersions. Detailed results, including those obtained using diverse EAM potentials, can also be found in the Figs. S6 and S7 in Supplementary Material.

As shown in Fig. 7(a), there are no notable distinctions in the icosahedral structure content (including both imperfect and perfect C15-type clusters) of damaged bcc Fe, comparing uniform and localized SIA

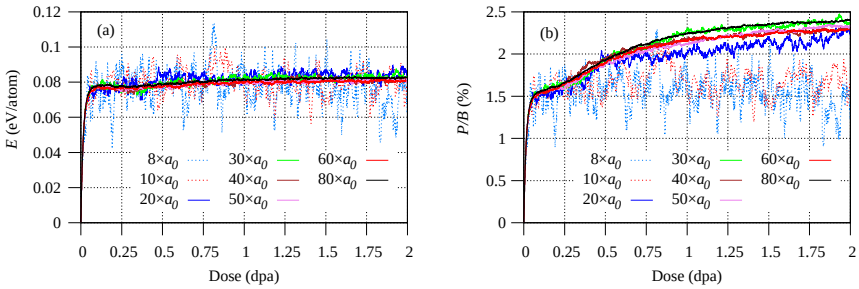

Fig. 5. The evolution of a) ΔE per atom and b) $\Delta P/B$ ratio as functions of dose in different simulation cell sizes.

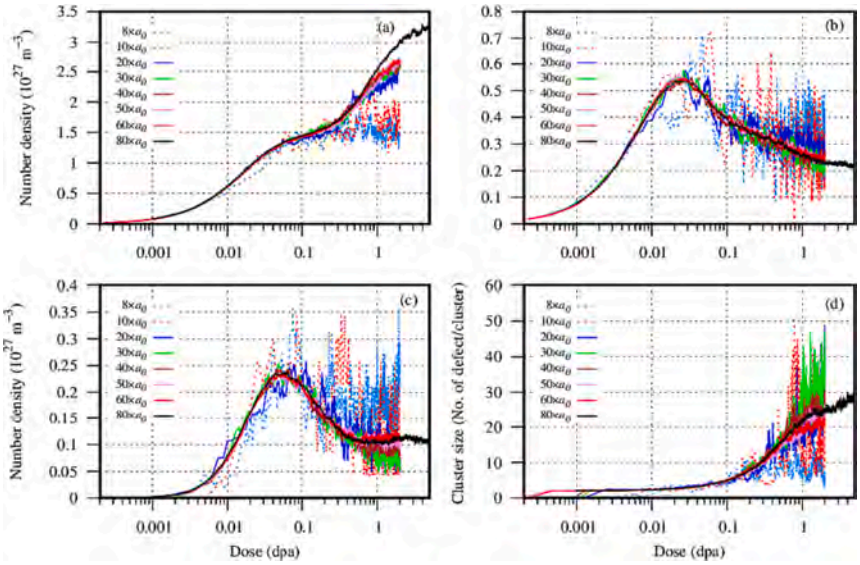

Fig. 6. The dose-dependent evolution of the total number of a) FP content, b) I_{mono}, c) I_C, and d) the average size of I_C for different supercell sizes.

distributions, particularly within dose limits beyond 0.2 dpa. Moreover, Fig. 7(b) highlights an obvious correlation among the total number of evolving perfect C15 clusters and the type of SIA displacement function used, notably within the dose limit of 0.2 dpa. This suggests that the nature of C15 cluster formation in response to irradiation may be slightly influenced by the type of SIA displacement distributions. However, a more pronounced influence is seen in the rate at which the SIAs start to accumulate. That is, the higher the accumulation rate is, the larger the number density and C15 cluster size would be expected, as one can see in Fig. 7(b) and (d).

Additionally, as indicated in Fig. 8, the MD-CRA simulations revealed evident variations in the size of C15 clusters among different calculation methods. Plainly, the EAM-MA07 calculations yielded the largest C15 cluster, comprising an impressive eighteen-fold C15 structure with a total of 109 SIAs, having an average elliptical area of 1×3.5 nm^2. Conversely, the EAM-ME03 potential simulations showed a considerably smaller maximal C15 cluster, incorporating only 24 SIAs and forming a four-fold C15 structure, with an average diameter of 0.9 nm.

In comparison to another bcc structure and in line with the experimental study conducted by Wang *et al.* [46], no trace of C15-type structures has been reported in heavily Cu^{3+}-ion irradiated tungsten. This, as mentioned, could be primarily attributed to the formation of relatively small-sized C15 clusters in irradiated materials. Therefore, despite the potential existence of these features, their small dimensions fall below the resolution limits of TEM, making them undetectable. However, our first-principles study indicates that C15-type clusters exhibit antiferromagnetic alignment with the bcc host atoms in defected iron [38], suggesting the possibility of detection using advanced magnetic-induced mapping techniques in TEM, as discussed in [47] and detection using high resolution TEM should also be possible.

The comparison between the predictions with the ME03 and MA07 potentials is presented in the Supplementary Material. There, we also included the result of simulation with the EAM potential by Ackland (AC04) [60] for a comprehensive comparison.

3.2. *Irradiation-induced microstructure evolution and dislocation network saturation*

Here we analyzed the evolution of the total and directional[4]

[4] The dislocation lines with different Burgers vectors such as ½⟨111⟩, ⟨100⟩, and ⟨110⟩.

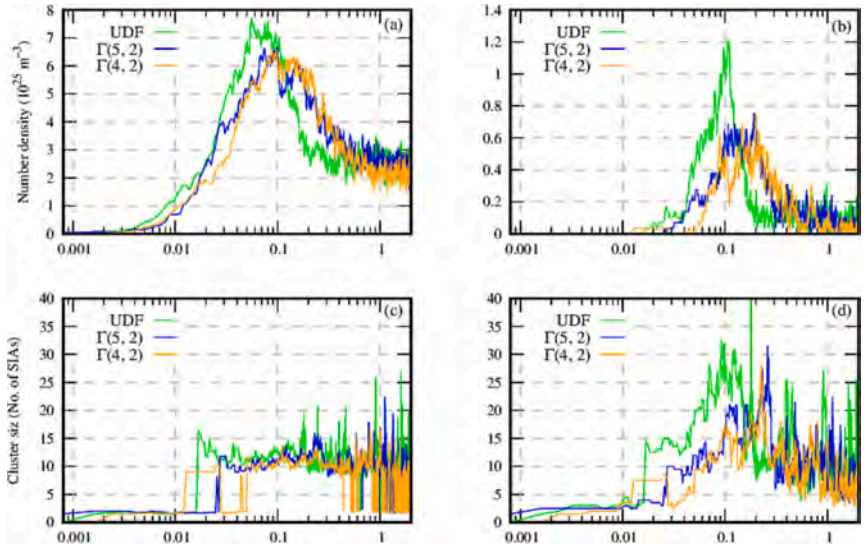

Fig. 7. The dose-dependent number density evolution of a) the imperfect and perfect C15-type clusters and b) perfect C15 clusters, accompanied by c) the average size of imperfect and perfect C15-type clusters, and d) the largest size of perfect C15 cluster formed in bcc Fe using uniform and localized SIA displacements.

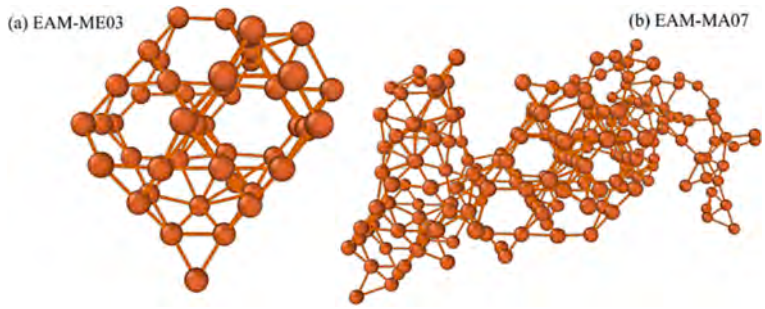

Fig. 8. Comparison of the largest C15 clusters formed in damaged bcc Fe using MD-CRA simulation with a) EAM-ME03 and b) EAM-MA07 potentials.

dislocation line densities (DLDs), ρ_D, for varying cell sizes in which the SIAs were either locally or uniformly distributed. The DLDs were evaluated by dividing the total dislocation line lengths by the corresponding supercell volumes. First, we examined the dependence of ρ_D on the choice of distribution of SIAs in the supercell of size $50 \times a_0$.

As indicated in Fig. 9(a), depending on the type of SIA distributions, the dislocation line densities begin to nucleate at around 0.04 dpa for UDF and 0.07 dpa for LDF-Γ(4, 2), through unfaulting of the growing dislocation lines. This corresponds to the irradiation doses at which the peak population of I_C starts diminishing (compare Figs. 3(b) and Fig. 9 (a)) and transforming into interstitial dislocation loops. Additionally, referring to Fig. 9(a) and (b), the transformation of I_C into dislocation loops is much faster with uniformly distributed SIAs than with localized SIA distribution. Using LDFs, however, the annihilation rate of FPs increases, and, thus, the ρ_D evolves with a slower accumulation rate.

Moreover, the peak for ½⟨111⟩-dislocation segment, with UDF, is about 12 % higher than those predicted with the LDFs, indicating a higher number of ½⟨111⟩ dislocation segment is formed using the UDF. This increase in the DLDs is a direct consequence of the formation of larger clusters that emerge from uniformly distributed SIAs. Moreover, there is a shift in the peaks of total DLDs towards higher irradiation doses with LDFs, compared to UDF.

Except for negligible ρ_D associated with the ⟨110⟩ Burgers vector (Fig. 9(d)), the ½⟨111⟩ dislocation segments dominate over ⟨100⟩ ones. This can be explained by the predicted lower formation energy of ½⟨111⟩ interstitial defects in bcc Fe, as indicated by both DFT [61] and EAM [62] calculations.

Additionally, a recent experimental observation of self-ion irradiated ultra-high purity (UHP) Fe at low temperature proved that the observable population of ½⟨111⟩ dislocation segments dominated over the ⟨100⟩ ones and that there was no trace of ⟨110⟩'s [17].

Finally, as shown in Fig. 10, we can classify the evolution of the dislocation segments into three distinct stages, as also qualeteitevelly observed in irradated bcc tungestan [46]. The first stage begins with the nucleation of dislocation loops in doses, ~ 0.05 dpa, where the peak population of I_C starts decreasing and then continues with the linear growth and accumulation of ½⟨111⟩ and ⟨100⟩ dislocation loops up to ~ 0.25 dpa, depending on the types of SIAs distributions. The second stage can be understood by decreasing DLDs after 0.3 dpa, indicating the accumulation and coalescence of dislocation loops into a dislocation network. Finally, the length of the dislocation networks ultimately reaches a steady state at an irradiation dose of > ~ 2.5 dpa, as indicated

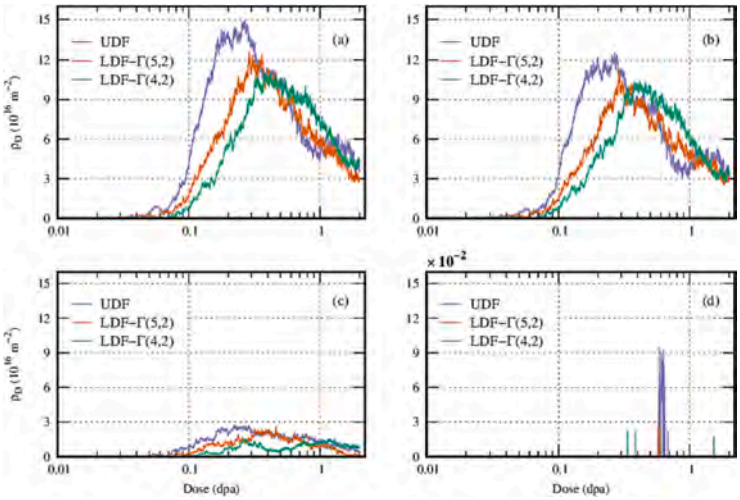

Fig. 9. The dose-dependent evolution of a) the total DLDs accompanied by directional DLDs with b) ½⟨111⟩, c) ⟨100⟩, and d) ⟨110⟩ Burgers vectors for uniform and localized distributions of the SIAs in the supercell size of 50 × a_0.

in Fig. 10.

While the direct quantitative comparison of dislocation loop densities predicted by MD-CRA simulation is not conclusively compelling, our results exhibit a promising qualitative agreement with experimental findings in irradiated systems such as Fe [17], W [46], and Zr [14]. This alignment suggests the reliability of the CRA model in reproducing irradiation-induced microstructure evolution trends in materials. Specifically, our observations mirror the behavior seen in irradiated tungsten [46], where the dislocation loop density evolution peaks at 0.1 dpa under room-temperature irradiation conditions, plateauing at 0.2 dpa. Referring to Fig. 11(a), a similar microstructure evolution is evident in defective Fe, as predicted by the CRA model. However, under low-temperature irradiation conditions, the peak dislocation density occurs at approximately 0.2 dpa before reaching saturation at around 0.6 dpa.

To further indicate the predictive power of our MD-CRA model, we conducted a comparative analysis of the dose-dependent evolution of dislocation loop densities along with their associated loop sizes in our study and compared them with other experimentally and theoretically reported quantities. These comparisons were made with the data obtained from self-ion irradiation experiments on UHP Fe at liquid nitrogen and room temperatures [17] and also with the results of high-dose, proton-irradiated Zr-based alloy at high temperature [14].

We initially evaluated the number density and dislocation loop sizes in our largest 20 nm supercell, i.e. 80 × a_0, approaching the dimensions of the samples used in [17], ranging from 50 nm to 80 nm.

As illustrated in Fig. 11, our MD-CRA simulations predicted a total loop number density, encompassing both ½⟨111⟩ and ⟨100⟩ dislocation loops, to be 9.8×10^{23} m^{-3} at absolute zero temperature for a dose level of 1 dpa. This value is relatively comparable to the experimentally reported density of 0.98×10^{23} m^{-3} at low temperature (93 K) and up to a dose limit of 1 dpa. In the analysis of dislocation loops using TEM in [17], the Burgers vector (***b***) determination was carried out using the operating diffraction ***g*** and an improved ***g***·***b*** analysis method, specifically employing the weak beam (WB) dark field imaging mode [63]. Notably, attempting to trace loops smaller than 10 nm at different diffraction conditions proved practically unfeasible [17]. To address this, a novel statistical Burgers vector analysis was introduced in addition to the conventional WB method [63]. This statistical approach enabled the precise determination of the absolute number density of dislocation loops per Burgers vector type. Consequently, in Fig. 11(a), the non-corrected black-squared data points, where the statistical Burgers vector analysis was not applied, are one or two orders of magnitude smaller than the corrected values, which account for the statistical Burgers vector analysis.

Moreover, as explained by Warwick *et al.* [14] and characterized by Boleininger *et al.* [64], the CRA simulations generally overestimate defect content at high doses due to the absence of re-crystallization induced by collision cascades. Despite this limitation, qualitative trends are accurately predicted under various conditions [14]. This overestimation may be attributed to the production of primary knock-on atoms with kinetic energies near the threshold displacement energy. When recoil energies are significantly higher, defect densities drop by a factor of approximately 10, as suggested in [14].

Additionally, such a discrepancy between our predicted dislocation loop density and the reported experimental values can also be attributed to other primary limitations, as elaborated in [17]. Primarily, the precision of experimental measurements is constrained by the visibility and detectability of dislocation loops. Smaller loops with dimensions less than 0.7 nm can escape detection entirely when their contrast amplitude falls below the micrograph noise threshold. Furthermore, loops smaller than the diffraction limit (~1 nm) exhibit a consistent contrast size of approximately 0.7 nm, which contributes significantly to the observed deviations from the experimental data. To clarify this, the distribution of average loop sizes, retrieved from our MD-CRA simulation, is presented in Fig. 12(a) and compared with those extracted from Ref. [17]. It is evident from MD-CRA predictions that the proposed percentage of dislocation loops with diameter down to 1 nm is significantly higher than those experimentally reported loop sizes which have not been detected due to the diffraction limit of the instrument.

Moreover, as indicated in Fig. 11(b), the dose-dependent evolution of average size of dislocation loops, predicated in this study, is in a reasonable agreement with those measured at room temperature. That is, the average loop sizes we detracted in our simulation is about 1.25 nm which is comparable to the reported 1.41 nm average loop size up to 0.05 dpa at room temperature. Concerning the formation of other interstitial clusters such as tridimensional C15 clusters and their interplay with ½⟨111⟩ or ⟨100⟩ dislocation lines reported in Ref. [39], we could not observe any correlated transformation of C15 cluster into any type of dislocation segments, vice versa.

Fig. 13 compares the dose-dependent evolution of DLD in different

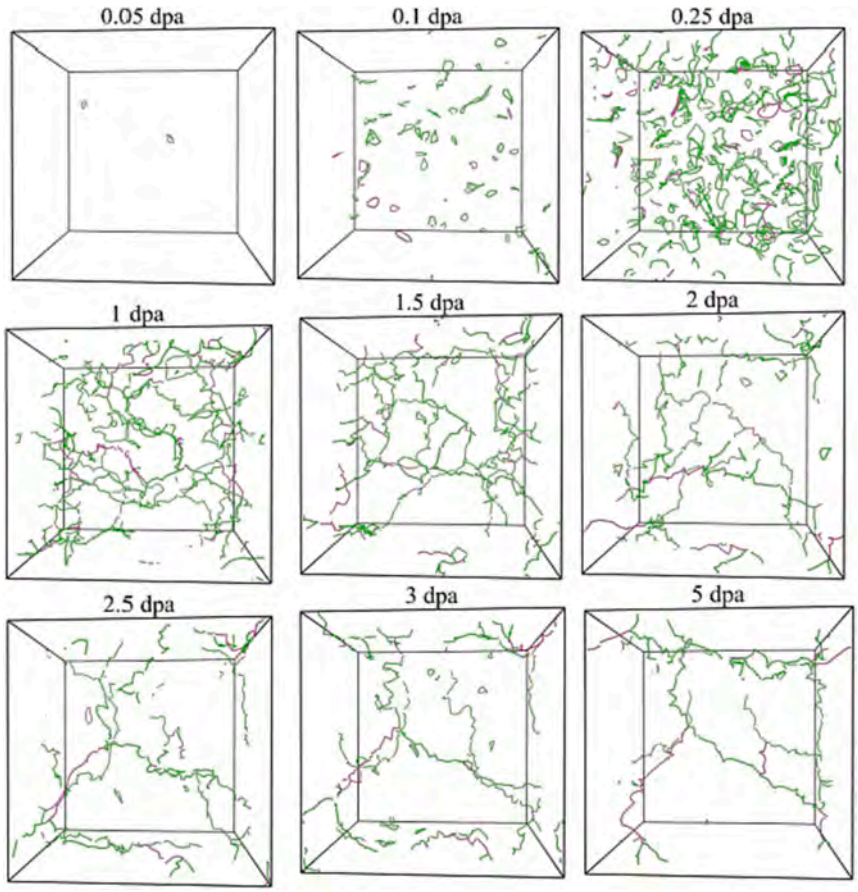

Fig. 10. The dose-dependent evolution of dislocation segments predicted by the MD-CRA model in Fe. At a dose of ~ 0.05 dpa, dislocation loops initiate nucleation and subsequently grow up to 0.25 dpa. Around 0.25 dpa, dislocation loops coalesce and transform into extended dislocation network up to ~ 2.5 dpa: Beyond 2.5 dpa, a steady state of the extended dislocation network occur. Dislocation segments with ½⟨111⟩ and ⟨100⟩ Burgers vectors are indicated with green and purple lines, respectively. (For interpretation of the references to colour in this figure legend, the reader is referred to the web version of this article.)

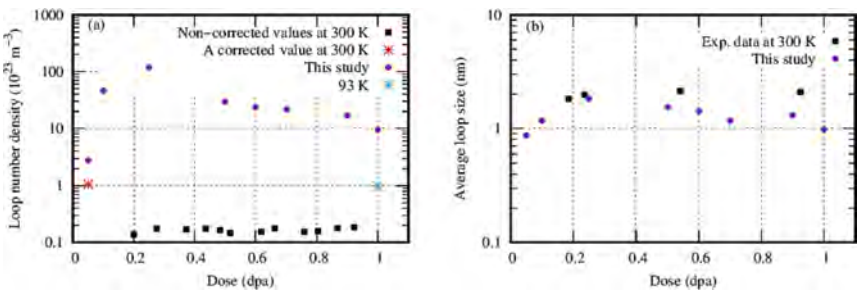

Fig. 11. Comparison of the dose-dependent evolution of a) the number density of visible loops and b) the average loop sizes in experimentally irradiated UHP Fe and in theoretically damaged Fe within MD-CRA simulation conditions. The black-square experimental data points are not corrected for invisibility due to $\boldsymbol{g}.\boldsymbol{b} = 0$, as described in [17,63].

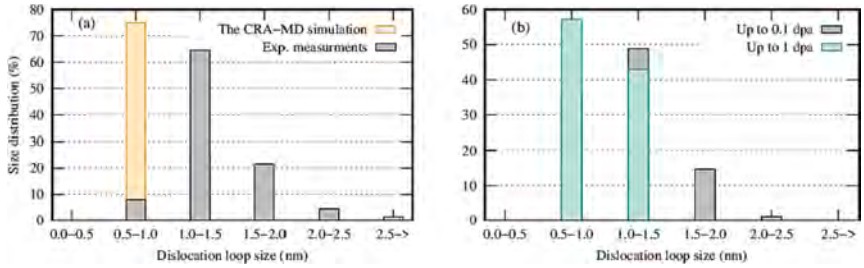

Fig. 12. Comparison of dislocation loop size distributions in UHP Fe following 500 k eV Fe+ ion beam irradiation at room temperature and in Fe resulting from MD-CRA calculation up to 0.05 dpa. b) The predicted dislocation loop size distributions at different irradiation doses using the MD-CRA model.

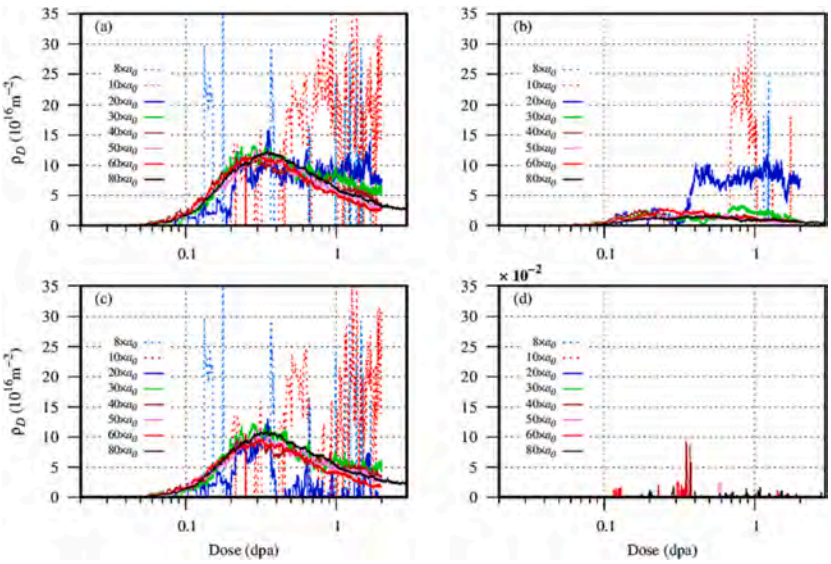

Fig. 13. The dose-dependent evolution of DLDs in various categories: a) the total DLDs along with directional DLDs with b) ⟨100⟩, c) ½⟨111⟩, and d) ⟨110⟩ Burgers vectors. The analysis is conducted across different supercell sizes.

supercells ranging from 8 to 80 × a_0. Notably, as shown in Fig. 13(b), the dislocation segments with ⟨100⟩ Burgers vector in the supercell sizes of 10 × a_0 and 20 × a_0 appear to have an artificial maximum in the DLD plot among all examined supercell sizes, and as the size of the cell increases, those artifices disappear. This can be generalized for other directional dislocation segments as well. We also noticed sizable planar interstitial clusters formed in the supercells smaller than 40 × a_0, displayed in Fig. S9 in Supplementary Material. Consequently, for investigating and analyzing the irradiation-induced extended defects, one must take into consideration that the size of the supercell needs to be larger than 40 × a_0 for Fe. The reason is that in the small-sized supercells ($\sim l < 20$), the size of interstitial cluster which needs to give birth to a dislocation segment shall be larger than the size of the cell within which it has been already nucleated. The dislocation structure then self-interacts across the entire simulation cell and forms an extremely stable faulted plane structure that is a simulation condition artifact.

Additionally, Fig. 14 compares the evolving DLDs for two scenarios: one with a supercell size of 50 × a_0, featuring an increased number of concurrent FPIs, and the other with a supercell size of 80 × a_0 with simulations using 500 concurrent FPIs, providing a comprehensive comparison. It is evident that irrespective of the supercell size or the number of inserted FPs, there is a strong agreement among all types of DLDs estimated under various scenarios.

4. Conclusion

In conclusion, our research has provided comprehensive insights into the irradiation-induced microstructure evolution in bcc Fe model material through the utilization of diverse interatomic potential methods and the application of the Creation-Relaxation Algorithm. We have studied and analyzed the development of defects and the associated cluster sizes as a function of irradiation dose in various supercell sizes with distinct displacement distributions of SIAs, either localized or uniformly dispersed.

Notably, spatial localization of the FPs led to a moderate growth of microstructural imperfections compared to uniformly distributed SIAs, resulting in the delayed nucleation of dislocation segments, especially at higher irradiation doses. Our study also revealed that the introduction of multiple FPs enabled rapid accumulation of a cumulative simulated irradiation dose of 5 dpa in relatively large supercells. In the smaller supercells used, the relatively close periodic boundaries caused an artificial self-interaction and stabilization of cell-traversing planar

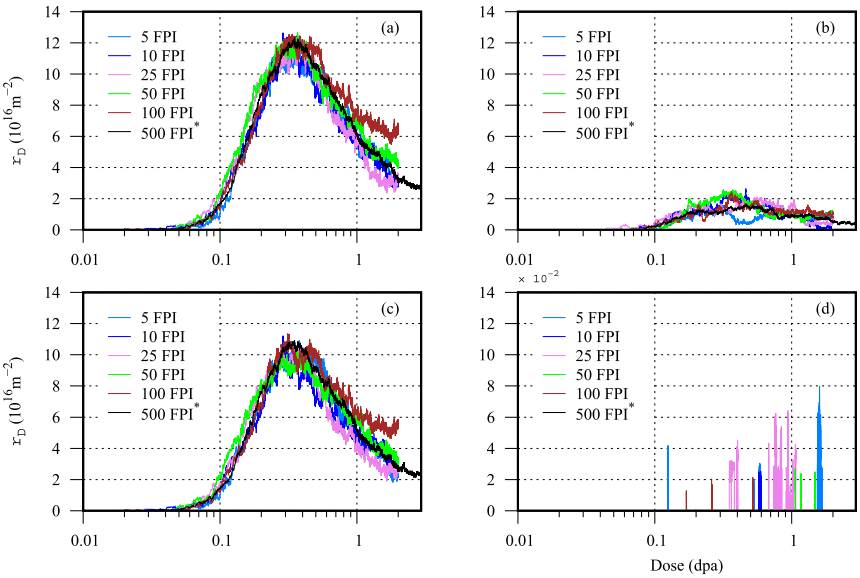

Fig. 14. The dose-dependent evolution of DLDs in different scenarios: a) the total DLDs along with directional DLDs with b) ⟨100⟩, c) ½⟨111⟩, and d) ⟨110⟩ Burgers vectors. The analysis is conducted in the supercell size of 50 × a_0 with diverse FPI numbers. *Results for 500 FPIs are obtained from a supercell with a side length of 80 × a_0.

interstitial clusters, prompting a recommendation for a minimum cell dimension of 10 nm to enhance the accuracy of modeling irradiation-induced damage evolution in Fe when the dislocation network formation stage is of interest.

Additionally, our findings highlighted that the evolving C15 structure tends to form larger clusters in the early stages of irradiation when using a uniform SIA distributed function in Fe. The sizes of the C15 structures depend significantly on the chosen interatomic potential. Among the potentials employed, the Marinica potential predicted the largest and more stable C15 cluster in damaged bcc Fe, while the Mendelev potential gave an evolution in better agreement with first-principles simulations when the sizes of included SIAs in C15 clusters were smaller than 4 SIAs. Additionally, regardless of the selected potential, the anticipated C15 cluster size appears to fall below the threshold detectable by the resolution limits of conventional TEM techniques,

Finally, a direct comparison with experimental measurements demonstrated a commendable alignment of characteristics. The interstitial dislocation loop statistics and sizes identified in our simulations closely match those observed in irradiated ultra-high purity Fe at low and room temperatures, as well as those qualitatively experimentally reported in other irradiated bcc tungsten and hexagonal zirconium at room and high-temperatures, respectively. The loop densities exhibited reasonable and explainable agreement, while the evolution of loop sizes demonstrated good correspondence.

CRediT authorship contribution statement

Ebrahim Mansouri: Writing – original draft, Methodology, Investigation, Formal analysis, Conceptualization. **Pär Olsson:** Writing – review & editing, Supervision, Funding acquisition, Conceptualization.

Declaration of competing interest

The authors declare that they have no known competing financial interests or personal relationships that could have appeared to influence the work reported in this paper.

Data availability

Data will be made available on request.

Acknowledgments

This work was conducted with financial support from the Swedish Foundation for Strategic Research (Stiftelsen för Strategisk Forskning, SSF) under Grant No. ARC19-0043 (the SUNRISE center) and the Swedish Research Council (VR) within projects 2017-06458 and 2019-04156. It was joined to the framework of the EUROfusion Consortium, funded by the European Union via the Euratom Research and Training Programme (Grant Agreement No. 101052200 — EUROfusion). The work was also partly funded by the Euratom Research and Training Programme 2019–2020 under grant agreements No 755039 (M4F project) and No 740415 (IL TROVATORE project). Views and opinions expressed are however those of the authors only and do not necessarily reflect those of the European Union or the European Commission. Neither the European Union nor the European Commission can be held responsible for them. The computational resources were provided by the Swedish National Infrastructure for Computing (SNIC) (PDC at KTH and NSC at LiU) and by the CINECA HPC center in Italy.

Appendix A. Spatial distribution functions

a) Uniform spatial continuous distribution function

For a uniform atom displacement, one can use a continuous linear distribution function. By definition, a continuous random variable x has a uniform distribution over an interval [a, b], shown as x ∈ uniform [a, b], if its probability density function (PDF) is given by [54,65]

$$f(x) = \begin{cases} \frac{1}{b-a} & for \quad a \le x \le b, \\ 0 & otherwise \end{cases}. \tag{3}$$

Using this function will uniformly produce a random number within the interval [a, b] and its expected value (i.e. mean displacement) is given by:

$$EX = \frac{b-a}{2}. \tag{4}$$

For example, the mean value of the atom displacement with the uniform distribution function in a box with side length of $50 \times a_0$ ($a_0 = 2.855$ Å) is 71.37 Å.

For the uniform distribution function we assigned the abbreviation UDF in the above.

b) Localized spatial continuous distribution function

For a localized atom displacement, we chose to apply the gamma distribution function. The gamma distribution function is a widely used distribution related to the exponential and normal distribution functions, and it can be argued that it provides a reasonable description of locality in the displacement of atoms from their lattice sites. The standard gamma distribution, $\Gamma(\alpha, \theta)$, has two free parameters, labeled as α and θ, and its PDF is given as [54]

$$f(x;\alpha,\theta) = \frac{x^{\alpha-1}e^{-x/\theta}}{\Gamma(\alpha)\theta^{\alpha}}, \qquad for \qquad 0 < x < \infty. \tag{5}$$

The parameter α and θ are shape and scale parameters, respectively. Γ(α) is also the gamma function. As shown in Fig. 15, the PDFs of standard gamma distribution are plotted for different α and θ parameters for comparison.

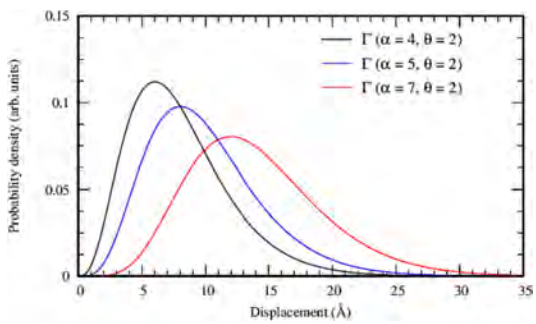

Fig. 15. Plot of PDFs of standard Γ(α, θ) distribution function for various shape and scale parameters.

The expected value, i.e. mean displacement, of the $\Gamma(\alpha, \theta)$ is given by the following formula.

$$EX = \alpha \times \theta. \tag{6}$$

Gamma distributions are used to model non-negative quantities skewed to the right. In other words, they can often be applied to model random times, weights, and lengths. In our study, we used two gamma distribution functions, Γ(4, 2) and Γ(5, 2), with mean displacements of 8 Å and 10 Å, respectively.

Appendix B. Supplementary data

Supplementary data to this article can be found online at https://doi.org/10.1016/j.commatsci.2024.112852.

References

[1] K.L. Murty, I. Charit, Structural materials for Gen-IV nuclear reactors: Challenges and opportunities, J. Nucl. Mater. 383 (2008) 189–195, https://doi.org/10.1016/j.jnucmat.2008.08.044.

[2] R.L. Klueh, Elevated temperature ferritic and martensitic steels and their application to future nuclear reactors, Int. Mater. Rev. 50 (2005) 287–310, https://doi.org/10.1179/174328005X41140.

[3] T. Allen, H. Burlet, R.K. Nanstad, M. Samaras, S. Ukai, Advanced structural materials and cladding, MRS Bull. 34 (2009) 20–27, https://doi.org/10.1557/mrs2009.8.

[4] K.A. Terrani, S.J. Zinkle, L.L. Snead, Advanced oxidation-resistant iron-based alloys for LWR fuel cladding, J. Nucl. Mater. 448 (2014) 420–435, https://doi.org/10.1016/j.jnucmat.2013.06.041.

[5] R.E. Smallman, I.R. Harris, M.A. Duggan, Microstructure and materials processing, J. Mater. Process. Technol. 63 (1997) 18–29, https://doi.org/10.1016/S0924-0136(96)02595-2.

[6] W.J. Weber, F.P. Roberts, A review of radiation effects in solid nuclear waste forms, Nucl. Technol. 60 (1983) 178–198, https://doi.org/10.13182/NT83-A33073.

[7] V.I. Malkovsky, S.V. Yudintsev, M.I. Ojovan, V.A. Petrov, The influence of radiation on confinement properties of nuclear waste glasses, Sci. Technol. Nucl. Install. 2020 (2020) e8875723, https://doi.org/10.1155/2020/8875723.

[8] A. Aitkaliyeva, L. He, H. Wen, B. Miller, X.M. Bai, T. Allen, Irradiation effects in Generation IV nuclear reactor materials, in: P. Yvon (Ed.), Structural Materials for Generation IV Nuclear Reactors, Woodhead Publishing, 2017, pp. 253–283, https://doi.org/10.1016/B978-0-08-100906-2.00007-0.

[9] B.I. Khripunov, V.S. Koidan, A.I. Ryazanov, V.M. Gureev, S.T. Latushkin, E. V. Semenov, V.G. Stolyarova, Impact of deuterium plasma flux on fusion reactor materials: radiation damage, surface modification, Erosion, Phys. at. Nucl. 84 (2021) 1252–1258, https://doi.org/10.1134/S1063778821070048.

[10] J.A. Brinkman, Production of atomic displacements by high-energy particles, Am. J. Phys. 24 (1956) 246–267, https://doi.org/10.1119/1.1934201.

[11] J. Eriksson, G. Sundell, P. Tejland, H.-O. Andrén, M. Thuvander, An atom probe tomography study of the chemistry of radiation-induced dislocation loops in Zircaloy-2 exposed to boiling water reactor operation, J. Nucl. Mater. 550 (2021) 152923, https://doi.org/10.1016/j.jnucmat.2021.152923.

[12] F. Granberg, F. Djurabekova, E. Levo, K. Nordlund, Damage buildup and edge dislocation mobility in equiatomic multicomponent alloys, Nucl. Instrum. Methods Phys. Res. Sect. B Beam Interact. Mater. at. 393 (2017) 114–117, https://doi.org/10.1016/j.nimb.2016.11.012.

[13] S.I. Choi, J.H. Kim, Radiation-induced dislocation and growth behavior of zirconium and zirconium alloys – a review, Nucl. Eng. Technol. 45 (2013) 385–392, https://doi.org/10.5516/NET.07.2013.035.

[14] A.R. Warwick, R. Thomas, M. Boleininger, Ö. Koç, G. Zilahi, G. Ribárik, Z. Hegedues, U. Lienert, T. Ungar, C. Race, M. Preuss, P. Frankel, S.L. Dudarev, Dislocation density transients and saturation in irradiated zirconium, Int. J. Plast. 164 (2023) 103590, https://doi.org/10.1016/j.ijplas.2023.103590.

[15] E.A. Kenik, Radiation-induced segregation in irradiated Type 304 stainless steels, J. Nucl. Mater. 187 (1992) 239–246, https://doi.org/10.1016/0022-3115(92)90503-D.

[16] G.S. Was, J.P. Wharry, B. Frisbie, B.D. Wirth, D. Morgan, J.D. Tucker, T.R. Allen, Assessment of radiation-induced segregation mechanisms in austenitic and ferritic–martensitic alloys, J. Nucl. Mater. 411 (2011) 41–50, https://doi.org/10.1016/j.jnucmat.2011.01.031.

[17] R. Schäublin, B. Décamps, A. Prokhodtseva, J.F. Löffler, On the origin of primary 1/2 a0 <111> and a0 <100> loops in irradiated Fe(Cr) alloys, Acta Mater. 133 (2017) 427–439, https://doi.org/10.1016/j.actamat.2017.02.041.

[18] L. Malerba, M.J. Caturla, E. Gaganidze, C. Kaden, M.J. Konstantinović, P. Olsson, C. Robertson, D. Rodney, A.M. Ruiz-Moreno, M. Serrano, J. Aktaa, N. Anento, S. Austin, A. Bakaev, J.P. Balbuena, F. Bergner, F. Boioli, M. Boleininger, G. Bonny, N. Castin, J.B.J. Chapman, P. Chekhonin, M. Clozel, B. Devincre, L. Dupuy, G. Diego, S.L. Dudarev, C.-C. Fu, R. Gatti, L. Gélébart, B. Gómez-Ferrer, D. Gonçalves, C. Guerrero, P.M. Gueye, P. Hähner, S.P. Hannula, Q. Hayat, M. Hernández-Mayoral, J. Jagielski, N. Jennett, F. Jiménez, G. Kapoor, A. Kraych, T. Khvan, L. Kurpaska, A. Kuronen, N. Kvashin, O. Libera, P.-W. Ma, T. Manninen, M.-C. Marinica, S. Merino, E. Meslin, F. Mompiou, F. Mota, H. Namburi, C.J. Ortiz, C. Pareige, M. Prester, R.R. Rajakrishnan, M. Sauzay, A. Serra, I. Simonovski, F. Soisson, P. Spätig, D. Tanguy, D. Terentyev, M. Trebala, M. Trochet, A. Ulbricht, M. Vallet, K. Vogel, T. Yalcinkaya, J. Zhao, Multiscale modelling for fusion and fission materials: the M4F project, Nucl. Mater. Energy 29 (2021) 101051, https://doi.org/10.1016/j.nme.2021.101051.

[19] D.J. Bacon, Y.N. Osetsky, Multiscale modelling of radiation damage in metals: from defect generation to material properties, Mater. Sci. Eng. A 365 (2004) 46–56, https://doi.org/10.1016/j.msea.2003.09.006.

[20] C.S. Becquart, C. Domain, Modeling microstructure and irradiation effects, Metall. Mater. Trans. A 42 (2011) 852–870, https://doi.org/10.1007/s11661-010-0460-7.

[21] L. Malerba, N. Anento, J.P. Balbuena, C.S. Becquart, N. Castin, M.J. Caturla, C. Domain, C. Guerrero, C.J. Ortiz, B. Pannier, A. Serra, Physical mechanisms and parameters for models of microstructure evolution under irradiation in Fe alloys – Part I: Pure Fe, Nucl. Mater. Energy 29 (2021) 101069, https://doi.org/10.1016/j.nme.2021.101069.

[22] C. Domain, C.S. Becquart, L. Malerba, Simulation of radiation damage in Fe alloys: an object kinetic Monte Carlo approach, J. Nucl. Mater. 335 (2004) 121–145, https://doi.org/10.1016/j.jnucmat.2004.07.037.

[23] M.J. Caturla, M.J. Aliaga, I. Martin-Bragado, I. Dopico, L. Malerba, M. Hernandez-Mayoral, Microstructure Evolution in Fe and Fe-Cr Alloys with OKMC Methods, EPJ Web Conf. 115 (2016) 03001, https://doi.org/10.1051/epjconf/201611503001.

[24] D.R. Mason, X. Yi, M.A. Kirk, S.L. Dudarev, Elastic trapping of dislocation loops in cascades in ion-irradiated tungsten foils, J. Phys. Condens. Matter 26 (2014) 375701, https://doi.org/10.1088/0953-8984/26/37/375701.

[25] T.S. Hudson *, S.L. Dudarev, M.-J. Caturla, A.P. Sutton, Effects of elastic interactions on post-cascade radiation damage evolution in kinetic Monte Carlo simulations, Philos. Mag. 85 (2005) 661–675, https://doi.org/10.1080/14786430412331320026.

[26] L. Casillas-Trujillo, A.S. Ervin, L. Xu, A. Barashev, H. Xu, Dynamics of interaction between dislocations and point defects in bcc iron, Phys. Rev. Mater. 2 (2018) 103604, https://doi.org/10.1103/PhysRevMaterials.2.103604.

[27] A. Chartier, C. Meis, J.-P. Crocombette, L.R. Corrales, W.J. Weber, Atomistic modeling of displacement cascades in ${\mathrm{La}}_{2}{\mathrm{Zr}}_{2}{\mathrm{O}}_{7}$ pyrochlore, Phys. Rev. B 67 (2003) 174102, https://doi.org/10.1103/PhysRevB.67.174102.

[28] S.J. Zinkle, B.N. Singh, Analysis of displacement damage and defect production under cascade damage conditions, J. Nucl. Mater. 199 (1993) 173–191, https://doi.org/10.1016/0022-3115(93)90140-T.

[29] J. Byggmästar, F. Granberg, A.E. Sand, A. Pirttikoski, R. Alexander, M.-C. Marinica, K. Nordlund, Collision cascades overlapping with self-interstitial defect clusters in Fe and W, J. Phys. Condens. Matter 31 (2019) 245402, https://doi.org/10.1088/1361-648X/ab0682.

[30] F. Granberg, J. Byggmästar, K. Nordlund, Molecular dynamics simulations of high-dose damage production and defect evolution in tungsten, J. Nucl. Mater. 556 (2021) 153158, https://doi.org/10.1016/j.jnucmat.2021.153158.

[31] G.S. Was, The Damage Cascade, in: Fundamentals of Radiation Materials Science, Springer, Berlin, Heidelberg, 2017, pp. 131–165, https://doi.org/10.1007/978-1-4939-3438-6_3.

[32] D.J. Bacon, A.F. Calder, F. Gao, V.G. Kapinos, S.J. Wooding, Computer simulation of defect production by displacement cascades in metals, Nucl. Instrum. Methods Phys. Res. Sect. B Beam Interact. Mater. at. 102 (1995) 37–46, https://doi.org/10.1016/0168-583X(95)80114-2.

[33] P.M. Derlet, S.L. Dudarev, Microscopic structure of a heavily irradiated material, Phys. Rev. Mater. 4 (2020) 023605, https://doi.org/10.1103/PhysRevMaterials.4.023605.

[34] A.E. Sand, J. Dequeker, C.S. Becquart, C. Domain, K. Nordlund, Non-equilibrium properties of interatomic potentials in cascade simulations in tungsten, J. Nucl. Mater. 470 (2016) 119–127, https://doi.org/10.1016/j.jnucmat.2015.12.012.

[35] C.P. Race, D.R. Mason, M.W. Finnis, W.M.C. Foulkes, A.P. Horsfield, A.P. Sutton, The treatment of electronic excitations in atomistic models of radiation damage in metals, Rep. Prog. Phys. 73 (2010) 116501, https://doi.org/10.1088/0034-4885/73/11/116501.

[36] A.E. Sand, S.L. Dudarev, K. Nordlund, High-energy collision cascades in tungsten: Dislocation loops structure and clustering scaling laws, Europhys. Lett. 103 (2013) 46003, https://doi.org/10.1209/0295-5075/103/46003.

[37] Y. Limoge, A. Rahman, H. Hsieh, S. Yip, Computer simulation studies of radiation induced amorphization, J. Non-Cryst. Solids 99 (1988) 75–88, https://doi.org/10.1016/0022-3093(88)90459-0.

[38] E. Mansouri, P. Olsson, Microstructure and magnetization evolution in bcc iron via direct first-principles predictions of radiation effects, Phys. Rev. Mater. 7 (2023) 123604, https://doi.org/10.1103/PhysRevMaterials.7.123604.

[39] A. Chartier, M.-C. Marinica, Rearrangement of interstitial defects in alpha-Fe under extreme condition, Acta Mater. 180 (2019) 141–148, https://doi.org/10.1016/j.actamat.2019.09.007.

[40] D.J. Bacon, F. Gao, Y.N. Osetsky, The primary damage state in fcc, bcc and hcp metals as seen in molecular dynamics simulations, J. Nucl. Mater. 276 (2000) 1–12, https://doi.org/10.1016/S0022-3115(99)00165-8.

[41] F. Gao, D.J. Bacon, Y.N. Osetsky, P.E.J. Flewitt, T.A. Lewis, Properties and evolution of sessile interstitial clusters produced by displacement cascades in α-iron, J. Nucl. Mater. 276 (2000) 213–220, https://doi.org/10.1016/S0022-3115(99)00180-4.

[42] M.-C. Marinica, F. Willaime, J.-P. Crocombette, Irradiation-Induced Formation of Nanocrystallites with $C15$ Laves Phase Structure in bcc Iron, Phys. Rev. Lett. 108 (2012) 025501, https://doi.org/10.1103/PhysRevLett.108.025501.

[43] L. Dézerald, M.-C. Marinica, L. Ventelon, D. Rodney, F. Willaime, Stability of self-interstitial clusters with C15 Laves phase structure in iron, J. Nucl. Mater. 449 (2014) 219–224, https://doi.org/10.1016/j.jnucmat.2014.02.012.

[44] M.I. Mendelev, S. Han, D.J. Srolovitz, G.J. Ackland, D.Y. Sun, M. Asta, Development of new interatomic potentials appropriate for crystalline and liquid iron, Philos. Mag. 83 (2003) 3977–3994, https://doi.org/10.1080/14786430310001613264.

[45] L. Malerba, M.C. Marinica, N. Anento, C. Björkas, H. Nguyen, C. Domain, F. Djurabekova, P. Olsson, K. Nordlund, A. Serra, D. Terentyev, F. Willaime, C. S. Becquart, Comparison of empirical interatomic potentials for iron applied to radiation damage studies, J. Nucl. Mater. 406 (2010) 19–38, https://doi.org/10.1016/j.jnucmat.2010.05.017.

[46] S. Wang, W. Guo, T. Schwarz-Selinger, Y. Yuan, L. Ge, L. Cheng, X. Zhang, X. Cao, E. Fu, G.-H. Lu, Dynamic equilibrium of displacement damage defects in heavy-ion irradiated tungsten, Acta Mater. 244 (2023) 118578, https://doi.org/10.1016/j.actamat.2022.118578.

[47] G. Varnavides, S. Ribet, R. Yalisove, J. Moore, C. Ophus, M.C. Scott, Simultaneous Electrostatic and Magnetic Vector Potential Phase Retrieval Using Electron Ptychography, Microsc. Microanal. 29 (2023) 278–279, https://doi.org/10.1093/micmic/ozad067.128.

[48] T. Harte, G.D. Bruce, J. Keeling, D. Cassettari, Conjugate gradient minimisation approach to generating holographic traps for ultracold atoms, Opt. Express 22 (2014) 26548–26558, https://doi.org/10.1364/OE.22.026548.
[49] K. Binder, J. Horbach, W. Kob, W. Paul, F. Varnik, Molecular dynamics simulations, J. Phys. Condens. Matter 16 (2004) S429, https://doi.org/10.1088/0953-8984/16/5/006.
[50] A.P. Thompson, H.M. Aktulga, R. Berger, D.S. Bolintineanu, W.M. Brown, P. S. Crozier, P.J. in 't Veld, A. Kohlmeyer, S.G. Moore, T.D. Nguyen, R. Shan, M. J. Stevens, J. Tranchida, C. Trott, S.J. Plimpton, LAMMPS - a flexible simulation tool for particle-based materials modeling at the atomic, meso, and continuum scales, Comput. Phys. Commun. 271 (2022) 108171, https://doi.org/10.1016/j.cpc.2021.108171.
[51] D.V. Schroeder, An introduction to thermal physics, 17th edition,, Addison Wesley, Francisco, CA, 2000.
[52] G. Bonny, R.C. Pasianot, D. Terentyev, L. Malerba, Iron chromium potential to model high-chromium ferritic alloys, Philos. Mag. 91 (2011) 1724–1746, https://doi.org/10.1080/14786435.2010.545780.
[53] K. Nordlund, N. Runeberg, D. Sundholm, Repulsive interatomic potentials calculated using Hartree-Fock and density-functional theory methods, Nucl. Instrum. Methods Phys. Res. Sect. B Beam Interact. Mater. At. 132 (1997) 45–54, https://doi.org/10.1016/S0168-583X(97)00447-3.
[54] J. Proakis, Probability, random variables and stochastic processes, IEEE Trans. Acoust. Speech Signal Process. 33 (1985) 1637, https://doi.org/10.1109/TASSP.1985.1164715.
[55] A. Stukowski, Visualization and analysis of atomistic simulation data with OVITO–the Open Visualization Tool, Model. Simul. Mater. Sci. Eng. 18 (2009) 015012, https://doi.org/10.1088/0965-0393/18/1/015012.
[56] D. Terentyev, C. Lagerstedt, P. Olsson, K. Nordlund, J. Wallenius, C.S. Becquart, L. Malerba, Effect of the interatomic potential on the features of displacement cascades in α-Fe: A molecular dynamics study, J. Nucl. Mater. 351 (2006) 65–77, https://doi.org/10.1016/j.jnucmat.2006.02.020.
[57] C. Björkas, K. Nordlund, Comparative study of cascade damage in Fe simulated with recent potentials, Nucl. Instrum. Methods Phys. Res. Sect. B Beam Interact. Mater. At. 259 (2007) 853–860, https://doi.org/10.1016/j.nimb.2007.03.076.
[58] A. Stukowski, K. Albe, Extracting dislocations and non-dislocation crystal defects from atomistic simulation data, Model. Simul. Mater. Sci. Eng. 18 (2010) 085001, https://doi.org/10.1088/0965-0393/18/8/085001.
[59] P.M. Larsen, S. Schmidt, J. Schiøtz, Robust structural identification via polyhedral template matching, Model. Simul. Mater. Sci. Eng. 24 (2016) 055007, https://doi.org/10.1088/0965-0393/24/5/055007.
[60] G.J. Ackland, M.I. Mendelev, D.J. Srolovitz, S. Han, A.V. Barashev, Development of an interatomic potential for phosphorus impurities in α-iron, J. Phys. Condens. Matter 16 (2004) S2629, https://doi.org/10.1088/0953-8984/16/27/003.
[61] F. Willaime, C.C. Fu, M.C. Marinica, J. Dalla Torre, Stability and mobility of self-interstitials and small interstitial clusters in α-iron: ab initio and empirical potential calculations, Nucl. Instrum. Methods Phys. Res. Sect. B Beam Interact. Mater. At. 228 (2005) 92–99, https://doi.org/10.1016/j.nimb.2004.10.028.
[62] R. Alexander, M.-C. Marinica, L. Proville, F. Willaime, K. Arakawa, M.R. Gilbert, S. L. Dudarev, Ab initio scaling laws for the formation energy of nanosized interstitial defect clusters in iron, tungsten, and vanadium, Phys. Rev. B 94 (2016) 024103, https://doi.org/10.1103/PhysRevB.94.024103.
[63] A. Prokhodtseva, B. Décamps, A. Ramar, R. Schäublin, Impact of He and Cr on defect accumulation in ion-irradiated ultrahigh-purity Fe(Cr) alloys, Acta Mater. 61 (2013) 6958–6971, https://doi.org/10.1016/j.actamat.2013.08.007.
[64] M. Boleininger, D.R. Mason, A.E. Sand, S.L. Dudarev, Microstructure of a heavily irradiated metal exposed to a spectrum of atomic recoils, Sci. Rep. 13 (2023) 1684, https://doi.org/10.1038/s41598-022-27087-w.
[65] F.M. Dekking, C. Kraaikamp, H.P. Lopuhaä, L.E. Meester, A Modern Introduction to Probability and Statistics: Understanding Why and How, Springer, London, 2010. https://link.springer.com/book/10.1007/1-84628-168-7 (accessed November 5, 2023.

Paper III

First-principles predictions of structural and magnetic phase stability in irradiated α-Fe

E. Mansouri and P. Olsson
Materials Research Letters 12, 477-483 (2024)

Materials Research Letters

ISSN: (Print) (Online) Journal homepage: www.tandfonline.com/journals/tmrl20

First-principles predictions of structural and magnetic phase stability in irradiated α-Fe

Ebrahim Mansouri & Pär Olsson

To cite this article: Ebrahim Mansouri & Pär Olsson (2024) First-principles predictions of structural and magnetic phase stability in irradiated α-Fe, Materials Research Letters, 12:7, 477-483, DOI: 10.1080/21663831.2024.2347305

To link to this article: https://doi.org/10.1080/21663831.2024.2347305

Published online: 10 May 2024.

MATER. RES. LETT.
2024, VOL. 12, NO. 7, 477–483
https://doi.org/10.1080/21663831.2024.2347305

MATERIALS RESEARCH LETTERS
Taylor & Francis
Taylor & Francis Group

ORIGINAL REPORTS

First-principles predictions of structural and magnetic phase stability in irradiated α-Fe

Ebrahim Mansouri and Pär Olsson

Nuclear Science and Engineering, KTH Royal Institute of Technology, Stockholm, Sweden

ABSTRACT

We here use density functional theory and the creation-relaxation algorithm to investigate the appearance of polymorphism in α-Fe, driven by irradiation-induced microstructural changes. Local constriction leads to magnetic instability and provides excess energy required for structural phase transformation. Under extreme conditions, α-Fe undergoes local transformations into icosahedral C15 Laves phase with highly close-packed stacking and internal short-range ferromagnetic ordering, antiparallel to the bulk magnetisation. Analysing local magnetic moments and atomic volumes, in conjunction with the magneto-volume relations of different Fe structures, suggests two other alternatives for local phase transformation under irradiation conditions: the double-layer antiferromagnetic γ-Fe and non-magnetic ϵ-Fe.

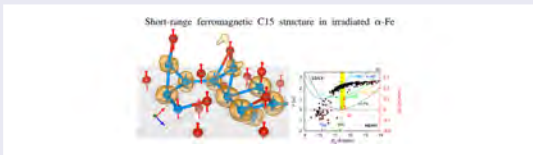

IMPACT STATEMENT

This work predicts the formation of icosahedral C15 Laves phase structure with short-range ferromagnetic order in irradiated α-Fe using dynamic first-principles calculations. This finding suggests potential detection through advanced magnetic-based transmission electron microscopy techniques, with implications for understanding radiation damage in structural materials.

ARTICLE HISTORY
Received 6 February 2024

KEYWORDS
Density functional theory; short-range ferromagnetic ordering; C15 Laves phase; polymorphism

1. Introduction

Iron undergoes several structural and magnetic phase transformations activated by temperature and/or pressure changes [1]. At ambient pressure, iron exhibits two primary crystal structures. In the ground state, the most stable form of iron is body-centred cubic (bcc) α-phase, and it demonstrates ferromagnetic (FM) ordering up to its Curie temperature of 1041 K [2]. By increasing temperature to 1184 K and at standard pressure, the α-phase transforms into the second form, i.e. the face-centred cubic (fcc) γ-phase, and it stabilises up to 1665 K. Within its stability range, the γ-phase exhibits paramagnetism, although theoretical studies reveal that its ground state is antiferromagnetic (AF) [3–5] at low temperature, far below its stability range. This AF ground state has been shown through low-temperature Mössbauer experiment [6] conducted on γ-phase precipitates in Cu [7] and CuAl [8], as well as on γ-phase thin films grown on Cu_3Au [9], confirming the predictions derived from first-principles calculations [4]. Furthermore, subjecting Fe films to cryogenic self-ion irradiation has been observed to bring about alterations in both structure and magnetism [10,11].

Additionally, according to first-principles predictions [5], γ-Fe not only exhibits the conventional AF ordering with alternating layers of up and down spin arrangements but also features an alternative AF state known as the double-layer antiferromagnetic (AFD) state. In this AFD state, there is a doubling of intra-layer coupling of short-range FM order, resulting in twice the number of parallel-aligned spins among nearest neighbours compared to the regular AF structure, as suggested by Herper *et al.* [5]. The AFD state demonstrates a higher μ of approximately 38% and a slightly larger equilibrium volume of about 3% compared to the regular AF state, aligning more closely with experimental observations of

CONTACT Ebrahim Mansouri mansouri.ebrahim@yahoo.com; Pär Olsson polsson@kth.se

the γ-phase [5,7]. The short-range FM coupling inherent in the AFD state plays a crucial role in explaining the anti-Invar effect in iron, providing additional experimental support for the existence of the AFD state in nature [5].

Under high pressures, iron can also adopt a hexagonal close-packed (hcp) ϵ-phase as a third form [12]. The experimental measurements of Mössbauer experiments on ϵ-Fe prove that no magnetic ordering occurs at low temperatures (T = 0.03 K) and pressures up to 21 GPa [13].

The existence of such multi-crystallographic states is a common phenomenon among elements and is known as polymorphism [14]. Therefore, investigating the polymorphism of iron under extreme conditions, particularly understanding the factors that stabilise its various forms under irradiation, is crucial for fundamental physics, and this letter addresses this inquiry from multiple perspectives. Theoretical investigations through comprehensive total energy calculations, including band energy analysis and examination of the density of states (DOS), offer valuable insights into the structural stability and magnetic phase of irradiated systems. By examining the total energy landscape and electronic structure, these calculations provide a basis for predicting the stable crystal structures and elucidating the magnetic behavior of the system under irradiation.

2. Methodology

In this letter, we applied electronic structure calculations in the framework of density functional theory (DFT) in order to illustrate the potential occurrence of polymorphism in an irradiated α-Fe. Drawing from our recent DFT-driven creation-relaxation algorithm (CRA) calculations [15], we demonstrated that, in low-energy and low-temperature irradiation conditions, α-Fe undergoes a transformation into locally formed icosahedral Laves phase structures, specifically the C15-type cluster. Furthermore, we observed that the constituent atoms in these C15-type clusters were in antiparallel alignment with the host bcc lattice atoms while locally exhibiting spontaneous short-range FM characteristics. Our supplementary analysis in this study suggests alternative possibilities, including the possible formation of the non-magnetic (NM) ϵ-phase and AFD γ-phase, induced by irradiation in α-Fe.

The details of the *ab initio* calculation for this study can be found in [15]. Moreover, for obtaining the equation of states and energy minimisation of the cubic structures like α-Fe and γ-Fe, we employed a conventional lattice structure with $11 \times 11 \times 11$ k-mesh sampling, while close-packed structures (i.e. ϵ-Fe and hypothetical icosahedral C15 structures) and body-centred tetragonal[1] AFD γ-Fe were treated with slightly smaller k-meshes ($11 \times 11 \times 9$), particularly in the c-axis directions. Other simulation criteria, e.g. cut-off energy of 350 eV and 0.1 meV energy minimisation convergence, remained consistent with the full volume relaxation calculations in [15].

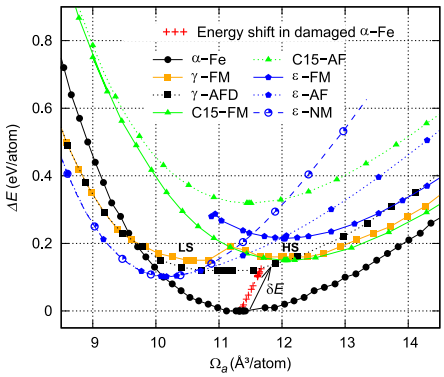

Figure 1. Equations of state representing distinct iron structures with diverse magnetic ordering. The arrow denotes the energy shift observed in the damaged α-Fe structure up to an irradiation dose of 0.35 dpa. To interpret the colour references in this figure legend, the reader is referred to the web version of the article.

3. Results and discussion

As shown in Figure 1, the total energies relative to the ground state energy of α-Fe are plotted as a function of the atomic volume (Ω_a) for various structures and magnetic states. Furthermore, we incorporated the average irradiation-induced energy (δE) accumulated in the damaged structure, i.e. 97.5 meV as determined in our recent DFT-CRA calculations [15] for an irradiation dose of 0.35 displacements per atom (dpa). This inclusion facilitates a comprehensive comparison with equation-of-state curves and allows for the prediction of potential phase transformations in damaged α-Fe. The calculated δE corresponds to 1131 K according to the energy-temperature equation ($E = k_B.T$), a magnitude sufficient to induce possible phase transformations, particularly those from FM α-phase to AFD γ-phase or to NM ϵ-phase.

Referring to Figure 1, the formation of new structures with diverse magnetic states in Fe strongly depends on the Ω_a and packing factor of the constituent atoms, as noted elsewhere [5,16–18]. Specifically, the energetics

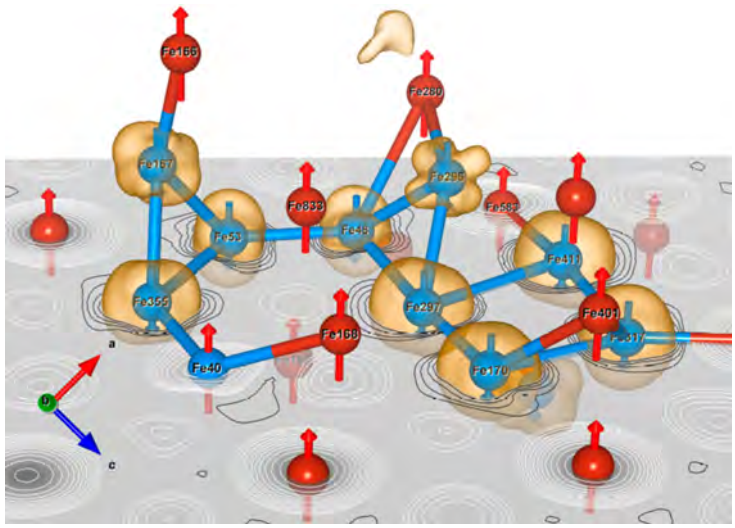

Figure 2. The formation of the short-range FM C15 Laves phase structure (blue atoms) among locally close-packed structure and bcc lattice atoms (red atoms) extracted from DFT-CRA calculation. The orange clouds, enveloping atoms with spin-down orientation (blue arrows), represent the three-dimensional spin density isosurfaces of atoms underwent spin flip or quench. Red arrows symbolize the spin-up orientations, while the white and black elliptical lines represent the logarithmic positive and negative drawing contours, respectively. For colour references, the reader is referred to the web version of the article.

of Fe indicate that for the lowest possible Ω_a of 10.2 Å^3/atom, the energetically most stable structure is NM ϵ-phase, as also experimentally reported under high pressure [13]. Whereas for the greater Ω_a of about 12.2 Å^3/atom, the two metastable states are either the high-spin (HS)[2] FM γ-phase or the hypothetical FM C15 Laves phase structure according to energetics of iron from our DFT calculations.

It is worth noting that the C15 Laves phase should be considered as a short-range ordered structure according to topological short-range order theory [12], rather than a long-range lattice structure. That is, within an irradiated structure, the irradiation-induced isolated self-interstitial atoms initially accumulate to form short-range order icosahedral clusters [15], as also demonstrated in Figure 2.

Therefore, for small interstitial clusters, there is necessarily no need to construct long-range lattice structure. Instead, the energetically most favorable configuration for the aggregation of self-interstitial atoms is expected to be the three-dimensional icosahedral C15 structure, among other possible cluster configurations, as previously demonstrated by Marinica *et al.* [19]. Additionally, in complete agreement with other first-principles studies [18,19], our DFT-CRA calculations also revealed energy relaxation of up to 6 eV once the C15-type structures (e.g. clusters of triangular or hexagonal di-interstitial rings) are formed, compared to the conditions with the same number of isolated self-interstitial defects. It is noteworthy that further increasing the size of the atomic icosahedral cluster leads to strong distortions and accompanying strains, therefore, the icosahedral structure will eventually, as it grows, become unstable and transform into other forms of extended defects such as 1/2⟨111⟩ or ⟨100⟩ dislocation loops in damaged α-Fe [20,21].

Figure 2 shows an example of a locally formed short-range FM C15 cluster (blue atoms) obtained from our first-principles DFT-CRA calculations at an irradiation dose of 0.22 dpa, accompanied by respective atomic site indices. As seen, although the constituent atoms of the imperfect C15 cluster antiferromagnetically align with host atoms of the α-phase (red atoms), they are internally coupled with a short-range FM ordering. This short-range FM ordering is visualized through the three-dimensional spin density map isosurfaces (orange clouds) surrounding the C15-type atoms among other close-packed or bcc lattice atoms. The C15-type atoms undergo reductions in their Ω_a, leading to increased atomic forces and pressure. Consequently, they exhibit spin flip or quench and stabilise at an average

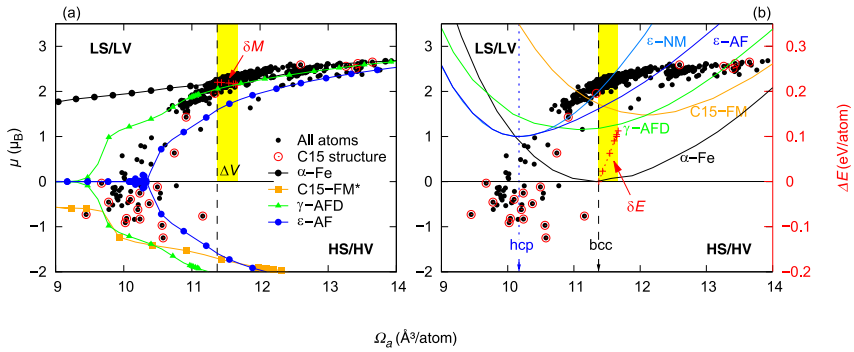

Figure 3. Distribution of local μ of 1024 Fe atoms in relation to their local Ω_a at 0.22 dpa. The μ – Ω_a data points are compared with (a) magneto-volume relations in different iron structures and (b) energetics of iron in various magnetic states with respect to the α-Fe ground state energy. The black-dashed line separates LS/LV and HS/HV regions, emphasizing deviations in local μ and Ω_a of the atoms in the damaged α-Fe compared to the undamaged bcc structure. The blue-dotted line on the right panel shows the equilibrium atomic volume of NM/AF hcp structure, while yellow-shaded regions depicts volume expansion (ΔV) in irradiated Fe. *In the left panel (a), the magneto-volume curve for the C15-FM structure is multiplied by −1 for better comparison with the irradiated α-Fe, indicating antiparallel spin orientation with respect to the host bcc lattice atoms. For colour references, the reader is referred to the web version of the article.

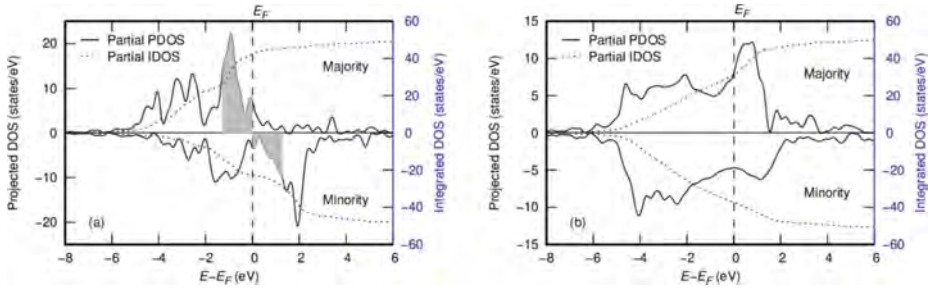

Figure 4. The comparison of partial PDOS and IDOS of C15-type atoms before and after irradiation: (a) illustration of transferred charge from majority into minority state before irradiation and (b) established partial DOS of atoms forming the imperfect C15 Laves phase structure after irradiation. The vertical dashed lines show the Fermi energy levels, set at $E_F = 0$.

μ of -0.7 μ_B, suggests a potential for detection using advanced magnetic-induced mapping technique coupled with transmission electron microscopy [22].

To examine more possible magnetic and/or structural phase transformation in the damaged α-Fe, we plotted the distribution of the local μ of all 1024 constituent atoms relative to respective local Voronoi polyhedral cell volumes (i.e. Ω_a) in Figure 3, corresponding to the irradiation dose of 0.22 dpa. Furthermore, to provide a thorough understanding of the potential irradiation-induced magnetic and structural phase changes, the magneto-volume relations (Figure 3(a)) and energetics (Figure 3(b)) of iron have been incorporated with the distribution of moment-volume (μ – Ω_a) data points of damaged lattice atoms.

In addition, to interpreter the correlations between atomic volume, magnetic moment and potential phase transformation in defected α-Fe, the plots are partitioned by vertical dashed lines in Figure 3(a) and (b), highlighting the high-spin/high-volume (HS/HV) and low-spin/low-volume (LS/LV) regions. These regions are referenced against the $\Omega_a = 11.37$ Å^3/atom and local $\mu = 2.2$ μ_B of an iron atom in a typical pristine α-Fe lattice. The yellow-shaded regions in Figure 3 also represent the predicted irradiation-induced volume expansion (ΔV) of about 2.2%, which has been reported in our recent study [15].

As seen in Figure 1, the increase in total energy ($\delta E = 97.5$ meV/atom) of the irradiated Fe is sufficiently high to thermodynamically initiate the FM α-phase

to AFD γ-phase or NM/FM ϵ-phase transformations. Significantly, the irradiated α-Fe undergoes an average reduction in total magnetisation (δM) by $-0.043\ \mu_B$/atom within the expanded volume of ΔV, as illustrated in Figure 3(a) and reported in [15]. This reduction intersects with the magneto-volume relation of the AFD γ-phase, emphasizing the potential transformation from α to γ induced by irradiation.

Furthermore, within the HS/HV region depicted in Figure 3(a), the distribution of $\mu - \Omega_a$ data aligns with the magneto-volume relation of the bcc structure. This observation suggests that, under irradiation conditions, the majority of the system retains its crystal structure, albeit with the formation and clustering of vacancies, as also demonstrated experimentally under cryogenic irradiation conditions [10]. Consequently, the local magnetic moments near vacant sites experience slight increases, asymptotically approaching the moment of a free Fe atom. In contrast, the LS/LV region exhibits a notable departure in the local moments from the magneto-volume relation of the bcc structure to those of highly close-packed structures such as FM-C15, AFD fcc, and even NM/AF hcp. To further substantiate this conclusion, a detailed examination involves comparing the equation of states of those aforementioned structures are compared with the $\mu - \Omega_a$ data distribution, as indicated in Figure 3(b).

As shown in Figure 3(a) and (b), the DFT-CRA model causes a rearrangement of atoms in the LS/LV region, resulting in a localized reduction in Ω_a. This leads to the formation of diverse stress fields around displaced atoms, consequently quenching their local moments. The spontaneous spins of atoms experiencing reductions in interatomic spacing are distributed between 1 and $-1\ \mu_B$, indicative of a potential AF ordering with a high packing density. Notably, certain atoms lose their local spins, resulting in their magnetic moments being distributed along or close to the horizontal line of $\mu = 0$. This behavior signifies a highly close-packed non-magnetic configuration similar to NM ϵ-Fe, as one can realize from Figure 3(a).

The formation of NM or even AF ϵ-Fe, as suggested by our DFT-CRA calculations, aligns seamlessly with the energetic considerations for NM and AF ϵ-Fe, as illustrated in Figure 3(b). Indeed, the clustering of $\mu - \Omega_a$ data points around a vertical blue-dotted line, representing the ground state of the NM/AF hcp phase, reinforces the evidence for the influence of this close-packed structure in irradiated bcc Fe.

As mentioned earlier, the first-principles prediction of irradiation-induced phase transformation from bcc to NM hcp under increased pressure is expected and experimentally demonstrated by x-ray magnetic circular dichroism spectroscopy [23,24]. This transformation is attributed to a reduction in interatomic distance, leading to an overlap between the 3*d*-state and 4*s*-state bands and inducing the delocalization of 3*d* electrons by lowering the DOS at Fermi energy (E_F) and weakening the condition for FM ordering [25,26].

Referring to Figure 3, an intriguing observation within the constrained atomic volume range ($9.5 < \Omega_a < 10.5$) reveals that C15-type atoms (depicted by data points enclosed within red circles) distinctly exhibit FM ordering. Clearly, these FM-ordered C15-type atoms demonstrate antiferromagnetic alignment with the host bcc lattice atoms (depicted as black circles).

A more in-depth analysis of the partial projected DOS (PDOS) for the atoms forming the C15 cluster (as shown in Figure 2) before and after irradiation unveils a charge transfer phenomenon. Specifically, as depicted in Figure 4, there is a charge transfer from majority states below the E_F into unoccupied minority states above it when the atom is moved into a constrained environment. As mentioned, by comparing the partial integrated DOS (IDOS), this charge transfer results in a reduction of the DOS at E_F by 26%, weakening the FM ordering, manifested by the upward shift of E_F to higher energy levels by approximately 1.3 eV (as illustrated in Figure 4(a)). Qualitatively, the transferred charge is schematically represented by the shaded area in the partial PDOS of the atoms in the undamaged structure (Figure 4(a)), which later form the C15 cluster following irradiation (Figure 4(b)).

4. Conclusions

In summary, our investigation, employing electronic structure calculations within the DFT framework, sheds light on the potential polymorphic transformations occurring in irradiated α-Fe. The extensive DFT-driven CRA simulations for modeling low-energy, low-temperature irradiation without thermally activated diffusion, unveil a noteworthy transformation leading to the emergence of locally formed icosahedral Laves phase structures, specifically in the form of C15-type clusters. Within this localized structure, constituent atoms exhibit antiferromagnetic orientation in relation to the host bcc lattice atoms, while displaying spontaneous short-range ferromagnetic characteristics. This dualistic magnetic behavior adds a layer of complexity to the understanding of the structural and magnetic responses of α-Fe under irradiation. Moreover, our study elucidates the impact of irradiation-induced pressure on the system, revealing the possibility of NM ϵ-phase formation with a highly close-packed structure. Concurrently, the emergence of the AFD γ-phase is anticipated from the average increase

in total energy and decrease in magnetisation of the irradiated α-Fe, respectively.

The transformations observed in the LS/LV regions result from a reduction in atomic volume, leading to the delocalization of 3d electrons at the Fermi level due to the overlapping of 3d and 4s bands. Consequently, the distinctive characteristics of the irradiation-induced polymorphism, such as spin–flip or quenching magnetisation traits, stabilise the local magnetic moment of the C15 cluster at approximately $-0.7\ \mu_B$. This suggests a remarkable potential for experimentally detecting C15 Laves phase structures using advanced magnetic-induced mapping techniques when coupled with transmission electron microscopy.

Notes

1. We selected the body-centred tetragonal cell with a ratio of $c/a = 2\sqrt{2}$ to represent the AFD structure, comprising two consecutive layers with up- and down-spin orientations. This choice, as described by Herper *et al.* [5], describes the short-range order FM within an antiferromagnetic ordering [5].
2. Depending on the Ω_a, γ-Fe exhibits two FM states. In small atomic volume, it has an unstable low-spin (LS) state with respect to AF states. The second form is associated with a high-spin (HS) state, which gains stability over AF state at expanded volumes [5].

Acknowledgments

Financial support was provided by the Swedish Foundation for Strategic Research (SSF) under grant number ARC19-0043 (SUNRISE centre) and the Swedish Research Council (VR) for projects 2017-06458 and 2019-04156. The work was also affiliated with the EUROfusion Consortium, funded by the European Union under Grant Agreement No 101052200. Additional funding was received from the Euratom Research and Training Programme under grant agreements No 755039 (M4F project) and No 740415 (IL TROVATORE project) during 2019–2020. The authors acknowledge computational resources from the Swedish National Infrastructure for Computing (SNIC; PDC at KTH and NSC at LiU) and CINECA HPC Center in Italy. The views expressed are solely those of the authors and do not necessarily represent the views of the European Union or the European Commission, which cannot be held responsible for them.

Disclosure statement

No potential conflict of interest was reported by the author(s).

Funding

This work was supported by European Union: [Grant Number 101052200]; Swedish Foundation for Strategic Research (SSF): [Grant Number ARC19-0043]; SUNRISE centre, Swedish Research Council (VR): [Grant Number 2017-06458].

ORCID

Ebrahim Mansouri https://orcid.org/0000-0001-8884-5267
Pär Olsson https://orcid.org/0000-0002-2381-3309

References

[1] Acet M, Zähres H, Wassermann EF, et al. High-temperature moment-volume instability and anti-Invar of γ-Fe. Phys Rev B. 1994;49:6012–6017. doi:10.1103/PhysRevB.49.6012
[2] Pepperhoff W, Acet M. The magnetism of iron. Constitution and magnetism of iron and its alloys [Internet]. Berlin, Heidelberg: Springer Berlin Heidelberg; 2001. p. 15–55. doi:10.1007/978-3-662-04345-5_2
[3] Moruzzi VL, Marcus PM, Kübler J. Magnetovolume instabilities and ferromagnetism versus antiferromagnetism in bulk fcc iron and manganese. Phys Rev B. 1989;39:6957–6961. doi:10.1103/PhysRevB.39.6957
[4] Uhl M, Sandratskii LM, Kübler J. Electronic and magnetic states of γ-Fe. J Magn Magn Mater. 1992;103:314–324. doi:10.1016/0304-8853(92)90202-Y
[5] Herper HC, Hoffmann E, Entel P. Ab initio full-potential study of the structural and magnetic phase stability of iron. Phys Rev B. 1999;60:3839–3848. doi:10.1103/PhysRevB.60.3839
[6] Vogl G, Schaefer A, Mansel W, et al. Mössbauer studies of low-temperature radiation damage in α-iron. Physica Status Solidi (b). 1973;59:107–120.
[7] Abrahams SC, Guttman L, Kasper JS. Neutron diffraction determination of antiferromagnetism in face-centered cubic (γ) iron. Phys Rev. 1962;127:2052–2055. doi:10.1103/PhysRev.127.2052
[8] Keune W, Ezawa T, Macedo WAA, et al. Magneto-volume effects in γ-Fe ultrathin films and small particles. Phys B. 1990;161:269–275. doi:10.1016/0921-4526(89)90147-6
[9] Carbone C, Sohal GS, Kisker E, et al. Spin-resolved photoemission from Fe3Pt(001) invar and γ-Fe films (invited). J Appl Phys. 1988;63:3499–3502. doi:10.1063/1.340722
[10] Papamihail K, Mergia K, Ott F, et al. Fe+ ion irradiation induced changes in structural and magnetic properties of iron films. Nucl Mater Energy. 2016;9:459–464. doi:10.1016/j.nme.2016.03.006
[11] Papamihail K, Mergia K, Ott F, et al. Magnetic effects induced by self-ion irradiation of Fe films. Phys Rev B. 2016;93:100404. doi:10.1103/PhysRevB.93.100404
[12] Pepperhoff W, Acet M. The structure of iron. Constitution and magnetism of iron and its alloys [Internet]. Berlin, Heidelberg: Springer Berlin Heidelberg; 2001. p. 1–13. doi:10.1007/978-3-662-04345-5_1
[13] Cort G, Taylor RD, Willis JO. Search for magnetism in hcp ϵ-Fe. J Appl Phys. 1982;53:2064–2065. doi:10.1063/1.330745
[14] Christian JW. Polymorphic changes. The theory of transformations in metals and alloys [Internet]. Oxford: Pergamon; 2002. p. 702–717. Available from: https://www.sciencedirect.com/science/article/pii/B9780080440194500209.
[15] Mansouri E, Olsson P. Microstructure and magnetization evolution in bcc iron via direct first-principles predictions of radiation effects. Phys Rev Mater. 2023;7:123604. doi:10.1103/PhysRevMaterials.7.123604

[16] Herper HC, Hoffmann E, Entel P. Ab initio investigations of iron-based martensitic systems. J Phys IV France. 1997;07:C5–76. doi:10.1051/jp4:1997511
[17] Domain C, Becquart CS. Ab initio calculations of defects in Fe and dilute Fe-Cu alloys. Phys Rev B. 2001;65:024103. doi:10.1103/PhysRevB.65.024103
[18] Dézerald L, Marinica M-C, Ventelon L, et al. Stability of self-interstitial clusters with C15 Laves phase structure in iron. J Nucl Mater. 2014;449:219–224. doi:10.1016/j.jnucmat.2014.02.012
[19] Marinica M-C, Willaime F, Crocombette J-P. Irradiation-Induced formation of nanocrystallites with $C15$ laves phase structure in bcc iron. Phys Rev Lett. 2012;108:025501. doi:10.1103/PhysRevLett.108.025501
[20] Chartier A, Marinica M-C. Rearrangement of interstitial defects in alpha-Fe under extreme condition. Acta Mater. 2019;180:141–148. doi:10.1016/j.actamat.2019.09.007
[21] Mansouri E, Olsson P. Modeling of irradiation-induced microstructure evolution in Fe: impact of Frenkel pair distribution. Comput Mater Sci. 2024;236:112852. doi:10.1016/j.commatsci.2024.112852
[22] Varnavides G, Ribet S, Yalisove R, et al. Simultaneous electrostatic and magnetic vector potential phase retrieval using Electron Ptychography. Microsc Microanal. 2023;29:278–279. doi:10.1093/micmic/ozad067.128
[23] Iota V, Klepeis J-HP, Yoo C-S, et al. Electronic structure and magnetism in compressed 3d transition metals. Appl Phys Lett. 2007;90:042505. doi:10.1063/1.2434184
[24] Barge NV, Boehler R. Effect of non-hydrostaticity on the α-ϵ transition of iron. High Press Res. 1990;6:133–140. doi:10.1080/08957959008203204
[25] Khmelevskyi S, Ruban AV, Mohn P. Electronic structure analysis of the pressure induced metamagnetic transition and magnetovolume anomaly in Fe3C—cementite. J Phys: Condens Matter. 2005;17:7345. doi:10.1088/0953-8984/17/46/018
[26] Ekman M, Sadigh B, Einarsdotter K, et al. Ab initio study of the martensitic bcc-hcp transformation in iron. Phys Rev B. 1998;58:5296–5304. doi:10.1103/PhysRevB.58.5296

Paper IV and Supplemental Material

***Ab initio* predictions of irradiation-induced imperfections in FeCr: alloying effects and magnetic ordering on C15 Laves phase stability**

E. Mansouri and P. Olsson
Submitted to Physical Review Letters

IV

Ab initio predictions of irradiation-induced imperfections in FeCr: alloying effects and magnetic ordering on C15 Laves phase stability

Ebrahim Mansouri[a, 1] and Pär Olsson[a, 2]

[a]*KTH Royal Institute of Technology, Nuclear Science and Engineering, Stockholm, Sweden*

Abstract

In the intricate interplay of atomic constituents, we uncover profound correlations that shape the non-linear magnetic properties of FeCr systems under irradiation. Our investigation unveils a striking relationship between the Cr content and the emergence of the swelling, a fundamental precursor to radiation-induced damage in FeCr alloys. Furthermore, we delve into the complex influence of alloying Cr content, shedding light on the formation and stabilization of C15 Laves phase clusters, offering crucial insights into the dynamics of these features under extreme conditions. Our findings not only deepen our understanding of the non-linear magnetic responses but also pave the way for advanced materials engineering with potential applications in nuclear environments.

I. Introduction

FeCr alloys hold a pivotal role in nuclear reactor technology due to their remarkable combination of properties [1,2]. The alloying of chromium in Fe-based alloys brings about several crucial improvements. FeCr alloys exhibit exceptional resistance to corrosion and oxidation [3], making them ideal candidates for structural materials within nuclear reactor technologies, where extreme environments can lead to material degradation [1]. The incorporation of Cr into Fe-based alloys demonstrably improves their resistance to high-temperature and high-radiation environments. Understanding the role of Cr content is of paramount importance in optimizing FeCr alloys for such applications. By tailoring the Cr content, the materials can be designed to better suit the demanding conditions within nuclear reactors, enhancing their overall efficiency and safety [2,4,5].

Furthermore, investigating radiation-induced damage and stability in relation to alloying effects is a critical aspect of materials science [6–8]. These alloying effects and correlated durability of Fe-based alloys can significantly impact the mechanical integrity and radiation tolerance of irradiated

1 Corresponding author: mansouri.ebrahim@yahoo.com
2 Corresponding author: polsson@kth.se

materials [9–12]. Thus, gaining insights into how the Cr content influences the development and stability of microstructure imperfections is essential for a fundamental understanding of material properties, ultimately contributing to the advancement and safety of structural materials used in nuclear reactors.

Investigating irradiation-induced degradation in Fe and FeCr systems, we employed a straightforward and productive model, known as creation-relaxation algorithm (CRA), to theoretically represent the low-energy, low-temperature irradiation events. The CRA model, which initially was introduced by Limoge *et al.* in the late 1980s [13], has been widely adopted by various researchers to study irradiation-induced microstructure evolution in different model materials [14–18]. This model progressively introduces point defects, specifically Frenkel pairs (FPs), into a pristine crystal lattice to simulate amorphization or radiation damage in solids. For the latter, the targeted irradiation dose is achieved by correlating the total number of inserted FPs (N_{FPI}) with the total number of lattice sites (N), expressed in displacements per atom (dpa)[3]. Notably, the generated defects primarily respond to the stress and strain fields induced by the FPs, mimicking actual low-energy damage events at very low-temperature regime. The CRA model used in this study has been thoroughly described in our recent publication [17]. Approximately, all model materials studied herein were subjected to 350 FP insertion (FPI) events, resulting in a cumulative irradiation dose of 0.35 dpa.

II. Methodology

In this letter, several different aspects of the irradiation-induced degradation were studied within the density functional theory (DFT) framework. The energy minimization calculation was conducted upon the CRA direct damage insertion. We used the projector-augmented plane wave method [19] implemented in the Vienna *ab initio* simulation package [20–23]. The conjugate gradient method [24] was employed to perform the total energy minimization after every FPI. The exchange–correlation term was treated in the generalized gradient approximation, as parameterized by Perdew, Burke, and Ernzerhof [25,26]. All calculations were spin-polarized, and periodic boundary conditions, along with the supercell approach, were employed.

We employed supercell sizes of 8 × 8 × 8 replicas of the bcc orthogonal unit cell, each containing 1024 atomic sites, for both Fe and FeCr systems. In dealing with these extensive electronic

3 The irradiation dose was assessed according to canonical displacement per atoms (dpa) [16], defined as the ratio of the FPI number to the total number of lattice sites ($\phi = N_{FPI}/N$). In this study, the total number of lattice sites are equal to 1024, regardless of Cr content.

structures, we sampled the Brillouin zones using the gamma point in *k*-space. For enhanced model prediction and reduced statistical noise, we utilized four and three distinct CRA trajectories for Fe and FeCr systems, respectively. Within each FeCr trajectory, the chromium contents of 5, 10, and 15 at.% were randomly distributed.

To optimize the balance between computational efficiency and accuracy, we employed two relaxation strategies. Full relaxation (FR) provided the most accurate representation, optimizing all degrees of freedom, but was computationally expensive. To address this, we primarily utilized ionic relaxation (IR) for computational feasibility. However, to ensure accuracy, we strategically interspersed FR calculations within each CRA trajectory for both Fe and FeCr systems. For volume-conserving simulations, we employed a pragmatic 250 eV cut-off energy and a self-consistent convergence criterion of 1 meV. Notably, fully relaxed calculations utilized a higher cut-off energy of 350 eV to mitigate volume-related artifacts, along with a stricter convergence criterion of 0.1 meV.

To better perceive the relationship between Cr additive and the stability of irradiation-induced defects, particularly the C15 Laves phase structure, we compared the formation energy, magneto-volume behavior, and local magnetic moments of these clusters in pure Fe and various spatial quasi-random (SQS) FeCr alloys. This analysis involved the systematic insertions of perfect C15 clusters into supercells containing 250 atoms and two additional self-interstitial atoms (SIAs), denoted as I_2^{C15} , employing a well-established methodology described in Refs. [27,28].

For these calculations, we utilized FR calculations with a $3 \times 3 \times 3$ *k*-point mesh, a 350 eV cut-off energy, and a convergence criterion of 0.1 meV. To ensure a comprehensive assessment of C15 cluster formation energy within FeCr systems, we employed a randomized distribution of these clusters within each SQS-FeCr alloy. This approach mitigates potential biases associated with Cr distribution in the matrix and provides more robust predictions.

Microstructure evolutions were characterized using the Wigner-Seitz analysis capabilities of OVITO [29]. Furthermore, polyhedral template matching analysis [30] with a root-mean-square deviation value of 0.25, was applied to recognize different structures as well as C15 clusters formed in damaged cells. Finally, the Supplemental Material pertinent to this study are comprehensively detailed in [31].

III. Results and discussion

In this study, we investigated the correlation between Cr content and irradiation-induced volume expansion, i.e. swelling, in FeCr alloys. Additionally, we systematically explored the alloying effect on the formation and stability of defect clusters, such as C15 Laves phase structures, particularly the three-dimensional C15-type clusters, formed in damaged Fe alloys.

Swelling was continuously monitored by calculating the ratio of the global pressure change (ΔP) to bulk modulus (B), i.e. $\Delta P/B$ [32], from IR calculations. Bulk moduli were selected for each FeCr system based on experimentally available data in the literature [33,34]. Additionally, swelling can be directly estimated by calculating the relative volume change, i.e. $\Delta V/V_0$, from FR calculations, wherein the volume and shape of the supercell along with ionic positions were consistently relaxed.

Direct first-principles calculations revealed a consistent two-stage swelling behavior across diverse Fe-based structures (Fig. 1). Initially, swelling exhibits a linear increase due to the rapid accumulation of point defects (Figs. S2 ans S3 in Supplemental Material [31]). These defects, generated by damage insertion (FPI), have differential relaxation volumes: SIA have a positive anisotropic volume relaxation (18.1 – 19.2 Å^3, depending on the type of SIAs), while vacancies posses negative isotropic small relaxation volume (3 and 6 Å^3). This interplay leads to the overall volume expansion or swelling. At low irradiation doses, about 0.05 dpa, a plateau emerges as stress and strain fields from defect clusters become constant. These fields, mediated by athermal interactions, influence defect behavior and potentially promote recombination or coalescence into more complex structures. This interplay between differential relaxation volumes and stress/strain field interactions governs the observed two-stage swelling behavior at low-temperature regime.

As shown in Fig. 1, our direct first-principles calculations reveal a consistent trend across different Fe-based structures: swelling initially increases linearly and then plateaus at the early stage of irradiation dose (0.05 dpa). This two-stage evolution of swelling corresponds to the direct response of materials to athermal interactions between point defects resulted from stress and strain field induced by FPI at low temperature. The linear accumulation of point defects, as also shown in Fig .1 and Fig. S1 [31] is a typical response of immobile SIAs and vacancies to irradiation at very low-temperature regime, where both SIAs and vacancies are athermally interact either recombine or coalesce to form related defect clusters.

Notably, a strong correlation exists between saturated swelling and Cr content in Fe-based alloys beyond 0.05 dpa. For instance, the irradiation-induced swelling of Fe is approximately 40% higher than that of Fe containing 15 at.% Cr. Experimental measurements of the alloying effect of Cr on

volumetric swelling under high-temperature and extensive irradiation conditions have been reported elsewhere [9,10,35]. Despite the high irradiation doses and elevated temperatures utilized in these experiments, it was found that even small quantities of Cr (~ 3 wt. %) significantly influenced the peak swelling of high purity FeCr alloys [10]. Pure Fe exhibited a maximum swelling of approximately 1%, while a reduction of about 90% was observed for other FeCr alloys, highlighting the substantial impact of Cr concentration in mitigating irradiation-induced swelling. This reduction in void swelling has been attributed to the formation of cavities, which were drastically reduced with increasing Cr content, rather than to the diffusivity of SIA clusters in FeCr alloys, as detailed by Terentyev *et al.* [36].

Considering the absence of thermally activated diffusion in our damaged structures, as well as the uniformity in the number density and size of vacancy clusters in the current study (see Fig. S2-S4 in Supplemental Material [31]), the magnetic properties of the FeCr system may play a role in differently responding to irradiation. Therefore, exploring the correlation between the change in total magnetization (M) and swelling may elucidate the relationship between Cr content and less volume expansion in damaged FeCr alloys, as illustrated in Fig. 2. This correlation emerges from various relaxation calculations, including IR and FR, derived from DFT-CRA calculations.

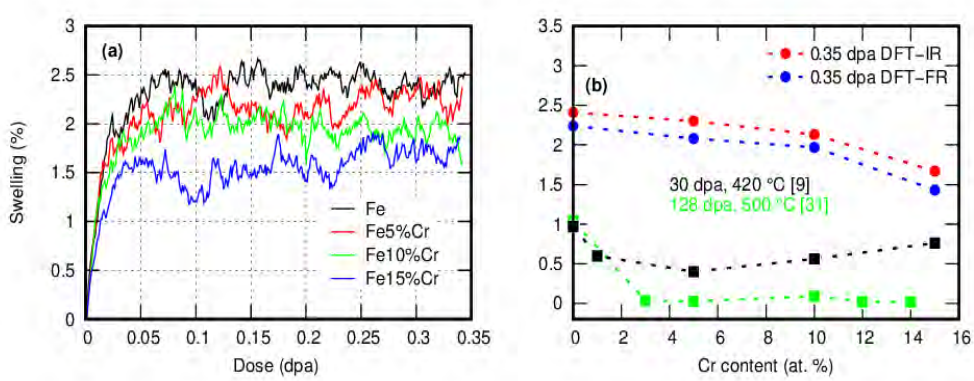

Figure 1: (a) Dose-dependent evolution of averaged irradiation-induced swelling in Fe and FeCr systems. (b) DFT prediction of swelling as a function of Cr content for pure Fe and binary FeCr alloys.

As depicted in Fig. 2(a), a clear linear correlation emerges between Cr content and the change in global M, leading to diverse responses of Fe-based alloys to irradiation damage. The incorporation of Cr atoms into the body-centered cubic (bcc) Fe structure results in a decrease in ferromagnetic (FM) ordering, thereby weakening ferromagnetism and resulting in a reduced magneto-volume

effect. The reduced magneto-volume in FeCr alloys with higher Cr content could be related to the different relaxation volume of Fe and Cr vacancies and interstitial defects, as investigated by Wróbel *et al*. [37] using DFT calculations. They showed that the surrounding elements (alloying environment) significantly impact the magnetic properties, formation energies and atomic-level distortions (elastic dipoles and relaxation volumes) of point defects in bcc Fe, Cr, and their random alloys. As demonstrated in [38], in binary FeCr alloys, the smaller relaxation volume of defects, in dumbbell configuration, are correlated with negatively larger ΔM.

Additionally, in an FeCr alloy, the elastic dipole tensors P and relaxation volume Ω_{relax} of vacancy and SIA defects vary significantly, with vacancies demonstrating negative relaxation volumes and SIAs exhibiting large positive values. Besides, the dipole tensors of vacancies exhibit near isotropy across the entire alloy composition range. Fe-Fe and Fe-Cr SIA dumbbells demonstrate greater anisotropy compared to Cr-Cr dumbbells. Fluctuations in the elastic dipole tensors of SIA defects are primarily attributed to the varying crystallographic orientations of the dumbbells.

Furthermore, there is a noticeable non-linear relationship between Cr content and irradiation-induced swelling in the damaged Fe-based alloys, as evidenced by performing DFT-FR calculations with enhanced accuracy (Fig. 2(b)). As seen in both Figs. 2(a) and (b), the ΔM, within the conditions applied in this study, drops linearly and then reach a saturated steady state where data points scattered around the final saturated swellings (see Fig. 1). However, each FeCr alloys differently response to irradiation with respect to magnetization change, compared to pure Fe. For instance, the addition of 5 at.% Cr hinders any change in total M, while further alloying of Cr accelerates the reduction in M and subsequently in swelling at a higher rate than pure Fe.

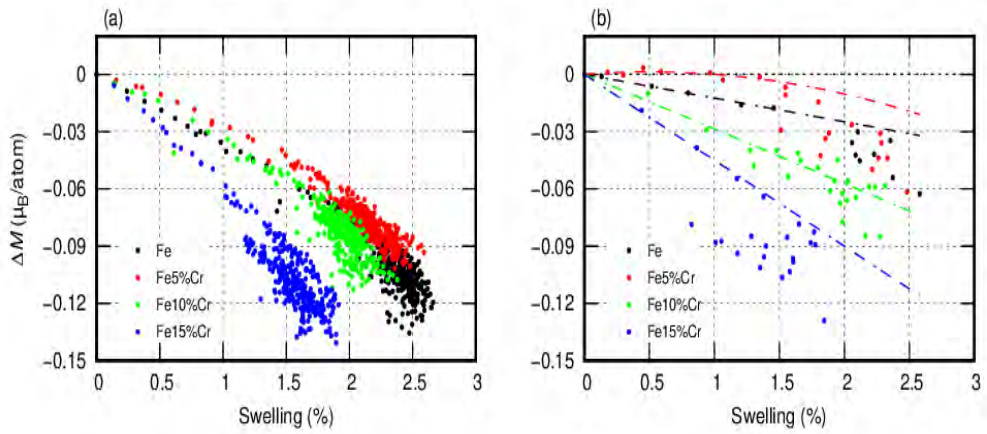

Figure 2: Averaged change in global M per atom relative to corresponding swelling in various Fe and FeCr systems. The left panel (a) displays the results of DFT-IR calculations ($\Delta P/B$), while the right panel (b) presents the outcomes of DFT-FR calculations ($\Delta V/V_0$) for several snapshots of the CRA trajectories. In the right panel, dashed lines fitted to the data points depict instances where ΔM has not yet reached saturation values.

The next step is to examine how the survived defect contents dynamically evolve to other forms of clusters as the results of developing stress fields in all damaged Fe-based alloys with respect to Cr contents. The dose-dependent evolutions of vacancies and interstitial defects and their relative clusters have been documented in Supplemental Material [31]. There, we showed that the defect number densities and the average and the largest sizes of defect clusters are not correlated to the Cr contents. As also indicated in Figs. S2-S4, the number density of survived isolated vacancies doubled the number density of mono interstitial, highlighting the higher tendency for interstitial defects to aggregate into larger clusters (see Fig. S4 in Supplemental Material [31]), even without thermally activated diffusion, a clear consequence of point defects evolution to irradiation-induced stress fields.

Although the defect statistics and cluster sizes are obviously independent of alloying element of Cr, formation energy, average local magnetic moments, size and stability of other three-dimensional cluster, i.e., C15 structures seem to be extremely affected by Cr percentage. Therefore, we focused on the formation and stability of the constrained defect clusters, especially C15 structures, and showed how increasing Cr content may effectively stabilize such complex defect clusters in irradiated bcc FeCr alloys.

As showed in other first-principles [17,27] and classical molecular dynamic simulations [28,39,18], the formation of C15 Laves phase structures is expected in irradiated bcc Fe lattice. Here, for the

first time, we also demonstrated not only the formation of imperfect and perfect C15-type structure, including clusters of triangular and/or hexagonal di-interstitial rings, is probable in Fe-based alloys but also the addition of more elemental Cr atoms leads to stabilization of such features and provide a condition for formation of even giant perfect C15-type structures, e.g., in Fe-15 at.% Cr alloys, according to our first-principles predictions and irradiation conditions applied in this study.

Figure 3 shows the dose-dependent evolution of atomic C15-type structures and the largest C15-type clusters found in damaged bcc Fe and FeCr alloys with divers Cr contents. As the antiferromagnetic (AF) alloying element of Cr increases, the C15-type structure content would increase and, therefore, may pave a way for formation of giant C15-type clusters (see Fig. 3(a)). Moreover, Fig. 3(b) highlights the higher tendency for SIAs to aggregate within giant C15 structures in a system with the higher Cr concentration.

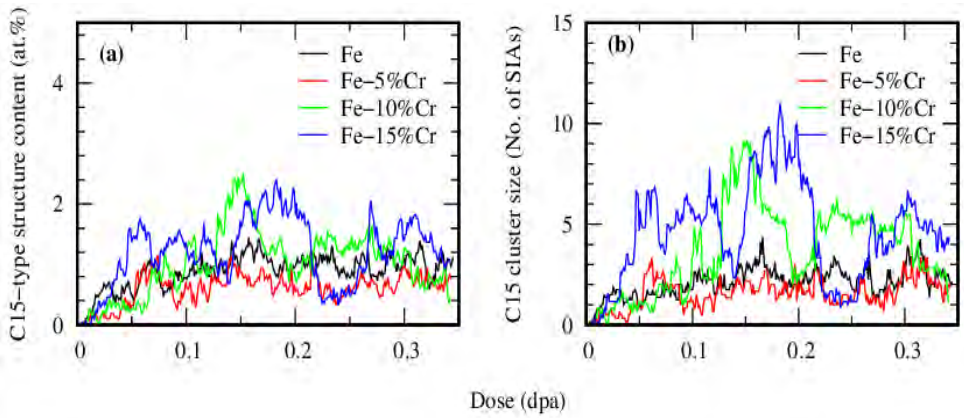

Figure 3: (a) Population of C15-type atomic structure and (b) the largest C15 Laves phase structures formed in Fe and FeCr alloys as a function of irradiation dose, represented by the Frenkel pair number divided by the total number of atoms.

As the system loses its ferromagnetic (FM) ordering due to the substitution of more Fe with Cr atoms, the stability of the C15 Laves phase appears to increase, facilitated by AF ordering and potentially quenching magnetization.

Consistent with prior studies [28], the formation energy of the three-dimensional C15 cluster which corresponds to 12 SIAs plus 10 vacancies (equivalent to net inclusion of two SIAs, noted as I_2) is higher than two SIAs with ⟨110⟩-dumbbell configuration in pure Fe. However, as we interfuse more Cr into bcc Fe lattice, the difference in formation energy of SIAs with C15 (I_2^{C15}) and parallel ⟨110⟩-dumbbell ($I_2^{\langle 110\rangle}$) configurations, denoted as $\Delta E^{I_2^{C15}-I_2^{\langle 110\rangle}}$, decreases from ~ 1 eV for pure Fe

to about 0.4 eV for Fe 15 at.% Cr, whit a 60% drop, highlighting the increased tendency of SIAs to form C15 cluster in FeCr alloys, compared to parallel ⟨110⟩-dumbbell, as showed in Fig. 4. The scattered data points in Fig. 4 are related to inclusion of C15 clusters at various locations within each SQS-FeCr alloy. It is worth noting that the formation energy of two SIAs with C15 configuration is even lower than that with parallel dumbbell for FeCr alloys with 15 - 20 at.% Cr, depending on the Cr atom distributions. Moreover, the incorporated C15 cluster in AF pure Cr led to a great $\Delta E^{I_2^{C15}-I_2^{\langle 110\rangle}}$ of 5.5 eV, signifying the optimized Cr content for stabilization of C15 clusters might be between 15 - 20 at.% Cr.

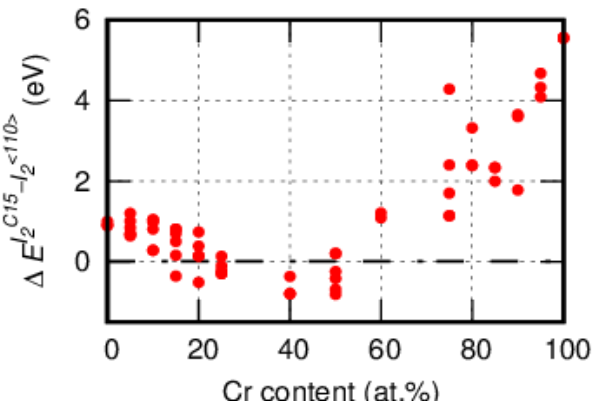

Figure 4: Difference in formation energy of intestinal cluster with C15 and <110>-dumbbell configurations as a function of Cr content.

Moreover, inspection of all CRA trajectories for both Fe and FeCr alloys showed that the formation of giant C15 with higher Cr content is not accidental, as the largest C15-type clusters among all Fe trajectories found to be open cage C15-type features consists of triangular and/or hexagonal di-interstitial rings, as indicated in Fig. 5(a). Whereas, formation of the perfect close cage of C15 cluster is common in the highest FeCr system with 15 at. % Cr, as illustrated in Fig. 5(b), and in 10 at. % Cr (Fig. S5 in Supplemental Material [31]).

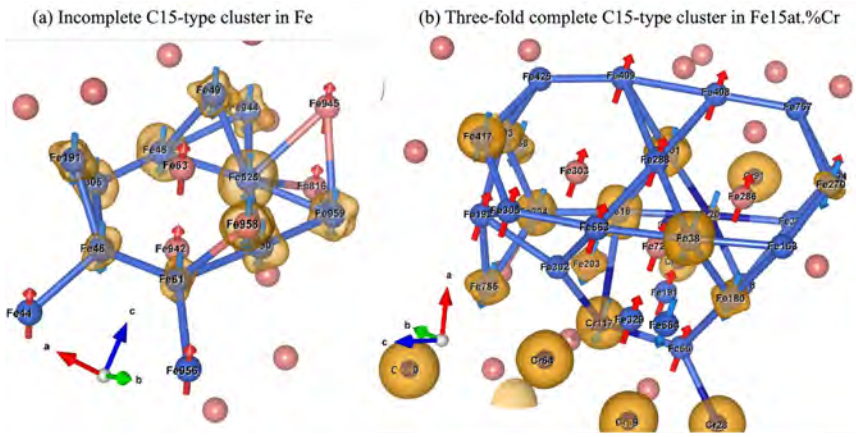

Figure 5: Comparison of a) an incomplete and b) a three-fold complete C15 clusters formed in damaged bcc Fe and Fe 15 at.% Cr, respectively. The orange clouds, enveloping atoms with spin-down orientation (blue arrows), represent the three-dimensional spin density isosurfaces of atoms which either underwent spin flip or possessing AF ordering. Red arrows symbolize the spin-up orientations. Pink atoms represent host lattice atoms, while blue atoms with no attached arrows underwent spin quench. For color references, the reader is referred to the web version of the article.

Interestingly, as noted in our recent studies [17,40] on pure Fe, the C15-type structures antiferromagnetically aligned with the bcc host Fe atoms while exhibiting a short-range ferromagnetism [40]. However, herein, as demonstrated in Figs. 6(a)-(d), the alloying Cr atoms weakens the short-range ferromagnetism of C15 cluster in host bcc Fe and transforms its magnetic state into locally short-range antiferromagnetism in FeCr alloys for higher atomic concentration of Cr. To elaborate this, the local magnetic moments of all 1024 atoms are plotted versus their related local atomic volumes (Voronoi cell) for each Fe and FeCr alloys in Fig. 6, at irradiation doses between 0.15 - 0.2 dpa, where the C15 Laves phases appear. As showed elsewhere, atoms forming C15 clusters tend to antiferromagnetically couple with FM atoms of host Fe lattice under constrain configuration [27,28,40,41]. Adding Cr atoms, weakening FM ordering and add more AF ordering into the host lattice.

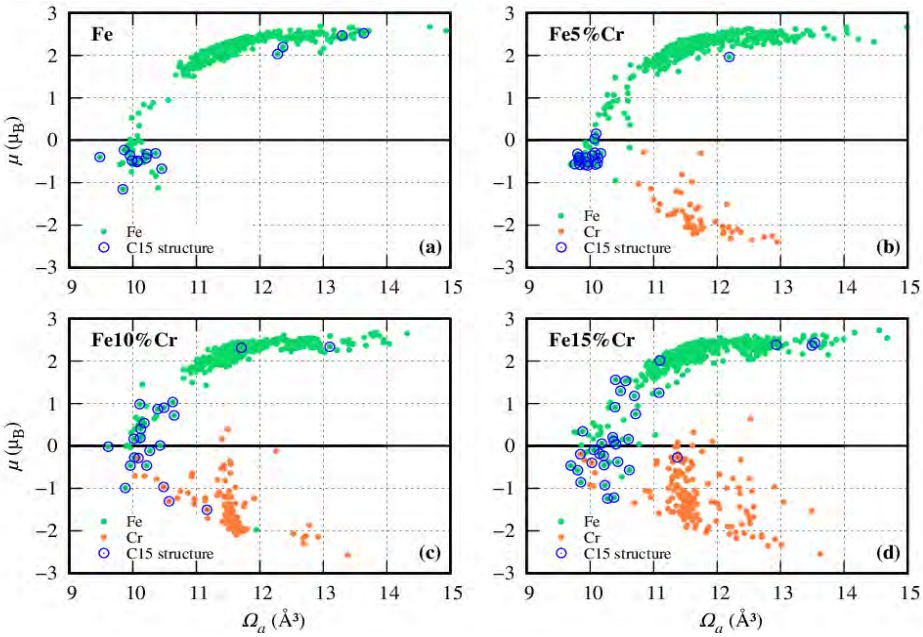

Figure 6: Distribution of local μ of atoms in relation to their local Ω_a in a) pure Fe, b) Fe 5 at.% Cr, c) Fe 10 at.% Cr, and d) Fe 15 at.% Cr at a dose range of 0.15-0.20 dpa. The blue circus surrounding some data points represent C15 Laves phase structure formed in damaged bcc Fe and FeCr systems. The green and orange data points represent the μ- Ω_a relationships for Fe and Cr, respectively.

The difference in behaviour of the C15 clusters in Fe and FeCr alloys could be related to the different magneto-volume effects of the systems, resulting from the different relaxation volumes of Fe and Cr vacancies and SIAs. A described by Wróbel *et al.* [38] using DFT calculations, the alloying environment significantly impacts the magnetic properties and atomic-level distortions (elastic dipoles and relaxation volumes) of point defects in bcc Fe, bcc Cr, and their disordered alloys. This influence arises from variations in the local volume and local moment of defects containing Fe-Fe and Fe-Cr dumbbells, as also reported in other studies [42–44]. Furthermore, variations in the magnitudes of magnetic moments associated with defects significantly affect the formation energy of these defects. With DFT ionic and full relaxation calculations, it has been demonstrated that the relaxation volumes and formation energies of SIA in dumbbell configurations within disordered FeCr alloys decrease with increasing Cr content. In addition, as shown by Marinica [16], the negative formation energy of clusters of four or more SIAs in the form of C15 structures, alongside the reduction in the formation energy of dumbbells with increasing Cr content in the SQS-FeCr alloys, supports that there is stabilization of the C15 clusters with increasing Cr content, as proposed in this study.

III. Conclusions

In conclusion, this study employed electronic structure calculations within the DFT framework to investigate the interplay between Cr alloying, irradiation-induced swelling, and the stability of the C15 Laves phase structure in irradiated Fe-Cr alloys. Utilizing dynamic DFT-driven CRA calculations, we studied the microstructural evolution under irradiation in terms of pressure changes and defect populations, particularly focusing on C15 Laves phase structure formation. While DFT-CRA simulations predicted minimal variations in total defect number densities between Fe and FeCr alloys, the size and stability of the observed C15 Laves phase were demonstrably influenced by the presence of Cr atoms in the irradiated structures. Furthermore, Cr addition not only suppressed irradiation-induced swelling, but also exhibited a non-linear response to irradiation, likely due to differing magneto-volume relationships. Finally, the observed decrease in total system magnetization with Cr addition is proposed to be responsible for the smaller relaxation volume and enhanced stability of C15 clusters formed within the damaged Fe alloys.

References

[1] R. L. Klueh and D. R. Harries, *High-Chromium Ferritic and Martensitic Steels for Nuclear Applications: (MONO 3)*, in ASTM International.

[2] J. Henry and S. A. Maloy, *9 - Irradiation-Resistant Ferritic and Martensitic Steels as Core Materials for Generation IV Nuclear Reactors*, in *Structural Materials for Generation IV Nuclear Reactors*, edited by P. Yvon (Woodhead Publishing, 2017), pp. 329–355.

[3] R. Klueh and D. Harries, editors , *Chapter 5-Oxidation, Corrosion, and Compatibility*, in *High-Chromium Ferritic and Martensitic Steels for Nuclear Applications*, Vols. MONO3-EB (ASTM International, 2001), p. 0.

[4] R. L. Klueh and A. T. Nelson, *Ferritic/Martensitic Steels for next-Generation Reactors*, J. Nucl. Mater. **371**, 37 (2007).

[5] R. Klueh and D. Harries, editors , *Chapter 9-Dimensional Stability-Swelling*, in *High-Chromium Ferritic and Martensitic Steels for Nuclear Applications*, Vols. MONO3-EB (ASTM International, 2001), p. 0.

[6] K. Vörtler, C. Björkas, D. Terentyev, L. Malerba, and K. Nordlund, *The Effect of Cr Concentration on Radiation Damage in Fe-Cr Alloys*, J. Nucl. Mater. **382**, 24 (2008).

[7] G. Bonny, C. Domain, N. Castin, P. Olsson, and L. Malerba, *The Impact of Alloying Elements on the Precipitation Stability and Kinetics in Iron Based Alloys: An Atomistic Study*, Comput. Mater. Sci. **161**, 309 (2019).

[8] A. Bakaev, D. Terentyev, G. Bonny, T. P. C. Klaver, P. Olsson, and D. Van Neck, *Interaction of Minor Alloying Elements of High-Cr Ferritic Steels with Lattice Defects: An Ab Initio Study*, J. Nucl. Mater. **444**, 237 (2014).

[9] E. A. Little and D. A. Stow, *Void-Swelling in Irons and Ferritic Steels: II. An Experimental Survey of Materials Irradiated in a Fast Reactor*, J. Nucl. Mater. **87**, 25 (1979).

[10] A. Bhattacharya, E. Meslin, J. Henry, A. Barbu, S. Poissonnet, and B. Décamps, *Effect of Chromium on Void Swelling in Ion Irradiated High Purity Fe-Cr Alloys*, Acta Mater. **108**, 241 (2016).

[11] V. Kuksenko, C. Pareige, and P. Pareige, *Cr Precipitation in Neutron Irradiated Industrial Purity Fe-Cr Model Alloys*, J. Nucl. Mater. **432**, 160 (2013).

[12] C. Pareige, V. Kuksenko, and P. Pareige, *Behaviour of P, Si, Ni Impurities and Cr in Self Ion Irradiated Fe–Cr Alloys – Comparison to Neutron Irradiation*, J. Nucl. Mater. **456**, 471 (2015).

[13] Y. Limoge, A. Rahman, H. Hsieh, and S. Yip, *Computer Simulation Studies of Radiation Induced Amorphization*, J. Non-Cryst. Solids **99**, 75 (1988).

[14] M. J. Sabochick and N. Q. Lam, *Radiation-Induced Amorphization of Ordered Intermetallic Compounds CuTi, $CuTi_2$, and Cu_4T_3: A Molecular-Dynamics Study*, Phys. Rev. B **43**, 5243 (1991).

[15] A. Chartier and M.-C. Marinica, *Rearrangement of Interstitial Defects in \alpha-Fe under Extreme Condition*, Acta Mater. **180**, 141 (2019).

[16] P. M. Derlet and S. L. Dudarev, *Microscopic Structure of a Heavily Irradiated Material*, Phys. Rev. Mater. **4**, 023605 (2020).

[17] E. Mansouri and P. Olsson, *Microstructure and Magnetization Evolution in Bcc Iron via Direct First-Principles Predictions of Radiation Effects*, Phys. Rev. Mater. **7**, 123604 (2023).

[18] E. Mansouri and P. Olsson, *Modeling of Irradiation-Induced Microstructure Evolution in Fe: Impact of Frenkel Pair Distribution*, Comput. Mater. Sci. **236**, 112852 (2024).

[19] P. E. Blöchl, *Projector Augmented-Wave Method*, Phys. Rev. B **50**, 17953 (1994).

[20] G. Kresse and J. Hafner, *Ab Initio Molecular Dynamics for Liquid Metals*, Phys. Rev. B **47**, 558 (1993).

[21] G. Kresse and J. Furthmüller, *Efficiency of Ab-Initio Total Energy Calculations for Metals and Semiconductors Using a Plane-Wave Basis Set*, Comput. Mater. Sci. **6**, 15 (1996).

[22] G. Kresse and J. Furthmüller, *Efficient Iterative Schemes for Ab Initio Total-Energy Calculations Using a Plane-Wave Basis Set*, Phys. Rev. B **54**, 11169 (1996).

[23] G. Kresse and D. Joubert, *From Ultrasoft Pseudopotentials to the Projector Augmented-Wave Method*, Phys Rev B **59**, 1758 (1999).

[24] T. Harte, G. D. Bruce, J. Keeling, and D. Cassettari, *Conjugate Gradient Minimisation Approach to Generating Holographic Traps for Ultracold Atoms*, Opt. Express **22**, 26548 (2014).

[25] J. P. Perdew, K. Burke, and M. Ernzerhof, *Generalized Gradient Approximation Made Simple*, Phys. Rev. Lett. **77**, 3865 (1996).

[26] J. P. Perdew, *Generalized Gradient Approximations for Exchange and Correlation: A Look Backward and Forward*, Phys. B Condens. Matter **172**, 1 (1991).

[27] M.-C. Marinica, F. Willaime, and J.-P. Crocombette, *Irradiation-Induced Formation of Nanocrystallites with C15 Laves Phase Structure in Bcc Iron*, Phys. Rev. Lett. **108**, 025501 (2012).

[28] L. Dézerald, M.-C. Marinica, L. Ventelon, D. Rodney, and F. Willaime, *Stability of Self-Interstitial Clusters with C15 Laves Phase Structure in Iron*, J. Nucl. Mater. **449**, 219 (2014).

[29] A. Stukowski, *Visualization and Analysis of Atomistic Simulation Data with OVITO–the Open Visualization Tool*, Model. Simul. Mater. Sci. Eng. **18**, 015012 (2009).

[30] P. M. Larsen, S. Schmidt, and J. Schiøtz, *Robust Structural Identification via Polyhedral Template Matching*, Model. Simul. Mater. Sci. Eng. **24**, 055007 (2016).

[31] *See Supplemental Material at [Http://Link.Aps.Org/Supplemental/ Xx.Xxxx/PhysRevLetters.Xx.Xxxxxx], for Further Details Regarding Comparisons of Defect Populations and Cluster Sizes in Various FeCr Alloys (with Varying Cr Content), Interstitial Cluster Size Variations with C15 Laves Phase Configurations Influenced by Cr Concentration, and the Intricacies of Irradiation-Induced Changes in Local Magnetization as a Function of Local Atomic Volume (Including Magneto-Volume Relations of C15 Cluster-Forming Atoms with Cr Content).*

[32] D. V. Schroeder, *Energy in Thermal Physics*, in *An Introduction to Thermal Physics*, edited by D. V. Schroeder (Oxford University Press, 2021), p. 0.

[33] G. R. Speich, A. J. Schwoeble, and W. C. Leslie, *Elastic Constants of Binary Iron-Base Alloys*, Metall. Trans. **3**, 2031 (1972).

[34] P. Olsson, I. A. Abrikosov, L. Vitos, and J. Wallenius, *Ab Initio Formation Energies of Fe–Cr Alloys*, J. Nucl. Mater. **321**, 84 (2003).

[35] Y.-R. Lin, A. Bhattacharya, D. Chen, Y. Zhao, J.-J. Kai, J. Henry, and S. J. Zinkle, *The Role of Cr Concentration and Temperature on Cavity Swelling with Co-Injected Helium in Dual-Ion Irradiated Fe and Fe-Cr Alloys*, Mater. Des. **223**, 111134 (2022).

[36] D. Terentyev, P. Olsson, L. Malerba, and A. V. Barashev, *Characterization of Dislocation Loops and Chromium-Rich Precipitates in Ferritic Iron–Chromium Alloys as Means of Void Swelling Suppression*, J. Nucl. Mater. **362**, 167 (2007).

[37] J. S. Wróbel, M. R. Zemła, D. Nguyen-Manh, P. Olsson, L. Messina, C. Domain, T. Wejrzanowski, and S. L. Dudarev, *Elastic Dipole Tensors and Relaxation Volumes of Point Defects in Concentrated Random Magnetic Fe-Cr Alloys*, Comput. Mater. Sci. **194**, 110435 (2021).

[38] J. S. Wróbel, M. R. Zemła, D. Nguyen-Manh, P. Olsson, L. Messina, C. Domain, T. Wejrzanowski, and S. L. Dudarev, *Elastic Dipole Tensors and Relaxation Volumes of Point Defects in Concentrated Random Magnetic Fe-Cr Alloys*, Comput. Mater. Sci. **194**, 110435 (2021).

[39] A. Esfandiarpour, J. Byggmästar, J. P. Balbuena, M. J. Caturla, K. Nordlund, and F. Granberg, *Effect of Cascade Overlap and C15 Clusters on the Damage Evolution in Fe: An OKMC Study*, Materialia **21**, 101344 (2022).

[40] E. Mansouri and P. Olsson, *First-Principles Predictions of Structural and Magnetic Phase Stability in Irradiated α-Fe*, Mater. Res. Lett. **12**, 477 (2024).

[41] F. Willaime, C. C. Fu, M. C. Marinica, and J. D. Torre, *Stability and Mobility of Self-Interstitials and Small Interstitial Clusters in α-Iron: Ab Initio and Empirical Potential Calculations*, Nucl. Instrum. Methods Phys. Res. Sect. B Beam Interact. Mater. At. **228**, 92 (2005).

[42] D. Nguyen-Manh, M. Yu. Lavrentiev, and S. L. Dudarev, *Magnetic Origin of Nano-Clustering and Point Defect Interaction in Fe–Cr Alloys: An Ab-Initio Study*, J. Comput.-Aided Mater. Des. **14**, 159 (2007).

[43] P. Olsson, C. Domain, and J. Wallenius, *Ab Initio Study of Cr Interactions with Point Defects in Bcc Fe*, Phys. Rev. B **75**, 014110 (2007).

[44] C. S. Becquart, R. Ngayam Happy, P. Olsson, and C. Domain, *A DFT Study of the Stability of SIAs and Small SIA Clusters in the Vicinity of Solute Atoms in Fe*, J. Nucl. Mater. **500**, 92 (2018).

Supplemental Material for

Ab initio predictions of irradiation-induced imperfections in FeCr: alloying effects and magnetic ordering on C15 Laves phase stability

Ebrahim Mansouri[a, 1] and Pär Olsson[a, 2]

[a]*KTH Royal Institute of Technology, Nuclear Science and Engineering, Stockholm, Sweden*

I. Dose-dependent energy and pressure changes with DFT-CRA model

Figure S1 compares the average change in energy per atom (ΔE/atom) and pressure (ΔP) as a function of displacement per atom (dpa) in bcc Fe and FeCr systems within supercells with side lengths of 8× a_0.

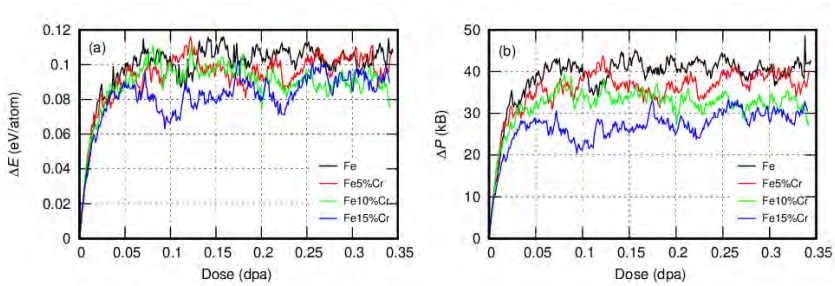

Figure S1: Comparison of (a) the dose-dependent ΔE/atom and (b) ΔP predicted by the DFT method.

II. Comparison of dose-dependent evolution of defect contents

Figure S2 compares the dose-dependent evolution of surviving Frenkel pair (FP), isolated interstitial (I_{mono}), and interstitial cluster (I_C) contents as functions of irradiation dose predicted by DFT-driven CRA simulations for Fe and FeCr systems within supercells with side lengths of 8×a_0.

[1]Corresponding author: mansouri.ebrahim@yahoo.com
[2]Corresponding author: polsson@kth.se

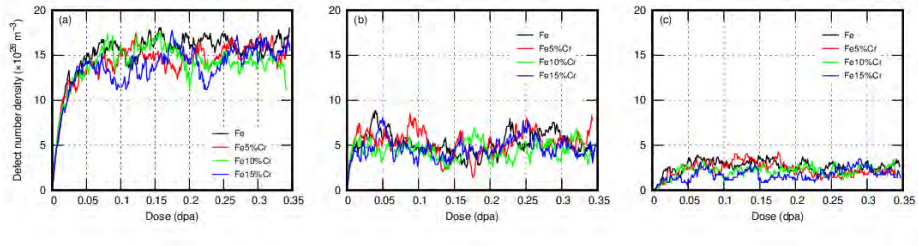

Figure S2: Dose-dependent number density of the a) FP, b) I_{mono}, and c) I_C for different Fe and FeCr systems.

Figure S2 compares the dose-dependent evolutions of survived FP, isolated vacancy (V_{mono}), and vacancy cluster (V_C) contents as functions of irradiation dose predicted by DFT-driven CRA calculations for Fe and FeCr systems within supercells with side lengths of $8\times a_0$.

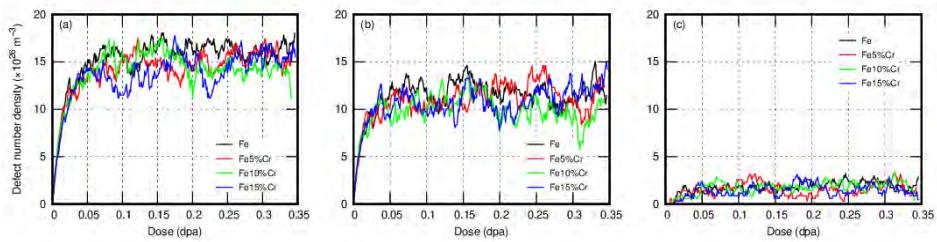

F

igure S3: Dose-dependent number density of the a) FP, b) V_{mono}, and c) V_C for different Fe and FeCr systems.

III. The dose-dependent evolutions of defect cluster sizes as functions of irradiation dose

Figure S4 displays the dose-dependent evolutions of the average (left panels) and largest (right panels) I_C and V_C in different Fe and FeCr systems

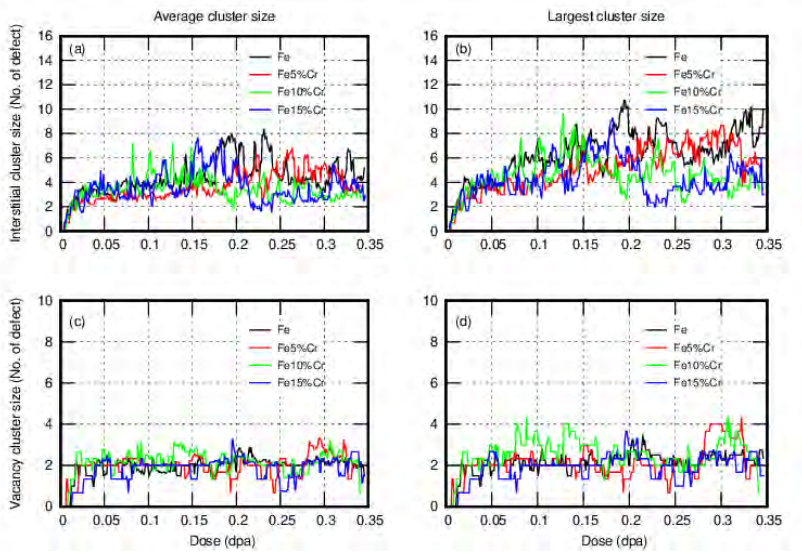

Figure S4: Dose-dependent evolutions of the a) average and b) largest interstitial clusters along with the c) average and d) largest vacancy clusters formed in Fe and FeCr alloys, resulting from DFT-CRA calculations.

IV. The size of C15 Laves phase structure with respect to Cr contents

Figure S5 indicates the size dependency of C15 Laves phase structure with respect to at. % Cr in Fe and FeCr alloys. As the Cr content increases, the formation and stability of such three-dimensional clusters are improved by increasing antiferromagnetic ordering.

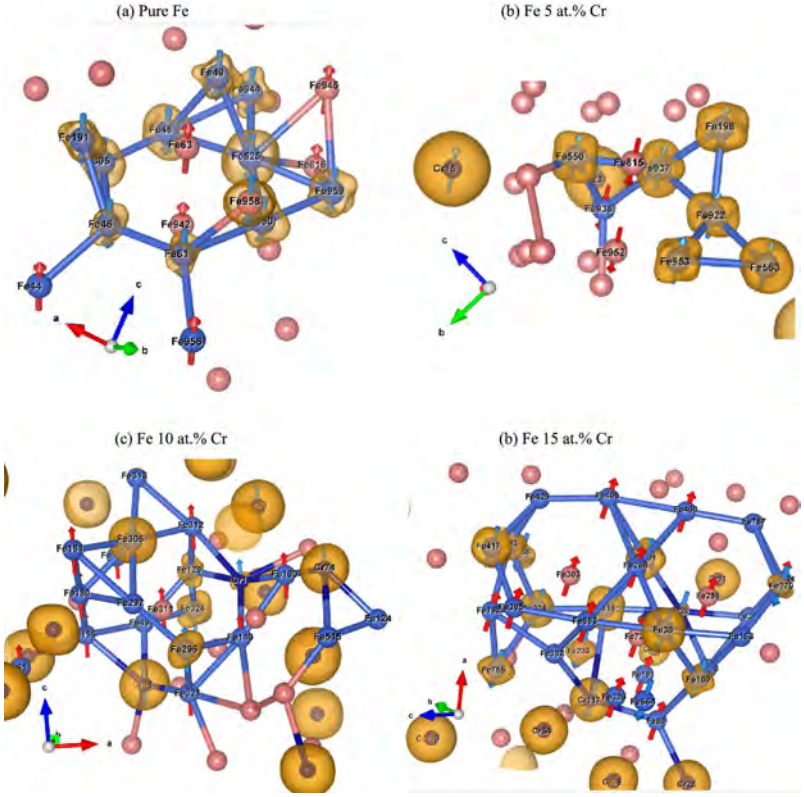

Figure S5: Evolution of C15 Laves phase structure with increasing Cr concentration in (a) Fe, (b) Fe-5 at.% Cr, (c) Fe-10 at.% Cr, and (d) Fe-15 at.% Cr as obtained form dynamic DFT-CRA calculations in supercells with side length of $8 \times a_0$. Orange clouds, enveloping atoms with spin-down orientation (blue arrows), represent the three-dimensional spin density isosurfaces of atoms either underwent spin flip or with antiferromagnetic ordering (Cr atoms). Red arrows symbolize spin-up orientations. Blue atoms without arrows have undergone spin quenching.

Paper V

Atomistic modelling of irradiation-induced microstructure evolution in FeCrAl and Al_2O_3: effects of high irradiation doses

E. Mansouri and P. Olsson
Manuscript in preparation

Atomistic modelling of irradiation-induced microstructure evolution in FeCrAl and α-Al_2O_3: effects of high irradiation doses

Ebrahim Mansouri[a, 1] and Pär Olsson[a, 2]

[a]*KTH Royal Institute of Technology, Nuclear Science and Engineering, Stockholm, Sweden*

Abstract

This study employs electronic structure calculations coupled with the creation-relaxation algorithm to model irradiation damage events and resulting microstructural imperfections in body-centred cubic (bcc) FeCrAl alloys and hexagonal close-packed (hcp) α-Al_2O_3. The resulting microstructure evolution is primarily driven by the stress fields induced by sequential direct damage insertions. Defect populations and their corresponding cluster characteristics are analysed as a function of modelled irradiation dose. We investigate the stability and magnetic characteristics, particularly in FeCrAl alloys, of the formed defect structures. Our first-principles simulations reveal that C15 Laves phase defect structures can form dynamically during irradiation in FeCrAl and are stabilized by increasing aluminium content. Under irradiation doses of approximately 1 displacement per atom (dpa), damaged α-Al_2O_3 experiences continuous irradiation-induced volume expansion, approaching a saturation state with around 7% swelling. In contrast, the metallic alloys reach a saturation level of 2.2% swelling, about three times lower than that predicted for alumina. Additionally, the formation of an amorphous phase in damaged corundum alumina supports the expectation of significant irradiation-induced swelling. The results show a net reduction in total magnetization per atom in FeCrAl. Furthermore, interstitial sites exhibit a tendency for spin polarization opposing the intrinsic atomic site spins when the coordination number increases compared to the pristine lattice structure. These findings suggest that radiation-induced damage could potentially be traced using non-destructive measurements of bulk magnetization changes.

1 Corresponding author: mansouri.ebrahim@yahoo.com
2 Corresponding author: polsson@kth.se

I. Introduction

The selection of appropriate structural materials is paramount in the pursuit of safer and more efficient nuclear energy systems [1]. These materials play a critical role in ensuring the integrity and longevity of nuclear reactors, including advanced liquid-lead fast reactors [2], light water reactor [3], and fusion systems [4]. Among these candidate materials are body-centred cubic (bcc) FeCrAl alloys, prized for their high oxidation resistance under irradiation and high-temperature environments, making them suitable for Generation IV fast reactor and accident tolerant fuel (ATF) cladding in the nuclear power industry [5]. A key consideration for such materials is the formation of alumina (Al_2O_3) scale for corrosion resistance. This alumina layer exhibits exceptional resistance to oxidation and corrosion, as well as its compatibility with various nuclear system coolants, such as supercritical water, heavy liquid metals, such as lead and lead–bismuth eutectic, and high-temperature helium gas. This protective alumina layer shields structural materials from the harsh environments prevalent in nuclear reactors.

Developing the ATF cladding presents a critical challenge. One particular concern is managing potential swelling at the interface between the metallic FeCrAl alloy and the protective alumina layer. This swelling needs to be balanced with maintaining the material mechanical stability throughout the operational lifespan of the nuclear reactor [6,7]. This study contributes to this ongoing effort by using theoretical simulation means to investigate how the irradiation-induced microstructure evolve in both bcc FeCrAl alloys and hexagonal close-packed (hcp) corundum alumina. Understanding these structural changes allows us to assess the mechanical stability and irradiation response of these combined materials (oxide and metal) and evaluate their suitability as robust alternatives for ATF cladding.

We employ a theoretical model known as the creation-relaxation algorithm (CRA) to simulate the formation and evolution of point defects and defect clusters within the materials as a function of irradiation dose. The CRA model has shown promise in predicting microstructure evolution and magnetization changes in different model materials such as Fe and FeCr alloys [8–11]. The CRA model is rooted in a similar method introduced by Limoge and Rahman in 1988 for studying irradiation damage in non-crystalline materials [12]. This technique involves successively introducing point defects, such as Frenkel pairs (FPs) or isolated interstitials, into a perfect lattice structure to model amorphization. More recently, Derlet and Dudarev refined this method to explore radiation-induced microstructure evolution in Fe and W [11].

While initially formulated for classical interaction models, we reformulated the CRA method for a first-principles paradigm. This approach is inspired by observations of irradiation-induced saturation under certain conditions [13]. Our method involves conjugate gradient relaxation following a designated number of random atomic displacements within a supercell, mimicking the insertion of randomly generated FPs. We construct supercells with a reasonable number of atoms (N). We randomly select an atom, displace it to a random location within the supercell, relax the system to a local energy minimum for the damaged structure, and repeat this process until a desired displacement per atom (dpa) is achieved.

In the CRA framework, the damage dose parameter in dpa becomes deterministic and straightforward [11]: each displacement contributes exactly $1/N$ dpa, where N is the total number of atoms in the supercell. Since it is feasible to perform many hundreds of creation-relaxation events sequentially [9], it is, therefore, possible to directly simulate doses up to 1 dpa using first-principles methods. In this study, we first applied the single Frenkel pair insertion (FPI) technique to the magnetically complex lattice of relevance: bcc Fe with 10 atomic percent (at.%) Cr and varying Al concentrations (2, 4, 6 at.%). For non-magnetic hcp alumina, however, we applied an accelerated method in which five FPI are implanted at each step and are relaxed simultaneously, in order to easily reach higher irradiation doses of the order of 1 dpa.

Using computationally demanding first-principles modelling offers significant advantages over classical interatomic potential methods because it handles chemical complexity with ease and provides the full electronic structure detail. For modelling irradiation-induced damage in FeCrAl or alumina, reliable interatomic potentials may not be readily available, making density functional theory (DFT) a more suitable approach.

The present study expands the capabilities of the CRA model by investigating its effectiveness with uniform self-interstitial atom (SIA) distributions and its applicability to studying irradiation damage in both FeCrAl and Al_2O_3 systems. However, the CRA model, by design, introduces single FPs, and therefore does not explicitly account for the high-energy defect production regime. Nevertheless, the model considers linear and non-linear lattice deformations induced by defect accumulation, making it suitable for predicting defect evolution at very low temperatures [11] and for dynamically evolving a relevant damaged microstructure to its saturation stage. In this regime, defect diffusion is primarily driven by stresses and strain fields generated by the FPI mechanisms.

The paper is organized into three distinct sections. Section II explains the details of the method used in this study, including the specific computational techniques employed. Section III delves into the results, providing a thorough discussion of the key findings from our DFT-driven CRA simulations.

II. Methodology

This study applied the DFT and used the CRA approach to directly generate damage events and to qualitatively investigate the resulting microstructure evolution in FeCrAl model alloys and the Al_2O_3 oxide. Comprehensive details of the CRA model can be found in Refs. [8,11]. The static DFT calculations give us access to total energies that can be translated into formation and binding energies for defects and complexes.

We used the projector-augmented plane wave (PAW) method [14] implemented in the Vienna *ab-initio* simulation package (VASP) [15–17]. The conjugate gradient method [18] was used to perform the energy minimization after every FP insertion. The exchange–correlation term was treated in the generalized gradient approximation, as parametrized by Perdew, Burke, and Ernzerhof [19,20]. All calculations for bcc FeCrAl were spin-polarized, and periodic boundary conditions, along with the supercell approach, were employed. For the CRA modelling of radiation-induced microstructure evolution, we used a supercell of 8 × 8 × 8 copies of the bcc orthogonal unit cell, comprised of 1024 atoms for FeCrAl. For this relatively large supercell, the Brillouin zone was sampled by the Gamma point in *k*-space. To improve the prediction of the model and lower the statistical noise, we used three distinct CRA trajectories for each condition.

For alumina, the non-magnetic calculations were performed using periodic boundary conditions with a supercell containing 5 × 5 × 2 hexagonal unit cells with a total number of 1500 atoms. The integrations over the Brillouin zone were performed using the Gamma point only. The electronic wave functions were expanded in a plane wave basis set with an energy cutoff of 450 eV. Like FeCrAl systems, to decrease the statistical noises, we used three different CRA trajectory tests. The total energy convergence was set to be 1 meV. The atomic coordinates were relaxed until the forces acting on each atom were reduced to less than 0.01 eV/Å.

In this study, we explored how damaged materials respond to simulated radiation exposure (FPI events) by considering different aspects of the system characteristics. These aspects include how the positions of atoms change, the overall size of the simulation, and its shape. Ideally, for materials undergoing intense radiation, we would fully relax the system after each damage event by adjusting atom positions, size, and shape of the simulation cell. However, doing this within DFT requires quite demanding

computing time. To find a balance, we focused on relaxing only the positions of atoms in our simulations, keeping the overall size and shape of the simulation space constant. We then systematically used full relaxation on specific snapshots in one single CRA trajectory to gain deeper insights without significantly increasing the computational cost.

For our simulations on FeCrAl alloys with constant volume (ionic relaxation), we used a cut-off energy of 250 eV and a 1 meV energy convergence criterion for the self-consistent electronic loop calculation. However, when fully relaxed the simulation cell, we used a higher cut-off energy of 350 eV to prevent volumetric changes from affecting energy and forces due to varying volume and the number of included plane waves. To enhance the accuracy, we also reduced the energy minimization convergence criterion to 0.1 meV in this simulation set.

Theoretically speaking, two primary approaches can be utilized to estimate irradiation-induced volume expansion (swelling). In the full relaxation calculation paradigm, insights into volumetric change is straightforward and can be obtained by monitoring the supercell volume. Alternatively, the ionic relaxation calculation method can track the changes in hydrostatic pressure. Full relaxation calculations achieve a global pressure convergence to zero, allowing both the supercell volume and shape to evolve during the simulation. This can lead to explicit volumetric swelling. In contrast, simulations conducted under fixed volume conditions can estimate radiation-induced swelling by relating the change in global hydrostatic pressure (ΔP) to the bulk modulus (B) of the material using the following relationship established by [21]:

$$\frac{\Delta V}{V_0} = \frac{-\Delta P}{B}. \quad (1)$$

Where $\Delta V/V_0$ is the relative volumetric change following a perturbation, here as a result of FPIs.

Using the DFT-CRA method, we also investigated the irradiation-induced change in the electronic charge distribution and in the global and local magnetization. Accordingly, isosurfaces depicting the variations in spin and charge densities surrounding those defects were computed using VESTA [22].

To identify and analyse the formation of defect clusters after irradiation, a Python code was used to simulate damage creation and insertion within the material. Microstructure evolution was then analysed using a combination of Python and the open-source visualization software OVITO [23]. The Wigner-Seitzs analysis tool in OVITO was also employed to pinpoint the remaining vacancies and SIAs in the simulated structures after relaxation.

To achieve an irradiation dose of 1 dpa accoutring to the canonical dpa definition [11], we employed two distinct approaches for FP defect insertion. The chosen approach depended on both the magnetic properties and system size. For smaller, actively magnetic systems like Fe and its alloys, we employed the strategy outlined previously in [8]. In such cases, where the desired dose is in the order of 1 dpa and the system size is computationally manageable, the ideal approach involves inserting one FP defect per lattice site (*n/N*) at a time into the supercell. Following this, for a supercell containing 1024 atomic sites, we should insert 1024 single FP defects to reach 1 dpa. This approach was continued until a dose of 0.35 dpa was achieved, consistent with our prior studies [8]. However, for larger and non-magnetic systems like Al_2O_3, this one-by-one insertion strategy becomes computationally inefficient to reach the target dose of 1 dpa. Therefore, we implemented an alternative method involving five simultaneous FPI insertions per each relaxation step, similar to the method used for molecular dynamic driven CRA simulation in [9], repeated 300 times. This approach successfully achieved the desired dose for the non-magnetic Al_2O_3 system within DFT-driven CRA simulation. It was first verified that the simulations involving a single FPI at a time, or five concurrent FPI gave nearly indistinguishable trajectories.

Moreover, for identifying defect clusters, we established specific criteria based on the distances between nearest-neighbour atoms. In FeCrAl alloys, vacancies were considered clustered if they were within 3.5 Å of each other, and SIAs were clustered if they were within 4.1 Å. These distances correspond to the midpoint between the second and third for vacancies, and third and fourth nearest-neighbour distances for SIAs, respectively, according to the literature [24,25].

Alumina required slightly different criteria for identifying defect clusters due to its unique atomic arrangement. This is because the distances between neighbouring atoms in Al_2O_3 differ from those in FeCrAl. In alumina, vacancies were considered clustered if they were within 2.7 Å of each other, and SIAs were clustered if they were within 3.35 Å. These specific distances were determined through a thorough coordination analysis performed using OVITO.

Furthermore, recognizing the unique coordination of C15 atoms, an additional analysis technique was implemented. The OVITO built-in polyhedral template matching (PTM) analysis [26] was utilized with a root-mean-square deviation value of 0.25 to effectively identify these specific atomic arrangements.

III. Results and discussion

1) Irradiation-induced pressure change in FeCrAl and Al_2O_3

To study the dose-dependent evolution of microstructure in damaged structure, one can trace the change in total energy and hydrostatic pressure. Figure 1 presents the change in hydrostatic pressure (ΔP) as a function of dpa for Fe alloys of increasing complexity (Fe, Fe-10%Cr, and Fe-10%Cr-4%Al) and for Al_2O_3, as derived from DFT-CRA calculations. The plot reveals an initial linear increase in pressure for all materials, eventually followed by a steady-stage saturation. This saturation occurs around 0.05 dpa for Fe-based alloys and around 0.1 dpa for alumina, which aligns with previous studies [8,11]. The significantly higher number of FPI required for reaching saturation in the microstructure of hcp Al_2O_3 can be attributed to its distinct crystal structure, the short ranged directional bonding and the nature of charged point defects within this ceramic structure. Furthermore, the observed pressure change in alumina at saturation is seven times higher than that in FeCrAl. This suggests a comparatively larger irradiation-induced swelling in alumina compared to FeCrAl. This observation is supported by Equation 1, considering the approximately similar bulk moduli of both structures. Table 1 summarizes the elastic properties of Fe alloys and Al2O3 extracted from different literature.

Table 1: The elastic properties of Fe alloys and alumina.

Structure	a_0 (Å)	c (Å)	B (GPa)
Fe	2.831	--	16.9[a]
Fe-10%Cr	2.839	--	15.6[a]
Fe-10%Cr-4%Al	2.845	--	15.6[*]
Al_2O_3	4.808	13.125	25.2[b]

a. Ref. [27,28] , b. Ref [29], * the bulk modulus for Fe10Cr4Al has been selected to be equal to that of Fe10Cr.

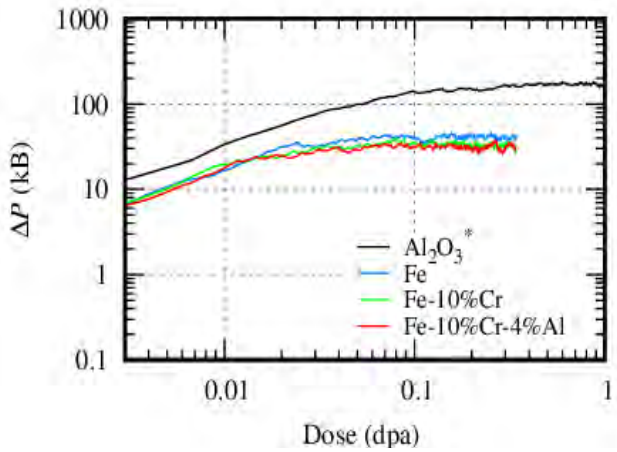

Figure 1: Comparison of the hydrostatic pressure change as a function of FPI for different bcc Fe alloys and hcp alumina.

2) Dose-dependent evolution of defect concentrations in Fe alloys

Figure 2 shows the dose-dependent evolution of defect number densities (FPs, isolated interstitials, and interstitial clusters) in different model material of Fe and its alloys with 10 at.% Cr [30] and varying Al concentrations (2, 4, and 6 at.%). As seen, there are no large differences among defect number densities for different Fe alloys. That is, the average number densities of both isolated interstitials (I_{mono}) and interstitial clusters (I_C) within the Fe-10Cr-*x*Al alloys exhibit minimal variation across the different Al concentrations. This suggests a relatively stable defect population in these FeCrAl systems with varying Al content. In addition, as shown in Figure 2, the FP evolves only within two distinct stages: a rapid, linear accumulation stage up to 0.05 dpa, which transitions smoothly into establishing a saturation steady state beyond 0.05 dpa.

Furthermore, a closer look at Figure 2(b) reveals a meaningful difference in the evolution of I_{mono} for the Fe-10Cr-6Al alloy with respect to the rest, specifically within the irradiation dose range of 0.2 - 0.35 dpa. This specific composition shows a pronounced decrease in the number density of isolated interstitial compared to the other Al concentrations. This observation suggests a potential transformation of these SIAs into larger defect clusters. This finding underscores the importance of analysing the dose-dependent evolution of icosahedral structure content, particularly for Fe-10Cr-6Al. Interestingly, DFT-CRA simulations (Figure 3) show a remarkable influence of Al on the formation of a specific type of cluster defect, i.e. the C15 cluster, within the matrix for the same dose range (0.2 - 0.35 dpa). At these specific doses, the Fe-10Cr-6Al alloy exhibits the highest atomic percentage of

icosahedral structures compared to other Fe-based alloys investigated in this study and the previous ones [8,30].

Consequently, as indicated in Figure 4, the DFT-CRA simulations reveal that the Fe-10Cr-6Al alloy exhibited the formation of the largest C15 cluster observed among all other model materials investigated in this and the previous studies [8,30]. This observation suggests that incorporating higher Al concentrations than about 4 at. % may significantly promote and stabilize the formation of C15 cluster defects within the FeCrAl matrix. This aligns with the previously reported stabilizing effect of chromium additions on C15 structures in binary FeCr alloys [30].

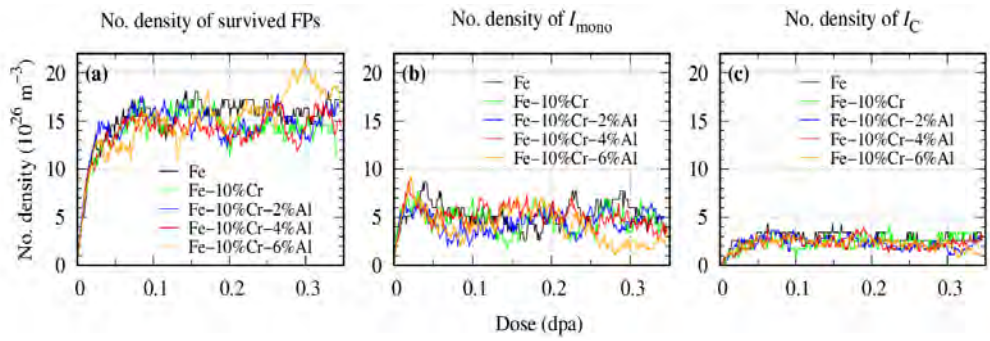

Figure 2: Dose-dependent number density of the a) FP, b) I_{mono}, and c) I_C for Fe, Fe-10at.%Cr and Fe-10 at.%Cr with different Al content.

As shown in Fig. 4, clustering of Cr and Al atoms is observed in proximity to the C15 structure formed in damaged Fe-10Cr-6Al alloys at an irradiation dose of 0.3 dpa. This highlights a synergistic effect between Cr and Al atoms in stabilizing this giant interstitial cluster. Based on the predicted magnetic characteristics of the C15 cluster using DFT-driven CRA calculations, these clusters might exhibit unique magnetic properties, potentially enabling their experimental detection. [10]. To further justify this, the total magnetization change in different FeCrAl systems is plotted in Fig. 5. It is obvious from Fig. 5 that during irradiation dose 0.25 – 0.35 dpa and in the systems with heights Al content, the total change in magnetization is pronounced, indicating a clear correlation between C15 cluster size and total magnetization change.

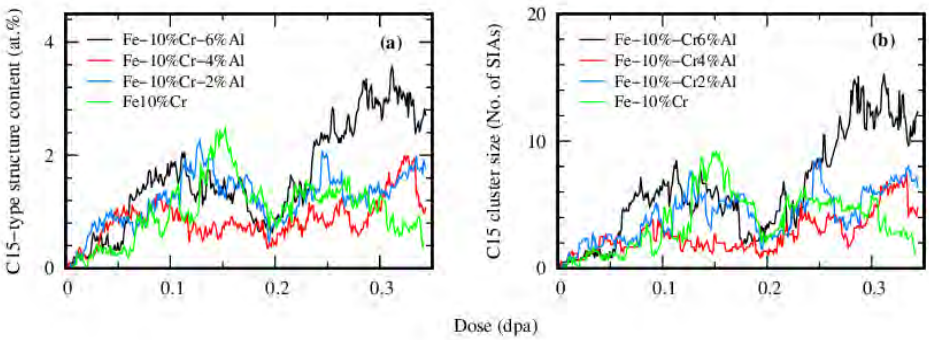

Figure 3: Population of C15 Laves phase atomic structure and (b) the largest C15 Laves phase structures formed in Fe10%Cr with diverse Al contents as a function of irradiation dose

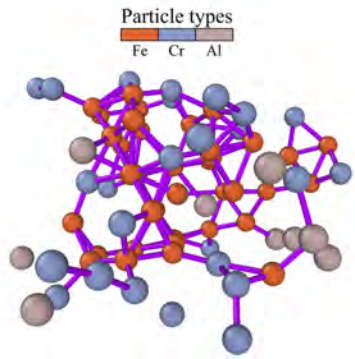

Figure 4: The largest C15 clusters formed in irradiated bcc Fe-10%Cr-6%Al applying DFT-CRA simulation, containing 23 self-interstitial atoms.

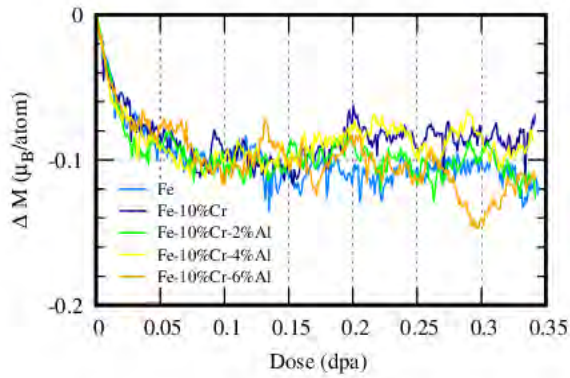

Figure 5: Total magnetisation changes as a function of irradiation dose for different FeCrAl systems.

3) Dose-dependent evolution of defect concentrations in Al_2O_3

In examining the defect number densities across FeCrAl alloys and in the aluminium oxide, the DFT-CRA predictions from this study predicts a notable discrepancy in these quantities between the oxide and metallic matrices. Specifically, our findings indicate a substantial difference in the concentration of surviving FPs at saturation levels (ranging from 0.5 to 1 dpa) within Al_2O_3 compared to FeCrAl alloys (see Fig. 6(a) and Fig. 2(a) respectively). Remarkably, the concentration of FPs in Al_2O_3 is approximately seven times higher than that obtained for FeCrAl alloys within the saturation range of 0.05 to 0.35 dpa. This discrepancy suggests a significantly lower rate of recombination between vacancies and SIAs in Al_2O_3, particularly within temperature ranges where both interstitials and vacancies are considered immobile, evolving primarily due to athermal interactions induced by irradiation-induced stress fields or lattice deformation. The disparity in surviving FP contents is likely attributed to the distinct crystal structures of hcp alumina and bcc FeCrAl alloys and the significant difference in the atomic bonding. This structural and bonding differences result in quite diverse recombination distances for FPs in the respective materials.

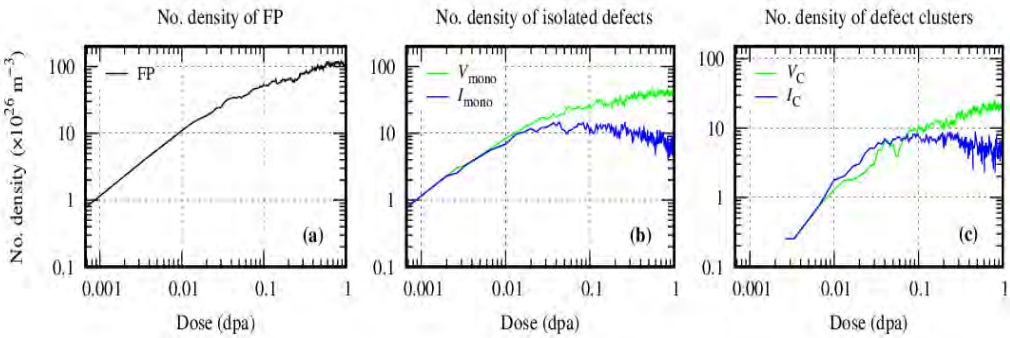

Figure 6: Dose-dependent number density of the a) FP, b) isolated defects (I_{mono} and V_{mono}), and c) defect clusters (I_C and V_C) in alumina.

The distinct characteristics of charged defects in Al_2O_3, including their distribution and different volume relaxation values, are likely to influence the recombination rate of FPs and thereby contribute to the observed differences in microstructure evolution under low-temperature irradiation conditions. Specifically, the higher concentration of FPs in Al_2O_3 compared to FeCrAl alloys, as illustrated in Fig. 7, manifests as a notable factor in the heightened irradiation-induced swelling observed in alumina. This difference, with FPs being approximately three times more abundant in Al_2O_3, underscores the significant impact of defect dynamics on swelling between the two materials.

In the hcp structure of alumina, the arrangement of atoms may provide fewer favourable sites for recombination, leading to a higher concentration of surviving FPs compared to FeCrAl alloys with a bcc structure. It can be understood by analysing radial pair distribution function, as shown in Fig. 7 Furthermore, *ab initio* calculations shows that migration of interstitial oxygen atoms leads to the formation of dumbbells with regular oxygen atoms. It has been proved that the optimized configuration of fixed dumbbell is a more preferable alternative to recombination of interstitial oxygen atom with oxygen vacancy [31].

Additionally, the presence of charged defects, such as oxygen vacancies, in Al_2O_3 could further affect defect recombination dynamics due to electrostatic interactions. Furthermore, given that a compound has distinct sublattices and that e.g. an Al SIA finding an O vacancy does not lead to recombination but to anti-site creation means that the interaction of newly created FPs with other pre-existing defects, such as interstitial clusters, will vary quite significantly between the two types of materials, influencing their recombination rates and ultimately impacting microstructure evolution. These factors collectively

contribute to the observed differences in FP behaviour and subsequent microstructural evolution between Al_2O_3 and FeCrAl alloys under the model conditions.

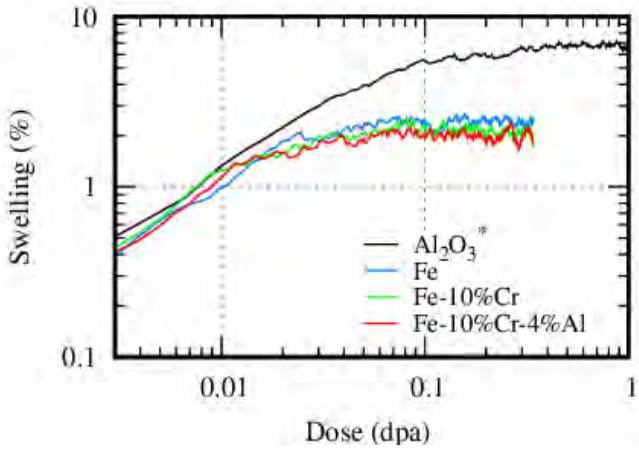

Figure 7: Comparison of irradiation-induced swelling in Fe-based alloys and in Al_2O_3.

A striking contrast between metallic alloys and the oxide compound alumina lies in their response to irradiation-induced phase transformations. Our recent first-principles investigation [10] into bcc Fe revealed the occurrence of polymorphism induced by irradiation, resulting in the emergence of antiferromagnetic face-centered cubic (fcc) and nonmagnetic hcp Fe structures, particularly evident under conditions of high pressure and very low temperature. Conversely, our analysis of damaged nonmagnetic Al_2O_3 structures suggests a distinct irradiation response, characterized primarily by amorphization without the formation of discernible polymorphic phases, as shown in Fig. 8.

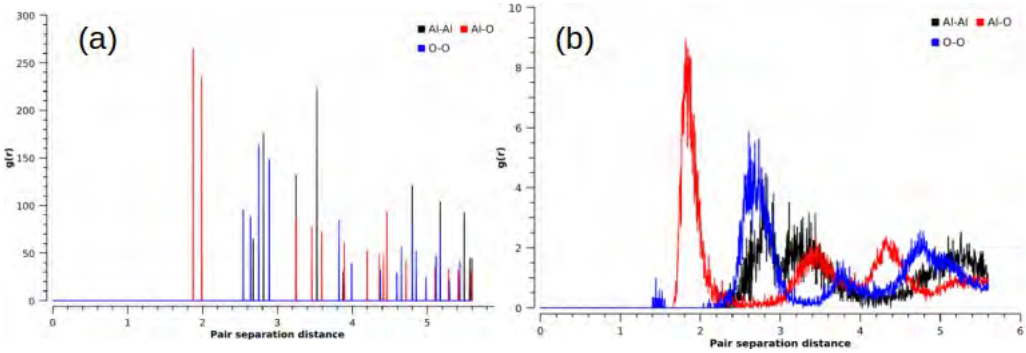

Figure 8: The radial pair distribution function of Al and O a) for a perfect corundum structure and b) at the end of irradiation dose of 1 dpa.

Moreover, Figure 9 depicts the predominant cluster formed in alumina at the highest irradiation dose (1 dpa) as a large interstitial cluster comprising oxygen and aluminum, with average contributions of 55% and 45%, respectively.

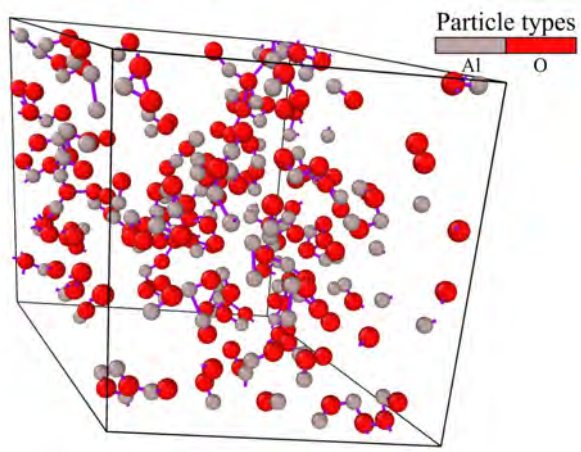

Figure 9: Structure of interstitial defect (clusters and isolated interstitial) in damaged Al_2O_3 at irradiation dose of 1 dpa.

IV. Conclusion

In summary, our investigation utilizing electronic structure calculations driving the creation-relaxation algorithm has provided valuable insights into the irradiation-induced damage mechanisms and ensuing microstructural evolutions in both bcc FeCrAl alloys and hcp α-Al_2O_3. Through the analysis of defect populations and cluster characteristics across varying irradiation doses, we have elucidated the intricate interplay between stress fields and direct damage insertions, driving the evolution of microstructures in these materials. Particularly noteworthy is the formation and stabilization of icosahedral structures akin to the C15 Laves phase in FeCrAl, a phenomenon correlated with increasing aluminium content in the Fe-10at.% Cr base matrix. Moreover, our simulations underscore the distinct and different response of metallic alloys and oxide compounds to irradiation, with alumina exhibiting significant volume expansion as a result of lower rate of Frenkel pair recombination, compared to FeCrAl alloys under similar damage insertion conditions. Contrastingly, metallic alloys manifest a saturation level of swelling that is established faster and results in a considerably lower value than that observed in alumina. For the industrial application of an FeCrAl alloy on which the alumina scale protects against a chemically and mechanically aggressive environment, this could have serious implications if the alumina scale were crystalline since a thin scale that swells faster than the substrate would be likely to spall off. From experimental investigation, the alumina on FeCrAl alloys preferentially forms a thin amorphous or mixed amorphous–nano-crystalline scale, which should be much less affected by irradiation damage. Notably, our findings also shed light on the magnetic properties of FeCrAl alloys, revealing a reduction in total magnetization per atom alongside intriguing spin polarization tendencies in interstitial sites. These discoveries hold promise for the potential utilization of non-destructive bulk magnetization measurements as a means to trace radiation-induced damage. Overall, our research contributes to a deeper understanding of irradiation effects on complex materials, paving the way for improved strategies in radiation damage mitigation and monitoring.

Acknowledgments

Financial support was provided by the Swedish Foundation for Strategic Research (SSF) under Grant No. ARC19-0043 (SUNRISE centre), as well as by the Swedish Research Council (VR) for projects 2017-06458 and 2019-04156. This work was partly affiliated with the EUROfusion Consortium, funded by the European Union under Grant Agreement No 101052200. Additional funding contributions were received from the Euratom Research and Training Programme under grant agreements No 755039 (M4F project) and No 740415 (IL TROVATORE project) during the period of

2019–2020. The authors express their gratitude for computational resources provided by the National Academic Infrastructure for Supercomputing in Sweden (NAISS; PDC at KTH and NSC at LiU), as well as from the CINECA HPC Center in Italy. It is important to note that the views expressed in this work are solely those of the authors and do not necessarily reflect the views of the European Union or the European Commission, which cannot be held accountable for them.

References

[1] K. L. Murty and I. Charit, *Structural Materials for Gen-IV Nuclear Reactors: Challenges and Opportunities*, Journal of Nuclear Materials **383**, 189 (2008).

[2] C. Ganguly and V. (Victor) Inozemtsev, *Structural Materials for Liquid Metal Cooled Fast Reactor Fuel Assemblies : Operational Behaviour* (International Atomic Energy Agency, Vienna, 2012).

[3] Y. Yamamoto, B. A. Pint, K. A. Terrani, K. G. Field, Y. Yang, and L. L. Snead, *Development and Property Evaluation of Nuclear Grade Wrought FeCrAl Fuel Cladding for Light Water Reactors*, Journal of Nuclear Materials **467**, 703 (2015).

[4] C. Cabet, F. Dalle, E. Gaganidze, J. Henry, and H. Tanigawa, *Ferritic-Martensitic Steels for Fission and Fusion Applications*, Journal of Nuclear Materials **523**, 510 (2019).

[5] K. Sakamoto et al., *Development of Accident Tolerant FeCrAl-ODS Fuel Cladding for BWRs in Japan*, Journal of Nuclear Materials **557**, 153276 (2021).

[6] J. Ejenstam, B. Jönsson, and P. Szakalos, *Optimizing the Oxidation Properties of FeCrAl Alloys at Low Temperatures*, Oxid Met **88**, 361 (2017).

[7] J. Engkvist, S. Canovic, K. Hellström, A. Järdnäs, J.-E. Svensson, L.-G. Johansson, M. Olsson, and M. Halvarsson, *Alumina Scale Formation on a Powder Metallurgical FeCrAl Alloy (Kanthal APMT) at 900–1,100 °C in Dry O2 and in O2 + H2O*, Oxid Met **73**, 233 (2010).

[8] E. Mansouri and P. Olsson, *Microstructure and Magnetization Evolution in Bcc Iron via Direct First-Principles Predictions of Radiation Effects*, Phys. Rev. Mater. **7**, 123604 (2023).

[9] E. Mansouri and P. Olsson, *Modeling of Irradiation-Induced Microstructure Evolution in Fe: Impact of Frenkel Pair Distribution*, Computational Materials Science **236**, 112852 (2024).

[10] E. Mansouri and P. Olsson, *First-Principles Predictions of Structural and Magnetic Phase Stability in Irradiated $\ alpha$-Fe*, Materials Research Letters **12**, 477 (2024).

[11] P. M. Derlet and S. L. Dudarev, *Microscopic Structure of a Heavily Irradiated Material*, Phys. Rev. Materials **4**, 023605 (2020).

[12] Y. Limoge, A. Rahman, H. Hsieh, and S. Yip, *Computer Simulation Studies of Radiation Induced Amorphization*, Journal of Non-Crystalline Solids **99**, 75 (1988).

[13] S. J. Zinkle, *1.03 - Radiation-Induced Effects on Microstructure, in Prepared for the Oak Ridge National Laboratory under Contract No. DE-AC05-000R22725*, in *Comprehensive Nuclear Materials*, edited by R. J. M. Konings (Elsevier, Oxford, 2012), pp. 65–98.

[14] P. E. Blöchl, *Projector Augmented-Wave Method*, Phys. Rev. B **50**, 17953 (1994).

[15] G. Kresse and J. Furthmüller, *Efficiency of Ab-Initio Total Energy Calculations for Metals and Semiconductors Using a Plane-Wave Basis Set*, Computational Materials Science **6**, 15 (1996).

[16] G. Kresse and J. Furthmüller, *Efficient Iterative Schemes for Ab Initio Total-Energy Calculations Using a Plane-Wave Basis Set*, Phys. Rev. B **54**, 11169 (1996).

[17] G. Sun, J. Kürti, P. Rajczy, M. Kertesz, J. Hafner, and G. Kresse, *Performance of the Vienna Ab Initio Simulation Package (VASP) in Chemical Applications*, Journal of Molecular Structure: THEOCHEM **624**, 37 (2003).

[18] T. Harte, G. D. Bruce, J. Keeling, and D. Cassettari, *Conjugate Gradient Minimisation Approach to Generating Holographic Traps for Ultracold Atoms*, Opt. Express, OE **22**, 26548 (2014).

[19] J. P. Perdew, *Generalized Gradient Approximations for Exchange and Correlation: A Look Backward and Forward*, Physica B: Condensed Matter **172**, 1 (1991).

[20] J. P. Perdew, K. Burke, and M. Ernzerhof, *Generalized Gradient Approximation Made Simple*, Phys. Rev. Lett. **77**, 3865 (1996).

[21] D. V. Schroeder, *An Introduction to Thermal Physics*, 17th edition (Addison Wesley, An Francisco, CA, 2000).
[22] K. Momma and F. Izumi, *VESTA: A Three-Dimensional Visualization System for Electronic and Structural Analysis*, J Appl Cryst **41**, 653 (2008).
[23] A. Stukowski, *Visualization and Analysis of Atomistic Simulation Data with OVITO–the Open Visualization Tool*, Modelling Simul. Mater. Sci. Eng. **18**, 015012 (2009).
[24] C. Björkas and K. Nordlund, *Comparative Study of Cascade Damage in Fe Simulated with Recent Potentials*, Nuclear Instruments and Methods in Physics Research Section B: Beam Interactions with Materials and Atoms **259**, 853 (2007).
[25] D. Terentyev, C. Lagerstedt, P. Olsson, K. Nordlund, J. Wallenius, C. S. Becquart, and L. Malerba, *Effect of the Interatomic Potential on the Features of Displacement Cascades in $\allpha$-Fe: A Molecular Dynamics Study*, Journal of Nuclear Materials **351**, 65 (2006).
[26] P. M. Larsen, S. Schmidt, and J. Schiøtz, *Robust Structural Identification via Polyhedral Template Matching*, Modelling Simul. Mater. Sci. Eng. **24**, 055007 (2016).
[27] P. Olsson, I. A. Abrikosov, L. Vitos, and J. Wallenius, *Ab Initio Formation Energies of Fe–Cr Alloys*, Journal of Nuclear Materials **321**, 84 (2003).
[28] G. R. Speich, A. J. Schwoeble, and W. C. Leslie, *Elastic Constants of Binary Iron-Base Alloys*, Metallurgical Transactions **3**, 2031 (1972).
[29] *High-temperature Elastic Constant Data on Minerals Relevant to Geophysics - Anderson - 1992 - Reviews of Geophysics - Wiley Online Library*, https://agupubs.onlinelibrary.wiley.com/doi/abs/10.1029/91RG02810.
[30] E. Mansouri and P. Olsson, *Ab Initio Predictions of Irradiation-Induced Imperfections in FeCr: Alloying Effects and Magnetic Ordering on C15 Laves Phase Stability*, Phys. Rev. Lett. **XX**, (Submitted manuscript).
[31] Y. F. Zhukovskii, A. Platonenko, S. Piskunov, and E. A. Kotomin, *Ab Initio Simulations on Migration Paths of Interstitial Oxygen in Corundum*, Nuclear Instruments and Methods in Physics Research Section B: Beam Interactions with Materials and Atoms **374**, 29 (2016).